TRANSONIC FLOW THROUGH SHARP-LIPPED CONVERGENT NOZZLES

George Maurice Alder

Thesis submitted for the Degree of

Doctor of Philosophy

University of Edinburgh

January 1976

CONTENTS

ACKNOWLEDGEMENTS

I would like to thank the many people whose help and good wishes have enabled me to complete this thesis.

My supervisors, Professor J.L. King and Dr. G.O. Goudie have given me much encouragement during the last few years. Professor King provided a great deal of valuable advice on both the work itself and the preparation of the thesis. Dr. Goudie's careful reading and criticism of the draft manuscript led to many improvements.

The experimental apparatus was skillfully constructed, and then patiently re-constructed by the Department's Technical Staff under the guidence of the late Mr. D. Pringle and, more recently, of Mr. G. Smith.

The presentation of the thesis owes much to the typing of Mrs. Avril Davies and of Miss Margaret Lindsay.

Most of all, I must thank my wife, Beth, who has lived with theses (firstly her own and then mine) for far too long. She has given more help and support than anybody else and performed the final task of turning my manuscrpt into readable English.

ABSTRACT

This work is a theoretical and experimental study of the flow of ideal gases through convergent nozzles with sharp lips. Two-dimensional flows between plane nozzle walls and axially symmetric flows through conical walls are considered. A particular case of the problem is the flow through a circular orifice. Downstream from the sharp lip the flow forms a jet bounded by a free streamline. Both subcritical (subsonic jet velocities) and supercritical (supersonic jet velocities) flows are examined.

The theoretical formulation of the problem considers the irrotational flow of an ideal gas, and the subsonic and supersonic (if present) regions are solved separately by numerical methods. The subsonic region is transformed to the hodograph plane and the governing equation solved by a finite - difference method. The supersonic region is solved in the physical plane by the method of characteristics. The two parts of the solution are matched by adjusting the common boundary condition on the sonic line. Truncation errors in the numerical solution have been estimated and techniques devised to reduce their magnitude. A computed survey of theoretical sharp-lipped nozzle performance is presented which examines discharge coefficients and flowfield velocity distributions for a range of wall angles.

Possible reasons for differences in nozzle performance between theory and practice are discussed. It is argued that such differences are mainly caused by departures from the ideal sharp-lipped geometry. An experimental investigation into the effect of lip geometry on discharge coefficient is described. A method is proposed for modifying the theoretical discharge coefficients to allow for small radii of curvature at the lip.

CHAPTER 1

INTRODUCTION

1.1 Description of Problem

The flow of fluids through nozzles and orifices has been a problem of practical interest for many years. The essential character of such flows is that they combine an internal flow bounded by fixed walls, with a jet flow bounded by a free streamline. In the latter part of the nineteenth century attention was directed towards the discharge of liquids beneath sluices, over weirs, and through slots and orifices. Experimental data were collected and theories were proposed for the simpler cases of these incompressible phenomena. During the early years of this century the growing importance of aeronautics and the internal combustion engine led to an interest in compressible flow. The growth of rocketry and the jet engine led, in the 1930's and 40's, to an intense study of the problems of high-pressure, high-speed gas flow. Today, it is still the applications within the aero-space field which are primarily responsible for maintaining interest in nozzle and orifice flows. However, other applications do exist in flow metering, in fluidics, and in the processing and transmission of natural gas.

We are concerned here with the irrotational, isentropic flow of ideal gases through symmetrical, convergent nozzles whose configuration is shown in the sketch on the following page.

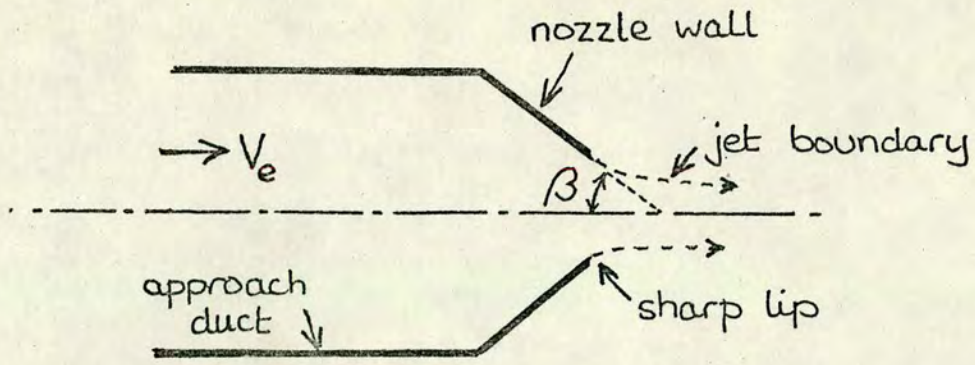

Two classes of nozzle are considered. These are axially symmetric, in which the nozzle wall is a conical surface, and two-dimensional, in which the walls are two convergent planes. An important geometric parameter in either class is the angle, β, which the wall makes with the axis. The case $\beta = 90^{\circ}$ is of particular interest because it defines a round orifice (axially symmetric) or a long slit (two-dimensional) in a plane wall. The above sketch also shows a parallel approach duct lying upstream of the convergent section. It is assumed that the duct is very long and that the gas enters it with a uniform approach velocity V_e. This represents, in an idealised form, an aircraft propulsion nozzle or (with $\beta = 90^{\circ}$) an orifice plate in a pipe. Particular attention will be paid, however, to the case of zero approach velocity in which the convergent part of the wall extends to infinity. It is an easier case to handle theoretically, and the assumption $V_e = 0$ gives adequate results in many practical applications.

The nozzle is assumed to discharge into a still atmosphere to form a jet on whose boundary streamline the gas is at the atmospheric pressure, p_a. It is assumed in the theoretical analysis of the problem that the nozzle lip, where the wall meets the exit plane, is sharp. The boundary streamline should therefore separate from the

wall at that point. A truly sharp lip is an ideal which cannot be achieved in practice. There will always be some blunting which affects the point of separation and the flow in the throat region. So long as we are considering isentropic flow, the velocity on the jet boundary is determined by the nozzle pressure ratio, r. This parameter is defined as $r = p_a/p_o$, the ratio of the downstream atmospheric pressure to the flow stagnation pressure. Important differences in the nature of the flow occur as r takes different values. When the pressure ratio is close to unity, the gas velocity is everywhere small and so are the effects of compressibility. We may therefore regard the limit $r = 1$ as representing incompressible flow. The most significant value of r is the "critical" pressure ratio, r_s, at which the gas on the jet boundary just reaches sonic velocity. For an ideal gas with constant specific heats of ratio γ we have the well-known result $r_s = (2/\gamma+1)^{\gamma/\gamma-1}$, which gives the value $r_s = 0.528$ for air ($\gamma = 1.4$). We define as "subcritical" those flows whose pressure ratio lies in the range $r_s < r \leqslant 1$. The gas velocity in a subcritical flow is subsonic at all points in the flowfield. The range $0 < r < r_s$ defines "supercritical" flows, where the gas velocity reaches supersonic values in the jet. Within the supercritical range lies the "choking" pressure ratio, r_c, below which the subsonic and transonic regions of the flowfield are independent of r.

The structure of the jet differs radically between subcritical and supercritical flow. The subcritical jet (if we discount viscous interaction with the atmosphere) tapers smoothly away from the nozzle exit plane, the streamlines eventually becoming parallel at an infinite distance downstream. The particular case of critical flow $r = r_s$ was examined by Ovsiannikov (1949) who showed that the streamlines became

parallel within a finite distance from the exit plane. The super-critical jet was described by Guderley (1947). The jet boundary initially converges to form a "vena contracta" a short distance outside the exit plane beyond which it diverges. There are two important regions of flow - subsonic flow, largely within the confines of the nozzle walls, and supersonic flow in the jet. These regions meet along the curved "sonic line" which extends from the lip to the axis. The downstream flowfield ultimately contains a complex shock-wave pattern, but we are concerned in this work only with the area close to the exit plane. Here the shockwaves have not yet formed and the general assumption of isentropic flow is still valid.

1.2 Survey of Previous Work

This section is devoted to a brief review of published work which is relevant to a study of sharp-lipped nozzle flows. It is convenient to subdivide the discussion into three parts: theoretical studies of two-dimensional flows, theoretical studies of axially symmetric flows, and experimental studies. One aspect of nozzle performance which has received considerable attention is the discharge coefficient (C_d) which we may define as the ratio of the actual mass flow to the mass flow given by uniform flow in the throat at the same pressure ratio. It is the only parameter of interest in many practical applications of nozzle flows such as flow metering, and it provides a useful parameter on which to centre a discussion. Discharge coefficients are relatively easy to measure experimentally although it is difficult to achieve high accuracy; they are often relatively easy to derive from theoretical solutions.

1.2.1 Two-dimensional flows

Incompressible, two-dimensional flows may be analysed by complex variable methods and, in the case of the nozzle problem, the foundations were laid by Helmholtz (1868) and Kirchoff (1869). Lord Rayleigh (1876) showed that the discharge coefficient of a slit in an infinite wall ($\beta = 90^{\circ}$; $V_e = 0$) was $C_d = 0.611$. Von Mises (1917) extended the complex variable analysis to cover a range of wall angles and approach velocities. More recent work (e.g. Larock 1969) has examined incompressible two-dimensional flows through nozzles with curved walls.

The theory of critical and subcritical, two-dimensional nozzle flows owes much to Chaplygin (1902) who used the hodograph transformation and expressed the solution of the problem as a series of hypergeometric functions. Chaplygin concentrated on the flow through a slit in a wall ($\beta = 90^{\circ}$) and derived the result $C_d = 0.74$ for the case of zero approach velocity. Jacob (1936) and Falkovich (1957) developed Chaplygin's analysis to cover a wider range of wall angles. Cohen (1960) has published an approximate solution to the two-dimensional subcritical nozzle problem. Arynov (1958) derived a simplified form of Chaplygin's results, valid for small wall angles. The case of the critical jet, in which the streamlines become parallel with uniform, sonic velocity at a plane situated a short distance from the nozzle exit, is of interest because it offers an approach to the design of convergent-divergent nozzles with uniform flow in the throat. Critical jets have been studied by Ovsiannikov (1949), Roumieu (1952) and Aslanov and Legova (1959). General treatments of the whole subcritical problem have been given by Gurevich (1965) and McLaughlin and Pack (1969).

The analysis of the supercritical nozzle problem is complicated by the presence of a transonic region where the governing equations change from elliptic to hyperbolic form. Methods usually applied to transonic flow in convergent-divergent nozzles (e.g. Sauer 1947 or Hall 1962) are not valid here because they require a continuous wall with finite curvature. The method of Hall (1962) involves expansions in terms of the radius of curvature of the nozzle throat wall. Kliegel and Levine (1969) improved Hall's solution and showed that the limit of zero radius of curvature could be reached. Kliegel and Levine claim to have thus solved, in principle, the supercritical sharp-lipped nozzle problem. This claim is, unfortunately, not valid since their analysis applies only to nozzles whose walls are circular in axial section and takes no account of the presence of the conical convergent portion. Hopkins and Hill (1966), Kliegel and Quan (1968), Prozan and Kooker (1970) and Stow (1972) studied the flow through nozzles which have a very high curvature at the throat, but none of these methods can be extended to the limit of infinite curvature.

The first theoretical solution of a supercritical, two-dimensional sharp-lipped nozzle problem was given by Frankl (1947) who extended Chaplygin's analysis into the supersonic region for the case of choked flow through a slit. Frankl found the discharge coefficient to be $C_d = 0.85$. Gushchin (1959) extended Frankl's method to include the effect of non-zero approach velocity. Norwood (1962) published a numerical solution to the supercritical problem in which the subsonic and supersonic parts of the flow were handled separately by finite-difference methods, and the assumed conditions along the sonic line were adjusted to give a continuous solution. Benson and Pool (1965a) used Norwood's method to analyse the structure of the supercritical jet.

Brown (1968) used an approximate solution of the subsonic region (requiring an experimentally determined parameter) and solved the supersonic region by the method of characteristics. It was these numerical methods, in particular Norwood's, involving separate subsonic and supersonic calculations, which inspired the present work to be described in Chapters 2 and 3.

1.2.2 Axially symmetric flow

By contrast with the two-dimensional problem, the axially symmetric nozzle problem has received comparatively little attention. The difficulty with axially symmetric flow is that the methods of analysis (complex variables or hypergeometric functions) which are so useful for two-dimensional flows are not available and it is necessary to resort to numerical methods. Most of the published work is concerned with the incompressible flow through a circular, sharp-lipped orifice ($\beta = 90^{\circ}$), although the analyses can be extended to cover other wall angles. The flow through a round orifice is a widely encountered physical problem and there has been considerable interest in producing a theoretical solution to compare with that of Lord Rayleigh (1876) for the corresponding two-dimensional case. The value of the discharge coefficient provides a convenient way of comparing the various axially symmetric methods.

Trefftz (1917) studied the incompressible, axially symmetric problem using integral equations and obtained the result $0.60 \leqslant C_d \leqslant 0.62$ for the flow through a circular orifice. Southwell and Vaisy (1948) and Rouse and Abul-Fetouh (1950) used relaxation methods and obtained the results 0.608 and 0.611 respectively. Garabedian (1956) considered related mathematical problems which had simpler solutions and

determined by interpolation the value $C_d = 0.579$. This result was also obtained by Jeppson (1969) who used a finite-difference method based on stream function and velocity potential as independent variables. Hunt (1967) used integral equations derived from surface vortex distributions and obtained the result $C_d = 0.578$. The disagreement between these results for the incompressible flow through an orifice was resolved by Bloch (1969) who used a conformal mapping technique and obtained the result $0.59131 < C_d < 0.59139$. Turning to compressible flows, we find that very little has been published. Alder (1974) examined the axially symmetric critical and subcritical problem. Supercritical flow was studied by Brown (1968), but his approximate method depended on an empirical parameter. Hebber et al (1970) proposed an approximate solution for conical, convergent nozzles but it relied on unjustifiable assumptions regarding the flow velocity and directions at the throat. Liepmann (1961), by considering the shape of the characteristics in the supersonic part of the flow, showed that the choked discharge coefficient would be slightly lower than the corresponding two-dimensional value, but he was unable to quantify the difference.

1.2.3 Experimental work

The greater part of the published experimental work in the field of sharp-lipped nozzle flows is concerned with axially symmetric, rather than two-dimensional flow. Interest lies mainly in discharge coefficients, although some papers examine pressure distributions and other details of the flowfield. Two-dimensional flows have been studied experimentally by Weir et al (1956), Benson and Pool (1965a,b) and Brown (1968). Weir et al took Schlieren photographs and pressure traverses for the flow through a parallel-throated slot ($\beta = 90^\circ$). Benson and Pool measured discharge coefficients, again for the flow

through a slot, and also took Schlieren and Interferometer photographs of the flowfield. Brown studied two nozzles ($\beta = 20^{\circ}$ and $\beta = 40^{\circ}$) and measured discharge coefficients and the locations of the sonic lines.

The most comprehensive experimental study of flow through axially symmetric nozzles is given by Brown (1968), together with additional material from the experimental program given by Thornock and Brown (1972). These two sets of data cover discharge coefficients and sonic line locations for several values of nozzle angle. Axial pressure distributions for orifices ($\beta = 90^{\circ}$) under various operating conditions have been published by Stanton (1926), Cunningham (1951) and Deckker and Chang (1966). The remaining papers to be mentioned in this section contain only discharge coefficient measurements. Some investigators were interested in the flow of gas through ports in reciprocating machinery (Reynolds 1916, Callaghan and Bowden 1949, Benson 1959). The performance of nozzles for aeronautical applications has been studied by Grey and Wilsted (1949) and Hebber et al (1970) who covered a range of nozzle angles. Perry (1949) and Grace and Lapple (1951) were concerned with the discharge coefficients of orifices for flow metering applications; Grace and Lapple give a good coverage of the subcritical range of pressure ratios. More recently, the cylindrical-throated or "thick" orifice has been used for flow metering because its discharge coefficient is constant over a wide range of pressure ratios. Studies of thick orifices have been published by Kastner et al (1964) and Brain and Reid (1973).

It is perhaps also worth mentioning the approximate method of Bragg (1960) which estimates the variation of discharge coefficient with pressure ratio provided that C_d has been determined (experimentally) at one point in the range. Bragg, developing the work of Jobson (1955),

assumed that the mass-flux (the product of gas velocity and density) at a point on the nozzle wall was proportional to the average mass-flux over the whole cross-section through that point. He assumed that the constant of proportionality was not dependent on pressure ratio. The momentum theorem could then be applied to the whole nozzle flow and an estimate of C_d derived. A single measurement for (e.g.) incompressible flow supplied a value for the constant of proportionality. When interest lies only in discharge coefficients, Bragg's method gives remarkably good results.

1.3 Objectives

The first objective of this work is to develop theoretical methods for analysing the class of nozzle flows outlined in Section 1. 1. In the case of plane, two-dimensional flows this objective may for the most part be achieved by drawing together the results of previous workers. In the case of axially symmetric flows little has been published except in connection with incompressible flow. The approach taken in the present work is to describe a numerical method for the solution of the supercritical, axially symmetric problem. Simplified forms of the method lead to subcritical and/or two-dimensional solutions. The basic theory is described in Chapter 2. The details of the numerical method are discussed in Chapter 3.

The second objective of this work (Chapter 4) is to study in some detail the theoretical flow through sharp-lipped nozzles. Features of interest are the discharge coefficient, the velocity (or pressure) distribution along the nozzle wall, and the shape and position of the streamlines. The effects of the controlling parameters - wall angle (β), approach velocity (V_e), pressure ratio (r), and the value of γ - are examined. A comparison is made between corresponding two-dimensional

and axially symmetric flows.

The final objective of the thesis is to assess the degree of confidence with which the results of the theoretical nozzle flow solutions can be applied in practice. Two important factors are not considered in the analysis - the effects of viscosity and the effects of departure from the ideal requirements of a sharp lip at the nozzle exit. A programme of experiments, described in Chapter 5, was carried out to supplement the data available from previously published work. Theoretical and experimental nozzle performance are compared and discussed in Chapter 6.

CHAPTER 2

PRESENTATION OF THEORY

This chapter is concerned with the derivation of the equations which describe the flow through a nozzle. It starts, in Section 2.1, with a summary of the standard relationships for the isentropic flow of ideal gases. These enable us to define the more important parameters which are used later on in this and subsequent chapters. Typical nozzle flowfields are described in Section 2.2. The complete solution to a supercritical nozzle problem requires the matching of separate solutions in the subsonic and supersonic regions. The different forms of the equations in the two regions are considered in Sections 2.3 and 2.4 respectively. The equations derived here must then be solved numerically. The particular numerical methods used to solve the equations, and to match the subsonic and supersonic regions will be discussed in Chapter 3.

2.1 Isentropic Flow Relationships and Definition of Flow Parameters

The local Mach number, M, is defined as:

$$M = V/c \qquad (2.1a)$$

where V is the local velocity and c is the local speed of sound. For an ideal gas with constant specific heats, c is given by:

$$c^2 = \gamma R T \qquad (2.1b)$$

where γ is the ratio of specific heats; R is the gas constant; and T is the temperature.

We are concerned only with isentropic flow with uniform stagnation conditions, and the local temperature, pressure and density are related to their stagnation values by the following well-known equations (e.g. see Shapiro, 1953):

$$T/T_o = 1/(1 + \frac{\gamma-1}{2} M^2) \qquad (2.2a)$$

$$p/p_o = 1/(1 + \frac{\gamma-1}{2} M^2)^{\gamma/\gamma-1} \qquad (2.2b)$$

$$\rho/\rho_o = 1/(1 + \frac{\gamma-1}{2} M^2)^{1/\gamma-1} \qquad (2.2c)$$

where T, p and ρ are the temperature, pressure and density; and T_o, p_o and ρ_o are the stagnation values. From equations 2.1b and 2.2a we obtain:

$$c = \left[\gamma RT_o/(1+ \frac{\gamma-1}{2} M^2)\right]^{\frac{1}{2}} \qquad (2.3)$$

We now let c* be the value of c where M = 1:

$$c^* = (\frac{2\gamma RT_o}{\gamma+1})^{\frac{1}{2}}$$

and define V' = V/c* and c' = c/c* to be the dimensionless velocity and speed of sound. From equations 2.1, 2.2a and 2.3 we then derive:

$$V' = \left[\frac{\gamma+1}{2} M^2/(1 + \frac{\gamma-1}{2} M^2)\right]^{\frac{1}{2}} \qquad (2.4a)$$

$$c' = \left[\frac{\gamma+1}{2} /(1 + \frac{\gamma-1}{2} M^2)\right]^{\frac{1}{2}} = \left[\frac{\gamma+1}{2} (1 - \frac{\gamma-1}{\gamma+1} V'^2)\right]^{\frac{1}{2}} \qquad (2.4b)$$

Henceforth it will be assumed, unless otherwise stated, that we are dealing with the dimensionless values of V and c as defined above and the primes will no longer be used. Similarly it will be assumed that T, p and ρ are dimensionless properties scaled by the appropriate stagnation values. Thus, from equations 2.2 and 2.4a, we may write:

$$T = 1/(1 + \frac{\gamma-1}{2} M^2) = (1 - \frac{\gamma-1}{\gamma+1} V^2) \qquad (2.5a)$$

$$p = 1/(1 + \frac{\gamma-1}{2} M^2)^{\gamma/\gamma-1} = (1 - \frac{\gamma-1}{\gamma+1} V^2)^{\gamma/\gamma-1} \qquad (2.5b)$$

$$\rho = 1/(1 + \frac{\gamma-1}{2} M^2)^{1/\gamma-1} = (1 - \frac{\gamma-1}{\gamma+1} V^2)^{1/\gamma-1} \qquad (2.5c)$$

The nozzle configuration with which we are concerned is shown in Fig. 2.1. The gas enters the semi-infinite duct BC with a uniform, subsonic approach velocity V_e and exhausts into the atmosphere where the dimensionless pressure is p_a. A jet is formed which is bounded by a free streamline on which the velocity is V_j and the Mach number is M_j. Whether the flow is subcritical, critical or supercritical depends on whether $V_j < 1$, $V_j = 1$ or $V_j > 1$. The value of V_j is related to p_a through equation 2.5b. It is convenient to use the "pressure ratio", r, which is numerically equal to p_a, but is more easily identifiable with a nozzle operating condition. Thus we have:

Subcritical: $V_j < 1$; $M_j < 1$; $r > (\frac{2}{\gamma+1})^{\gamma/\gamma-1}$

Critical: $V_j = 1$; $M_j = 1$; $r = (\frac{2}{\gamma+1})^{\gamma/\gamma-1}$

Supercritical: $V_j > 1$; $M_j > 1$; $r < (\frac{2}{\gamma+1})^{\gamma/\gamma-1}$

Values of the "critical pressure ratio", $r_s = (\frac{2}{\gamma+1})^{\gamma/\gamma-1}$, are given in Table 4.1 at the end of Chapter 4. For air we have $\gamma = 1.4$ and $r_s = 0.528$.

An important flow parameter is the nozzle "discharge coefficient", C_d, defined as follows:

$$C_d = \dot{m}/\dot{m}_t \qquad (2.6a)$$

where $\dot{m}$ is the actual rate of mass flow through the nozzle and $\dot{m}_t$ is the rate which would exist at the same pressure ratio if the flow in the throat were uniform in velocity and parallel to the axis. The discharge coefficient used here is synonymous with the "contraction coefficient" used by some other workers, so far as a theoretical solution to the nozzle flow is concerned. The value of $\dot{m}$ is determined by integrating the solution across the lip plane (L'EL in Fig. 2.1):

$$\dot{m} = \int_0^{y_1} \rho V \cos\theta (2\pi y)^k dy \qquad (2.6b)$$

where y is the coordinate normal to the axis; y_1 is the value of y at the lip; θ is the angle between the direction of flow and the axis; and k = 0 for two-dimensional flow or k = 1 for axially symmetric flow. The value of $\dot{m}_t$ is given by:

$$\dot{m}_t = (\pi y_1)^k V_1 \rho_1 y_1 \qquad (2.6c)$$

where V_1 is the velocity at the lip and ρ_1 (related to V_1 through equation 2.5c) is the density at the lip. For critical and supercritical flow $V_1 = 1$; for subcritical flow $V_1 = V_j$.

The geometry of the nozzle shown in Fig. 2.1 is defined by the wall angle β and by the "area contraction ratio" $(y_1/y_e)^{1+k}$, where y_e is the value of y on the surface of the inlet duct. Since the solution to be described below in Section 2.3 is obtained in terms of the hodograph variables, V and θ, the area contraction ratio is not a convenient independent parameter. The "approach velocity", V_e, is more appropriate. If the flow through the nozzle were one-dimensional, the cross-section area would be related to the velocity or Mach number by the following well-known equation (details given by, e.g. Shapiro 1953):

$$\frac{A^*}{A} = M\left[\left(\frac{\gamma+1}{2}\right)/\left(1 + \frac{\gamma-1}{2} M^2\right)\right]^{\frac{\gamma+1}{2(\gamma-1)}} = V\left[\left(\frac{\gamma+1}{2}\right)\left(1 - \frac{\gamma-1}{\gamma+1} V^2\right)\right]^{1/\gamma-1}$$

where A is the cross-section area of the flow and A* is the value of A at the plane where M = V = 1. We may use this equation to relate the area contraction ratio and the approach velocity by introducing the discharge coefficient:

$$\left(\frac{y_1}{y_e}\right)^{1+k} = \frac{1}{C_d} \frac{V_e}{V_1} \left[\frac{\left(1 - \frac{\gamma-1}{\gamma+1} V_e^2\right)}{\left(1 - \frac{\gamma-1}{\gamma+1} V_1^2\right)}\right]^{1/\gamma-1} \qquad (2.7)$$

2.2 Description of Flowfield

The important features of nozzle flowfields at subcritical, critical and supercritical pressure ratios are shown in Figs. 2.2a-c. In subcritical flow (Fig. 2.2a) the gas forms a tapering jet in which the streamlines become parallel, with uniform velocity, at an infinite distance downstream from the lip plane L'EL. In critical flow (Fig. 2.2b), the gas on each streamline accelerates to the sonic

velocity at a plane F'OF situated a finite distance from the lip plane. Supercritical flow (Fig. 2.2c) has a region of subsonic flow inside the nozzle which is separated from the supersonic jet by the curved sonic line. It is useful to consider the supersonic flowfield in terms of its characteristics (Shapiro 1953) along which discontinuities in boundary condition can be propagated. Centred on the lip, L, is a Prandtl-Meyer expansion in which the boundary streamline pressure is reduced to the atmospheric value and the velocity increases to V_j. Characteristics originating either in the expansion or on the free streamline intersect the sonic line. So long as a characteristic connects the free surface and the sonic line, variations in atmospheric pressure can affect the subsonic region and the rate of flow through the nozzle. The limit of choked flow occurs at that pressure ratio, when the 'final' characteristic F'OF (Fig. 2.2c) is part of the expansion fan at the lip.

2.3 Subsonic Flow Equations

The continuity equation is:

$$\frac{\partial}{\partial x}(\rho u y^k) + \frac{\partial}{\partial y}(\rho v y^k) = 0 \qquad (2.8)$$

where x and y are the physical coordinates parallel and normal to the axis; u and v are the dimensionless velocity components in the x and y directions (i.e. $u^2+v^2 = V^2$); and k = 0 for two-dimensional flow or k = 1 for axially symmetric flow.

The condition for irrotational motion is:

$$\frac{\partial u}{\partial y} - \frac{\partial v}{\partial x} = 0 \qquad (2.9)$$

Equations 2.8 and 2.9, together with equation 2.5c, are sufficient to determine the flow through the nozzle. Confining our attention to the subsonic region, the boundary conditions in the notation of Fig. 2.2c are:

(a) $u \to V_e$ and $v \to 0$ when $x \to -\infty$

(b) $v = 0$ along the axis AO

(c) $v = 0$ along the wall BC

(d) $v/u = \tan \beta$ along the wall CL

(e) $V = 1$ along the sonic line LO.

In the case of subcritical flow, the boundary condition (e) is modified as follows:

(e) $V = V_j$ along the free streamline

(f) $u \to V_j$ and $v \to 0$ as $x \to +\infty$

It is convenient to transform the problem into the hodograph coordinates, V and θ, defined as follows:

$$V^2 = u^2 + v^2$$

$$\theta = \tan^{-1}(v/u)$$

This has the effect of removing some of the difficulties associated with the above boundary conditions, where the location of the sonic line (or free streamline in the case of subcritical flow) in the physical

coordinate system is not known initially, and some of the boundary lies at infinity. Another advantage of the hodograph transformation is that it leads, for two-dimensional flow, to a linear partial differential equation. When transformed, the lower half of the physical supercritical flowfield in Fig. 2.2c maps into the rectangle shown in Fig. 2.3a. The transformed subcritical flow field has a similar appearance (Fig. 2.3b). Rectangular coordinates are used here to represent the hodograph plane rather than the more conventional polar coordinates because they will be more convenient in the discussion of numerical methods given in Chapter 3. The derivation of the hodograph equations given below follows the conventional lines for two-dimensional flow (e.g. Shapiro 1953) except that here the additional terms for axially symmetric flow are included.

The continuity equation (equation 2.8) allows us to define the stream function, ψ, by the following expressions:

$$\left.\begin{aligned} u &= \frac{1}{\rho y^k}\frac{\partial \psi}{\partial y} \\ v &= -\frac{1}{\rho y^k}\frac{\partial \psi}{\partial x} \end{aligned}\right\} \qquad (2.10)$$

We may define the velocity potential, ϕ, in the usual way as follows:

$$\left.\begin{aligned} u &= \frac{\partial \phi}{\partial x} \\ v &= \frac{\partial \phi}{\partial y} \end{aligned}\right\} \qquad (2.11)$$

Thus we may write:

$$\left.\begin{aligned} u = V\cos\theta = \phi_x = \alpha\psi_y \\ v = V\sin\theta = \phi_y = -\alpha\psi_x \end{aligned}\right\} \qquad (2.12)$$

where the subscripts on ϕ and ψ denote partial differentiation and $\alpha = (\rho y^k)^{-1}$. Since ϕ and ψ are functions of x and y we have:

$$\left.\begin{aligned} d\phi = \phi_x\,dx + \phi_y\,dy = V(\cos\theta\,dx + \sin\theta\,dy) \\ d\psi = \psi_x\,dx + \psi_y\,dy = \frac{V}{\alpha}(-\sin\theta\,dx + \cos\theta\,dy) \end{aligned}\right\} \qquad (2.13)$$

Equations 2.13 may be solved for dx and dy giving:

$$\left.\begin{aligned} dx = \frac{\cos\theta}{V}\,d\phi - \frac{\alpha}{V}\sin\theta\,d\psi \\ dy = \frac{\sin\theta}{V}\,d\phi + \frac{\alpha}{V}\cos\theta\,d\psi \end{aligned}\right\} \qquad (2.14)$$

Since ϕ and ψ are also functions of V and θ we may write:

$$\left.\begin{aligned} d\phi = \phi_V\,dV + \phi_\theta\,d\theta \\ d\psi = \psi_V\,dV + \psi_\theta\,d\theta \end{aligned}\right\} \qquad (2.15)$$

Substitution of equations 2.15 in equations 2.14 leads to:

$$\left.\begin{aligned} dx = \left[\frac{\cos\theta}{V}\phi_V - \alpha\frac{\sin\theta}{V}\psi_V\right]dV + \left[\frac{\cos\theta}{V}\phi_\theta - \alpha\frac{\sin\theta}{V}\psi_\theta\right]d\theta \\ dy = \left[\frac{\sin\theta}{V}\theta_V + \alpha\frac{\cos\theta}{V}\psi_V\right]dV + \left[\frac{\sin\theta}{V}\phi_\theta + \alpha\frac{\cos\theta}{V}\psi_\theta\right]d\theta \end{aligned}\right\} \qquad (2.16)$$

Regarding equations (2.16) as expressing x and y as functions of V and θ, we arrive at the following expressions:

$$x_V = \frac{\cos\theta}{V}\phi_V - \alpha\frac{\sin\theta}{V}\psi_V \qquad (2.17a)$$

$$x_\theta = \frac{\cos\theta}{V}\phi_\theta - \alpha\frac{\sin\theta}{V}\psi_\theta \qquad (2.17b)$$

$$y_V = \frac{\sin\theta}{V}\phi_V + \alpha\frac{\cos\theta}{V}\psi_V \qquad (2.17c)$$

$$y_\theta = \frac{\sin\theta}{V}\phi_\theta + \alpha\frac{\cos\theta}{V}\psi_\theta \qquad (2.17d)$$

Since $\frac{\partial^2 x}{\partial V\partial\theta} \equiv \frac{\partial^2 x}{\partial\theta\partial V}$ and $\frac{\partial^2 y}{\partial V\partial\theta} \equiv \frac{\partial^2 y}{\partial\theta\partial V}$, x and y may be eliminated from equations 2.17 by differentiation and, after some reorganisation, the following equations may be derived.

$$\phi_\theta = \alpha V\psi_V \qquad (2.18a)$$

$$\phi_V = (\alpha_V - \tfrac{\alpha}{V})\psi_\theta - \alpha_\theta\psi_V \qquad (2.18b)$$

Elimination of ϕ from equations 2.18 by a further stage of differentiation leads to:

$$V\psi_{VV} + \left[1 + \frac{V\alpha_V}{\alpha} + \frac{\alpha_{\theta\theta}}{\alpha}\right]\psi_V + \frac{\alpha_\theta}{\alpha}\psi_{V\theta}$$

$$+ \left[\frac{1}{V}\frac{\alpha_\theta}{\alpha} - \frac{\alpha_{V\theta}}{\alpha}\right]\psi_\theta + \left[\frac{1}{V} - \frac{\alpha_V}{\alpha}\right]\psi_{\theta\theta} = 0 \qquad (2.19)$$

Since $\alpha = (\rho y^k)^{-1}$ we may re-write equation 2.19 as follows:

$$V\psi_{VV} + \left[(1 - \frac{V\rho_V}{\rho}) - k\left(V\frac{y_V}{y} + \frac{y_{\theta\theta}}{y} - 2\frac{y_\theta^2}{y^2}\right)\right]\psi_V$$

$$-k(\frac{y_\theta}{y})\psi_{V\theta} + k\left[\frac{y_{V\theta}}{y} - \frac{2y_V y_\theta}{y^2} - \frac{1}{V}(1 + V\frac{\rho_V}{\rho})\frac{y_\theta}{y}\right]\psi_\theta$$

$$+\left[\frac{1}{V}(1 + V\frac{\rho_V}{\rho}) + k\frac{y_V}{y}\right]\psi_{\theta\theta} = 0 \qquad (2.20)$$

Substitution of equations 2.18 into equations 2.17 leads to the following expressions for the derivatives of x and y in terms of ψ and the hodograph variables:

$$x_V = \frac{1}{\rho V y k}\left[-(\frac{\rho_V}{\rho} + k\frac{y_V}{y} + \frac{1}{V})\cos\theta.\psi_\theta + (k\frac{y_\theta}{y}\cos\theta - \sin\theta)\psi_V\right] \qquad (2.21a)$$

$$y_V = \frac{1}{\rho V y k}\left[-(\frac{\rho_V}{\rho} + k\frac{y_V}{y} + \frac{1}{V})\sin\theta.\psi_\theta + (k\frac{y_\theta}{y}\sin\theta + \cos\theta)\psi_V\right] \qquad (2.21b)$$

$$x_\theta = \frac{1}{\rho V y k}\left[V\cos\theta.\psi_V - \sin\theta.\psi_\theta\right] \qquad (2.21c)$$

$$y_\theta = \frac{1}{\rho V y k}\left[V\sin\theta.\psi_V + \cos\theta.\psi_\theta\right] \qquad (2.21d)$$

We may obtain from equations 2.21b and 2.21d expressions for those terms in equation 2.20 which involve derivatives of y as follows:

$$\left.\begin{aligned}
\frac{y_\theta}{y} &= \frac{1}{\rho V y^2}\left[V\sin\theta.\psi_V + \cos\theta.\psi_\theta\right] \\
\frac{y_V}{y} &= \frac{\frac{1}{\rho V y^2}\left[V\left(-\frac{\psi_\theta}{V} - \frac{\rho_V}{\rho}\psi_\theta + V\frac{y_\theta}{y}\psi_V\right)\sin\theta + V\cos\theta\,\psi_V\right]}{V(1 + \frac{1}{\rho V y^2}\sin\theta\,\psi_\theta)} \\
\frac{y_{\theta\theta}}{y} &= \frac{1}{\rho V y^2}\left[(V\psi_V + \psi_{\theta\theta})\cos\theta + (V\psi_{V\theta} - \psi_\theta)\sin\theta\right] - (\frac{y_\theta}{y})^2 \\
\frac{y_{V\theta}}{y} &= \frac{1}{\rho V y^2}\left[V\sin\theta\,\psi_{VV} + (V\psi_{V\theta} - \psi_\theta)\frac{\cos\theta}{V}\right] - \frac{y_\theta}{y}(\frac{y_V}{y} + \frac{\rho_V}{\rho})
\end{aligned}\right\} \qquad (2.22)$$

After substitution of equations 2.22 into equation 2.20 and a little reorganisation, we finally obtain:

$$\left[V^2\psi_{VV} + V\psi_V(1 - V\frac{\rho_V}{\rho}) + \psi_{\theta\theta}(1 + V\frac{\rho_V}{\rho})\right]$$

$$+ \frac{2k}{\rho y^2}\left\{\sin\theta\left[V\psi_{VV}\psi_\theta + (1 - V\frac{\rho_V}{\rho})\psi_V\psi_\theta - V\psi_V\psi_{V\theta}\right]\right.$$

$$\left. - \cos\theta\left[\frac{1}{V}(1 + V\frac{\rho_V}{\rho})\psi_\theta^2 + V\psi_V^2\right]\right\}$$

$$+ \frac{k}{\rho^2 y^4}\left\{\sin^2\theta\left[\frac{1}{V}(3 + V\frac{\rho_V}{\rho})\psi_\theta^2\psi_V + 2V\psi_V^3 - 2\psi_{V\theta}\psi_\theta\psi_V + \psi_V^2\psi_{\theta\theta} + \psi_\theta^2\psi_{VV}\right]\right.$$

$$\left. + \sin\theta\cos\theta\left[\frac{1}{V^2}(1 + V\frac{\rho_V}{\rho})\psi_\theta^3 + \psi_V^2\psi_\theta\right]\right\} = 0 \qquad (2.23)$$

We require a solution to equation 2.23 over the rectangular region shown in Fig. 2.3a or 2.3b. The boundary values of the dependent variable ψ may be assigned as follows:

(a) $\psi = \psi_{min}$ on the axial streamline AO

(b) $\psi = \psi_{max}$ on the wall streamline BCL

(c) subcritical: $\psi = \psi_{max}$ along the line LF ($V=V_j$)

supercritical: $\psi = \psi_s(\theta)$ along the sonic line LO

It is convenient to make the choice $\psi_{min} = 0$ and $\psi_{max} = 1$. The function $\psi_s(\theta)$ is to be determined in conjunction with the supersonic solution so as to ensure a continuous solution across the sonic line. In the particular case of zero approach velocity a different upstream boundary condition applies. The streamlines in the physical plane all converge towards the lip plane. If we assume that, a long way

upstream from the lip plane, the streamlines are straight and converge towards a point on the axis, then we can show that in two-dimensional flow the stream function is proportional to the flow angle, θ, and in axially symmetric flow it is proportional to $(1 - \cos\theta)$. The hodograph flowfield for the case $V_e = 0$ is shown in Fig. 2.3c. The boundary values of ψ are:

(a) $\psi = \psi_{min}$ on the axis AO

(b) $\psi = \psi_{max}$ on the wall BL

(c) $\psi = \psi_s(\theta)$ (or $\psi = \psi_{max}$ for critical and subcritical flow) on LO

(d) two-dimensional: $\psi/\psi_{max} = \theta/\beta$

axially symmetric: $\psi/\psi_{max} = \frac{1-\cos\theta}{1-\cos\beta}$ } on AB

Equation 2.23 is linear for two-dimension flow (when k=0) and its solution may be expressed analytically as a series of hypergeometric functions (Chaplygin, 1902). For axially symmetric problems, when the nonlinear terms involving the physical coordinate y are present, the equation must be solved numerically. The incompressible solution is given when $\rho = 1$ and $\rho_V = 0$. For compressible flow we have, from equation 2.5c:

$$\rho_V/\rho = - \frac{2V}{(\gamma+1) - (\gamma-1)V^2} \qquad (2.24)$$

The solution of equation 2.23 is obtained by an iterative process. In cases where k = 1, values of the physical coordinate y are required. These are obtained by integration of the current approximate solution of equation 2.23 using equations 2.21b or 2.21d. It is most convenient

to integrate along lines of constant V because equation 2.21d may be integrated by parts to give:

$$\frac{y^2}{2} = \frac{1}{\rho V}\left\{\left[\int_o^\theta (\psi + V\psi_V)\sin\theta \, d\theta\right]_{V \text{ const.}} + \psi\cos\theta\right\} \qquad (2.25)$$

where $y = 0$ and $\theta = 0$ on the axis.

Once the solution to equation 2.23 has been obtained, the physical coordinates x and y are given by integration of equations 2.21. In particular, the coordinates of the sonic line are required at each step in the solution of a supercritical problem. Equations 2.21c and 2.21d are less complex and may be integrated to give lines of constant velocity, including the sonic line. For two-dimensional problems ($k = 0$), equations 2.21c and 2.21d may be integrated by parts giving:

$$x - x_o = \frac{1}{\rho V}\left\{-\psi_o\sin\theta + \left[\int_o^\theta (\psi + V\psi_V)\cos\theta \, d\theta\right]_{V \text{ const.}}\right\} \qquad (2.26a)$$

$$y = \frac{1}{\rho V}\left\{\psi\cos\theta + \left[\int_o^\theta (\psi + V\psi_V)\sin\theta \, d\theta\right]_{V \text{ const.}}\right\} \qquad (2.26b)$$

where $y = 0$, $x = x_o$ and $\theta = 0$ on the axis.

2.4 Supersonic Equations

When the equations 2.10 for the velocity components u and v are substituted into equation 2.9 — the condition for irrotationality — then the following equation may be derived (see Shapiro 1953 for details):

$$\left(1 - \frac{u^2}{c^2}\right)\psi_{xx} + \left(1 - \frac{v^2}{c^2}\right)\psi_{yy} - 2\frac{uv}{c^2}\psi_{xy} - k\frac{\psi_y}{y} = 0 \qquad (2.27)$$

where u and v are the dimensionless velocity components; and c is the dimensionless speed of sound for which (from equation 2.4b) we may write:

$$c^2 = \frac{\gamma+1}{2} - \frac{\gamma-1}{2}(u^2 + v^2) = \frac{\gamma+1}{2} - \frac{\gamma-1}{2} v^2 \qquad (2.28)$$

We may examine the characteristics of equation 2.27 in the usual way (e.g. Ames 1969) by considering the conditions under which the derivatives ψ_{xx}, ψ_{yy} and ψ_{xy} are indeterminate. Such conditions apply if the determinants of the following system are zero:

$$\begin{bmatrix} (1 - \frac{u^2}{c^2}) & -\frac{2uv}{c^2} & (1 - \frac{v^2}{c^2}) \\ dx & dy & 0 \\ 0 & dx & dy \end{bmatrix} \times \begin{bmatrix} \psi_{xx} \\ \psi_{xy} \\ \psi_{yy} \end{bmatrix} = \begin{bmatrix} k\frac{\psi_y}{y} \\ d(\psi_x) \\ d(\psi_y) \end{bmatrix} \qquad (2.29)$$

i.e. that we have:

$$\begin{vmatrix} (1 - \frac{u^2}{c^2}) & -\frac{2uv}{c^2} & (1 - \frac{v^2}{c^2}) \\ dx & dy & 0 \\ 0 & dx & dy \end{vmatrix} = \begin{vmatrix} (1 - \frac{u^2}{c^2}) & k\frac{\psi_y}{y} & (1 - \frac{v^2}{c^2}) \\ dx & d(\psi_x) & 0 \\ 0 & d(\psi_y) & dy \end{vmatrix} = 0 \qquad (2.30)$$

When these determinants are evaluated we obtain the following equations defining the characteristics of equation 2.27, noting that (from equations 2.10) $\psi_x = -\rho y^k v$ and $\psi_y = \rho y^k u$:

$$\frac{dy}{dx} = \frac{-uv \pm c\sqrt{u^2 + v^2 - c^2}}{c^2 - u^2} \qquad (2.31a)$$

$$\frac{dv}{du} = \frac{uv \pm c\sqrt{u^2 + v^2 - c^2}}{c^2 - v^2} - \frac{c^2 v}{c^2 - v^2} \cdot \frac{k}{y}\frac{dy}{du} \qquad (2.31b)$$

Setting $u = V\cos\theta$ and $v = V\sin\theta$ in equations 2.31 we obtain after some reorganisation:

$$\frac{dy}{dx} = \tan(\theta \pm \mu) \qquad (2.32a)$$

$$\frac{1}{V}\left(\frac{dV}{d\theta}\right) = \pm\tan\mu + \frac{\sin\mu\tan\mu\sin\theta}{\sin(\theta\pm\mu)}\frac{k}{y}\frac{dy}{d\theta} \qquad (2.32b)$$

where μ, the Mach angle, is defined by $\sin\mu = c/V = 1/M$. It is convenient to work with the Mach number M, rather than the non-dimensional velocity V, in the supersonic part of the problem. Substitution from equation 2.4a into equations 2.32b therefore leads to:

$$\frac{d\theta}{dM} = \pm\frac{\sqrt{M^2 - 1}}{M\left(1 + \frac{\gamma-1}{2}M^2\right)} \mp \frac{\sin\mu\sin\theta}{\sin(\theta\pm\mu)}\frac{k}{y}\frac{dy}{dM} \qquad (2.33)$$

Integration of equation 2.33 with respect to M leads to:

$$\theta = \pm\omega(M) \mp k\int\frac{\sin\mu\sin\theta}{\sin(\theta\pm\mu)}\frac{dy}{y} + C \qquad (2.34)$$

where C is a constant of integration and $\omega(M)$ is given by:

$$\omega(M) = \left(\frac{\gamma+1}{\gamma-1}\right)\arctan\left[\left(\frac{\gamma-1}{\gamma+1}\right)(M^2-1)\right]^{\frac{1}{2}} - \arctan\left[M^2-1\right]^{\frac{1}{2}} \qquad (2.35)$$

In supersonic flow when $M>1$ the characteristics defined by equations 2.32a and 2.34 are real. We may identify two families of characteristics

depending on whether the upper or lower signs are used and these are:

$$\text{1st family:} \begin{cases} \dfrac{dy}{dx} = \tan(\theta+\mu) & (2.36a) \\ \theta = \omega(M) - k \displaystyle\int \frac{\sin\mu \sin\theta}{\sin(\theta+\mu)} \frac{dy}{y} + C_I & (2.36b) \end{cases}$$

$$\text{2nd family:} \begin{cases} \dfrac{dy}{dx} = \tan(\theta-\mu) & (2.37a) \\ \theta = -\omega(M) + k \displaystyle\int \frac{\sin\mu \sin\theta}{\sin(\theta-\mu)} \frac{dy}{y} + C_{II} & (2.37b) \end{cases}$$

where C_I and C_{II} are the appropriate constants of integration.

The characteristic equations 2.36 and 2.37 enable calculations in the supersonic flowfield to be performed. If the values of x, y, M and θ are known at two points A and B, then the values at a point C where a 1st family characteristic through A intersects a 2nd family characteristic through B may be estimated by numerical solution of the equations. This procedure, applicable to any hyperbolic system, is usually known as the method of characteristics. A typical characteristics network for a supercritical flowfield is shown in Fig. 2.4. The points L, P_1, P_2, ..., O define the sonic line and their coordinates are derived from the subsonic hodograph solution through equations 2.21c and 2.21d. A knowledge of x, y, M and θ at the sonic line points is sufficient to calculate those parameters at all points in the network shown in Fig. 2.4. It is assumed in this figure that the distribution of stream function along the sonic line has been correctly determined, $\psi = \psi_s(\theta)$, so that the boundary conditions in the lip region are satisfied. The conditions are firstly, that there is a Prandtl-Meyer expansion centred on the lip in which the Mach number increases to the free streamline value M_j,

and secondly, that the locus of $\psi = 1$ which defines the jet boundary is also the locus of $M = M_j$. The numerical operations necessary to determine $\psi_s(\theta)$ will be described in Chapter.3.

The procedure adopted here is to solve the subsonic region of flow in the hodograph plane and to solve the supersonic flow in the physical plane by the method of characteristics. An alternative approach is to extend the use of the hodograph plane into the supersonic region and to use characteristic equations derived from equation 2.23. The characteristic variables are then V, θ, ψ_V and ψ_θ, and the solution is again started at the sonic line where the values of these variables are known or can be derived from the subsonic solution. This approach was used by Norwood (1962) and Benson and Pool (1965a) to solve the two-dimensional problem and perhaps results in a slightly tidier computational procedure. Any such advantage is lost in the axially symmetric case, where the physical variable, y, appears in the equations.

Consideration of the characteristics network in Fig. 2.4 enables us to derive an expression for the jet Mach number, $M_j = M_c$, at which choking occurs. The flow inside the nozzle will cease to be affected by the external pressure when all 2nd family characteristics reaching the sonic line originate in the Prandtl-Meyer expansion at the lip. This occurs when the point H in Fig. 2.4 is coincident with L. The limiting case is when $M = M_j = M_c$ at H and we now apply equation 2.36b to the 1st family characteristic LH, and equation 2.37b to the 2nd family characteristic OH, denoting conditions at O, L and H by the appropriate subscripts.

$$\theta_h - \theta_1 = \omega(M_h) - \omega(M_1) - k\int_{y_1}^{y_h} \frac{\sin\mu \sin\theta}{\sin(\theta+\mu)} \frac{dy}{y} \qquad (2.38a)$$

$$\theta_h - \theta_o = -\omega(M_h) + \omega(M_o) + k\int_{y_o}^{y_h} \frac{\sin\mu \sin\theta}{\sin(\theta-\mu)} \frac{dy}{y} \qquad (2.38b)$$

Noting that $M_h = M_c$, $\theta_1 = -\beta$, $\theta_o = 0$, $M_1 = M_o = 1$, $y_h = y_1 = 0$, and that the integral in equation 2.38a is zero we may solve equations 2.38 to give:

$$\omega(M_c) = \beta/2 + \frac{k}{2}\int_o^{y_1} \frac{\sin\mu \sin\theta}{\sin(\theta-\mu)} \qquad (2.39)$$

The relationship between $\omega(M_c)$ and M_c is given in equation 2.35 and the choking pressure ratio, r_c, is given by equation 2.2b. For two-dimensional flow equation 2.39 may be evaluated at once and r_c is seen to be a function of γ and β. For axially symmetric flow, a full solution of the flowfield is needed before the integral in equation 2.39 can be evaluated. We then find that the choking pressure ratio is slightly lower than the corresponding two-dimensional value. Values of r_c for a range of values of β are given in Table 4.1 at the end of Chapter 4.

The characteristic OFH in Fig. 2.4 marks the limit of the region which has to be considered when solving a supercritical flow problem. Downstream from this "last" characteristic, conditions on the outer boundary do not influence the subsonic and transonic region. We can use the method of characteristics to extend the solution step-by-step further into the jet, giving a network similar to that shown in Fig. 2.5. Along the jet boundary we have $M = M_j$ and $dy/dx = \tan\theta$; along the axis we have $\frac{dy}{dx} = \theta = 0$. The jet boundary first passes through a

minimum point close to the lip and then expands to its maximum width some distance downstream. The point of inflexion, G in Fig. 2.5, lies on, or just upstream from in the axially symmetric case, the 1st family characteristic starting at the foot of the sonic line, O. Within the region OFG, the flow is accelerating. Beyond G, the characteristics running forward from the jet surface are compressive and eventually merge to form a pattern of shockwaves. The assumption of isentropic flow on which the derivation of the characteristic equations 2.36 and 2.37 is based breaks down at this stage.

CHAPTER 3

NUMERICAL METHODS

The details of the numerical methods which were used to solve the equations derived in Chapter 2 are presented in this chapter. In Section 3.2.1, we shall examine the finite-difference solution of equation 2.23, which describes subsonic flow in the hodograph plane. The integration of the hodograph solution to determine the physical coordinates will be discussed in Section 3.2. The accuracy of the results of the numerical solution will be considered in Section 3.3. Section 3.4, which is relevant only to supercritical problems, deals with the application of the characteristic equations 2.36 and 2.37 to the supersonic flow region. Finally, in Section 3.5, the problem of matching the subsonic and supersonic parts of a supercritical solution will be considered.

3.1 Solution of the Subsonic Hodograph Equation

The solution of equation 2.23 for two-dimensional flow ($k = 0$) may be expressed as the sum of a series of hypergeometric functions (Chaplygin 1902). However, considerable computation would be involved in the evaluation of the terms in the series and this, together with the fact that no such analytical form exists for axially symmetric flow, makes a numerical solution more attractive. A finite-difference method, similar to that used by Norwood (1962) and Benson and Pool (1965a), is an obvious choice since we are dealing with a rectangular region (Fig. 2.3) with the value of the dependent variable, ψ, known on the boundary. The only disadvantage of a finite-difference method is its insensitivity in the neighbourhood of the singularities on

the axis in Fig. 2.3. Although a certain amount can be done to reduce this problem, we must accept that the solution may be inadequate near these points.

The hodograph region over which the solution of equation 2.23 is required, is shown in Fig. 3.1. It is divided into a NxN rectangular finite-difference mesh (where in this case N=8). Equal numbers of subdivisions in the V and θ directions are used throughout, so that the single parameter N determines the mesh density. It is possible that unequal numbers of subdivisions might lead to a reduction in truncation errors for a given number of mesh nodes, but this has not been investigated. The values of ψ at the boundary nodes in Fig. 3.1 are given as follows:

(a) $\psi = 1$ on B C' C" L

(b) $\psi = 0$ on A O

(c) $\psi = \psi_s(\theta)$ on L O

(d) $\psi = 0.5$ at the singularity at A, B where $\theta = 0$ and $V = V_e$.

In the case of subcritical flow we have $\psi_s(\theta) = 1$. In the case of zero approach velocity ($V_e = 0$) we have:

(a) $\psi = 1$ on C" L

(b) $\psi = 0$ on C' O

(c) $\psi = \psi_s(\theta)$ on L O

(d) $\psi = \theta/\beta$ (two-dimensional)

$\psi = (1-\cos\theta)/(1-\cos\beta)$ (axially symmetric) } on C' C"

The finite-difference mesh in Fig. 3.1 is shown to be concentrated near the line $\theta = 0$. This has the intention of reducing the effects of the singularities at A, B and O. If we introduce an auxilliary independent variable σ replacing θ and defined as follows:

$$\theta = \beta . \sigma^{t} \tag{3.1}$$

then the value of the exponent t determines the degree to which the constant-Θ lines in the mesh are concentrated. The value t=1 gives equal subdivisions in θ; the effect of $t = 1.5$ is illustrated in Fig. 3.1. We shall return later, in Section 3.2, to the question of how the value of t is to be selected in a given problem. The range $0 \leq \sigma < 1$ covers the range $0 < \theta < \beta$, and an equally spaced finite-difference mesh in the V-σ plane is used for the hodograph solution. A similar attempt to concentrate the constant-V lines near V=1 did not lead to any obvious benefits. For the purposes of numerical solution the derivatives ψ_{θ}, $\psi_{\theta\theta}$ and $\psi_{V\theta}$ are replaced by the following equivalent expressions in terms of σ:

$$\psi_{\theta} = \frac{\sigma^{1-t}}{\beta t} . \psi_{\sigma} \tag{3.2a}$$

$$\psi_{\theta\theta} = \frac{\sigma^{1-t}}{\beta t}^{2} \psi_{\sigma\sigma} + \frac{1-t}{\beta^{2} t^{2}} . \sigma^{1-2t} \psi_{\sigma} \tag{3.2b}$$

$$\psi_{V\theta} = \frac{\sigma^{1-t}}{\beta t} \psi_{V\sigma} \tag{3.2c}$$

It is necessary to represent equation 2.23 in finite-difference form at each of the $(N-1)^2$ interior nodes in the mesh. This leads to a set of $(N-1)^2$ algebraic equations to be solved for the values of ψ at the nodes. The following conventional central-difference approximations for the partial differential coefficients ψ_{VV}, ψ_{V}, $\psi_{V\sigma}$,

ψ_σ, and $\psi_{\theta\theta}$ are used:

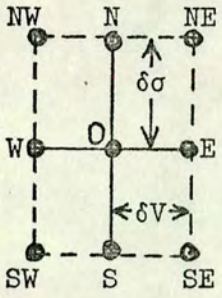

$$\psi_{VV} \doteq (\psi_E + \psi_W - 2\psi_O)/(\delta V)^2$$

$$\psi_V \doteq (\psi_E - \psi_W)/(2\delta V)$$

$$\psi_{V\theta} \doteq \left[(\psi_{NE} + \psi_{SW}) - (\psi_{NW} + \psi_{SE})\right]/(4\delta V \delta\sigma) \qquad (3.3)$$

$$\psi_\sigma = (\psi_N - \psi_S)/(2\delta\sigma)$$

$$\psi_{\sigma\sigma} = (\psi_N + \psi_S - 2\psi_O)/(\delta\sigma)^2$$

where O identifies the node in question; N, E, S, W, etc. identify its nearest neighbours; $\delta\sigma = 1/N$ and $\delta V = V_1/N$. The approximations represented by equations 3.3 have truncation errors of order $(1/N)^2$. When these approximate expressions for the partial differential coefficients are substituted into equation 2.23 a set of non-linear algebraic finite-difference equations is given, each of which has the form:

$$f_i = F_i(\underline{\Psi}, V_i, \sigma_i) \to 0; \quad i = 1, (N-1)^2 \qquad (3.4)$$

where $\underline{\Psi}$ is the vector of nodal values of ψ. The iterative solution starts from an initial estimate $(\underline{\Psi})_o$ and we have $f_i \to 0$ as the iteration progresses.

The method which Ames (1969) has called "Non-Linear Over-Relaxation", or "NLOR", is used to solve the finite-difference equations. In this method the nodes are scanned sequentially and at each step the value of ψ at the node in question is immediately updated as follows:

$$(\psi_i)_{new} = \left[\psi_i - \nu \cdot f_i \cdot \left(\frac{\partial f_i}{\partial \psi_i}\right)^{-1}\right]_{old} \qquad (3.5)$$

where ν is a constant acceleration factor whose value is discussed below in Section 3.1.1. The derivative $\partial f_i/\partial \psi_i$ is estimated numerically by perturbing ψ_i. The NLOR process is continued until the required corrections to ψ_i are acceptably small. In axially symmetric problems equation 2.23 contains terms involving the physical coordinate y. The values of y at any stage in the iteration are evaluated by integration of the current estimate of $\underline{\Psi}$ along lines of constant V, using equation 2.25. The sequence of scan in the NLOR iteration also progresses along lines of constant V thus allowing the integration for y to be performed simultaneously.

For two-dimensional problems when k = 0 in equation 2.23 the finite-difference equations are linear, and the NLOR method reduces to the well-known linear "Successive Over-Relaxation", or "SOR" method (Young 1954). The SOR method will converge from an arbitrary first estimate of $\underline{\Psi}$. In axially symmetric problems (k = 1), a reasonable first estimate of $\underline{\Psi}$ is required in order to produce reasonable values of y and therefore the corresponding two-dimensional problem (k = 0) is solved in the first instance. This initial use of the SOR method offers the further advantage that the optimum value of the acceleration factor ν in equation 3.5 may be estimated (see Section 3.1.1). It is particularly important in supercritical problems to use a good estimate of ν because the finite-difference procedure is entered several times and economy in computation time is desirable. The NLOR process was found to converge satisfactorily for axially symmetric problems, so long as negative excursions in the nodal values of ψ were suppressed.

The following subsection is concerned with the estimation of the optimum value of ν.

3.1.1 The NLOR and SOR acceleration factor

The purpose of the acceleration factor, ν, in equation 3.7 is to speed up the rate of convergence of the NLOR process and thus reduce computation time. There is an optimum value, ν_{opt}, in the range $1<\nu<2$ which is well worth the extra computation necessary to estimate it. For two-dimensional problems ($k = 0$) where the finite difference equations are linear, the NLOR process reduces to the SOR process for which Young (1954) has shown that ν_{opt} may readily be estimated. We find, by performing a few numerical experiments, that the same value is also near-optimum for the corresponding axially symmetric problem.

When the finite-difference approximation (equation 3.3) at each interior mesh node are substituted into equation 2.23 for the case $k = 0$, a system of $(N-1)^2$ linear algebraic equations may be derived which, after some reorganisation, takes the form:

$$\underline{\underline{A}}.\underline{\Psi} = \underline{B} \qquad (3.6)$$

where $\underline{\underline{A}}$ is an $(N-1)^2 \times (N-1)^2$ matrix, whose diagonal elements equal unity and most of whose off-diagonal elements are zero; $\underline{\Psi}$ is an $(N-1)^2$ vector of the unknown nodal values of ψ; and $\underline{B}$ is an $(N-1)^2$ vector. The system represented by equation 3.6 is typical of finite-difference problems and is ideally suited to iterative methods of solution, whose general form may be written:

$$\underline{\Psi}^j = \underline{\underline{M}}.\underline{\Psi}^{j-1} + \underline{C} \qquad (3.7)$$

where j refers to the jth iteration; the matrix $\underline{\underline{M}}$ and vector $\underline{C}$ are derived from $\underline{\underline{A}}$ and $\underline{B}$; and the iteration process is started from an estimate $\underline{\Psi}^{\circ}$. We may define the "displacement vector" $\underline{D}^j$ as $\underline{D}^j = \underline{\Psi}^j - \underline{\Psi}^{j-1}$. If n^j is a norm of $\underline{D}^j$ (the modulus of its largest element is a convenient choice), then it can be shown (Ames, 1969) that:

$$\lim_{j\to\infty} (n^j/n^{j-1}) = \lambda_m \qquad (3.8)$$

where λ_m is the spectral radius of $\underline{\underline{M}}$. The rate of convergence is given by λ_m. For the iteration process to converge we require that $\lambda_m < 1$, and it is desirable to select $\underline{\underline{M}}$ so that λ_m is as small as possible.

The following forms for $\underline{\underline{M}}$ and $\underline{C}$ are used for the Successive Over-Relaxation procedure:

$$\left.\begin{aligned} \underline{\underline{M}} &\equiv -\left[\nu\underline{\underline{L}} - \underline{\underline{I}}\right]^{-1}\left[\nu\underline{\underline{U}} - (\nu-1)\underline{\underline{I}}\right] \\ \underline{C} &\equiv \left(-\frac{1}{\nu}\underline{\underline{I}} + \underline{\underline{L}}\right)^{-1}\cdot\underline{B} \end{aligned}\right\} \qquad (3.9)$$

where $\underline{\underline{I}}$ is the unit matrix; and $\underline{\underline{L}}$ and $\underline{\underline{U}}$ are lower and upper triangular matrices with zeros on the diagonal such that:

$$\underline{\underline{A}} = \underline{\underline{L}} + \underline{\underline{U}} + \underline{\underline{I}}$$

Young (1954) showed that:

$$\left[\lambda_m + \nu - 1\right]^2 = \nu^2 \lambda_m \lambda_a^2 \qquad (3.10)$$

where λ_a is the largest eigenvalue of $(\underline{\underline{A}} - \underline{\underline{I}})$ and is assumed to be real. The value of λ_a depends only on the set of finite-difference equations being solved. The value of λ_m depends also upon ν through equation 3.10. A typical plot of $|\lambda_m|$ against ν is shown by the continuous line in Fig. 3.2. Our interest lies in ν_{opt}, the value of ν where $|\lambda_m|$ is a minimum. Examination of equation 3.10 shows that ν_{opt} occurs where λ_m just ceases to be real, from which we get:

$$\nu_{opt} = \frac{2}{1 + \sqrt{1 - \lambda_a^2}} \qquad (3.11)$$

where it can be seen that $1 \leq \nu_{opt} < 2$.

The value of ν_{opt} may be estimated by the following procedure:

(i) assume a trial value, ν_1

(ii) perform sufficient iterations to give a reasonable estimate of λ_m by means of equation 3.8

(iii) calculate λ_a from equation 3.10 and ν_{opt} from equation 3.11.

Carré (1961) examined the practical problems in the application of Young's results and found that step (ii) posed most difficulties. An unsuitable choice of ν_1 might require a very large number of iterations before equation 3.8 yielded a steady estimate of λ_m. This is due to interference from other, subdominant, eigenvalues of $\underline{\underline{M}}$. Carré recommended that steps (ii) and (iii) above should be repeated with a second trial value ν_2 given by:

$$\nu_2 = (\nu_{opt})_1 - \left[2 - (\nu_{opt})_1\right]/4 \qquad (3.12)$$

where $(\nu_{opt})_1$ is the estimate corresponding to ν_1.

Young (1954) derived his results (equations 3.10 and 3.11) for the case where $\underline{\underline{A}}$ is a symmetric, positive-definite matrix and results from a "consistently ordered" set of finite-difference equations. For our purposes, "consistent ordering" means that the mesh nodes are systematically scanned row-by-row or column-by-column and is a condition which is easily met. The two-dimensional hodograph finite-difference equations do not lead to a symmetric matrix $\underline{\underline{A}}$. Despite this, trial computations show (Fig. 3.2) that the optimum value of ν agrees with the estimate based on equations 3.10 and 3.11. It seems probable that Young's results can be extended to any case where λ_a is real.

It is worthwhile performing the extra computation to determine ν_{opt} because of the potential saving of computing time over the rest of the problem. The process of determining ν_{opt} results, of course in a partial solution. The advantages of using an optimum acceleration factor are most apparent in supercritical problems where the iteration procedure is entered several times with the same matrix $\underline{\underline{A}}$. In the case of axially symmetric problems, numerical experiments show that the value of ν_{opt} estimated for the corresponding two-dimensional problem is also nearly optimum for the NLOR iterative procedure. Results from a typical numerical experiment are shown in Fig. 3.2.

3.2 Integration of Hodograph Solution

The physical coordinates of the subsonic flowfield are recovered from the hodograph solution by integration of equations 2.21 along lines of constant V or constant θ. This leads to a map in the physical plane of points defined by the intersection of those lines. Integration along lines of constant V is more satisfactory because

equations 2.21c and d are less complex than equations 2.21a and b. In fact, the whole subsonic flowfield could readily be established relative to the line $\theta = 0$ were it not for the singularities at $(V_j, 0)$ and, possibly, at $(V_e, 0)$.

We may assume that the most serious effects of the singularities are confined to the adjacent nodes in the finite-difference mesh. By integrating equations 2.21c and d along the line $V = \frac{1}{2}(V_j + V_e)$ (line RS in Fig. 3.3a), the physical coordinates of point S on the upper boundary may be established most accurately relative to the axis. The coordinates of the nozzle wall CSL (i.e. the line $\theta = \beta$) may then be calculated through equations 2.21a and b. The rest of the physical flowfield is then plotted by integration of the hodograph solution along lines of constant V from the wall towards the axis, as shown in Fig. 3.3. In critical and super-critical problems, the step PO at the foot of the sonic line is covered by an approximate analytical solution valid for small perturbations about the state $\theta = 0$ and $V = 1$, which is described in Appendix A.

The integration of the hodograph solution along lines of constant V is performed by means of equations 2.21c and 2.21d:

$$\left(\frac{\partial x}{\partial \theta}\right)_V = \frac{1}{\rho V y^k}\left[V\cos\theta\,\psi_V - \sin\theta\,\psi_\theta\right] \qquad (2.21c)$$

$$\left(\frac{\partial y}{\partial \theta}\right)_V = \frac{1}{\rho V y^k}\left[V\sin\theta\,\psi_V + \cos\theta\,\psi_\theta\right] \qquad (2.21d)$$

These equations may be integrated between any two points 1 and 2 as follows:

$$V \text{ constant} \begin{cases} \left[x_2 - x_1\right] = \frac{1}{\rho V} \int_{\theta_1}^{\theta_2} \left[V \cos\theta \psi_V - \sin\theta \psi_\theta \right] \frac{d\theta}{y^k} & (3.13a) \\ \left[y_2^{k+1} - y_1^{k+1}\right] = \frac{k+1}{\rho V} \int_{\theta_1}^{\theta_2} \left[V \sin\theta \psi_V + \cos\theta \psi_\theta \right] d\theta & (3.13b) \end{cases}$$

where, for the case k=1, values of y needed in equation 3.13a are first obtained by integration of equation 3.13b. The integrands are defined only at the mesh nodes and the Euler-Lagrange formulae (e.g. Trapezium rule or Simpson's rule) may be used to perform the integrations. Simpson's rule was used in the present work because its truncation error is of order $(1/N)^4$ and is negligible compared to the truncation errors in the finite-difference equations. The derivatives ψ_V and ψ_θ in equations 3.13 are evaluated by the conventional central-difference approximations (equations 3.3), except at points on the hodograph boundary where the corresponding forward - or backward - difference formulae are used.

Along the nozzle wall - CL in Fig. 3.3 - we have $\theta = \beta$, $\psi_V = 0$ and equation 2.21b becomes, after some rearrangement:

$$\left(\frac{\partial y}{\partial V}\right)_\theta = \frac{-\left(\frac{\rho_V}{\rho} + \frac{1}{V}\right)\psi_\theta \sin\beta}{\left(\rho V y^k + k/y\, \psi_\theta \,.\, \sin\beta\right)} \qquad (3.14)$$

Integration of equation 3.14 between two points 1 and 2 for the case k = 0 gives:

$$y_2 - y_1 = -\frac{\sin\beta}{\rho V} \int_{V_1}^{V_2} (1/V + \rho_V/\rho)\psi_\theta \, dV \qquad (3.15)$$

and, for the case k = 1;

$$\log(y_2/y_1) = -\sin\beta \int_{V_1}^{V_2} \frac{(1/V + \rho_V/\rho)\psi_\theta \, dV}{\rho V y^2 + \sin\beta \, \psi_\theta} \qquad (3.16)$$

where iteration is necessary to determine y^2 in the integrand.

In both cases we have:

$$x_2 - x_1 = (y_2 - y_1)\cot(-\beta)$$

3.3 Accuracy of Numerical Solution

We now turn to the question of the accuracy of the numerical solution. Our interest lies in the value of the discharge coefficient and in features of the physical flowfield, all of which are determined by integrating the subsonic hodograph finite-difference solution. The scale of the whole solution is determined by the number of points in the finite-difference mesh used for the subsonic part of the calculation. We are considering cases where the rectangular hodograph region shown in Fig. 2.3 is divided into an equal number, N, of strips in the two coordinate directions. The single parameter, N, determines the size of the subsonic finite-difference mesh, the number of points on the sonic line and the number of points in the supersonic characteristics network. It is assumed that the results of a numerical solution to the nozzle flow problem approach the "true" results of a hypothetical exact solution as $N \to \infty$ or, to use a form more convenient for our present purposes, as $1/N \to 0$.

The limitations posed by computer storage and execution time mean that it is impracticable to use very large values of N. This is especially true in the axially symmetric case. It is impossible, therefore, always to ensure acceptably small truncation errors by using a sufficiently dense finite-difference mesh. We can, however, improve the accuracy of a given problem by extrapolating the results of computations with different values of N. The nature of the finite-difference approximations used here (equations 3.3) means that the truncation errors in most of the computed results are proportional to $(1/N)^2$ in the limit $1/N \to 0$. For the computed value, X, of a given parameter we may then write:

$$X = X_o + X_2 (1/N)^2 + \varepsilon \qquad (3.17)$$

where X_o is the true value of X in the limit $1/N \to 0$; X_2 is a coefficient to be determined; and ε represents higher order terms. If N is large enough to render the higher order terms negligible, then we may use equation 3.17 to estimate X_o from two values, X_a and X_b, calculated for $N = N_a$ and $N = N_b$.

$$X_o = (N_a^2 X_a - N_b^2 X_b)/(N_a^2 - N_b^2) \qquad (3.18)$$

The principle source of error in the results of the subsonic part of the nozzle calculation is the truncation error in the finite-difference approximations to the partial differential coefficients (equations 3.3). A second, less important source of inaccuracy arises from the use of numerical integration formulae to determine the physical coordinates from the hodograph solution. The most serious truncation errors in the finite-difference equations occur in the region

of the singularity at the point O in Fig. 3.1 where the derivatives of ψ become infinite. A similar situation exists for problems where $V_e \neq 0$ near the singularity at P in Fig. 3.1.

There are several ways of improving the accuracy of a finite-difference solution in the region of a singularity, including:

(a) transformation of coordinates to remove singularity

(b) use of a local analytical solution

(c) use of a locally concentrated finite-difference mesh.

Method (a) is potentially the most satisfactory, but it seems unlikely that a suitable transformation could be found for the nozzle problem. An analytical solution is described in Appendix A which is valid for small perturbations about the state V = 1, θ = 0 - i.e. the region of the singularity where the sonic line intersects the axis in critical and supercritical problems. This local analysis was found useful in determining the physical coordinates of the point of intersection, but an attempt to use it to improve the hodograph finite-difference solution was not successful. Concentrating the finite-difference mesh near the line θ = 0 in the way defined by equation 3.1 was found in many cases to give a reduction in trucation error. The degree of concentration depends on the value of the parameter t in equation 3.1 and there is an optimum value for a given problem. Since the optimum can only be found by performing numerical experiments, and its value varies from one problem to another, it is not worth spending too much computer time on the task. Our purpose is to present broad criteria for the choice of t and to indicate the probable magnitudes of truncation error in the final results.

We shall consider the following six classes of problem - incompressible, critical and choked flow for both the two-dimensional and axially symmetric cases. Computed results are given in Figs. 3.4-3.9 for the case $\beta = 90^{\circ}$. The corresponding truncation errors for $\beta < 90^{\circ}$ were found to be smaller. The results are plotted against 1/N, although the values of N itself are marked. Calculated parameters at t = 1.0, 1.5 and 2.0 are shown, together with estimates of the true solutions obtained by extrapolation with equation 3.18. The computed parameters which have been chosen for discussion are:

(a) the discharge coefficient

(b) the value of y/y_1 on the nozzle wall at the point where $V = 0.25\ V_j$ (subcritical) or $V = 0.25$ (critical and supercritical).

(c) the coordinates x and y on the free streamline where $\theta = \beta/8$

(d) (critical and supercritical) the value of x where the sonic line crosses the axis.

(e) (choked, axially symmetric) the choking pressure ratio, r_c.

The wall coordinate (b) is a measure of the success of the numerical method in predicting the physical coordinates of the subsonic flow inside the nozzle. Parameters (c) and (d) test the accuracy of the solution in the region of the singularity in the hodograph plane at the point where the line $V = V_j$ or $V = 1$ meets the axis.

The magnitudes of all the parameters of interest are of order unity. Discharge coefficients lie in the range $0.6 < C_d < 1$. The physical coordinates are scaled by the throat width, y_1, and our main concern is with the flowfield in the region of the lip plane. In most problems the sonic velocity, V = 1, features strongly and the gas properties are all scaled by their stagnation values.

Two-dimensional, incompressible flow (Fig. 3.4)

The results in Fig. 3.4 show that no particular advantage is gained by using $t > 1.0$ unless we are interested in the physical coordinates of the free streamline. This involves integration of the solution near the singularity on the hodograph axis. The estimates of the true solutions which are shown in Fig. 3.4 were obtained by applying equation 3.18 to the results for $t = 1.5$, $N = 16$ and $N = 24$. The value of the discharge coefficient is in excellent agreement with the well-known analytical solution, $C_d = \pi/(2+\pi) = 0.61102$ (Lord Rayleigh, 1876). These results suggest that for two-dimensional, incompressible flow, errors smaller than 0.005 are given by a single solution with $t = 1.5$ and $N = 24$.

Two-dimensional, critical flow (Fig. 3.5)

A significant reduction in truncation error for computed values of C_d and free streamline coordinates is shown for $t > 1.0$. The distance, x_o, downstream from the lip plane at which the jet streamlines become parallel to the axis was computed by the method described in Appendix A and the truncation error appears to be a linear function of $1/N$. Aslanov and Legova (1959) published the analytical solution $x_o = 1.201$, and this is also shown in Fig. 3.5d. The estimates of the true solutions shown in Figs. 3.5a-c were obtained from equations 3.18 using the results for $t = 1.5$, $N = 16$ and $N = 24$. The value of the discharge coefficient agrees with the solution $C_d = 0.7447$ also given by Aslanov and Legova. The results suggest that errors of about 0.005 would be given for a single two-dimensional, critical solution with $t = 1.5$ and $N = 24$.

Two-dimensional, choked flow (Fig. 3.6)

The results in Fig. 3.6 show that the solution near the foot of the sonic line is improved for $t > 1.0$. The value of x_o is a linear function of $1/N$. The estimates of the true solutions were obtained from equation 3.18 using the results for $t = 1.5$, $N = 16$ and $N = 24$. The value of the discharge coefficient is a slight improvement on the solution $C_d = 0.85$ given by Frankl (1947). The results again suggest errors of about 0.005 for a single two-dimensional choked solution with $t = 1.5$ and $N = 24$.

Axially symmetric, incompressible flow (Fig. 3.7)

The results in Fig. 3.7 again show that $t > 1.0$ only gives an improvement in accuracy for the solution close to the singularity. The true solution estimates were obtained from $t = 1.5$, $N = 16$ and $N = 24$. The value for discharge coefficient agrees well with the solution $0.59131 < C_d < 0.59139$ given by Bloch (1969). Errors better than 0.005 are given by the solution with $t = 1.5$, $N = 24$.

Axially symmetric, critical flow (Fig. 3.8)

The results in Figs. 3.8a-c show that the solution with $t = 1.5$, $N = 24$ is subject to errors of about 0.001. The estimates of the true solutions were obtained by extrapolation from $t = 1.5$, $N = 16$ and $N = 24$. The results in Fig. 3.8d for the sonic line axis intersection coordinate, x_o, were computed by the method of Appendix A. The estimate $x_o = 0.88$ is based on the solutions for $t = 1.0$.

Axially symmetric, choked flow (Fig. 3.9)

The results in Fig. 3.9 a - c show that the solution depends upon t and N in a similar way to the other cases which have been considered except for the sonic line/axis intersection coordinate, x_o. This parameter is determined by the method of Appendix A, and is a linear function of $1/N$. The amount of computation time necessary for axially symmetric supercritical problems means that N = 16 is the largest practicable mesh density. This leads to an error in x_o of about 0.01 and errors in physical coordinates elsewhere of about 0.002. Fig. 3.9d shows the computed values of the choking pressure ratio which appears to be a linear function of $1/N$. The estimates of the true solutions shown in Fig. 3.9 were obtained from the results for t = 1.5, N = 12 and N = 16.

We may now summarise this discussion of the accuracy of the numerical solution. A reduction of the error in the solution near the sonic line (or free streamline in subcritical problems) is given by concentrating the hodograph finite-difference mesh towards the line $\theta = 0$. A single solution with t = 1.5 in equation 3.1 and N = 24 (N = 16 in axially symmetric, choked problems) will result in truncation errors within $\pm$ 0.005. Extrapolation by equation 3.18 will give results correct to $\pm$ 0.001. These remarks do not apply to the solution at the point where the sonic line intersects the axis. For choked flow, the error with t = 1.5 and N = 16 or 24 is about + 0.01. Extrapolation improves the error to about $\pm$ 0.002.

3.4 The method of characteristics

Supercritical problems involve calculations in the supersonic region of the flowfield where the governing equations are hyperbolic. The method of characteristics is used for the calculation and was described in outline in Section 2.4. The supercritical solution is thus subject to truncation errors in both its subsonic and supersonic regions. It is not possible to study these sources of error separately because the two regions of calculation are inter-dependant. All that can be done is to examine the increase or decrease in overall error caused by particular changes to the numerical procedure. In this section, the details of the method of characteristics calculation are considered with the objective of reducing its contribution to the error in the final results.

Calculation by the method of characteristics have been widely used for many years and basic details are given by Shapiro (1953). A network of points originating from a "starting line" - in this case, the sonic line - is built up. Each step consists of calculating the physical and hodograph coordinates of a point C (see sketch below) which lies at the intersection of 1st and 2nd family characteristics passing respectively through points A and B, whose coordinates are known.

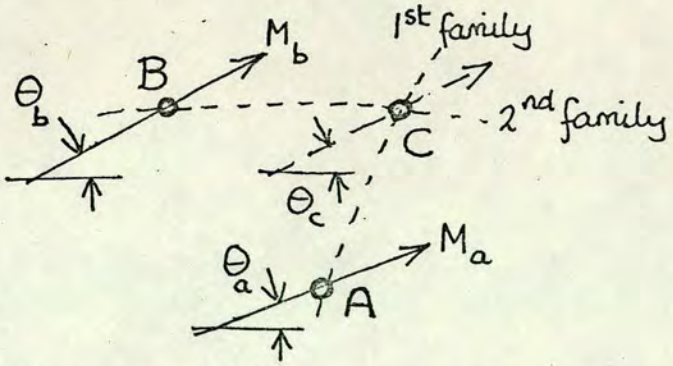

The first and second families are defined by equations 2.36 and 2.37.

1st family

$$dy/dx = \tan(\theta + \mu) \qquad (2.36a)$$

$$\theta = \omega(M) - k\int \frac{\sin\mu \sin\theta}{\sin(\theta+\mu)} \frac{dy}{y} + C_I \qquad (2.36b)$$

$$\text{2nd family} \begin{cases} dy/dx = \tan(\theta-\mu) & (2.37a) \\ \theta = -\omega(M) + k\int \frac{\sin\mu\sin\theta}{\sin(\theta-\mu)}\,\frac{dy}{y} + C_{II} & (2.37b) \end{cases}$$

where M is the Mach number; $\mu = \sin^{-1}(1/M)$; and the function $\omega(M)$ was defined in equation 2.35.

An alternative pair to equation 2.36 is obtained as follows by substitution of 2.36a into 2.36b:

$$\text{1st family} \begin{cases} dy/dx = \tan(\theta+\mu) & (3.19a) \\ \theta = \omega(M) - k\int \frac{\sin\mu\sin\theta}{\cos(\theta+\mu)}\,\frac{dx}{y} + C_{I} & (3.19b) \end{cases}$$

Equations 3.19 are more suitable than equation 2.36 for the flowfield calculations because in many instances we have $(\theta+\mu)\approx 0$ which raises problems with the integral term in equation 2.36b.

The values of θ and M at C are given in terms of the values at A and B by the solution of the following equations which are derived from equation 3.19b and 2.37b:

$$\left.\begin{aligned} \theta_c - \theta_a &= \omega(M_c) - \omega(M_a) - kZ_{ac} \\ \theta_c - \theta_b &= \omega(M_b) - \omega(M_c) + kZ_{bc} \end{aligned}\right\} \quad (3.20)$$

where the suffices denote quantities at A,B or C; and Z_{ac} and Z_{bc} are the values of the integrals along AC and BC. It is necessary to express Z_{ac} and Z_{bc} in finite-difference form because the integrands are only defined at the points A,B or C. The following forms were used :

$$\left.\begin{aligned} Z_{ac} &= \left[\frac{\sin\mu_a\sin\theta_a}{y_a\cos(\theta_a+\mu_a)} + \frac{\sin\mu_c\sin\theta_c}{y_c\cos(\theta_c+\mu_c)}\right]\frac{(x_c-x_a)}{2} \\ Z_{bc} &= \left[\frac{\sin\mu_b\sin\theta_b}{y_b\sin(\theta_b-\mu_b)} + \frac{\sin\mu_c\sin\theta_c}{y_c\sin(\theta_c-\mu_c)}\right]\frac{(y_c-y_b)}{2} \end{aligned}\right\} \quad (3.21)$$

If either A or B lies on the axis we have, as $\theta \to 0$ and $y \to 0$:

$$\left.\begin{aligned} \left[\frac{\sin\mu_a \sin\theta_a}{y_a \cos(\theta_a+\mu_a)}\right]_{\substack{\theta_a\to 0\\ y_a\to 0}} &\longrightarrow \tan\mu_a \cdot \left(\frac{d\theta}{dy}\right)_a \\ \left[\frac{\sin\mu_b \sin\theta_b}{y_b \sin(\theta_b-\mu_b)}\right]_{\substack{\theta_b\to 0\\ y_b\to 0}} &\longrightarrow -\left(\frac{d\theta}{dy}\right)_b \end{aligned}\right\} \qquad (3.22)$$

For two-dimensional problems, where $k=0$, the solution of equations 3.20 leads straight away to values of M_c and θ_c. Axially symmetric problems require iteration because Z_{ac} and Z_{bc} involve values of x_c and y_c which have yet to be determined. The iteration is started by assuming $Z_{ac} = Z_{bc} = 0$.

The physical coordinates, x_c and y_c, are obtained from equations 2.36a and 2.37a. The conventional procedure adopted in most standard texts (e.g. Shapiro, 1953) is to express these equations in finite-difference form as follows:

$$\left.\begin{aligned} \frac{y_c - y_a}{x_c - x_a} &= \tan\left(\bar{\theta}_{ac} + \bar{\mu}_{ac}\right) \\ \frac{y_c - y_b}{x_c - x_b} &= \tan\left(\bar{\theta}_{bc} - \bar{\mu}_{bc}\right) \end{aligned}\right\} \qquad (3.23)$$

where $\bar{\theta}_{ac}$ and $\bar{\mu}_{ac}$ average values of θ and μ along the segment AC; and $\bar{\theta}_{bc}$ and $\bar{\mu}_{bc}$ are average values along BC. Standard practice is to take a simple arithmetic mean for $\bar{\theta}_{ac}$ and $\bar{\mu}_{ac}$:

$$\left.\begin{aligned} \bar{\theta}_{ac} &= \tfrac{1}{2}\left(\theta_a + \theta_c\right) \\ \bar{\mu}_{ac} &= \tfrac{1}{2}\left(\mu_a + \mu_c\right) \end{aligned}\right\} \qquad (3.24)$$

and similarly for $\bar{\theta}_{bc}$ and $\bar{\mu}_{bc}$. Equations 3.24 assume an essentially linear variation of θ and μ with distance along the characteristic. Satisfactory results are given except in the region near $M = 1$ where the rate of change of μ is very large. Accurate computation near the sonic line is important for supercritical nozzle problems,

and possible alternatives to equations 3.24 were considered. Best results were obtained when the average value of μ over the interval of M along the characteristic segment was used, as follows:

$$\bar{\theta}_{ac} = \tfrac{1}{2}(\theta_a + \theta_c) \tag{3.25a}$$

$$\bar{\mu}_{ac} = \int_{Ma}^{Mc} \mu\, dM \Big/ (M_c - M_a) = \int_{Ma}^{Mc} \sin^{-1}(1/M)\, dM \Big/ (M_c - M_a)$$

$$= \frac{\left[M \sin^{-1}(1/M) + \log\left(M + \sqrt{M^2-1}\right)\right]_{Ma}^{Mc}}{(M_c - M_a)} \tag{3.25b}$$

and similarly for $\bar{\theta}_{bc}$ and $\bar{\mu}_{bc}$. Computed results obtained with equations 3.25 are compared in Fig. 3.10 with results given by equations 3.24, and a general reduction in truncation error is shown.

When the values of M, θ, x, and y at point C have been computed it only remains for the stream function, ψ_c, to be evaluated. At any point in the flowfield we may write:

$$d\psi = \left(\frac{\partial \psi}{\partial x}\right)_y dx + \left(\frac{\partial \psi}{\partial y}\right)_x dy$$

$$= -\rho y^k V \sin\theta\, dx + \rho y^k V \cos\theta\, dy \tag{3.26}$$

where equations 2.10 and 2.12 have been used to express the partial derivatives $\left(\frac{\partial \psi}{\partial x}\right)_y$ and $\left(\frac{\partial \psi}{\partial y}\right)_x$ in terms of the components of velocity. The density ρ and velocity V may be written in terms of M by using equations 2.4a and 2.5c, and equation 3.26 may be integrated along the characteristic segment AC to give:

$$\psi_c - \psi_a = \left(\frac{\gamma+1}{2}\right)^{\frac{1}{2}} \left\{ -\int_{x_a}^{x_c} \frac{M \cdot y^k \sin\Theta}{\left(1+\frac{\gamma-1}{2}M^2\right)^{\frac{(\gamma+1)}{2(\gamma-1)}}} \, dx + \int_{y_a}^{y_c} \frac{M y^k \cos\Theta}{\left(1+\frac{\gamma-1}{2}M^2\right)^{\frac{\gamma+1}{2(\gamma-1)}}} \, dy \right\} \quad (3.27)$$

The integrands in equation 3.27 are defined only at A and C, and a linear variation was assumed in the calculation.

3.5 Matching of subsonic and supersonic calculations

A supercritical nozzle problem involves both subsonic calculations (in the hodograph place) and supersonic calculations (by the method of characteristics in the physical plane). Linking the two regions of calculation is the function $\psi_s(\theta)$ defining the distribution of stream function along the sonic line. The function $\psi_s(\theta)$ must fulfill two conditions. Firstly, the complete solution must be continuous across the sonic line. Secondly, it must satisfy the boundary conditions imposed by the Prandtl - Meyer expansion at the lip and by the free streamline. The determination of $\psi_s(\theta)$ is an iterative process in which the function is initially guessed and then modified by one of two possible strategies. The first of these is to ensure that the boundary conditions at the lip and free streamline are satisfied and to modify $\psi_s(\theta)$ until the derivatives of ψ are continuous across the sonic line. The second is to take a continuous solution across the sonic line and to use the outer boundary condition to guide the iteration. The first strategy is only practicable if both the subsonic and the supersonic parts of the calculation are performed in the hodograph plane, because the physical variables x and y, are not involved. Norwood (1962)

took this approach for his two-dimensional solution, although the iterative scheme which he used was very slow to converge and sometimes unstable. Even though a much better numerical procedure would be devised to replace Norwood's, the more complex axially symmetric equations make an approach using the second strategy more practicable.

The subsonic calculation uses a finite-difference method based on a rectangular mesh in the hodograph plane. The function $\psi_s(\theta)$ on the sonic line takes the form of a vector $\underline{\psi}_s$ of (N-1) discrete values $(\psi_s)_1, (\psi_s)_2, \ldots\ldots (\psi_s)_{N-1}$, where N is the number of subdivisions of the finite-difference mesh in the range $0 \leq \theta \leq \beta$. The values of $\underline{\psi}_s$ are initially estimated, the solution of equation 2.23 in the hodograph plane is performed, and the physical coordinates of the sonic line are determined by integration of equations 2.21c and 2.21d. The physical coordinates locate the points P_1, P_2, etc shown in Fig. 3.11a which correspond to each of the original sonic line points represented by the elements of $\underline{\psi}_s$. The characteristics network shown also in Fig. 3.11a is now calculated. We may examine conditions near the top of the second - family characteristics P_i Q_i. If $\underline{\psi}_s$ is the true solution then one of the following conditions should apply:

(a) $1 < (M_q)_i \leq M_j$: $\psi = 1$ at Q_i

where $(M_q)_i$ is the value of Mach number at the point Q_i (defines a characteristic originating in the Prandtl - Meyer expansion)

(b) $(M_q)_i > M_j$: $\psi = 1$ when $M = M_j$

(defines the free steamline boundary condition).

In general, since the choice of $(\psi_s)_1, (\psi_s)_2, \cdots, (\psi_s)_{N-1}$ is only an estimate, conditions (a) or (b) will not apply and a vector $\underline{\delta\Psi}$ of errors $(\delta\psi)_1$, $(\delta\psi)_2$, etc. will be generated, where $\delta\psi_i = (\psi_b)_i - 1$ and $(\psi_b)_i$ is the actual value of ψ at point Q_i or $M = M_j$ under conditions (a) or (b). By evaluating the matrix of partial differential coefficients:

$$\underline{\underline{Z}} \equiv \left[\frac{\partial(\delta\psi)_i}{\partial\psi_j}\right]_{\substack{i=1,N-1 \\ j=1,N-1}} \tag{3.29}$$

Newton's method may be used to correct the estimate $\underline{\Psi_s}$:

$$(\underline{\Psi_s})_{new} = (\underline{\Psi_s})_{old} - \underline{\underline{Z}}^{-1}\,\underline{\delta\Psi} \tag{3.30}$$

and the whole procedure is repeated until the elements of $\underline{\delta\Psi}$ are acceptably small. The elements of $\underline{\underline{Z}}$ are evaluated numerically be perturbing $(\psi_s)_1$, $(\psi_s)_2$, etc. in turn and repeating the solution. For two-dimensional flow, the relationship between $\underline{\delta\Psi}$ and $\underline{\Psi_s}$ is linear and so is the finite-difference solution in the hodograph plane. This means that in priniciple only one application of equation 3.30 is necessary. In practice, it requires an unreasonable quantity of computing time to carry the finite-difference solution to the precision at which round-off errors are negligible. The matrix $\underline{\underline{Z}}$ need only be evaluated once, but two or three applications of equation 3.30 may be necessary. Axially symmetric problems are non-linear and require about eight iterations, although it was found unnecessary to evaluate $\underline{\underline{Z}}$ on every iteration.

The "final" characteristic, OH in Fig. 3.11, does not feature in the procedure which has just been described. This is a short-coming

of the present supercritical method, because changes in boundary condition between the final characteristic and the one preceding it do not influence the solution. However, to compensate for this deficiency, we may use the surplus information to improve the value of the x-coordinate of the point O, where the sonic line meets the nozzle axis. Such an improvement is desirable because the derivatives ψ_θ and ψ_ν on the sonic line become very large near the axis and introduce large errors when integration by equation 2.21c is performed. The position of the point O is therefore established by calculating a "final" characteristic which satisfies the appropriate condition on the outer boundary. Calculations in the characteristic mesh interval next to the point O may be made more reliable by the use of the analytical solution, valid for small perturbations from the state $M = 1$, $\theta = 0$, which is described in Appendix A.

3.6 Discussion

This chapter has been concerned with the details of the numerical techniques used in the solution of the sharp-lipped nozzle problem. The objective has been to study the factors which affect the truncation errors. One way of ensuring that errors are sufficiently low is to use a very dense finite-difference mesh (i.e. a large value of N). This, however, might lead to unacceptably large computation times. Computation time depends to a certain extent on the accuracy to which the various iteration procedures are carried. All the results discussed are based on stream-function values computed to within a tolerance of $\pm 5.10^{-6}$ - a level at which rounding errors are small compared to truncation errors. But the main factor which determines the computation time is the mesh size. Time was found to be roughly

proportional to $N^{3.5}$; a two-dimensional, supercritical solution at N = 16 took about 60 seconds on an ICL 4-75 computer and the corresponding axially symmetric problem took about 300 seconds. Subcritical solutions took only two or three seconds.

The results shown in Figs. 3.4 - 3.9 indicate that, for t = 1.5, a (16 x 16) mesh will give an accuracy of about $\pm$ 0.0 1 and a (24 x 24) mesh will give about $\pm$ 0.005. However, the combination of (16 x 16) + (24 x 24) together with extrapolation by equation 3.18 will give a solution correct, for the most part, to $\pm$ 0.001. It would require a single (64 x 64) solution taking about 25 times the (24 x 24) time to achieve this accuracy.
A look at the results of other workers supports the view that the present numerical method is comparatively economic. Norwood (1961) solved the two-dimensional, choked problem by a similar method and achieved 3 - figure accuracy with a (60 x 90) mesh. Bloch (1969) used a finite - difference method to solve the axially symmetric, incompressible problem and achieved 3 - figure accuracy with an (80 x 80) mesh.

Chapter 4 will be devoted to a discussion of sharp-lipped nozzle performance. Most of the results have been obtained from the combination of (16 x 16) and (24 x 24) numerical solutions with extrapolation by equation 3.18. Truncation errors lie within $\pm$ 0.002.

CHAPTER 4

THEORETICAL FLOW THROUGH SHARP-LIPPED NOZZLES

The equations for compressible flow through sharp-lipped nozzles and the numerical methods for solving them have been described in chapters 2 and 3. This chapter is devoted to a survey of theoretical sharp-lipped nozzle performance. The results presented here were obtained from a computer program written for the purpose. Details of the program itself will not be discussed, except to say that it amounted to some 1,500 statements in IMP, a programming language used at Edinburgh University.

The survey of nozzle performance covers both two-dimensional and axially symmetric flows and examines the effect of the following four parameters:

(a) the nozzle wall angle, β,

(b) the pressure ratio, r (with particular attention paid to incompressible, critical and choked flows),

(c) the ideal gas specific heat ratio, γ ,

and (d) the approach velocity, V_e (two-dimensional flow only).

To begin with, in section 4.1, some plots of complete nozzle flowfields are considered. Section 4.2 is concerned with discharge coefficients; Section 4.3 is concerned with the velocity distribution along the nozzle wall and axis; and Section 4.4 with the shapes of the sonic line and the supercritical jet boundary.

4.1 Nozzle Flowfield

We shall consider some representative nozzle flowfields in this section. Attention is directed towards streamlines (lines of constant ψ) and lines of constant velocity or Mach number. In the subsonic region the dimensionless

velocity (V) (defined in Section 2.1) is a convenient parameter, while the Mach number (M) is used in the supersonic region. The constant V or M lines are also lines of constant gas pressure, density and temperature (through equations 2.5). This work is primarily concerned with calculations through the subsonic and transonic parts of the flowfield up to the final characteristic which connects the outer boundary to the point where the axis intersects the sonic line. Calculations downstream from this line can be performed by the method of characteristics as far as the stage at which shockwaves begin to develop in the flow. Alternatively, other numerical methods may be used (e.g. Taylor, 1968) which will allow for the presence of shockwaves. The results shown here include calculations in the shock-free region which extends well towards the plane at which the jet reaches its maximum width.

The first three figures show a comparison between corresponding two-dimensional and axially symmetric flowfields for choked flow at $\beta = 90^\circ$ (Figs. 4.1a and b), critical flow at $\beta = 90^\circ$ (Figs. 4.2a and b), and choked flow at $\beta = 30^\circ$ (Figs. 4.3a and b). There is insufficient space to show more of the two-dimensional 90° jet in Fig. 4.1a but a more complete picture, similar to this one, is given by Benson and Pool (1965a). The axially symmetric jet in Fig. 4.1b extends to the point at which focussing of the characteristics indicates the presence of a shockwave.

Figs. 4.4 and 4.5 show how the shapes of the streamlines and constant velocity lines are affected by the presence of an approach duct. The case $V_e = 0.5$ is shown for critical and choked two-dimensional flow at $\beta = 90^\circ$ (Figs. 4.4a and b) and $\beta = 30^\circ$ (Figs. 4.5a and b).

4.2 Discharge Coefficient

The discharge (or contraction) coefficient is the most prominent of the nozzle performance parameters. The effect of pressure ratio is shown in Fig. 4.6 for two-dimensional and axially symmetric flow. The three most significant pressure ratios in the operating range of a nozzle are those giving incompressible, critical and choked flow. The values of these pressure ratios depend on β and γ and are tabulated in Table 4.1. The corresponding values of discharge coefficient are given in Table 4.2 (two-dimensional) and Table 4.3 (axially symmetric). The effect of wall angle, β, on discharge coefficient at the three significant pressure ratios is shown graphically in Fig. 4.7. The effect of γ on C_d for axially symmetric flow has not been computed, except in the case $\beta = 90^\circ$. However, the results in Fig. 4.8 show that dependence of C_d on γ is similar for both classes of flow.

Figure 4.9 shows how the approach velocity influences the two-dimensional discharge coefficient. We have already seen in Section 2.1, equation2.7, that the approach velocity is closely related to the nozzle area ratio. The area ratio is perhaps more useful for practical purposes, but the approach velocity is the more convenient parameter for a solution in the hodograph plane. The relationship between these two parameters is shown for two-dimensional choked and critical flow in Fig. 4.10.

4.3 Velocity Distributions on Nozzle Wall and Axis

This section is concerned with the variation of velocity with distance from the lip along the nozzle wall, and with the variation of velocity along the axis. For compressible flow, the dimensionless velocity, V, is related to the pressure, p, by the following equation, first introduced in Section 2.1:

$$p/p_o = \left(1 - \frac{\gamma-1}{\gamma+1} V^2\right)^{\gamma/\gamma-1} \qquad (2.3)$$

where p_o is the stagnation pressure. For incompressible flow, Bernoulli's equation applies:

$$p = p_o - \tfrac{1}{2} \rho V^2 \qquad (4.1)$$

where, in this case, ρ and V refer to the absolute density and the absolute velocity.

The results for wall velocities show V plotted against $(y_1 / y)^{k+1}$ for incompressible flow (where V_1 is the velocity at the lip). The ratio y_1 / y allows us conveniently to plot the whole range of wall coordinates: $y_1 \leqslant y < \infty$. This ratio is raised to the power (k + 1) because the velocity inside the nozzle is closely related to cross-section area and, in the limit $\beta \to 0$, is given by the one-dimensional flow equation 2.6. When plotted in this way, axially symmetric results (k = 1) differ only slightly from the corresponding two-dimensional results (k = 0). The axial wall coordinate, x, is given by the relationship:

$$\frac{y - y_1}{x - x_1} = - \tan \beta \qquad (4.2)$$

Wall velocity distributions are given in Figs. 4.11 a-c for incompressible, critical and choked flow with zero approach velocity. The effect of nozzle pressure ratio (shown here as a variation in the jet boundary Mach number, M_j) is given in Figs. 4.12 a-c. It can be seen that there is only a small change to the velocity pattern between the critical and the choked conditions. The influence of γ on the wall velocity distribution is negligible and is therefore not shown here.

This last parameter would, however, be more significant if pressures were to be determined by equation 2.3.

When we come to consider the influence of approach velocity on the wall velocity pattern, we must also take into account the velocities on the surface of the approach duct. The gas on the boundary streamline decelerates along the duct surface from V_e to zero at the stagnation point where the approach duct meets the convergent nozzle wall. It then accelerates again up to the lip velocity. This pattern is illustrated in Figs. 4.4 and 4.5. The velocity distribution along the approach duct surface is shown for choked, two-dimensional flow at a range of values of V_e in Fig. 4.13. Here, V is plotted against X/y_1 where X is the distance upstream from the stagnation point. Velocities along the convergent nozzle wall are shown in Figs. 4.14 a-d.

The velocity distribution along the nozzle axis is shown in Figs. 4.15 a & b for critical and choked flow.

4.4 The Sonic Line and Supercritical Jet Boundary

Two important features of the supercritical flowfield are the sonic line and the jet boundary. Their dependence on the nozzle parameters is shown in Figs. 4.16 - 4.19. The shapes of these lines in axially symmetric flow are given for three values of β in Figs. 4.16. The shapes where the flow is choked are shown in Fig. 4.16a, and Fig. 4.16b shows how the shapes vary with β at a given pressure ratio (in this case, the value corresponding to a jet boundary Mach number of $M_j = 1.6$). The effect of γ and approach velocity is shown for two-dimensional flow in Figs. 4.17 and 4.18. The effect of pressure ratio is shown in Fig. 4.19. In the limit of critical flow, the sonic line and the boundary streamline coincide and the whole flow reaches sonic velocity at a plane situated a finite distance

from the nozzle lip plane. This result the "length" of a critical jet - was shown for two-dimensional flow by Ovsiannikov (1949) and the value of the length in the case $\beta = 90^{\circ}$ was evaluated by Roumieu (1952) who obtained the value 1.20. Aslanov and Legova (1959) studied the effect of approach velocity and found that the critical jet length was virtually unchanged until $V_e > 0.5$. Values of the critical jet length ($\gamma = 1.4$, $V_e = 0$), including axially symmetric results, are given in Table 4.4.

Another aspect of the sonic line is the variation of the stream function with flow, $\psi_s(\theta)$, which plays an important part in the numerical solution of supercritical problems. Typical functions $\psi_s(\theta)$ are plotted for choked and supercritical flow in Fig. 4.22 In the supercritical case the derivative $d\psi_s/d\theta$ is discontinuous at a point which corresponds to the change in boundary condition from a centred expansion to a free streamline. The discontinuity does not seriously affect the integration of the hodograph solution leading to physical coordinates.

TABLE 4.1

Choked and Critical Pressure Ratios for Two-dimensional and Axially Symmetric Sharp-lipped Nozzles.

		γ = 1.0		1.2		1.4		1.667	
		2 D	axi	2 D	axi	2 D	axi	2 D	axi
Choked Flow	β =90°	0.107	0.100	0.066	0.061	0.039	0.035	0.017	0.016
	75°	0.145	-	0.098	-	0.066	0.059	0.036	-
	60°	0.194	-	0.142	-	0.104	0.096	0.067	-
	45°	0.256	-	0.202	-	0.159	0.150	0.115	-
	30°	0.335	-	0.280	-	0.234	0.224	0.186	-
	15°	0.435	-	0.384	-	0.340	0.330	0.289	-
Critical Flow		0.607		0.565		0.528		0.487	

Table 4.2

Discharge Coefficients for Two-dimensional Flow (V_e = 0)

nozzle angle (β)	Choked Flow				Critical Flow				incompressible flow
	γ=1.0	1.2	1.4	1.667	γ=1.0	1.2	1.4	1.667	
90°	0.863	0.856	0.849	0.840	0.754	0.749	0.745	0.739	0.611
75°	0.881	0.875	0.870	0.862	0.785	0.781	0.777	0.772	0.647
60°	0.902	0.897	0.893	0.887	0.822	0.818	0.814	0.810	0.692
45°	0.926	0.922	0.919	0.915	0.864	0.860	0.858	0.854	0.747
30°	0.951	0.948	0.947	0.944	0.911	0.908	0.906	0.903	0.814
15°	0.977	0.976	0.976	0.975	0.959	0.958	0.957	0.955	0.897

Table 4.3

Discharge Coefficients for Axially Symmetric Flow ($V_e = 0$)

β		Choked Flow	Critical Flow	incom-pressible
90°	$\gamma = 1.0$	0.845	0.736	0.591
	1.2	0.837	0.731	
	1.4	0.830	0.726	
	1.667	0.821	0.721	
75°		0.850	0.757	0.625
60°		0.874	0.794	0.669
45°		0.902	0.839	0.723
30°		0.934	0.891	0.793
15°		0.970	0.949	0.883

Table 4.4

Length of Critical Jet - x_o / y_1 ($V_e = 0$; $\gamma = 1.4$)

Wall angle (β)	15°	30°	45°	60°	75°	90°
two-dimensional	1.15	1.19	1.20	1.20	1.20	1.20
axially symmetric	0.72	0.80	0.85	0.87	0.88	0.88

CHAPTER 5

EXPERIMENTAL WORK

5.1 Introduction

The programme of experiments on flow through sharp-lipped nozzles is described in this chapter. This part of the work had two objectives. The first was to provide information on typical nozzle performance to supplement that available in the published literature. The second objective was to study some of the factors which might cause real nozzle flows to differ from the theoretical predictions. In particular, the effect of departures from the ideal "sharp lip" geometry was studied.

The experiments were performed on axially symmetric and two-dimensional nozzles whose general configuration is shown in Figs. 5.1 and 5.2. The axially symmetric nozzles had an entry diameter of 50mm and a nominal throat diameter of 12.5mm (0.5 inch). The two-dimensional nozzles were made by enclosing two 10mm thick wedges between plane perspex walls; the entry width was 100mm and the nominal throat width was 10mm. Such a nozzle can only be regarded as being "two-dimensional" if the effects of boundary layer growth on the side walls are considered to be negligible. The inlet: throat area ratio for all the nozzles was large enough for any entry effects to be negligible. The experiments are therefore concerned with nozzles having an essentially zero approach velocity.

The flow of air ($\gamma = 1.4$) was studied for wall angles in the range $15^\circ \leq \beta \leq 90^\circ$ at pressure ratios in the range $0.2 \leq r \leq 1.0$. Most of the measurements taken were for mass flow (leading to discharge coefficients), although some of the axially symmetric nozzles were provided with pressure tappings on the walls. The side walls of the two-dimensional nozzles had

tappings along the axis. The remaining sections of this chapter are concerned with the details of the experiments. Section 5.2 describes the apparatus used for the tests. The nozzles themselves are described in Section 5.3. Details of the evaluation of the experimental results are discussed in Section 5.4.

5.2 Description of apparatus

It was necessary to base the design of the apparatus on existing equipment. The components of a blow-down supersonic wind tunnel seemed particularly appropriate. The decision to use an intermittent rather than a steady-flow technique was made at the outset because it placed a less severe restriction on the air flow rate. A nominal throat diameter of 12.5 mm (0.5 inch) was selected as being a reasonable compromise between the desire for a long run-time to avoid transient problems, and the need for a nozzle large enough to be easily made and supplied with pressure tappings.

Two sets of apparatus were constructed for this work. The first operated on the "blow-down" principle, using the compressor and storage tank of the supersonic wind tunnel. The layout is shown in Fig. 5.3. After the tank had been charged by the compressor it was discharged to atmosphere through the test nozzle. The parameters to be measured were monitored at regular intervals and logged on paper tape to be processed later by computer. This experimental system was not wholly satisfactory, in particular because it did not allow the accurate measurement of mass flow. Although many of the short-comings could have been eliminated by suitable modifications, it was decided instead to develop an alternative system. The second apparatus is shown in Fig. 5.4 and operated on the "indraught" principle.

Temperatures and pressures were measured directly with thermocouples and manometers. The indraught system was very successful and provided all the results to be discussed later. However, the development of the blowdown apparatus occupied a significant period of time and it will be described in more detail in Section 5.2.1 which follows. A detailed description of the indraught apparatus is given in Section 5.2.2.

5.2.1 The Blowdown Apparatus

The layout of the blowdown system is shown in Fig. 5.3 and the apparatus itself in the photograph in Plate I. The volume of the storage tank was about $10m^3$ and the maximum pressure was 10 bar absolute. The rate of discharge through a typical test nozzle caused the tank pressure to fall from 10 bar to 2 bar absolute in about 5 minutes. Such a low rate of change meant that wave effects upstream of the nozzle were negligible and the flow could be regarded as "steady" at any instant in time. The static pressure just upstream of the nozzle (effectively the stagnation pressure) and various surface pressures to be recorded were led to a 16 - channel switching valve which was designed for the purpose and which is shown in the photograph in Plate II. The switching valve was rotated from one position to the next at a constant rate, connecting each pressure input in turn to the transducer and, after allowing time for transients to die away, automatically logging the signal on punched tape. Although the switching valve had nominally sixteen pressure channels, two channel positions were occupied by separate transducer signals sensing the venturi pressure drop and air stream temperature. The logging process proceeded steadily throughout the test run at a rate of 24 channels / minute which meant that each measurement point was visited every 40 seconds. Smoothing and interpolation of the paper tape record eventually yielded sets of "simultaneous" pressures, temperatures and rates of flow.

The blowdown system worked well for the recording of nozzle surface pressures. Any errors introduced by the numerical processing of the results were small compared to the inherent error in the transducer, which was about 1%. Mass flow measurement with the apparatus was not so satisfactory. The particular needs of the present project demand that the random errors in flow measurement be less than 1%. Such accuracy could not be achieved, firstly because of errors introduced in the transducer - logger - interpolation sequence, and secondly because of uncertainties in the stream temperature which dropped considerably as the air in the storage tank expanded.

Several weak points existed in the design of the apparatus. Many of these could have been eliminated by appropriate modifications. It was, however, felt that the nature of the blowdown system was not suited to the precision required in the results and that the indraught system offered better chances of success.

5.2.2 The Indraught Apparatus

The indraught system is shown in Fig. 5.4. A photograph of the test section is shown in Plate III and details are given in Fig. 5.5. The design of the system was largely carried out as a project by a final-year undergraduate working under my supervision and details are given in his report (Miller, 1975). Much of Miller's project was devoted to the design and commissioning of a water ejector pump to perform the task of evacuating the $10m^3$ tank. This took advantage of an existing elevated reservoir which provided 46 m^3 of water at 20m head. The water drained into a sump and could then be pumped back into the reservoir. The ejector pump evacuated the air tank to 0.2 bar in about 45 minutes.

Nozzle throat diameters of 12.5 mm gave typical times of about 3 minutes for the tank pressure to rise from 0.2 bar to 0.53 bar (i.e. the critical pressure ratio). Air was drawn from the atmosphere through an orifice flow

meter (see Fig 5.5). Provision was also made for the air to be first dried with a silica gel drier, but this part of the apparatus was not used for reasons which will be discussed below. The stagnation pressure was virtually constant at the atmospheric value, apart from the small drop across the drier and orifice plate. The orifice pressure drop was measured on a water micromanometer, the total drop between atmosphere and nozzle inlet was measured on a water manometer; and the pressures in the nozzle exhaust region and on the nozzle surfaces were measured on a bank of mercury manometers. All the manometer readings could be simultaneously isolated by a multi-channel switch. The switch consisted of a row of parallel, thick-walled neoprene tubes which could be sealed by a bar depressed by a lever and cam. The experimental procedure was to wait for the manometer readings to settle and then to close both the manometer isolating switch and the main flow valve before recording the readings.

The function of the silica gel drier is to reduce any effects caused by water vapour in the air. Undried atmospheric air in the laboratory had a specific humidity of about 0.007. This proportion of vapour would not significantly alter the thermodynamic properties of the air but it might affect the flow if it condensed to form liquid water or ice droplets. As the Mach number of flow increases, the local temperature decreases. Under equilibrium conditions we would expect condensation to take place as soon as the temperature reached the dewpoint. In practice, the air-vapour mixture continues in a state of metastable equilibrium, the vapour becoming supercooled by $30^{\circ}C$ or more. The formation of water (or ice) droplets takes place at a finite rate and the actual degree of supercooling depends on the physical dimensions of the flowfield. By initially drying the air, the onset of condensation is delayed because the dewpoint is lower and the ulitmate effects are less serious because there is less water present.

It seems probable that condensation, even when using undried air, is not an important factor in the sharp-lipped nozzle experiments which are discussed here. The lowest exhaust pressure reached in experiments on the indraught apparatus was 0.2 bar which corresponds to a local stream temperature of -90°C. Undried atmospheric air would at this stage have a dewpoint of about -15°C (the dewpoint is itself a function of Mach number). The only part of the transonic flowfield which experiences the extreme Mach numbers is the comparatively small region near the lip containing the Prandtl-Meyer expansion. Pope and Goin (1965) quote evidence that a flow where the rate of change of temperature is 100°C per centimetre can sustain as much as 100°C supercooling before condensation can be detected. The rate of cooling near the lip in the nozzle experiments was several times greater than this and lends support to the proposition that no significant condensation takes place within the transonic flowfield.

The experimental procedure with the drier present would be more complicated and less accurate because of the need to record temperature differences. It was therefore decided to omit the drier from all the experiments whose results are reported here. In the event, there was insufficient time to commission that part of the apparatus and to investigate possible condensation effects.

5.3 Description of Tests

It was convenient to divide the experiments into three series. Series A consisted of tests on axially symmetric, conical nozzles covering a range of wall angles. Discharge coefficients and wall surface pressures were determined as functions of pressure ratio. Series B was concerned with two-dimensional nozzles and discharge coefficients and pressure distributions along the axis were obtained. The purpose of the

Series C experiments was to examine the effects of lip geometry and wall surface finish.

5.3.1 Series A - Axially Symmetric Nozzles

The following axially symmetric nozzles were constructed:

No. 1*, 2, 3 } $\beta = 90^\circ$

4* $\beta = 60^\circ$

No. 5 $\beta = 45^\circ$

6*, 7 } $\beta = 30^\circ$

8 $\beta = 15^\circ$

The nozzles conformed to the basic design shown in Fig. 5.1, but only those marked with an asterisk in the above list (nos. 1,4 & 6) were provided with wall pressure tappings. All the nozzles were machined from mild steel and the flange dimensions (see Fig. 5.1) were designed originally for use with the blow-down apparatus. Photographs of nozzle nos. 1,4,5,6 and 8 are shown in Plates IV and V. Three nozzles with $\beta = 90^\circ$ and two with $\beta = 30^\circ$ were made so that the duplicates could be used for the experiments of Series C. Each nozzle had an inlet diameter of 100mm and a nominal throat diameter of 12.5 mm. These figures represent an area contraction ratio of about 16:1 and mean that flow conditions at the inlet plane have a negligible influence on the flow in the throat.

Details of the exact dimensions of the nozzles are given in Appendix B. The throat diameters were determined with a "Shadowmaster" profile projector. The model mounting table on this instrument is fitted with a micrometer and accurate measurements can be made by moving the silhouette across a fixed line on the screen. The radial locations of the centres of the pressure tapping holes on the nozzle walls were obtained by a travelling microscope. The lip profile shapes were obtained by the method described below in Section 5.3.4.

The surface finish on each nozzle wall was measured by a Taylor Hobson "Talysurf". The results are given in Appendix B as "Centre - line Averages" (C.L.A.). This parameter is defined as the average depth below a relatively large plate skating across the surface. It is arguable whether this is the best way of describing a surface profile, but it is certainly the easiest to determine. The Talysurf automatically records the C.L.A. value, although some difficulty was encountered in obtaining consistent readings on the conical surfaces.

Discharge coefficients for this series of axially symmetric nozzles are shown in Fig. 5.6 plotted against pressure ratio. Wall pressures for nozzles 4 and 6 ($\beta = 60^\circ$ and $\beta = 30^\circ$) are shown in Fig. 5.7, also plotted against pressure ratio. It was found that the wall pressure tappings on nozzle no. 1 ($\beta = 90^\circ$) had been placed too far away from the lip to detect any appreciable pressure drop from the stagnation value. No wall pressures for this nozzle have therefore been shown.

5.3.2 Series B - Two-Dimensional Nozzles

The experimental arrangement for testing two-dimensional nozzles is shown in Fig. 5.2 and in Plate VI. It consisted or a rectangular duct with perspex side-walls 100m high and 10mm wide. Air from the drier and flow meter entered the duct through a faired inlet and discharged into the pipe leading to evacuated tank. The nozzle was formed by attaching wedges to the top and bottom surfaces of the duct, resulting in a throat which was nominally 10mm square. The area contraction ratio from duct to throat was thus 10:1 which again means that flow conditions in the approach region will have a negligible effect on the results. One of the duct side-walls was provided with pressure tappings along the axis. All dimensions were obtained by a travelling microscope and are given in Appendix B. Wall surface finish was measured by the Talysurf. Lip profiles were determined by the method of Section 5.3.4.

The following two nozzles were tested:

No. 9 $\beta = 90^\circ$ No. 10 $\beta = 30^\circ$

Discharge coefficients are shown in Fig. 5.8 as a function of pressure ratio. It can be seen that the results for nozzle 9 ($\beta = 90^\circ$) are not satisfactory, probably because of interference between the jet free surfaces and the downstream faces of the wedges (inclined in this case at 30° to the axis). Pressures on the axis for nozzle 10 only are given in Fig. 5.9.

5.3.3 Series C - Lip Profile and Wall Roughness Effects

(i) Finite radius of curvature at the lip. The effects of small radii of curvature on the lips of axially symmetric nozzles were studied for the cases $\beta = 90^\circ$ and $\beta = 30^\circ$. The lips of nozzles nos. 2 and 7 were progressively blunted with fine emery paper. At each step the discharge coefficient was measured as a function of pressure ratio, and the lip profile obtained by the method of Section 5.3.4. This technique resulted in lip profiles which were sufficiently close to circular arcs for the purposes of the investigation. The results for two pressure ratios $r = 0.53$ (critical) and $r = 0.25$ (choking in the case $\beta = 30^\circ$) are shown in Table 5.1. In the case of nozzle no. 7 ($\beta = 30^\circ$) some smaller values of lip radius were obtained by re-machining the sharp-lip and repeating the blunting procedure in a more cautious way.

(ii) Finite Throat Thickness. We are concerned here with the case where the throat has a short cylindrical section. The effects of finite throat thickness were studied for axially symmetric flow at $\beta = 90^\circ$. Nozzle no. 11, shown in Fig. 5.10 was constructed for this purpose. The downstream end of the throat section was progressively machined away and the range $0.04 \leq t_1/d \leq 0.5$ was covered, where t_1 is the throat thickness and d its diameter. At each stage, the

discharge coefficient and the pressure in the throat bore just downstream from the lip were measured as functions of pressure ratio. The results are shown in Figs. 5.11 and 5.12. The process of machining away the throat resulted eventually in the formation of an 20mm diameter counter - bore on the downstream side of the nozzle. It is probable that, at the lower pressure ratios, the jet would expand to this diameter and attach to the counter-bore surface, thus altering the downstream conditions experienced by the flow in the throat. This would explain the discontinuities in the results at the lower pressure ratios and lower values of t_1/d which are especially noticeable in Fig. 5.12

(iii.) Wall Surface Finish The influence of wall roughness on the discharge coefficient for the axially symmetric case $\beta = 90^{\circ}$ was studied. Nozzle no. 3 was first of all polished and then progressively roughened by emery cloth. At each stage, discharge coefficients were obtained and the roughness measured by the Talysurf. No significant differences in C_d were found for C.L.A. values of 0.05 μm, 0.3 μm, and 0.4 μm. A final test with a C.L.A. value of 3.3 μm, obtained by machining the upstream face of the nozzle, produced reductions in C_d of about 0.013 at given pressure ratios. However, the effect may have been partly due to distortion of the nozzle lip. A more carefully planned series of experiments is needed before firm conclusions about the effect of wall roughness can be drawn.

5.3.4. Measurement of Lip Profiles

The shapes of the nozzle lips were obtained by a casting technique. A mould was made by slitting a 10mm length of 5mm bore polythene tube and placing it astride the lip. The mould was sealed and held in position by plasticine. Quick - setting Araldite epoxy resin was then injected into the mould. When the casting had hardened, it was removed from the nozzle lip, laid on a horizontal surface, surrounded by a larger mould and a

second resin (Araldite 219) was poured round it. When this had also hardened, the original lip casting was now embeded in a block about 20mm high and 30mm in diameter. The surface of the block was ground away until an axial cross-section of the original nozzle lip was revealed. The block surface was then polished and photographed using a Zeiss microscope fitted with camera attachment. Some typical lip profiles obtained in this way are shown in Plates VII - IX. A scale to the photographs was provided by photographing a 10 - micron grid at the same magnification.

This technique for determining lip profiles is similar in principle to that used at the National Engineering Laboratory and described by Gallacher (1968). It is less elaborate (little attempt was made to eliminate air bubbles from the quick-set Araldite) and is probably less accurate because the two resins are not dimensionally stable. There was also difficulty in ensuring that the casting was sectioned and polished across the correct plane. Some of these errors were reduced by averaging the results of three or four castings. It was estimated that the lip radii could be determined to an accuracy of $\pm$ 10 μm, which is adequate for our present puposes.

5.4 Evaluation of results and estimation of errors

5.4.1 Discharge coefficient

The discharge coefficient is defined as:

$$C_d = \dot{m}/\dot{m}_t \qquad (5.1)$$

where $\dot{m}$ is the actual mass flow through the test nozzle and $\dot{m}_t$ is the theoretical value assuming one-dimensional flow in the throat. The orifice flowmeter is used to measure $\dot{m}$ and we may write:

$$\dot{m} = (C_d)_m A_m \rho_m u_m = (C_d)_m A_m \frac{p_m u_m}{R T_m} \qquad (5.2)$$

where $(C_d)_m$ is the orifice discharge coefficient; A_m is the orifice throat cross-section area; and p_m, ρ_m, T_m and u_m are the pressure density, temperature and velocity of the jet issuing from the orifice. The effects of compressibility are small but not negligible, and it is necessary to introduce M_m, the Mach number of the jet. The usual isentropic flow relationships can be used to express u_m, T_m and p_m in terms of M_m and the stagnation properties, p_o and T_o, upstream of the orifice:

$$u_m = M_m \sqrt{\gamma R T_m} \tag{5.3}$$

$$T_m = T_o \Big/ \left(1 + \tfrac{\gamma-1}{2} M_m^2\right) \tag{5.4}$$

$$p_m = p_o \Big/ \left(1 + \tfrac{\gamma-1}{2} M_m^2\right)^{\gamma/\gamma-1} \tag{5.5}$$

Since M_m is small, equation 5.5 can be expanded by the binomial theorem to give:

$$p_m \doteq p_o \left(1 - \tfrac{\gamma}{2} M_m^2\right) \tag{5.6}$$

from which we get:

$$M_m^2 = \frac{2}{\gamma} \frac{p_o - p_m}{p_o} = \frac{2\Delta p}{\gamma p^o} \tag{5.7}$$

where Δp is the orifice pressure drop. Substitution into equation 5.2 gives:

$$\dot{m} = (C_d)_m A_m \sqrt{\frac{2 p_o \Delta p}{R T_o}} \Big/ \left(1 + \tfrac{\gamma-1}{2} M_m^2\right)^{\frac{\gamma+1}{2(\gamma-1)}} \tag{5.8}$$

The orifice discharge coefficient is also a function of M_m. We may use the numerical solution to axially symmetric flow through an orifice to determine the following expression which is valid for small M_m^2 :

$$(C_d)_m = (C_d)_o \left(1 + 0.12\, M_m^2\right) \tag{5.9}$$

where $(C_d)_o$ is the discharge coefficient for incompressible flow.
Substitution into equation 5.8 leads to:

$$\dot{m} = (C_d)_o A_m \sqrt{\frac{2 p_o \Delta p}{R T_o}} \frac{(1 + 0.12 M_m^2)}{(1 + \frac{\gamma-1}{2} M_m^2)^{\frac{\gamma+1}{2(\gamma-1)}}} \qquad (5.10)$$

We may set $\gamma = 1.4$ for air in equation 5.10, expand again by the binomial theorem for small M_m^2, and substitute from equation 5.7 to obtain:

$$\dot{m} = (C_d)_o A_m \sqrt{\frac{2 p_o \Delta p}{R T_o}} \left(1 - 0.34 \frac{\Delta p}{p_o}\right) \qquad (5.11)$$

The final term in equation 5.11 is the compressibility correction for the orifice meter. Some of the larger mass flows in these experiments led to orifice pressure drops of 100 mm of water, involving a compressibility correction to $\dot{m}$ of about 0.4%.

The theoretical, one-dimensional mass flow through the test nozzle, $\dot{m}_t$, is given by the following equation:

$$\dot{m}_t = A \rho_L u_L = A \frac{p_L u_L}{R T_L} \qquad (5.12)$$

where A is the throat area; and ρ_1, u_1, p_1 and T_1 are the density, velocity, pressure and temperature at the nozzle lip. By expressions similar to equations 5.3 - 5.5 we may express $\dot{m}_t$ in terms of M_1, the Mach number at the lip, and p_s and T_s, the stagnation conditions upstream from the nozzle, as follows:

$$\dot{m}_t = \frac{A p_s}{\sqrt{R T_s / \gamma}} \frac{M_L}{(1 + \frac{\gamma-1}{2} M_L^2)^{\frac{\gamma+1}{2(\gamma-1)}}} \qquad (5.13)$$

The value of M_1 depends on the nozzle pressure ratio r, as follows:

Subcritical, $r \geq \left(\frac{2}{\gamma+1}\right)^{\gamma/\gamma-1} : M_L^2 = \left(\frac{2}{\gamma-1}\right)\left(r^{\frac{\gamma-1}{\gamma}} - 1\right)$

Supercritical, $r < \left(\frac{2}{\gamma+1}\right)^{\gamma/\gamma-1} : M_L^2 = 1$

Substituting equations 5.11 and 5.13 into equation 5.1, we obtain the following expression for the discharge coefficient of the test nozzle:

$$C_d = (C_d)_o \frac{A_m}{A} \sqrt{\frac{2 p_o \Delta p}{\gamma p_s^2} \left(\frac{T_s}{T_o}\right)} \left(1 - 0.34 \frac{\Delta p}{p_o}\right) \frac{\left(1 + \frac{\gamma-1}{2} M_L^2\right)^{\frac{\gamma+1}{2(\gamma-1)}}}{M_L} \tag{5.14}$$

we may note that $p_s = p_o - \Delta p$ and that $\Delta p / p_o$ is small.
Thus we have:

$$\sqrt{\frac{p_o}{p_s^2}} \doteq \sqrt{\frac{1}{p_o}} \left(1 + \frac{\Delta p}{p_o}\right) \tag{5.15}$$

Substituting equation 5.15 into 5.14, and taking $\gamma = 1.4$, we obtain:

$$C_d = (C_d)_o \frac{A_m}{A} \sqrt{\frac{\Delta p}{0.7 p_o} \left(\frac{T_s}{T_o}\right)} \left(1 + 0.66 \frac{\Delta p}{p_o}\right) \frac{\left(1 + 0.2 M_L^2\right)^3}{M_L} \tag{5.16}$$

The experiments discussed here were conducted without the silica gel drier so that $T_s = T_o = T_a$, the atmospheric temperature. The effect of the drier would be to heat the air so that $T_o > T_a$. Some of this heat is then lost again to the duct wall giving $T_s < T_o$.

Assuming that individual errors obey a Gaussian distribution, the following expression gives the error in C_d:

$$\frac{\delta C_d}{C_d} = \left\{ \left[\frac{\delta (C_d)_o}{(C_d)_o}\right]^2 + \left[\frac{\delta A}{A}\right]^2 + \left[\frac{\delta p_o}{2 p_o}\right]^2 + \left[\frac{\delta (\Delta p)}{2 \Delta p}\right]^2 + \left[\frac{\delta T_o}{2 T_o}\right]^2 + \left[\frac{\delta T_s}{2 T_s}\right]^2 \right\}^{1/2} \tag{5.17}$$

Other errors in equation 5.16 arising from the terms involving M_1 are assumed to be negligibly small. No error in A_m has been given because it is included in the error for $(C_d)_o$. We shall now consider each of the error terms in equation 5.17.

(a) Error in $(C_d)_o$. The metering orifice was calibrated by using a test nozzle of known discharge coefficient. Stratford (1964) has shown that a convergent - divergent nozzle whose wall profile is a circular arc of radius equal to about twice the throat diameter makes a suitable calibration nozzle. Its discharge coefficent can be estimated by considering small perturbations from one-dimensional flow and by calculating the boundary - layer displacement thickness along its wall. The calibration nozzle used here was estimated by Stratford's method to have a C_d of 0.992 $\pm$ 0.002. After allowing for the errors in the other quantities involved in the calibration the metering orifice was estimated to have a coefficient of $(C_d)_o = 0.612 \pm 0.003$

(b) Error in A. The throat diameter could be measured on the profile projector to within $\pm$ 0.01mm. The nozzle throats were not quite circular and the average of four diameters was assumed to be correct to $\pm$ 0.02 mm leading to an error in A (for a nominal 12.5 diameter throat) of $\pm$ 0.3%.

(c) Error in p_o The atmospheric pressure could be measured with a mercury barometer to an accuracy of $\pm$ 0.05%. When the silical gel drier is not present p_o is equal to the atmospheric pressure. The additional term introduced by the pressure drop across the drier was estimated to produce an error of $\pm$ 0.1% in p_o.

(d) Error in Δp. The micromanometer accuracy is estimated to be $\pm$ 0.2%.

(e) Errors in T_s and T_o. The errors are only present when the silica gel drier is used. It would be possible to measure these temperatures to an accuracy better than 1° C - giving an error of $\pm$ 0.3% in the absolute temperature.

When these errors are substituted into equation 5.17, the estimated error in the determination of discharge coefficient is found to be 0.5%. With the drier present the error rises slightly to 0.6%. The dominant error arises from the determination of the throat area and in the calibration of the metering orifice. The situation is improved slightly if we are interested only in comparison between results, for then the orifice calibration error is not important.

5.4.2 Pressure ratios

The pressures on the nozzle surfaces and the exhaust pressures were measured on a bank of mercury manometers whose readings were preserved by the operation of the isolating switch. Absolute pressures were measured directly to an accuracy of 0.5mm Hg by including a barometer in the manometer bank (which had a common mercury reservoir). All the tubes were of the same diameter so as to eliminate any errors due to surface tension. The only other possible source of error was manometer lag due to the fact that the pressures being measured were slowly changing. An analysis of the motion of a mercury column before and after the closing of the isolating valve showed that, for the size of pressure tappings being used (1mm diameter or larger), manometer lag was not a significant factor.

The most serious error arose when metering measurements at the lower pressure ratios. The error in the nozzle stagnation pressure, p_s, is about 0.1%. This means that the accuracy of the manometer reading is the dominant factor. Pressure ratios are therefore accurate to about 0.5% at the lowest

exhaust pressures and accurate to about 0.2% near the critical pressure ratio. Nozzle wall pressures are all greater than the critical pressure because the flow along the wall is subsonic. They are therefore correct to within 0.2%.

TABLE 5.1

Effect of Lip Radius on Discharge Coefficient

	throat diameter (d mm)	lip radius (r_1 μm)	r_1/d	C_d (r = 0.25)	C_d (Critical)
Nozzle No. 7 $\beta = 30^\circ$	12.80	80	0.006	0.947	0.914
	12.97	230	0.018	0.946	0.915
	13.12	240	0.018	0.948	0.917
	13.37	290	0.022	0.954	0.926
	13.55	280	0.021	0.951	0.922
	13.68	10	0.001	0.944	0.910
	14.90	40	0.003	0.945	0.912
Nozzle No. 2 $\beta = 90^\circ$	12.78	10	0.001	0.822	0.738
	12.98	140	0.011	0.844	0.763
	13.13	170	0.013	0.856	0.776
	13.28	300	0.023	0.880	0.803

CHAPTER 6

DISCUSSION

6.1 Introduction

We now turn to the question of how well the numerical results presented in Chapter 4 predict what happens in practice. The theoretical results are based on the following assumptions:

(a) the gas is ideal, with constant specific heats.

(b) the flow discharges into a still atmosphere.

(c) the approach velocity to the nozzle is uniform

(d) the flow is irrotational

(e) the nozzle has a sharp lip

The ideal gas assumption (a) is not an essential restriction to the theory. Any appropriate equation of state could be used to provide gas properties in equations 2.23 and 2.27. However, most of the available experimental data refer to the flow of air which may be regarded as an ideal gas for all practical purposes. It is also easy to satisfy assumption (b), a still atmosphere downstream of the nozzle. Difficulties would only arise if the cross-section area change between the throat and the exhaust duct were so small that significant recirculation velocities were induced by entrainment at the jet surface.

Assumption (c) - uniform approach velocity - is a condition which cannot be totally satisfied in practice. This discussion is mainly concerned with a comparison of theory and experiment for the case of zero approach velocity and the computed results given in Chapter 4 show that, for area contraction ratios greater than 10:1, the flow in

the throat region is virtually independent of the upstream boundary condition. We will therefore assume that experimental results from nozzles having area contraction ratios greater than 10:1 may be compared with theoretical values for zero appraoch velocity.

The assumption (d) of irrotational flow is not valid in practice. There will be boundary layer growth along the nozzle wall, and there will be interaction between the surface of the jet and the atmosphere. These viscous effects will be considered in greater detail in Section 6.3. Shocks in the flow will also introduce rotational effects, but these are well downstream from the lip plane and do not concern us here.

It is not possible to manufacture a nozzle which has a truly sharp lip - assumption (e). An actual lip profile will always have a finite radius of curvature. The throat section may also be cylindrical for a short length. These geometric factors are an important source of discrepancy between theory and experiment and are examined in detail in Section 6.4.

In section 6.2 we shall consider the available experimental data on sharp-lipped nozzle flows and compare them with the predictions of Chapter 4. The most likely causes of discrepancy between theory and practice are viscous effects and departures from the ideal lip geometry which are discussed in Sections 6.3 and 6.4.

6.2 Comparison of Theoretical and Experimental Results

Two classes of data are available for comparison between theory and experiment - discharge coefficients and flowfield pressures. We shall consider results from the experimental programme described in Chapter 5 and from previously published work.

6.2.1 Discharge Coefficients

Measurements of discharge coefficients form the greater part of the available data. Most workers have been concerned either with the performance of metering orifices ($\beta = 90^\circ$) or with aircraft propulsion nozzles ($\beta \leq 40^\circ$). There is a lack of published information in the range $40^\circ < \beta < 90^\circ$. Axially symmetric results for $\beta = 90^\circ$ have been published by Callaghan & Bowden (1949), Grey & Wilsted (1949), Perry (1949), Grace & Lapple (1951), Liepmann (1961) and Brown (1968). These results are plotted against pressure ratio in Fig. 6.1 where the theoretical curve and experimental values for nozzle no.1 in the present study are also shown. Fig. 6.2 shows experimental points for nozzles no. 4 (60°) and no.5 (45°) together with the corresponding theoretical curves. Discharge coefficients for axially symmetric nozzles in the range $0 < \beta \leq 40^\circ$ have been published by Grey & Wilsted (1949), Brown (1968), Hebbar el al (1970) and Thornock & Brown (1972). These are shown in Figs. 6.3 ($\beta = 40^\circ$), 6.4 ($\beta = 30^\circ$) and 6.5 ($\beta = 20^\circ$) together with the appropriate theoretical curves. The results obtained here for nozzles nos. 6 and 7 ($\beta = 30^\circ$) and nozzle no. 8 ($\beta = 15^\circ$) are also shown in Figs. 6.4 and 6.5.

Two broad observations can be made about the information given in Figs. 6.1 - 6.5. Firstly, the general shape of the experimental results, plotted as a function of pressure ratio, agrees with the theoretical curves. Secondly, there is a tendency for the observed values to be larger than the theoretical predictions, particularly for those results obtained in the present study. In no other workers' results have error estimates been given.

In the present study, we can say that the discrepancy between theory and experiment is considerably larger than the estimated experimental error - several percent in some cases. These differences are largely

due to deviations from the ideal sharp-lip geometry, a matter discussed in section 6.4 below.

Only two sets of experimental results for flow through two-dimensional nozzles appear to have been published. Benson & Pool (1965 b) examined $\beta = 90^\circ$, and Brown (1968) $\beta = 20^\circ$ and $\beta = 40^\circ$. Discharge coefficients from these sources are shown in Fig. 6.6, where the theoretical curves and the experimental data obtained in the present study from nozzle no. 10 ($\beta = 30^\circ$) are also shown. The observed results for nozzle no. 10 are lower than predicted, perhaps on account of the presence of side-wall boundary layers. Brown's results are too high, probably because his flow measurement technique was inadequate (he quotes $C_d > 1.0$ in the case $\beta = 20^\circ$). The values given by Benson & Pool are also high at low pressure ratios, and the authors themselves express doubts about their flow metering devices.

To conclude this discussion of discharge coefficients, it is worth mentioning the data given by Liepmann (1961) who investigated the effect of γ on choked flow through an orifice ($\beta = 90^\circ$, axially symmetric). His results are shown in Fig. 6.10, together with the theoretical values for two-dimensional and axially symmetric flow. A virtually linear relationship between C_d and γ appears to be confirmed.

6.2.2 Flowfield Pressures

The measurement of static pressures in the flowfield provides more data for a comparison between theory and experiment. Little information of this nature exists. The experiments described in Chapter 5 yield wall pressures for axially symmetric flow at $\beta = 30^\circ$ and $\beta = 60^\circ$. They also yield pressures along the axis for two-dimensional flow at $\beta = 30^\circ$. The ratio of local static to stagnation pressure is related to the local

velocity or Mach number through equation 2.5b. The experimental results first shown in Figs. 5.8 and 5.10 are compared with theory at selected jet Mach numbers in Fig. 6.7 (axially symmetric wall velocities) and Fig. 6.8 (two-dimensional axis velocities).

Brown (1968) studied axially symmetric flow through "half-nozzles" which were sectioned across an axial plane and attached to a flat plate provided with pressure tappings. Stanton (1926) and Cunningham (1951) made pressure traverses with fine probes along the axes of circular orifices. The coordinate, x_o, at which the sonic line crosses the axis, is a convenient parameter to examine. The values of x_o/y_1 (where y_1 is the lip radius) from these three sources are shown as a function of nozzle pressure ratio in Fig. 6.9, where the theoretical curve is also given.

We may conclude from this evidence that theoretical and observed flowfield pressures are in satisfactory agreement. The observed axially symmetric wall velocities shown in Fig. 6.7 are slightly lower than those predicted by theory, particularly in the case of choked flow. A clearer picture would have been given if the pressure tapping points could have been placed closer to the lip on these nozzles. The two-dimensional jet velocities (Fig. 6.8) are slightly lower than predicted at the critical pressure ratio. This is probably due to viscous interaction between the jet and the (supposedly stationary) surrounding atmosphere.

6.3 Viscous Effects

The purpose of the discussion in this section is to assess the degree to which viscosity affects the theoretical predictions of nozzle performance presented in Chapter 4. Sharp-lipped nozzle flows experience the following viscous effects:

(a) boundary layer development in the approach duct for cases of non-zero approach velocity

(b) interactions between the jet and its surroundings in the downstream exhaust chamber

(c) boundary layer growth in the flow along the nozzle wall towards the lip.

The flow in the approach duct does not concern us here, since we are only considering cases of zero approach velocity. It was explained in Section 6.1 that, for practical purposes, nozzle flows experiencing an area contraction ratio of 10:1 or more may be assumed to fall into this category.

Interaction between the jet and its surrounding atmosphere will have two effects. Firstly, the shear layer at the interface will thicken and the consequent change to the boundary condition will influence the whole jet. The evidence on the behaviour of high-speed jets (e.g. Ladenburg et al, 1948) suggests, however, that the "blurring" of the jet boundary is negligible for the first two or three throat diameters downstream from the exit plane. The flow through the throat is therefore unlikely to be significantly affected. The second consequence of a shear layer along the jet boundary is that the entrainment of surrounding gas will induce recirculating flow in the exhaust chamber. An important factor here is the ratio of the downstream duct cross-section area to the throat area. In the case of the axially symmetric experiments described in Chapter 5 this ratio is about 64:1 (see Fig. 5.5) and it is unlikely that induced velocities will be significant. The two-dimensional duct (Fig. 5.2) has a downstream area ratio of only 10:1 which might be low enough to cause significant pressure variations within the recirculation zone.

In order to discuss the boundary layer growth along the nozzle wall, it is worth obtaining an estimate of its displacement thickness, in the

case of the nozzles described in Chapter 5. The boundary layer is assumed to be laminar and the following formula (Stratford, 1964) will be used:

$$\delta^*/X = 1.32 \ (1 + 0.28 \ M^2) \ Re_X^{-1/2} \qquad (6.1)$$

$$X = M^{-5} \int M^5 \ ds$$

where δ^* is the displacement thickness; M is the wall Mach number; s is the physical distance along the nozzle wall; and Re_X is the wall Reynolds number based on X. The variation of M can be obtained from the computed wall velocity distributions (Figs. 4.11 and 4.12). Even though the validity of equation 6.1 should be questioned in the region of high acceleration just upstream from the lip, we can still use it to obtain order - of - magnitude estimates of the displacement thickness. When the calculation is performed for critical or supercritical flow through an orifice ($\beta = 90^\circ$) with a throat diameter of 12.5mm, we find that δ^* is fairly constant at about 6 μm as the boundary layer approaches the lip and then drops rapidly to 1 μm at the lip itself. We would expect larger values of δ^* for $\beta < 90^\circ$ because the velocity gradients become less steep.

A boundary layer of finite thickness at the lip will have several effects. It will tend to block the throat and so reduce C_d. However, the rapid reduction in δ^* just before the lip will "round off" the effective nozzle wall and thus increase C_d. There is also the possibility of exhaust pressure changes influencing the flow inside the nozzle through the subsonic part of the boundary layer, even if the nozzle is operating below the choking pressure ratio. Further investigation is needed to determine the relative importance of these effects.

The overall influence of viscosity on a nozzle flow can be discussed in terms of the lip Reynolds number, Re_l, defined as:

$$Re_l = \frac{d V_l \rho_l}{\mu_l}$$

where d is the throat diameter; V_l is the lip velocity (actual, not dimensionless); and ρ_l and μ_l are the density and viscosity at the lip. In critical and supercritical flow, the lip conditions are the sonic conditions. It is not easy with most experimental arrangements to achieve a wide variation in Re_l, and the task was not attempted in the present work. Several studies of the influence of Re_l on C_d for orifice flows have been published. Grace and Lapple (1951) considered incompressible flow, and their results can be summarised in the following equation:

$$C_d = (C_d)_o \left[1 + 80 / Re_l \pm .... \right] \qquad (6.2)$$

where $(C_d)_o$ is the inviscid value of C_d. A typical working value for incompressible application is $Re_l \sim 10^4$, in which case discrepencies from theory of about 1% are to be expected..

The effect of Reynolds number on C_d for critical and supercritical orifice flow was investigated by Liepmann (1961), Deckker & Chang (1966) and Brian & Reid (1973). These authors all found that C_d at a given pressure ratio was independent of Re_l for $Re_l > 10^4$. Callaghan & Bowden (1949) also studied critical and supercritical flow, and found a two percent drop in C_d as Re_l increased from 1×10^5 to 5×10^5. However, the results of Callaghan & Bowden are not as useful in this respect as they seem, because they used orifices of different diameters to achieve their range of Reynolds number. As we shall see in Section 6.4, the change in C_d might well have been due to small differences in lip geometry.

The results quoted in the previous paragraph suggest that C_d is independent of Reynolds number when that parameter is greater than 10^4. The experiments described in Chapter 5 were all carried out with $Re_1 = 2.10^5$. It does not, however, necessarily mean that the limiting value of C_d is the inviscid value. The wall boundary layer displacement thickness will eventually become comparable in magnitude with the height of the irregularities in surface finish. These will then become the dominant influence on the boundary layer thickness at the lip. In the experiments on wall roughness effects described in Chapter 5, the flow through an orifice was studied at C.L.A. roughness values of 0.05, 0.04 and 3.3 μm. Only in the last case, when the C.L.A. value was comparable with the estimated displacement thickness, was an effect on discharge coefficient detected. This single experiment is hardly conclusive, and the effect of surface finish on nozzle flows would benefit from further study.

6.4 Lip Geometry

It is impossible in practice to manufacture a nozzle with a perfectly sharp lip. At best there will be a small radius of curvature to the profile, and it may well be distorted and burred. Any attempt to clear burrs afterwards will simply result in a greater radius of curvature. The easiest way to ensure a clean nozzle or orifice lip is to provide a short, parallel throat section. This is reflected in the various standards for metering orifices (e.g. BSS 1042 pt.1 : 1964) which allow an orifice with a sharp leading edge to have a cylindrical throat whose length may be up to 0.05 times its diameter. There are therefore two ways in which the geometry of a real nozzle lip can differ from the ideal sharp lip. It can have a finite radius of curvature and it can have a finite thickness. Even these two categories are idealisations, for the lip profile can take any shape.

We will assume, however, that a nozzle lip will have a "round" component and a "thick" component and that, for small departures from perfect sharpness, the effects of the two components are separable. The next two subsections will examine each in turn.

The presence of a rounded lip or parallel throat modifies the boundary conditions in the throat region. Small changes in the structure of the flowfield take place, so that zones of supersonic flow may form even at "subcritical" pressure ratios. In the discussions which follow, the "critical" pressure ratio will still refer to the ideal sharp-lipped value (i.e. $r_c = 0.528$ for air). For similar reasons the nozzle may become choked (i.e. the transonic flowfield may become independent of pressure ratio) at pressure ratios higher than the theoretical sharp-lipped value. The use of the term "choked" will, in the following discussion, refer to the actual, rather than the theoretical state of the flow.

6.4.1 Finite Lip Radius of Curvature

This feature is described in terms of the "radius ratio", r_1/d where r_1 is the lip profile radius and d the throat diameter. Careful manufacture can achieve values of r_1 of the order 2 μm (Crockett & Upp, 1973). The nozzles made for the present work were crude by comparison, with values of r_1 in the range 20 μm to 40 μm.

The effect of radius ratio on C_d for incompressible, axially symmetric orifice flow was studied experimentally by Crockett & Upp (1973). Their results, for the range $10^{-4} \ll r_1/d \ll 10^{-3}$ can be summarised by the following equation:

$$C_d = (C_d)_{r_1/d \to 0}\left[1 + 10\,(r_1/d) \pm \cdots\right] \qquad (6.3)$$

Kastner et al (1964) studied experimentally the effect of radius ratio on the value of C_d for a choked orifice. They were concerned with fairly large values (the smallest was $r_1/d = 0.05$) and it is not possible

to draw conclusions from their results in the limit $r_1/d \to 0$. The only results for compressible flow at small values of r_1/d appear to be those obtained in the present study. It is shown theoretically in Appendix C that the following equation gives the initial rate of change of C_d with r_1/d for supercritical flow:

$$\frac{dC_d}{d(r_i/d)} = \lambda (k+1)(1 - \cos\beta)(C_d)_{r_i/d \to 0} \qquad (6.4)$$

where k = 0 for two-dimensional flow and k = 1 for axially symmetric flow. The analysis leading to equation 6.4 is based on the sharp-lipped solution and considers a streamline close the nozzle wall. This streamline is then assumed to define the wall of a new nozzle and expressions for its discharge coefficient and throat radius of curvature are derived.

An experimental study of the effects or artificially blunting the lips of two axially symmetric nozzles with wall angles $\beta = 90^\circ$ and $\beta = 30^\circ$ was described in Chapter 5. The lip profiles turned out to be approximately circular, although there was no way of controlling their shape. Photographs of two stages in the blunting sequence for the 90° nozzle are shown in Plates VII and VIII. Plate VII shows the original "sharp" lip; plate VIII shows the profile after it had been blunted by fine emery cloth. The results of the study were given in Table 5.1 and are shown again in Fig. 6.11. Also shown are straight lines based on equation 6.4:

$$\beta = 90^\circ : \quad C_d = (C_d)_{r_i/d \to 0}\left[1 + 4(r_i/d)\right] \qquad (6.5a)$$

$$\beta = 30^\circ : \quad C_d = (C_d)_{r_i/d \to 0}\left[1 + 0.54(r_i/d)\right] \qquad (6.5b)$$

The results in Fig 6.11 suggest that equation 6.4 can be used with a certain degree of confidence to predict lip radius effects.

6.4.2 Finite Throat Thickness

We are primarily concerned here with the influence of a small length of cylindrical throat on the theoretical sharp-lipped flow. The relevant parameter is the "thickness ratio", t_1/d, where t_1 is the throat length. Incompressible flow through thick orifices was studied by Grace & Lapple (1951). They found that discharge coefficients were unpredictable and unreproducible for cases where $t_1/d > 0.1$. Even for smaller values of thickness ratio the most definite conclusion to be drawn from their results is that the incompressible C_d increases slightly with increasing t_1/d.

Discharge coefficients for compressible flow through thick orifices have been published by Kastner et al (1964), Deckker & Chang (1966), Rhodes et al (1969) and Brain & Reid (1973). Only Brain & Reid looked at values less then $t_1/d = 0.5$. Their results, together with results obtained in the present study (originally given in Fig. 5.11), are shown in Fig. 6.12. We may tentatively write the following equation for the effect of small thickness ratio on the discharge coefficient of an orifice:

$$C_d = (C_d)_{t_1/d \to 0} \left[1 + A\,(t_1/d) \pm \ldots \right] \qquad (6.6)$$

where the parameter A takes the value 0.08 at the critical pressure ratio ($r = 0.53$) and $A = 0.05$ at the pressure ratio $r = 0.3$. Further data is needed before a more definite conclusion can be drawn. There is no information available at all for nozzle angles other than $\beta = 90^\circ$.

Orifices of relatively large thickness ratio are used for flow metering and control because their discharge coefficients are constant over a range of pressure ratios extending up to and sometimes above the nominal value for critical flow. There is a lower limit of thickness ratio for which this property is exhibited. The experimental results given in Fig. 5.11 show that

the limit is round about $t_1/d = 0.3$. Other workers (e.g. Deckker & Chang, 1966: Brain & Reid, 1973) have found the limit to be $t_1/d = 0.5$.

The structure of the flowfield in the throat of an orifice with large thickness ratios (i.e. $t_1/d > 0.5$) is interesting. What appears to happen is that the flow separates at the lip in the usual way and re-attaches further down the bore, enclosing a separation zone (see sketch below). The pressure in the zone is independent of the downstream conditions,

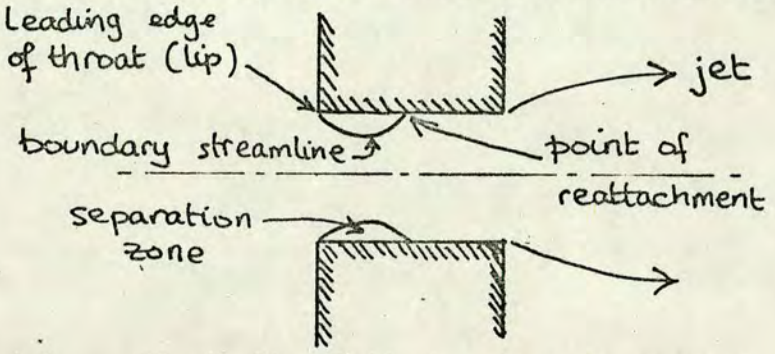

and the experimental results in Fig. 5.12 show it to be 0.23 times the stagnation pressure. The pressure difference across the orifice eventually becomes too small to sustain the flow pattern. This occurred at a pressure ratio of about 0.5 in the case of the results in Fig. 5.12. Below this value we therefore have at the upstream end of the throat a local "sharp-lipped" nozzle flowfield corresponding to a pressure ratio of 0.23. This in turn corresponds to a free streamline Mach number of about 1.6. The theoretical shape of the free streamline for $M_j = 1.6$ is shown in Fig. 4.16b. It can be seen that the jet radius expands to a value equal to the lip radius at a distance of about 0.3 lip diameters downstream. This suggests that a separation zone with a dimensionless pressure of 0.23 cannot exist if $t_1/d < 0.3$, a view supported by the results in Figs. 5.11 and 5.12

6.5 Final Comments

The effects of viscosity and lip geometry on discharge coefficient have been examined in Sections 6.3 and 6.4 because they are the probable explanations for differences between theory and experiment. Critical and

supercritical flows appear to be independent of lip Reynolds number, but there may be small limiting effects due to such factors as wall surface roughness. Lip geometry has a more important influence. We can use equation 6.4 to "correct" for lip radius effects, the experimental discharge coefficients obtained in the present investigation. Values of lip radii are given in Appendix B. Corrected values of C_d are marked on Figs. 6.1, 6.2, 6.4 and 6.5 at two representative pressure ratios. It can be seen in Fig. 6.1 for nozzle no. 1 ($\beta = 90^\circ$) that the correction brings theoretical and observed discharge coefficients within the estimated experimental error band. The same is true for choked, or near - choked flow for nozzle no.5 ($\beta = 45^\circ$, Fig. 6.2), nozzle no. 7 ($\beta = 30^\circ$, Fig. 6.4), and nozzle no. 8 ($\beta = 15^\circ$, Fig. 6.5). However, the lip radius correction does not account for the whole difference between theory and experiment at the critical pressure ratio in these latter cases. Nor is the correction sufficient, even for choked flow, for nozzle no. 4 ($\beta = 60^\circ$, Fig. 6.2) or nozzle no. 6 ($\beta = 30^\circ$, Fig. 6.4).

It is interesting that the lip profiles of these last two nozzles show a signigicant length of parallel throat in addition to a radius of curvature - see Plate IX and details in Appendix B. This may explain the larger differences between predicted and observed discharge coefficients in these two cases. If so, it suggests either that the parallel throat has a more significant effect for $\beta < 90^\circ$, or that lip radius and lip thickness effects interact and cannot be studied separately in the simple manner attempted here.

The study of lip geometry presented here is by no means complete. There is no data for subcritical pressure ratios, nor for incompressible flow apart from the lip radius results of Crockett & Upp (1973) for $\beta = 90^\circ$

given in equation 6.3. At supercritical pressure ratios we only have lip thickness data for the case $\beta = 90^{\circ}$. Performance parameters other than discharge coefficients have not been considered. Further investigation in these areas would improve our understanding of the relationship between theoretical sharp-lipped flows and their real counterparts.

CHAPTER 7

CONCLUSIONS

1. A theoretical and experimental investigation has been carried out into compressible flow of ideal gas through sharp-lipped convergent nozzles and orifices.

2. Equations have been derived for irrotational flow through two-dimensional and axially symmetric nozzles at subcritical and supercritical pressure ratios. The subsonic region of flow is transformed into the hodograph coordinate system. The supersonic region (if present) is solved in the physical plane. The necessary conditions at the sonic line to ensure a continuous solution across it are determined iteratively.

3. Numerical methods have been developed for the solution of the equations. A finite-difference method is used in the subsonic region and the finite - difference equations are solved by non-linear over - relaxation. Regions of supersonic flow are handled by the method of characteristics. Attention has been paid to computational efficiency in the overall solution of the problem. Truncation errors in the results have been estimated, and techniques have been devised for reducing their magnitude.

4. A computer program using the numerical methods described has been written to solve two-dimensional and axially symmetric sharp—lipped nozzle flows over the complete range of pressure ratios.

5. A theoretical survey of sharp-lipped nozzle performance has been presented. Wide ranges of nozzle angle and pressure ratio have been covered for both two-dimensional and axially symmetric flow. Representative

nozzle flowfields (streamlines and lines of constant velocity) are given, together with discharge coefficients and nozzle surface velocity distributions.

6. An experimental study of nozzle performance has been made. Axially symmetric nozzles covering a range of wall angles and one two-dimensional nozzle have been tested at a throat Reynolds number (based on throat diameter and sonic flow conditions) of 2×10^5. Discharge coefficients and nozzle surface pressure distributions are given.

7. Theoretical and experimental results have been compared. Surface pressure distributions agree well, but experimental discharge coefficients tend to be higher than predicted.

8. Possible reasons for the differences between predicted and observed discharge coefficients at a critical and supercritical pressure ratios have been discussed. It is argued that, for throat Reynolds numbers greater than 10^4, viscosity does not have an important effect and that small departures from the ideal sharp-lipped geometry are mainly responsible. The effects of two factors, a small radius of curvature at the lip and a short cylindrical throat section, have been studied experimentally. The lip radius is the more important factor. An equation for its effects is proposed which allows theoretical discharge coefficients to be corrected. Further investigation of lip geometry effects is required.

APPENDIX A

ANALYSIS NEAR THE INTERSECTION OF THE SONIC LINE AND THE AXIS

A1 Approximate equation for transonic flow

The numerical method described in this thesis rests upon the solution of finite-difference equations in the hodograph plane. Such a solution does not yield very useful information about the physical flowfield near the singularity at the point where the sonic line meets the axis. This region can be analysed separately in the physical plane by considering small perturbations about the condition $V = 1, \theta = 0$. Full details of the analysis are given by Shapiro (1953) and Guderley (1961) and only an outline will be given here.

From the conditions for continuity (equation 2.8) and irrotational flow (equation 2.9), together with equation 2.5c for the gas density, the following equation may be derived (for details, see Shapiro, 1953):

$$\left(1 - \frac{u^2}{c^2}\right)\frac{\partial u}{\partial x} + \left(1 - \frac{v^2}{c^2}\right)\frac{\partial v}{\partial y} - 2\frac{uv}{c^2}\frac{\partial u}{\partial y} + \frac{kv}{y} = 0 \qquad \text{(A1)}$$

where u and v are the components of the dimensionless velocity V; and the dimensionless speed of sound, c, is given by equation 2.4b We now assume that $u = 1 + u'$ and $v = v'$, where u' and v' are small. Substitution into equations A1 and 2.4b and elimination of second-order terms leads to:

$$(\gamma+1)u'\frac{\partial u'}{\partial x} - \frac{\partial v'}{\partial y} + 2v'\frac{\partial u'}{\partial y} - k\frac{v'}{y} = 0 \qquad \text{(A2)}$$

The product $v'\frac{\partial u'}{\partial y}$ is also negligible if we restrict attention to flow near the axis of symmetry, and we finally obtain:

$$(\gamma+1)u'\frac{\partial u'}{\partial x} - \frac{\partial v'}{\partial y} - k\frac{v'}{y} = 0 \qquad \text{(A3)}$$

We now define a parameter ϕ' as follows:

$$\phi' = \phi - x \tag{A4}$$

where ϕ is the velocity potential, defined by equations 2.11 by which we may write:

$$u' = \frac{\partial \phi'}{\partial x}$$
$$v' = \frac{\partial \phi'}{\partial y} \tag{A5}$$

substitution of equations A5 into A3 yields:

$$(\gamma+1)\,\phi'_x \phi'_{xx} - \phi'_{yy} - k\,\frac{\phi'_y}{y} = 0 \tag{A6}$$

Equation A6 describes small perturbations about the state $V = 1$, $\Theta = 0$ and can be applied to the zone surrounding the intersection of sonic line and axis. Figure A1a shows the relevant portion of the hodograph plane, and Figs A1b and A1c show the corresponding regions of the physical plane for critical and supercritical flow. There are two ways in which a local solution of equation A6 might help the main solution. Firstly, the stream function value, ψ_q, can be fixed at the point Q (see Fig. A1a) in the hodograph finite-difference mesh – this is the point most likely to experience large truncation errors due to the singularity. Secondly, the local solution can be used to estimate coordinates in the physical flowfield in a region where the finite-difference results are inadequate. In particular, the location of point O (Fig. A1) can be determined relative to point P. Different methods of solution to equation A6 are used for critical and supercritical problems, and these will now be considered in turn.

A2 Transonic analysis - critical flow

We consider solutions to equation A6 of the form $\phi' = f(x).g(y)$ and the equation may then be written:

$$(\gamma+1)\,\frac{df}{dx}\,\frac{d^2f}{dx^2}\Big/ f = \left(\frac{d^2g}{dy^2} + \frac{k}{y}\,\frac{dg}{dy}\right)\Big/ g^2 = K \tag{A7}$$

where K is an arbitrary constant. Setting K = 1 leads to the following pair of equations:

$$-(\gamma+1)\frac{df}{dx}\cdot\frac{d^2f}{dx^2} + f = 0 \qquad \text{(A8a)}$$

$$\frac{d^2g}{dy^2} + \frac{k}{y}\frac{dg}{dy} - g^2 = 0 \qquad \text{(A8b)}$$

The relevant solution to equation A8a is $f = \dfrac{x^3}{18(\gamma+1)}$ which gives $u' = v' = 0$ along the line $x = 0$. We then have:

$$\phi' = \frac{x^3}{18(\gamma+1)}\,g \qquad \text{(A9a)}$$

$$u' = \frac{x^2}{6(\gamma+1)}\,g \qquad \text{(A9b)}$$

$$v' = \frac{x^3}{18(\gamma+1)}\frac{dg}{dy} \qquad \text{(A9c)}$$

The boundary conditions to equation A8b are $g = 0$ at $y = 1$ (defining the free streamline) and $\frac{dg}{dy} = 0$ at $y = 0$ (for symmetry). Equation A8b is then easily solved numerically for the two cases $k = 0$ and $k = 1$. The solutions are plotted in Fig. A2.

Estimation of γ_q

We have, in terms of the approximate theory, $\gamma_q/\gamma_p = (y_q/y_p)^{k+1} = y_q^{k+1}$ where the subscripts refer to the points P and Q in Figs A1a and A1b. For convenience we may assume that $y_p = 1$. The hodograph coordinates of Q are:

$$\left.\begin{aligned} V_q &= 1 + u'_q = 1 - \Delta V \\ \theta_q &= \tan^{-1}\left(v'/(1+u')\right) \doteq v' = -\Delta\theta \end{aligned}\right\} \qquad \text{(A10)}$$

Where ΔV and $\Delta\theta$ are the intervals in the finite-difference mesh. Equations A10 may be substituted into euqations A9 and x eliminated to give:

$$\left[g\left(\frac{dg}{dy}\right)^{-2/3}\right]_q = -\Delta V\left[\frac{2(\gamma+1)}{3(\Delta\theta)^2}\right]^{1/3} \qquad \text{(A11)}$$

from which y_q may be determined.

It was found in practice that no particular advantage derived from estimating the value of ψ_q by the methods described in this Appendix, rather than computing it as part of the finite-difference solution. The reason is probably that the errors inherent in the approximate solution are of the same order of magnitude as the truncation errors in the finite-difference method.

Estimation of physical coordinates

A streamline in the jet is given by:

$$\frac{dy}{dx} = \tan\theta = v'/1+u' \doteq v'$$

Thus, from equation A9c, we get:

$$\frac{dy}{dx} = \frac{x^3}{18(\gamma+1)} \frac{dg}{dy} \qquad \text{(A12)}$$

leading to:

$$y = y_o + \frac{x^4}{74(\gamma+1)} \frac{dg}{dy} \qquad \text{(A13)}$$

where y_o is the value of y at x = 0. The streamlines are thus 4th order polynomials in this region. The values of x and y at point P in Fig A1b and the value of y at point O_b may be determined from the finite-difference solution. Equation A13 allows the value of x at O_b to be estimated.

A3 Transonic analysis - supercritical flow

The hodograph and physical flowfields in the neighbourhood of the intersection of sonic line and axis are shown in Figs A1a and A1c. The physical flowfield is very similar to the flow in a De Laval nozzle whose upper boundary is the streamline through P. We assume a solution to equation A6 of the following form, symmetrical about the axis:

$$\phi' = f_0(x) + y^2 f_2(x) + y^4 f_4(x) \tag{A14}$$

where the origin is placed at point O.

In addition we assume that the velocity on the axis is a linear function of x:

$$(u')_{y=0} = \left(\frac{\partial \phi'}{\partial x}\right)_{y=0} = f_0'(x) = ax \tag{A15}$$

where a is constant. This latter assumption is shown by Guderley (1961) to be generally true for De Laval nozzles near V = 1. Equations A14 and A15 are substituted into equation A6; like powers of y are equated; and the following results are given:

$$\phi' = \frac{a}{2}x^2 + \frac{\gamma+1}{2(k+1)}a^2 x y^2 + \frac{(\gamma+1)^2 a^3}{8(3+5k)}y^4 \tag{A16a}$$

$$u' = ax + \frac{\gamma+1}{2(k+1)}a^2 y^2 \tag{A16b}$$

$$v' = \frac{\gamma+1}{k+1}a^2 x y + \frac{(\gamma+1)^2 a^3}{2(3+5k)}y^3 \tag{A16c}$$

An expression for the constant a can be found by considering conditions at the point P in Fig. A1 where we have u' = 0 and $v' = -\Delta\theta$ Equations A16b and A16c then give:

$$0 = x_p + \frac{\gamma+1}{2(k+1)}a y_p^2 \tag{A17a}$$

$$-\Delta\theta = \frac{\gamma+1}{k+1}a^2 x_p y_p + \frac{(\gamma+1)^2}{2(3+5k)}a^3 y_p^3 \tag{A17b}$$

Elimination of x_p between equation A17 leads to

$$a = \frac{1}{y_p} \left\{ \frac{\Delta\theta}{\frac{(\gamma+1)^2}{2}} \left[\frac{1}{(k+1)^2} - \frac{1}{(3+5k)} \right] \right\}^{1/3} \qquad \text{(A18)}$$

Since the coordinates x_p and y_p relative to the nozzle lip may be computed from the hodograph finite-difference solution, the coordinate x_o may be estimated by equation A17 and A18.

APPENDIX B

DIMENSIONS OF NOZZLES TESTED

Series A - Axially Symmetric Nozzles

No. 1 — Wall angle: 90° Throat diameter: 12.71 ± 0.01mm
Lip radius : 30 ± 10 μm Surface finish (C.L.A.) : 0.2μm
Pressure tappings on wall radial distances of centres from axis:
7.6; 9.1; 11.0; 13.3 (± 0.1 mm)

No. 2 — Wall angle : 90° Throat diameter : 12.78 mm
Lip radius : 10 ± 10 μm Surface finish (C.L.A.) : 0.4 μm

No. 3 — Wall angle : 90° Throat diameter : 12.71 ± 0.01 mm
Lip radius : 40° ± 10 μm Surface finish (C.L.A.) : 0.3 μm

No. 4 — Wall angle : $60^{\circ} \pm 0.2^{\circ}$ Throat diameter : 12.72 ± 0.01 mm
Lip radius : 50 ± 10 μm (followed by cylindrical throat of length 110 ± 10 μm)
Surface finish (C.L.A.): 0.8 μm
Pressure tappings on wall, radial distances of centres from axis:
7.7; 7.8; 9.3; 10.7; 12.0; 13.3; (± 0.2 mm)

No. 5 — Wall angle : $45^{\circ} \pm 0.2^{\circ}$ Throat diameter : 13.77 ± 0.02 mm
Lip radius : 50 ± 10 μm Surface finish (C.L.A.): 0.6 μm

No. 6 — Wall angle : $30^{\circ} \pm 0.2^{\circ}$ Throat diameter : 13.25 ± 0.01 mm
Lip radius : 30 ± 10 μm (Followed by cylindircal throat of length 60 ± 10 μm)
Surface finish (C.L.A.): 0.5 μm
Pressure tappings on wall, radial distances of centres from axis:
7.4; 7.5; 8.5; 8.7; 9.3; 10.0; 11.0 (± 0.2mm)

No. 7 — Wall angle : $30^{\circ} \pm 0.2^{\circ}$ Throat diameter : 12.80 ± 0.02 mm
Lip radius : 80 ± 10 μm Surface finish (C.L.A.): 0.6 μm

No. 8 Wall angle : $15^{\circ} \pm 0.02^{\circ}$ Throat diameter : 12.79 ± 0.01 mm
Lip radius : $30 \pm 10\ \mu m$ Surface finish (C.L.A.): $0.2\ \mu m$

Series B - Two-Dimensional Nozzles

No. 9 Wall angle : 90° Throat width : 10.00 ± 0.05mm
Throat height : 12.96 ± 0.02mm Lip radius: $10 \pm 10\ \mu m$
Surface finish (C.L.A.): $0.2\ \mu m$

No. 10 Wall angle : $30^{\circ} \pm 0.5^{\circ}$ Throat width : 10.00 ± 0.05mm
Throat height : 13.20 ± 0.02mm Lip radius : $10 \pm 10\ \mu m$
Surface finish (C.L.A.): $0.2\ \mu m$
Pressure tappings on axis, distance downstream from lip plane:
-10.0; -5.2; -2.5; 0.2; ($\pm$ 0.1mm)
2.6; 5.1; 10.1; 10.3; ($\pm$ 0.1mm)

Series C - Axially Symmetric Cylindrical - Throat Nozzle

No. 11 Wall angle : 90° Throat diamter: 12.81 ± 0.01 mm
Lip radius : $30 \pm 10\ \mu m$ Surface finish (C.L.A.); $0.2\ \mu m$
Bore pressure tapping 0.5 ± 0.1mm downstream from lip plane.

APPENDIX C

An estimate of the effects of finite curvature at the lip

The method of analysis described in this thesis refers to a nozzle with a sharp lip. This is an ideal which cannot be achieved in practice. Any manufactured nozzle must have a small but finite radius of curvature at the lip. We may estimate the effect of such a radius on choked flow by considering the family of nozzles whose boundaries are defined by the streamlines in a sharp-lipped solution. The family will have a radius of curvature at the throat which tends to zero as the lip is approached. Although the profile in the throat region will not be circular, we shall assume here that it is, and that its radius is equal to the radius of curvature of the streamline as it crosses the sonic line.

The geometry under consideration is shown in Fig. C1, and we shall first examine the value of the discharge coefficient, C_d given by the following expression:

$$C_d = \left(y_{t'}/y_t\right)^{k+1} = \frac{(k+1)\psi}{\rho\left[y_s - R(1-\cos\theta_s)\right]^{k+1}} \qquad (C1)$$

where ψ is the stream function along the streamline; y_t is the throat coordinate; $y_{t'}$ is the throat coordinate which would exist if all the streamlines were parallel; R, y_s and θ_s are the radius of curvature, the coordinate and the inclination of the streamline as it crosses the sonic line. Our interest lies in the variation of C_d with the ratio R/Y_t since it is the actual throat dimension which characterises a given nozzle. Differentiation of equation C1 leads to:

$$\frac{dC_d}{d\left(R/y_t\right)} = \frac{dC_d}{d\theta_s}\left[\frac{1}{y_t}\frac{dR}{d\theta_s} - \frac{R}{y_t^2}\frac{dy_t}{d\theta_s}\right]^{-1}$$

$$= \frac{k+1}{\rho}\,\frac{\left\{\left(\frac{\partial\psi}{\partial\theta}\right)_s\left[y_s - R(1-\cos\theta_s)\right] - \psi(k+1)\left[\left(\frac{\partial y}{\partial\theta}\right)_s - (1-\cos\theta_s)\frac{dR}{d\theta_s} - R\sin\theta_s\right]\right\}}{\left[y_s - R(1-\cos\theta_s)\right]^{k+2}\left[\frac{1}{y_t}\frac{dR}{d\theta_s} - \frac{R}{y_t^2}\frac{dy_t}{d\theta_s}\right]} \qquad (C2)$$

Confining attention to the case $R \to 0$ we have : $R \approx 0$, $\psi = 1$, $\theta_s = \beta$, $y_s = y_t$, $(k+1)/\rho y_t^{k+1} = (C_d)_o$ and equation C2 becomes:

$$\left[\frac{dC_d}{d(R/y_t)}\right]_{R=0} = (C_d)_o \left\{\left[y_t\left(\frac{\partial \psi}{\partial \theta}\right)_s - (k+1)\psi\left(\frac{\partial y}{\partial \theta}\right)_s\right]\left(\frac{d\theta_s}{dR}\right) + (k+1)(1-\cos\beta)\right\} \tag{C3}$$

The radius of curvature of a streamline at any point is given by:

$$R = \left[1 + \left(\frac{\partial y}{\partial x}\right)_\psi^2\right]^{3/2} \Big/ \left(\frac{\partial^2 y}{\partial x^2}\right)_\psi \tag{C4}$$

We have $\left(\frac{\partial y}{\partial x}\right)_\psi = \tan\theta$ and $\left(\frac{\partial^2 y}{\partial x^2}\right)_\psi = \sec^2\theta\left(\frac{\partial \theta}{\partial x}\right)_\psi$ and equation C4 becomes:

$$R = \sec\theta\left(\frac{\partial x}{\partial \theta}\right)_\psi \tag{C5}$$

since x is a function of V and θ we may write:

$$dx = \left(\frac{\partial x}{\partial V}\right)_\theta dV + \left(\frac{\partial x}{\partial \theta}\right)_V d\theta$$

thus:

$$\left(\frac{\partial x}{\partial \theta}\right)_\psi = \left(\frac{\partial x}{\partial V}\right)_\theta \left(\frac{\partial V}{\partial \theta}\right)_\psi + \left(\frac{\partial x}{\partial \theta}\right)_V$$

$$= -\left(\frac{\partial x}{\partial V}\right)_\theta \left(\frac{\partial V}{\partial \psi}\right)_\theta \left(\frac{\partial \psi}{\partial \theta}\right)_V + \left(\frac{\partial x}{\partial \theta}\right)_V$$

Substitution in equation C5 yields :

$$R = \sec\theta\left[\left(\frac{\partial x}{\partial \theta}\right)_V - \left(\frac{\partial x}{\partial V}\right)_\theta \left(\frac{\partial \psi}{\partial \theta}\right)_V \Big/ \left(\frac{\partial \psi}{\partial V}\right)_\theta\right] \tag{C6}$$

substitution from equations 2.21, noting that $\left(\frac{1}{V} + \frac{\rho_V}{\rho}\right) = 0$ on the sonic line, leads to:

$$R = \frac{1}{\rho y_s^k}\left[\psi_V + k\left(\frac{y_V}{y_s}\frac{\psi_\theta^2}{\psi_V} - \frac{y_\theta}{y_s}\psi_\theta\right)\right] \tag{C7}$$

where the derivatives ψ_v, ψ_θ etc. refer to $\left(\frac{\partial \psi}{\partial v}\right)_\theta$, $\left(\frac{\partial \psi}{\partial \theta}\right)_v$ etc. on the sonic line. From equations 2.22 we have:

$$\left(\frac{y_v}{y_s}\frac{\psi_\theta^2}{\psi_v} - \frac{y_\theta}{y_s}\psi_\theta\right) = \frac{-\psi_v \psi_\theta \sin\theta_s}{\rho y_s^2 + \psi_\theta \sin\theta_s}$$

which leads to

$$R = \frac{1}{\rho y_s^k}\left[\psi_v - \frac{k\psi_v\psi_\theta \sin\theta_s}{\rho y_s^2 + \psi_\theta \sin\theta_s}\right] \qquad (C8)$$

Differentiation of equation C8 gives:

$$\frac{dR}{d\theta_s} = -\frac{kR}{y_s}\left(\frac{\partial y}{\partial \theta}\right)_s + \frac{1}{\rho y_s^k}\left[\psi_{v\theta} - \frac{k\left(\psi_v\psi_\theta\cos\theta_s + \psi_{v\theta}\psi_\theta \sin\theta_s + \psi_v\psi_{\theta\theta}\sin\theta_s\right)}{\left(\rho y_s^2 + \psi_\theta \sin\theta_s\right)}\right.$$

$$\left. + \frac{k\psi_v\psi_\theta \sin\theta_s \frac{\partial}{\partial\theta}\left(\rho y_s^2 + \psi_\theta \sin\theta_s\right)}{\left(\rho y_s^2 + \psi_\theta \sin\theta_s\right)^2}\right] \qquad (C9)$$

In the case $R \to 0$ we have $\psi_v = 0$ and equation C9 reduces to:

$$\frac{dR}{d\theta_s} = \frac{1}{\rho y_t^k}\left[\psi_{v\theta} - \frac{k\psi_\theta\psi_{v\theta}\sin\beta}{(k+1)/(C_d)_o + \psi_\theta \sin\beta}\right] \qquad (C10)$$

If we substitute equation C10 for $\frac{dR}{d\theta_s}$ and equation 2.21d for $\left(\frac{\partial y}{\partial \theta}\right)_s$ into equation C3 we obtain:

$$\left[\frac{dC_d}{d(R/y_t)}\right]_{R=0} = (C_d)_o \left\{\frac{\left[\left[\frac{k+1}{(C_d)_o} - \cos\beta\right]\psi_\theta}{\left[1 - \frac{k\psi_\theta \sin\beta}{\frac{k+1}{(C_d)_o} + \psi_\theta \sin\beta}\right]\psi_{v\theta}} + (k+1)(1-\cos\beta)\right\} \qquad (C11)$$

The values of ψ_θ and $\psi_{v\theta}$ at the lip may be evaluated from the sharp-lipped solution and it turns out in practice that the ratio $\psi_\theta/\psi_{v\theta}$ is fairly small. It is reasonable, therefore, to use a simplified form of equation C11 to predict the variation of C_d:

$$C_d = (C_d)_o\left[1 + (k+1)(1-\cos\beta)\frac{R}{y_t} + \cdots\right] \qquad (C12)$$

REFERENCES

ALDER, G.M. 1974 Compressible, subcritical flow through axially symmetric sharp-lipped orifices and nozzles. The Institute of Mathematics and it Applications; Conference on Computational Methods in Aeronautical Fluid Dynamics. (In the press.)

AMES W.F. 1969 Numerical Methods for Partial Differential Equations. LONDON : Nelson

ARYNOV, A. 1958 Gas flow from a vessel with plane walls forming a small angle $2\theta_o$. Doklady. Akad. Nauk. SSSR. 123, 47.

ASLANOV, S.K. & LEGCKOVA, V.A. 1959 Outflow of a gas from a vessel of finite size. Prinkl. Mat. Mekh. 23, 190.

BENSON, R.S. 1959 Experiments on two-stroke engine exhaust ports under steady flow conditions. Proc. Inst. of Mech. Engrs. 173, 511.

BENSON. R.S. & POOL, D.E. 1965a Compressible flow through a two-dimensional slit. Int. J. Mech. Sci. 7, 315.

BENSON, R.S. & POOL, D.E. 1965b Compressible flow discharge coefficients for a two-dimensional slit. Int. J. Mech. Sci. 7 337.

BLOCH, E. 1969 Numerical solution of free boundary problems by the method of steepest descent. The Physics of Fluids Supplement II - High Speed Computing in Fluid Dynamics.

BRAGG, S.L. 1960 Effect of compressibility on the discharge coefficients of orifices and convergent nozzles. J. Mech. Eng. Sci. 2 , 35.

BRAIN, T.J.S. & REID, J. 1973 Performance of small diamter cylindrical critical - flow nozzles. N.E.L. Report no. 546.

BROWN, E.F. 1968 Compressible flow through convergent conical nozzles with emphasis on the transonic region. Ph.D. thesis: University of Illinois.

CALLAGHAN, E.E. & BOWDEN, D.T. 1949 Investigation of flow coefficients of circular, square and elliptical orifices at high pressure ratios. NACA TN1947.

CARRÉ, B.A. 1961 The determination of the optimum accelarating factor for successive over-relaxation. Computer J. 4, 73.

CHAPLYGIN, S.A. 1904 Sur les jets gazeux. Ann. Sci. Univ. Moscow 21, 1.

COHEN, M.J. 1960 Two-dimensional gas jets. Trans ASME: J. Appl. Mech. 82, 603.

CROCKETT, K.A. & UPP, E.L. 1973 The measurement and effects of edge sharpness on the flow coefficients of standard orifices. Trans. ASME: J. Fluids Eng. 95, 271.

CUNNINGHAM, R.G. 1951 Orifice meters with supercritical compressible flow. Trans. ASME 73, 625.

DECKKER, B.E.L. & CHANG, Y.F. 1966 An investigation of steady compressible flow through thick orifices. Proc. Inst. Mech. Eng. 180.

FALKOVICH. S.V. 1957 Theory of gas jets. Prinkl. Mat. Mech. 21 4.

FRANKL,F.I. 1947 The flow of a supersonic jet from a vessel with plane walls. Dokl. Akad. Nauk. SSSR 58, 381.

GALLACHER, G.R. 1968 Measuring edge sharpness of orifice plates. The Engineer 225, 783.

GARABEDIAN, P. 1956 Calculation of axially symmetric cavities and jets. Pacific Jl. Maths 6, 611

GRACE, H.P. & LAPPLE,L.E. 1951 Discharge coefficients of small diameter orifices and flow nozzles. Trans ASME 73, 639

GREY, R.E. & WILSTED, H.D. 1949 Performance of conical jet nozzles in terms of flow and velocity coefficients. NACA Report no. 933

GUDERLEY, G. 1947 Considerations on the structure of mixed subsonic - supersonic flow patterns. Tech. Rep. No. F - TR - 2168 - ND, H.Q. Air Mat. Command (Wright Field).

GUDERLEY, G. 1962 The theory of transonic flow. Pergamon, Oxford.

GUREVICH, M.I. 1965 The theory of jets in ideal fluids (Tr. Street & Zagustin). Academic Press, New York.

GUSHCHIN, B.A. 1959 Flow of a gas stream from a container of finite width at maximum discharge. Prinkl. Mat. Mekh 23, 770

HALL, I.M. 1962 Transonic flow in two-dimensional and axially symmetric nozzles. Quart. J. Mech. Appl. Math. 15, 487.

HEBBAR, K.S. SRIDHARA, K & PARANJPE, P.A. 1970 Performance of conical jet nozzles in terms of discharge coefficient. J. Aero. Soc. India 22, 3.

von HELMHOLTZ, H. 1868 Phil. Mag. (4th series) 36, 337.

HOPKINS, D.F. & HILL, D.E. 1966 Effect of small radius of curvature on transonic flow in axisymmetric nozzles. AIAA Jl. 4, 1337.

HUNT, B.M. 1968 Numerical solution of an integral equation for flow from a circular orifice. J. Fluid Mech. 31, 361

JACOB, C. 1936 Sur un jet gazeux. Comptes - Rendus Acad. Sci. Paris 203, 423

JEPPSON, R.W. 1969 Free streamline problems solved by inverse formulation and finite differences. Proc. 11th Midwestern Mech. Conf. (Iowa State University) 23.

JOBSON, D.A. 1955 On the flow of a compressible fluid through orifices. Proc. I. Mech. E. 169, 767

KASTNER, L.J. WILLIAMS, T.J. & SOWDEN, R.A. 1964 Critical flow nozzle meter and its application to the measurement of mass flow in steady and pulsating streams of gas. J. Mech. Eng. Sci. 6, 88

KIRCHOFF, G. 1869 Zur Theorie freier Flüssigkeitsstrahlen. J. reine u. angewandte Math 70, 289

KLIEGEL, J.R. & LEVINE, J.N. 1969 Transonic flow in small throat radius of curvature nozzles. AIAA Jl. 7, 1375.

LADENBURG, R., VAN VOORHIS, C.C. & WINCKLER, J. 1949 Interferometric studies of faster than sound phenonema. Part II, Analysis of supersonic air jets. Physical Review 76, 662.

LAROCK, B.E. 1969 Jets from two-dimensional symmetric nozzles of arbitrary shape. J. Fluid Mech. 37, 479.

LIEPMANN, H.W. 1961 Gas kinetics and gas dynamics of orifice flow. J. Fluid Mech. 10, 65.

MCLAUGHLIN, M.D. & PACK, D.C. 1969 Compressible flows with circular sector hodographs. Proc. Cambridge Phil. Soc. 66, 629.

MILLER, A.J. 1975 The design and construction of compressible flow apparatus. University of Edinburgh, Dept. of Mechanical Engineering B.Sc. Honours Project Report.

von MISES, R. 1917 Berechnung von Ausflüss - und Überfall - zahlen. Z.V.D.I. 61, 447, & 493.

NORWOOD, R.E. 1962 Two-dimensional transonic gas jets. Proc. 4th U.S. Nat'l. Cong. Appl. Mech. 2, 1359

OVSIANNIKOV, L.V. 1949 Gas flow with straight transition line. Prik. Mat. i Mekh. 13, 537 [Trans: NACA TM 1295, 1951]

PERRY, J.A. 1949 Critical flow through sharp-edged orifices. Trans. ASME 71, 757.

POPE, A. & GOIN, K.L. 1965 High Speed Wind Tunnel Testing. Wiley, New York.

PROZAN, R.J. & KOOKER, D.E. 1970 The error minimisation technique with application to a transonic nozzle solution. J. Fluid. Mech. 43, 269.

Lord RAYLEIGH 1876 The contracted vein. Phil. Mag. (5th series) 2. 441.

ROUMIEU, C. 1952 Recherches sur le jet critique plan. Comptes Rendus Acad. Sci. Paris (Ser A-B) 234, 52.

ROUSE, H. & ABUL-FETOUH. A. 1950 Characteristics of irrotational flow through axially symmetric orifices. Trans ASME 72, 421

SALAMATOV, D. 1959 Flow of a fluid out of an infinitely long axisymmetric vessel. Prinkl. Math. Mekh. 23, 361

SAUER, R. 1947 General characteristics of the flow through nozzles at near - critical speeds NACA TM 1147

SHAPIRO, A.H. 1953 The dynamics and thermodynamics of compressible fluid flow, vols, I & II. Ronald Press, New York.

SOUTHWELL, R. & VAISY, G. 1948 Fluid motions characterised by free streamlines. Phil. Trans. Roy. Soc. London A240, 117

STANTON, T.E. 1926 On the flow of gases at high speeds. Proc. Roy. Soc. London A111, 306

STOW, P. 1972 The solution of isentropic transonic flow. J. Inst. Maths. Applics. 9, 35

STRATFORD , B.S. 1964 The calculation of the discharge coefficient of profiled choked nozzles and the optimum profile for absolute airflow measurement. Roy. Aero. Soc. Jl. 68, 237.

TAYLOR, D.B. 1968 The calculation of steady plane supersonic gas flows containing an arbitrarily large number of shocks. J. Comp. Phys. 3 273.

THORNOCK, R.L. & BROWN, E.F. 1972 An experimental study of compressible flow through convergent conical nozzles, including a comparison with theoretical results. Trans. ASME : J. Bas. Eng. 84, 926

TREFFTZ, E. 1916 Z. Math. Phys. 64, 34.

WEIR, A., YORK, J.L. & MORRISON, R.B. 1956 Two - and three-dimensional flow of air through square -edged sonic orifices. Trans. ASME 78, 481

YOUNG, D.M. 1954 Iterative methods of solving partial differential equations of elliptic type. Trans Amer. Math. Soc. 76, 92

PRINCIPAL NOTATION

A - Flow cross-section area in Chapter 5; coefficient in equation 6.6

c - speed of sound

c^* - speed of sound when M = 1

C_d - discharge coefficient

d - nozzle throat diameter

k - k = 0 for two-dimensional flow; k = 1 for axially symmetric flow

$\dot{m}$ - mass flow through nozzle

$\dot{m}_t$ - theoretical mass flow, assuming uniform flow in throat

M - Mach number

M_j - Mach number on jet boundary

N - number of subdivisions in hodograph finite difference mesh

p - local static pressure (assumed to be fraction of stagnation pressure except where otherwise stated)

p_a - atmospheric pressure surrounding jet

p_o - stagnation pressure

r - nozzle operating pressure ratio ($r = p_a / p_o$)

r_c - pressure ratio for choked flow

r_s - pressure ratio for critical flow ($M_j = 1$)

r_l - radius of curvature at nozzle lip (Chapter 6)

R - gas constant per unit mass

Re_X - Reynolds number defined in equation 6.1

Re_1 - nozzle throat Reynolds number ($Re_1 = dV_1 \rho_1 / \mu_1$)

s - distance along nozzle wall, used in equation 6.1

t - exponent defined in equation 3.1 which determines degree of concentration of finite - difference mesh in hodograph plane

t_1 - nozzle lip thickness (Chapter 6)

T - local stream temperature

T_o - stagnation temperature

u - axial component of dimensionless velocity

v - component of dimensionless velocity normal to axis

V - velocity (assumed to be fraction of c^* except where otherwise stated)

V_e - approach velocity

V_j - velocity on jet boundary

V_1 - velocity at lip ($V_1 = V_j$ for subcritical flow; $V_1 = 1$ for critical and supercritical flow)

x - axial coordinate (usually assumed to be dimensionless fraction of y_1)

x_o - value of x where sonic line crosses axis

X - coordinate defined in equation 6.1

y - coordinate normal to axis (usually assumed to be fraction of y_1)

y_e - value of y on wall of approach duct

y_1 - value of y at the lip

Z_{ac}, Z_{bc} - non-linear terms in equation 3.20

α - $\alpha = (\rho y^k)^{-1}$

β - nozzle wall angle

γ - ideal gas specific hear ratio

δ^* - nozzle wall boundary layer displacement thickness.

λ_a - eigenvalue defined in equation 3.10

λ_m - eigenvalue defined in equation 3.8

μ - $\mu = \arcsin (1/M)$

μ_1 - gas viscosity at lip

ν - iteration acceleration factor in equation 3.5

ρ - local gas density (assumed to be fraction of stagnation density except where otherwise stated)

ρ_o - stagnation density

σ - independent variable defined in equation 3.1

ϕ - velocity potential (defined in equation 2.11)

ψ - stream function (defined in equation 2.10)

$\psi_s(\theta)$ - stream function distribution along sonic line

θ - angle of flow relative to axis

$\omega(M)$ - function defined in equation 2.35

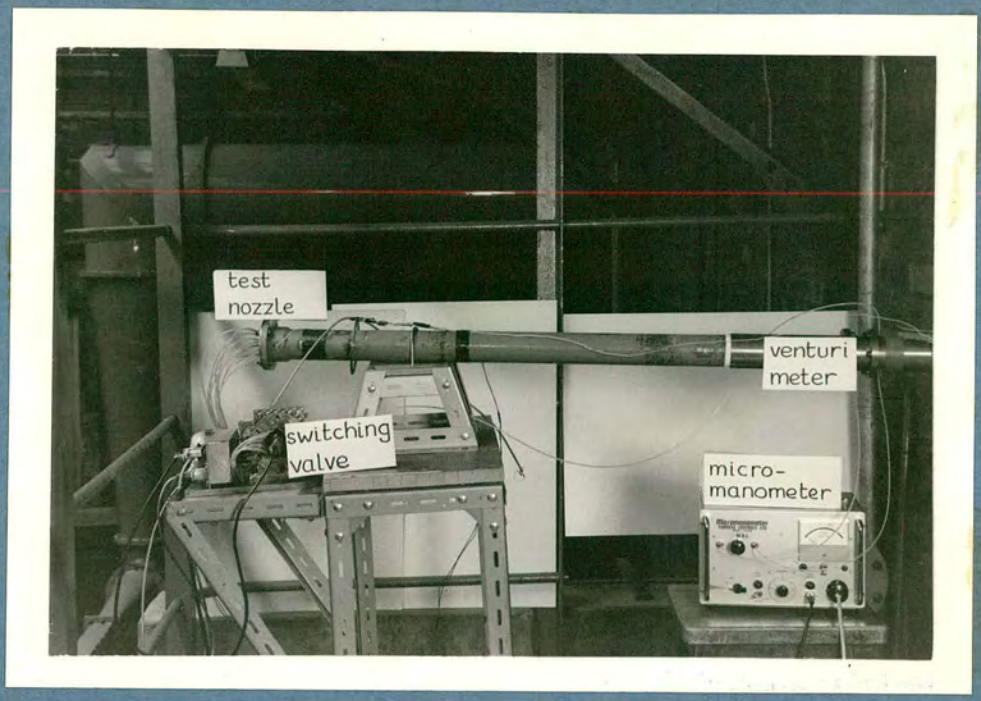

PLATE I The blow-down apparatus.

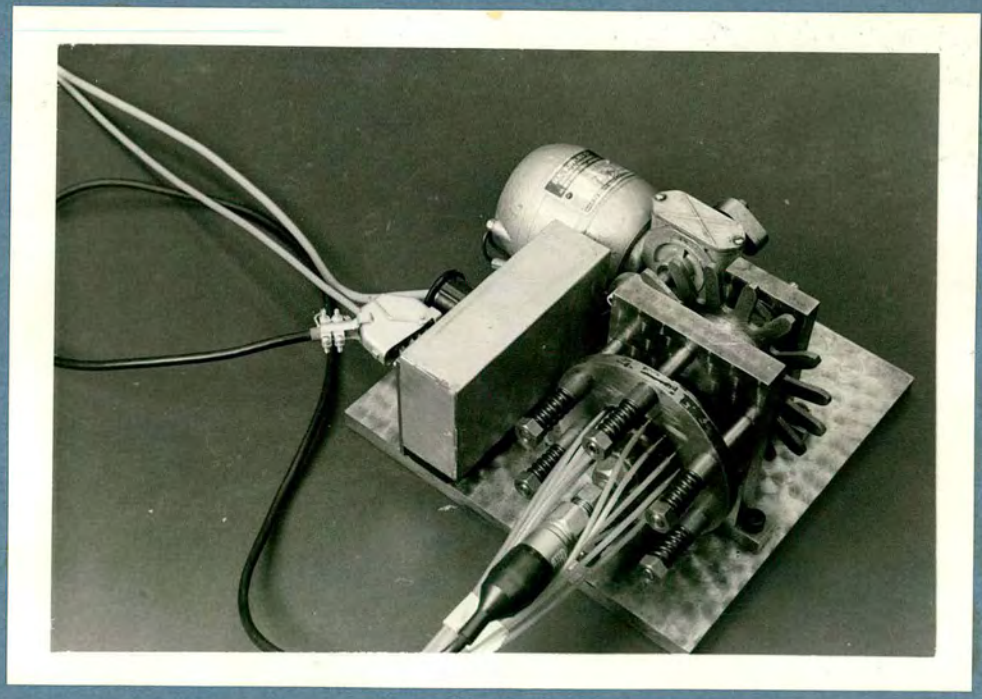

PLATE II 16-channel pressure switching valve

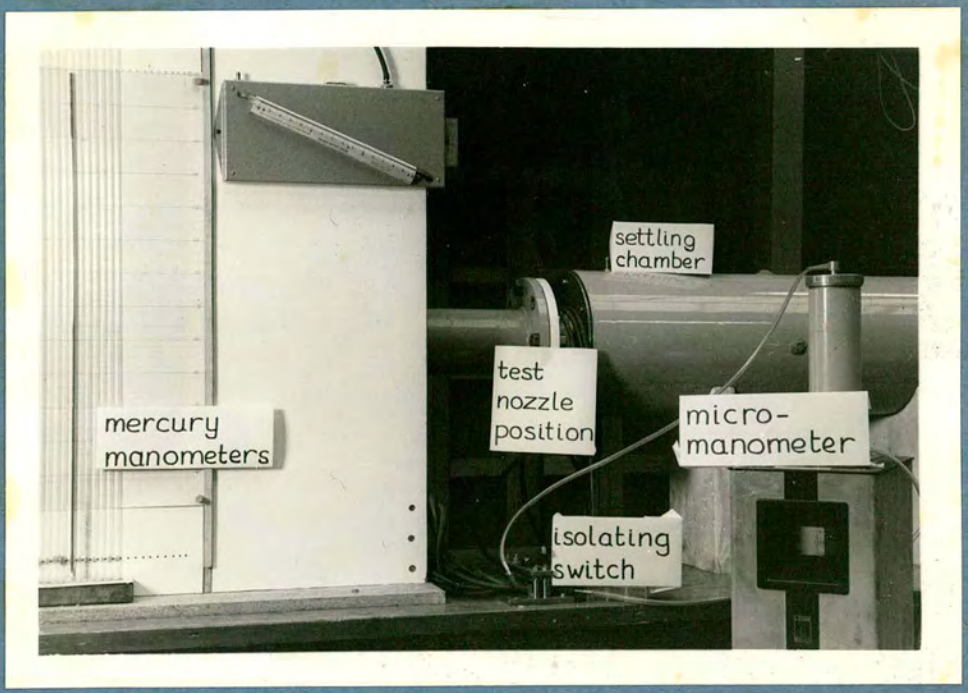

PLATE III The indraught apparatus

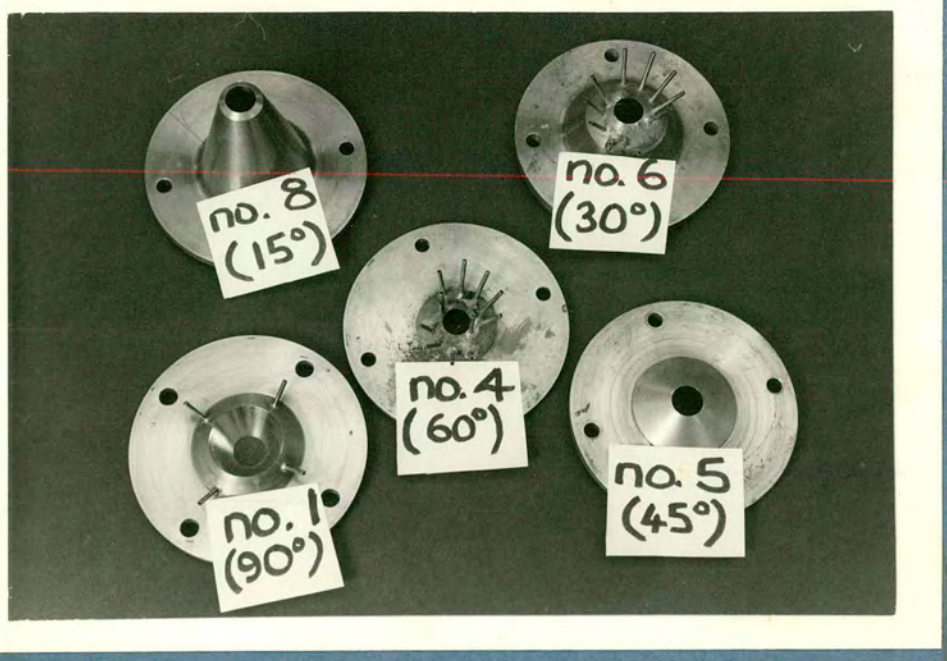

PLATE IV

PLATE V

The axially symmetric test nozzles

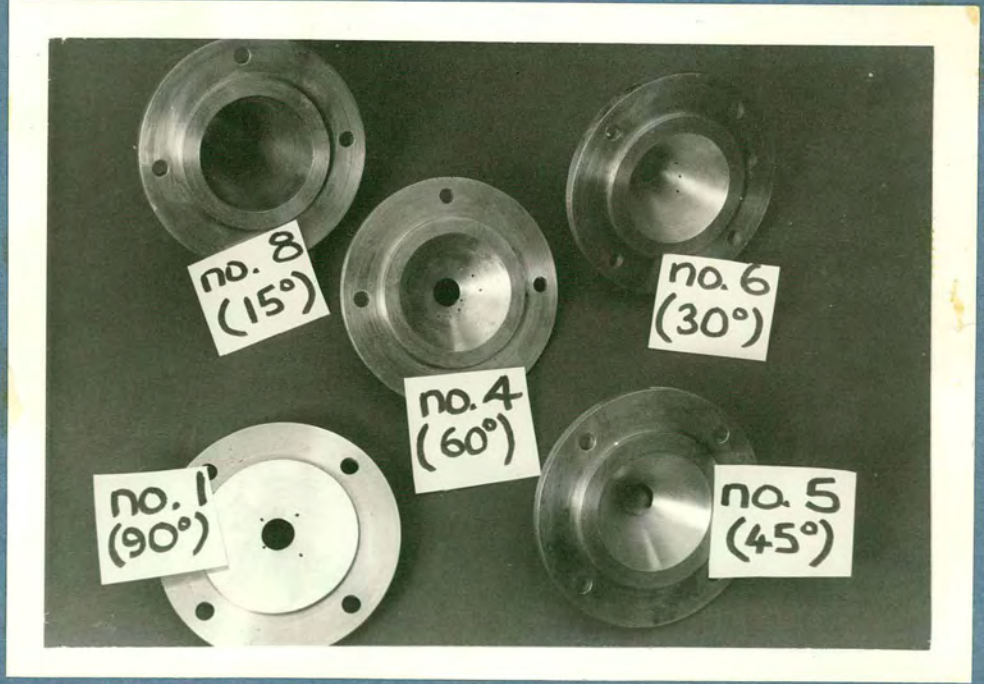

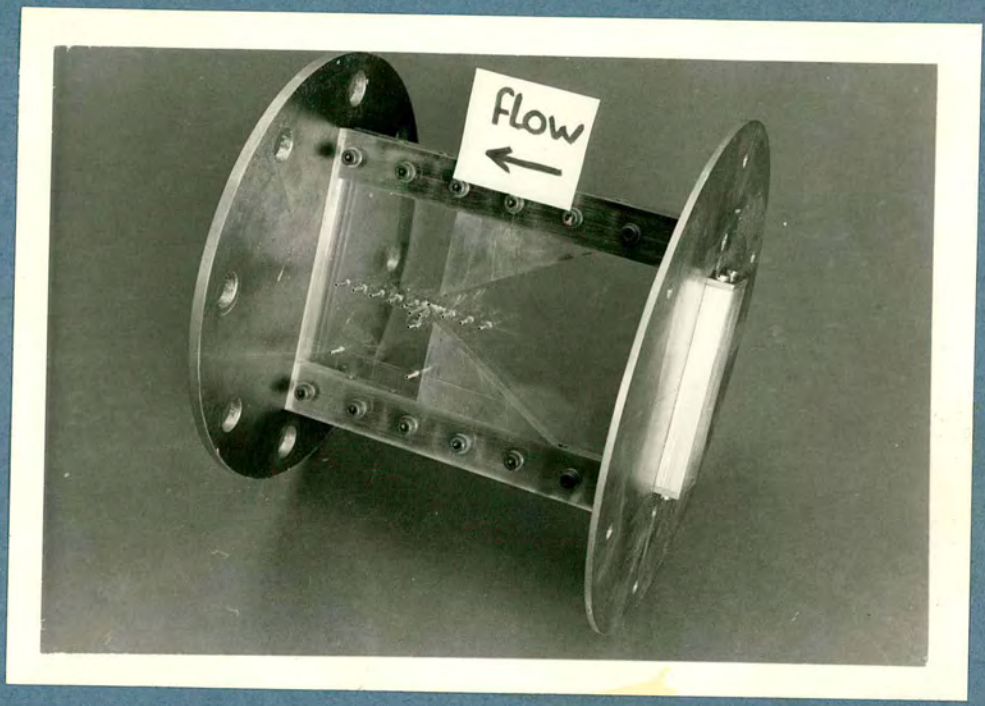

PLATE VI The two-dimensional test section, showing 30° nozzle

PLATE VII "Sharp" lip of 90° nozzle

(upstream face shown horizontal)

(magnification : x 100)

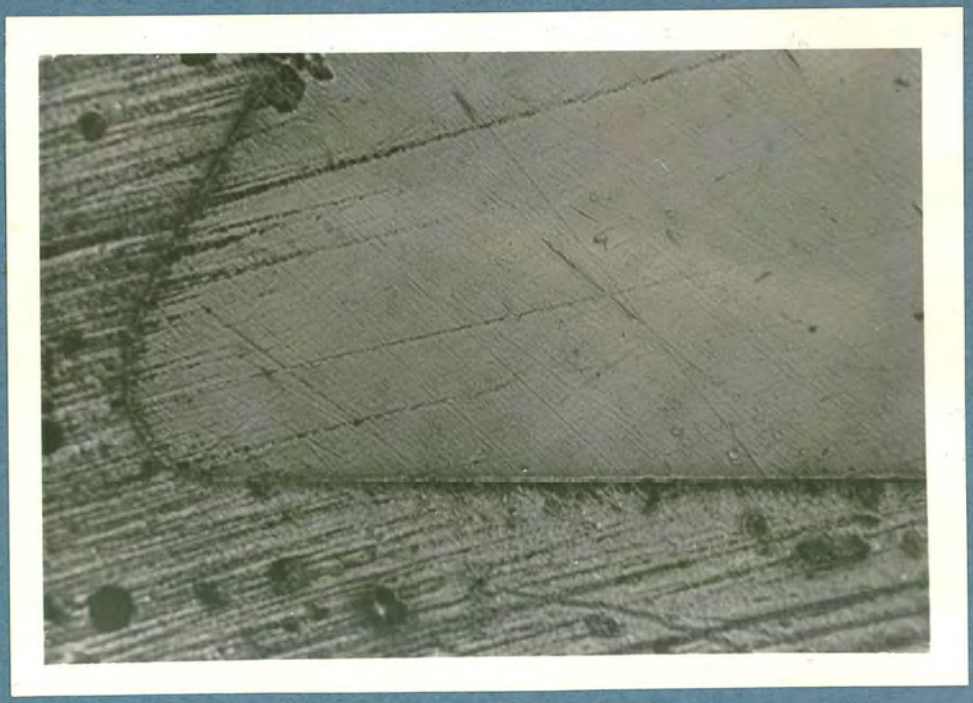

PLATE VIII The same lip after one

stage of blunting

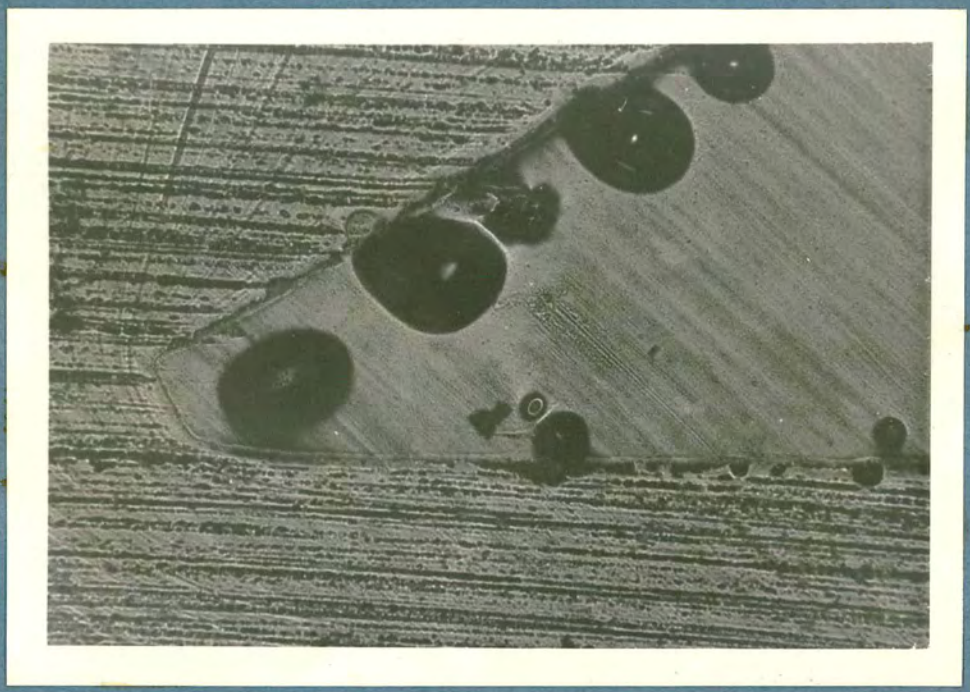

PLATE IX Lip of 60° nozzle showing parallel throat section.

[nozzle wall shown horizontal

magnification : x 100]

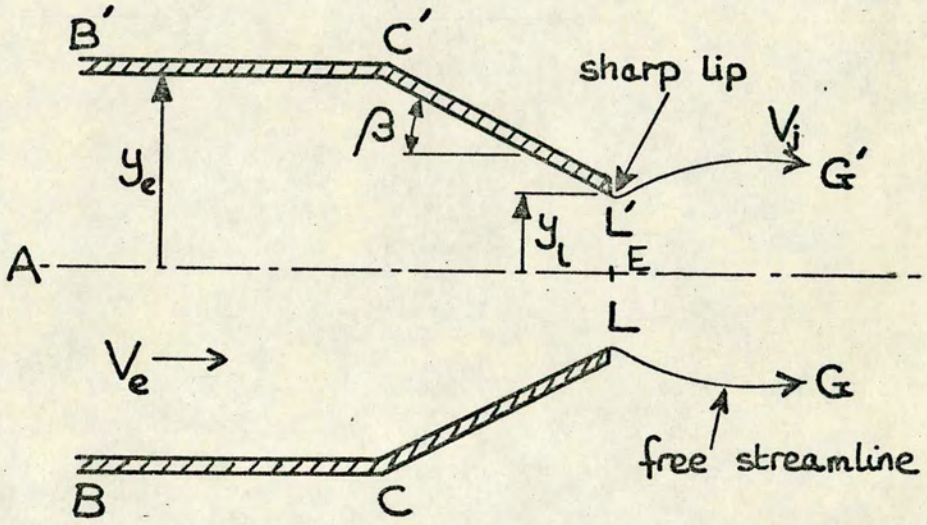

Fig. 2·1 Nozzle geometry

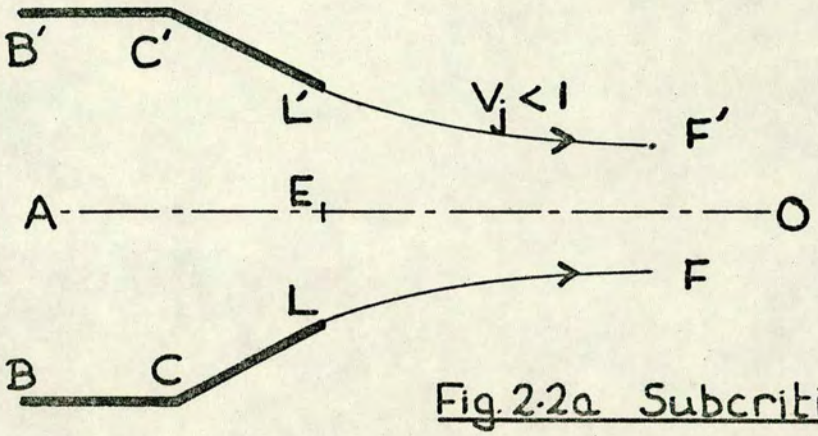

Fig. 2·2a Subcritical flow

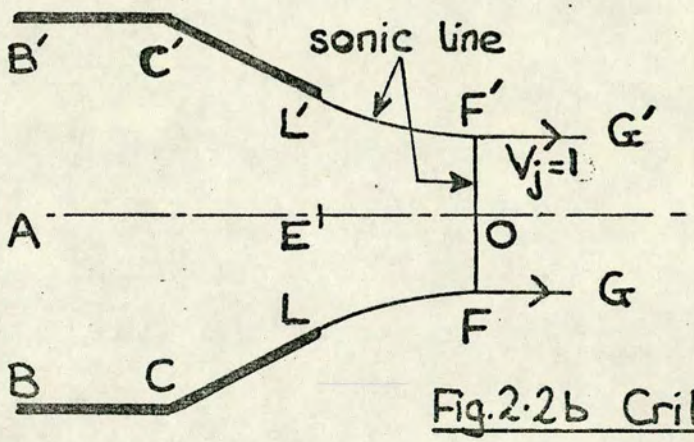

Fig. 2·2b Critical flow

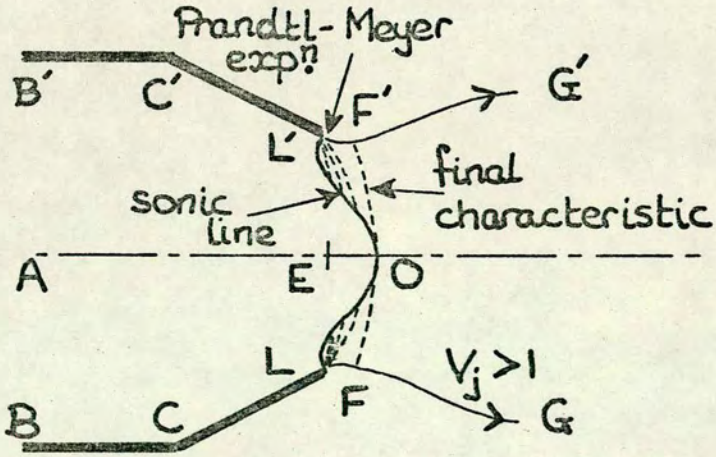

Fig. 2·2c Supercritical flow

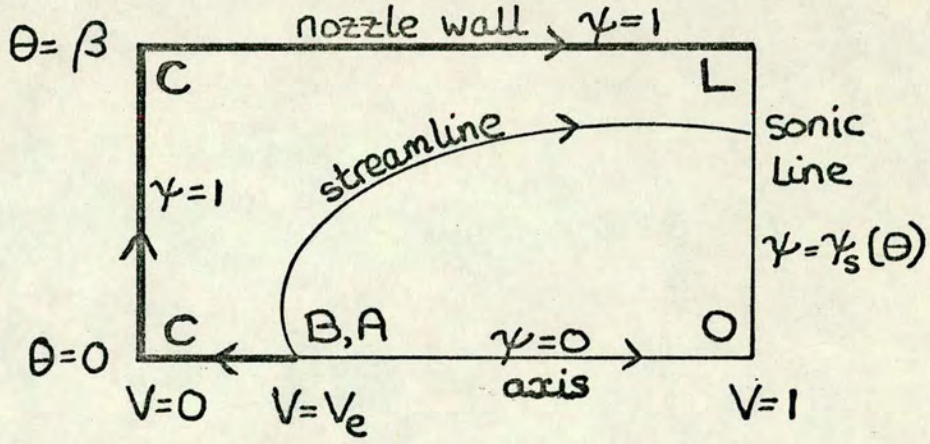

Fig. 2·3a Hodograph plane (supercritical)

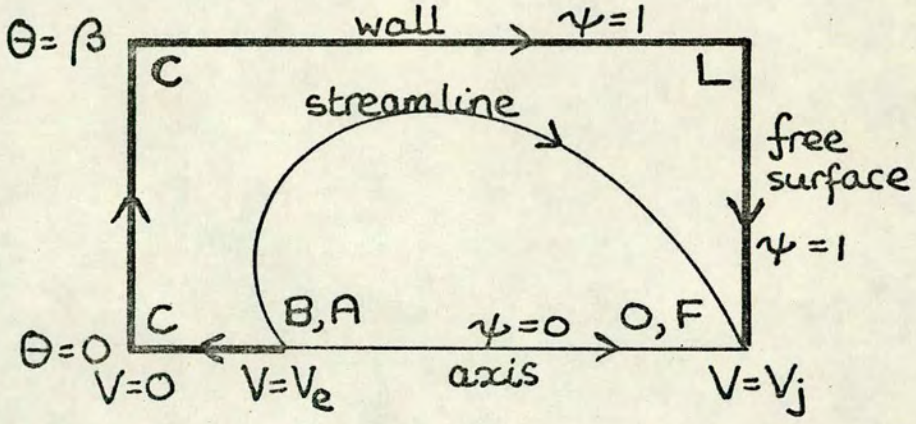

Fig. 2·3b Hodograph plane (subcritical)

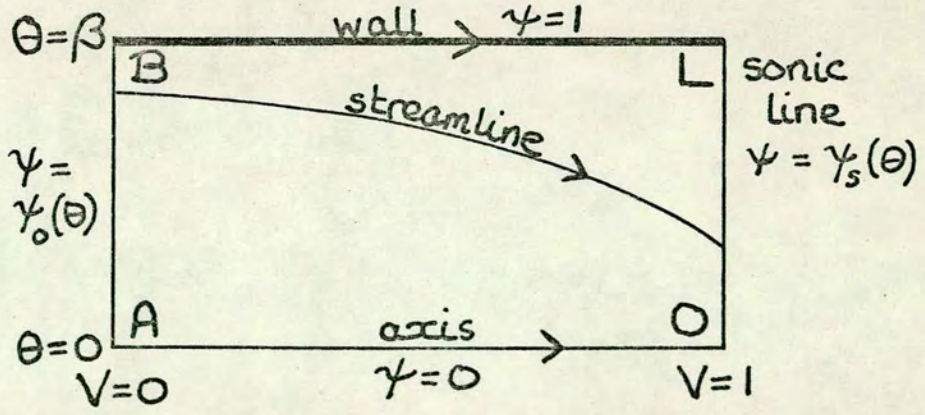

Fig. 2·3c Hodograph plane ($V_e = 0$)

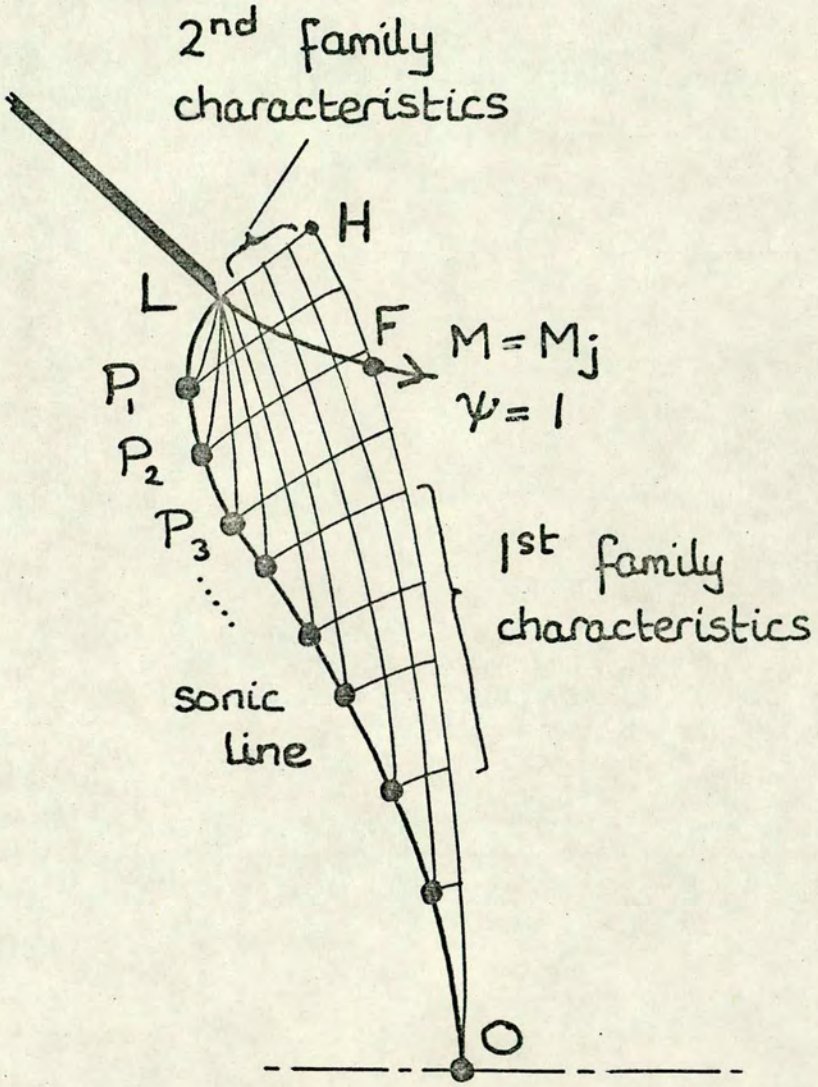

Fig. 2.4 Supercritical flowfield showing characteristics network.

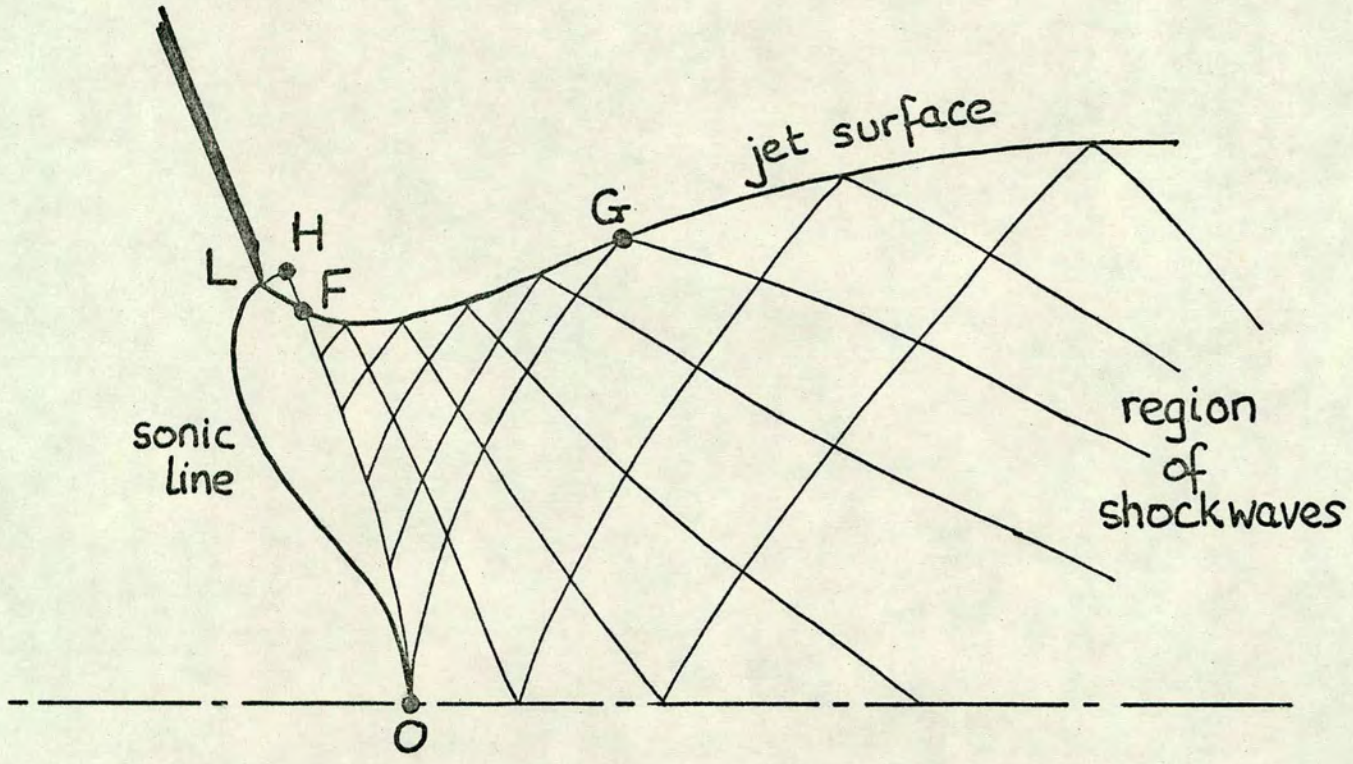

Fig. 2·5 Characteristics network in supercritical jet

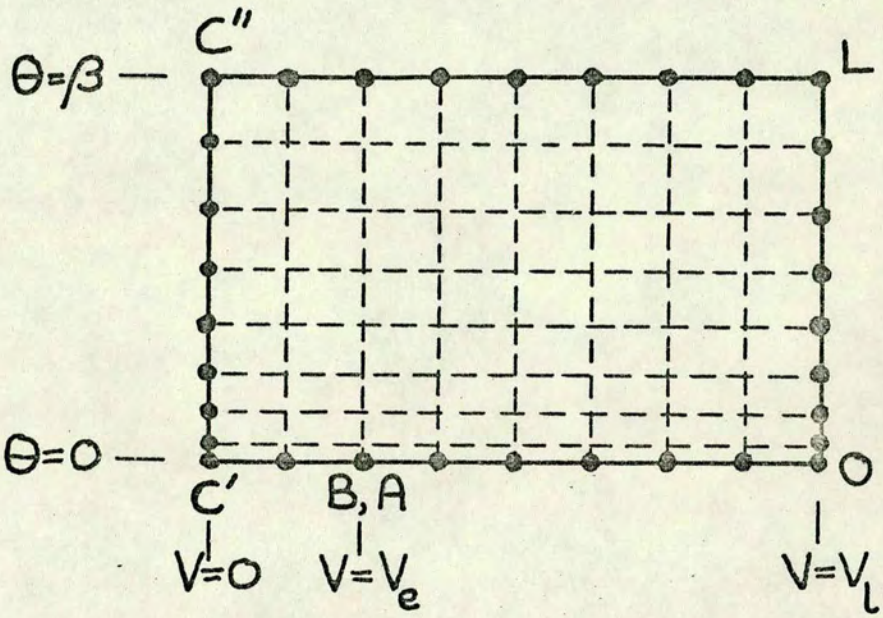

Fig. 3·1 Subsonic hodograph plane, showing finite-difference mesh. (N=8 ; t=1·5)

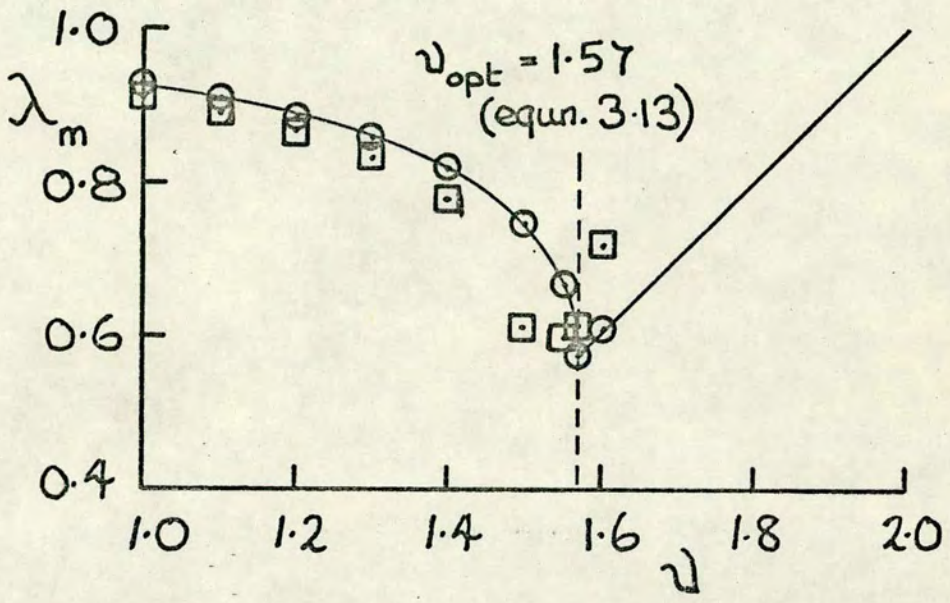

Fig. 3·2 S.O.R. and N.L.O.R. iterations.

Rate of convergence (λ_m) as function of acceleration factor (ν) for a typical problem.
($\beta = 90°$; $\gamma = 1.4$; $V_l = 1$; $N = 12$; $t = 2.0$)

——— : $|\lambda_m|$ from equation 3·12

⊙ : observed rate for S.O.R. ($k=0$)

⊡ : observed rate for N.L.O.R. ($k=1$)

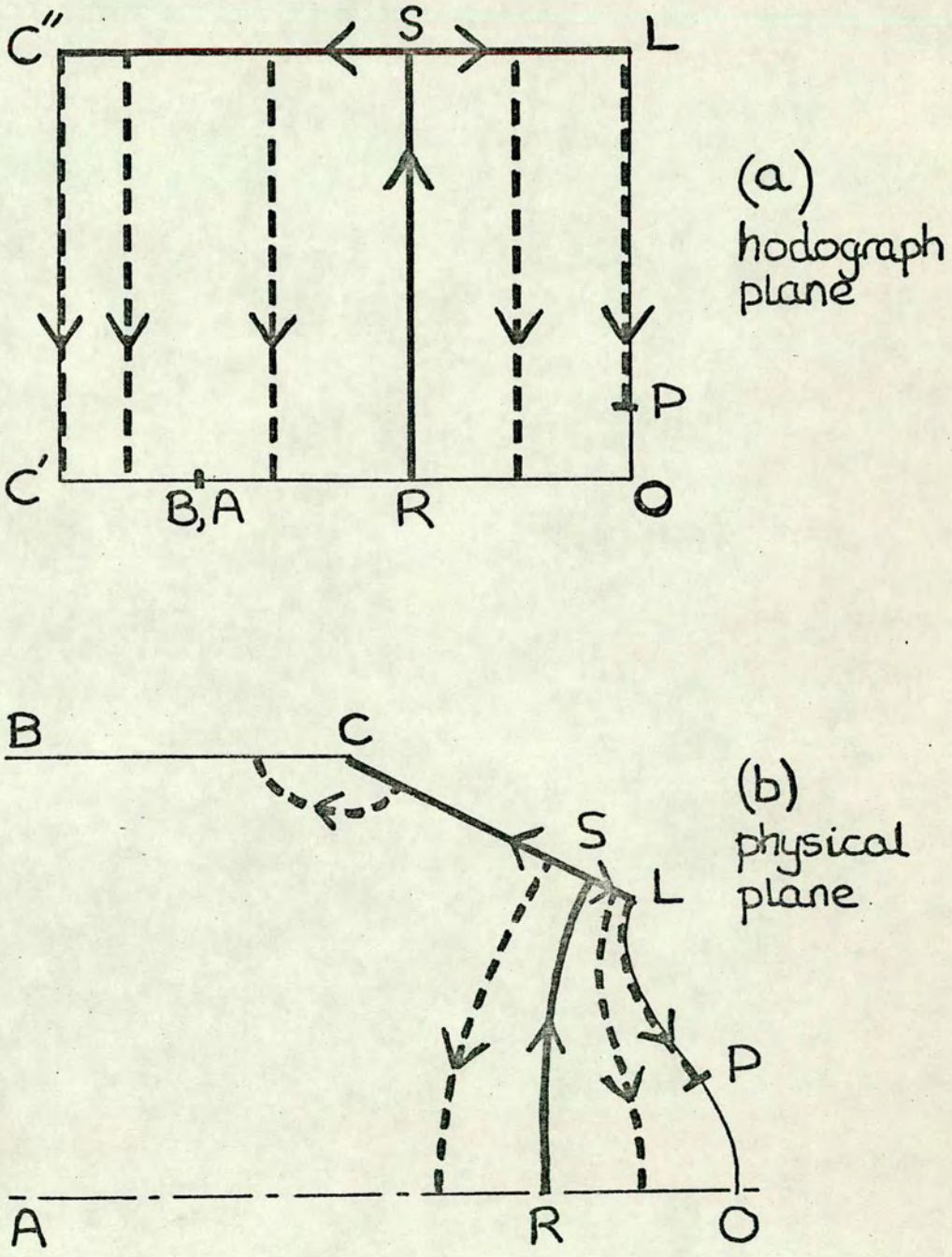

Fig.3·3 Integration paths for deriving physical coordinates from subsonic hodograph solution.

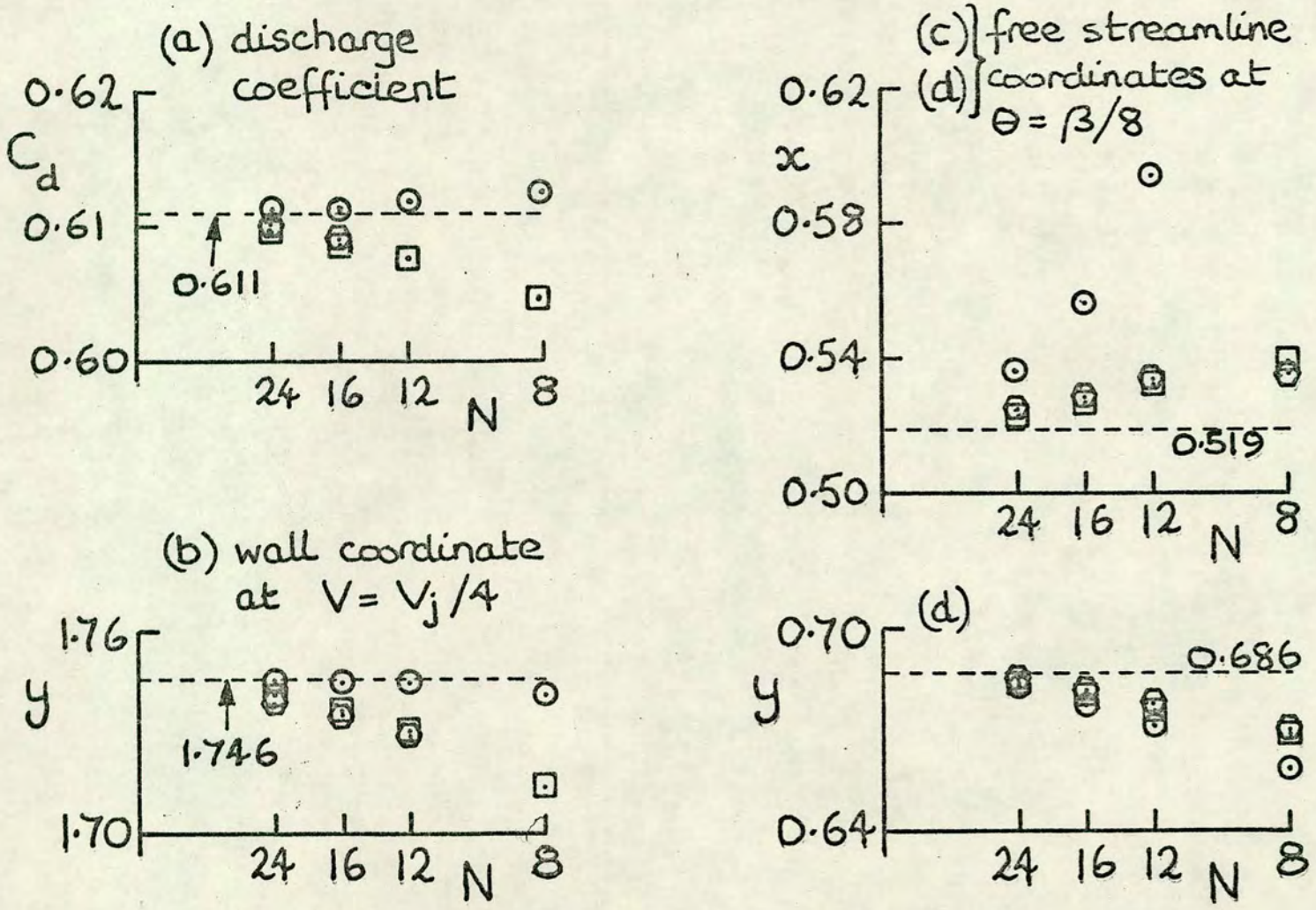

Fig. 3·4 Computed results: 2-D, incompressible ($\beta = 90°$, $V_e = 0$)
values of t: 1·0 - ⊙ 1·5 - ⊡ 2·0 - ⊙

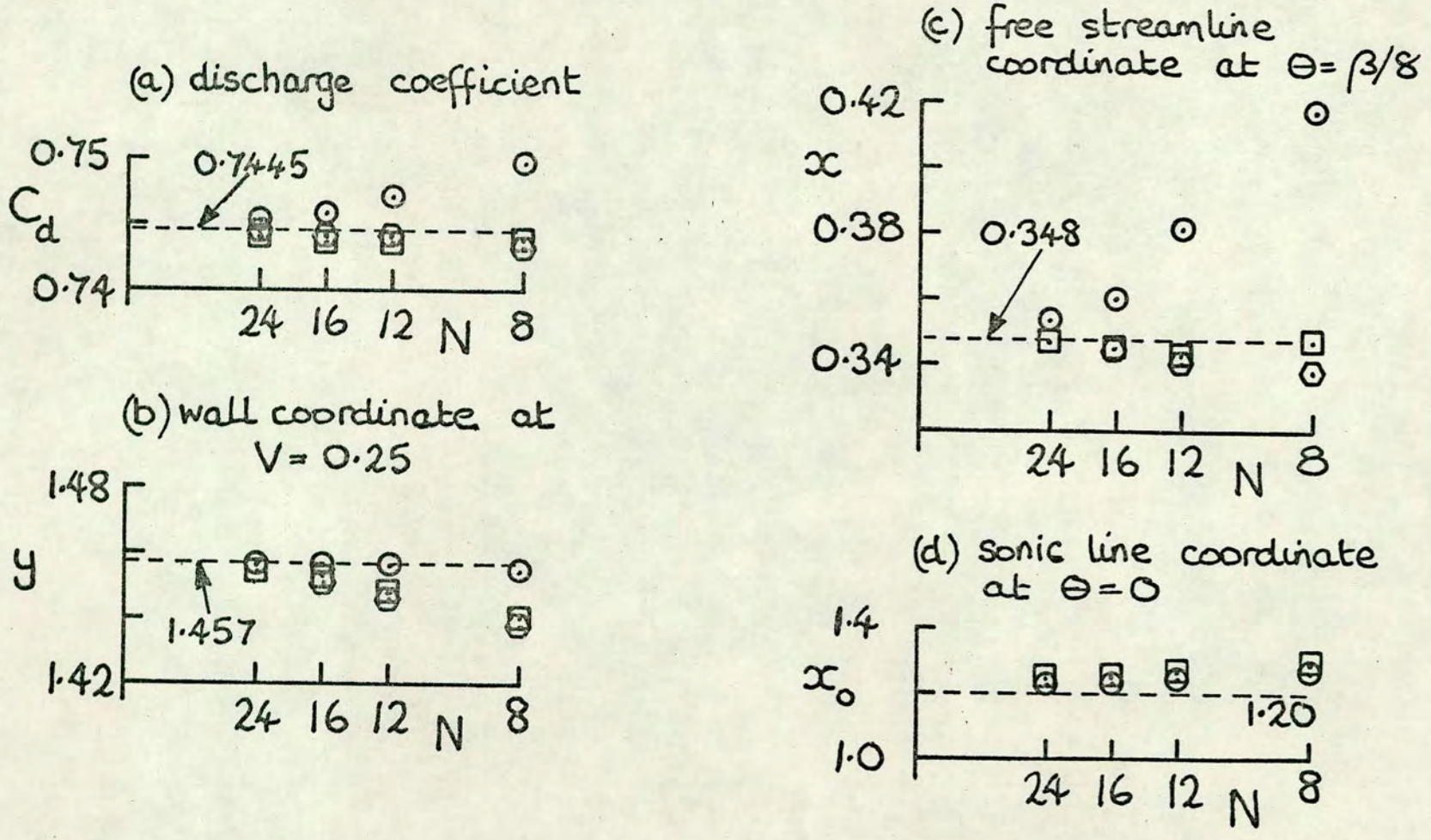

Fig. 3·5 Computed results : 2-D, critical flow ($\beta = 90°$, $\gamma = 1.4$, $V_e = 0$)

values of t : 1·0 – ⊙ 1·5 – ⊡ 2·0 – ⊙

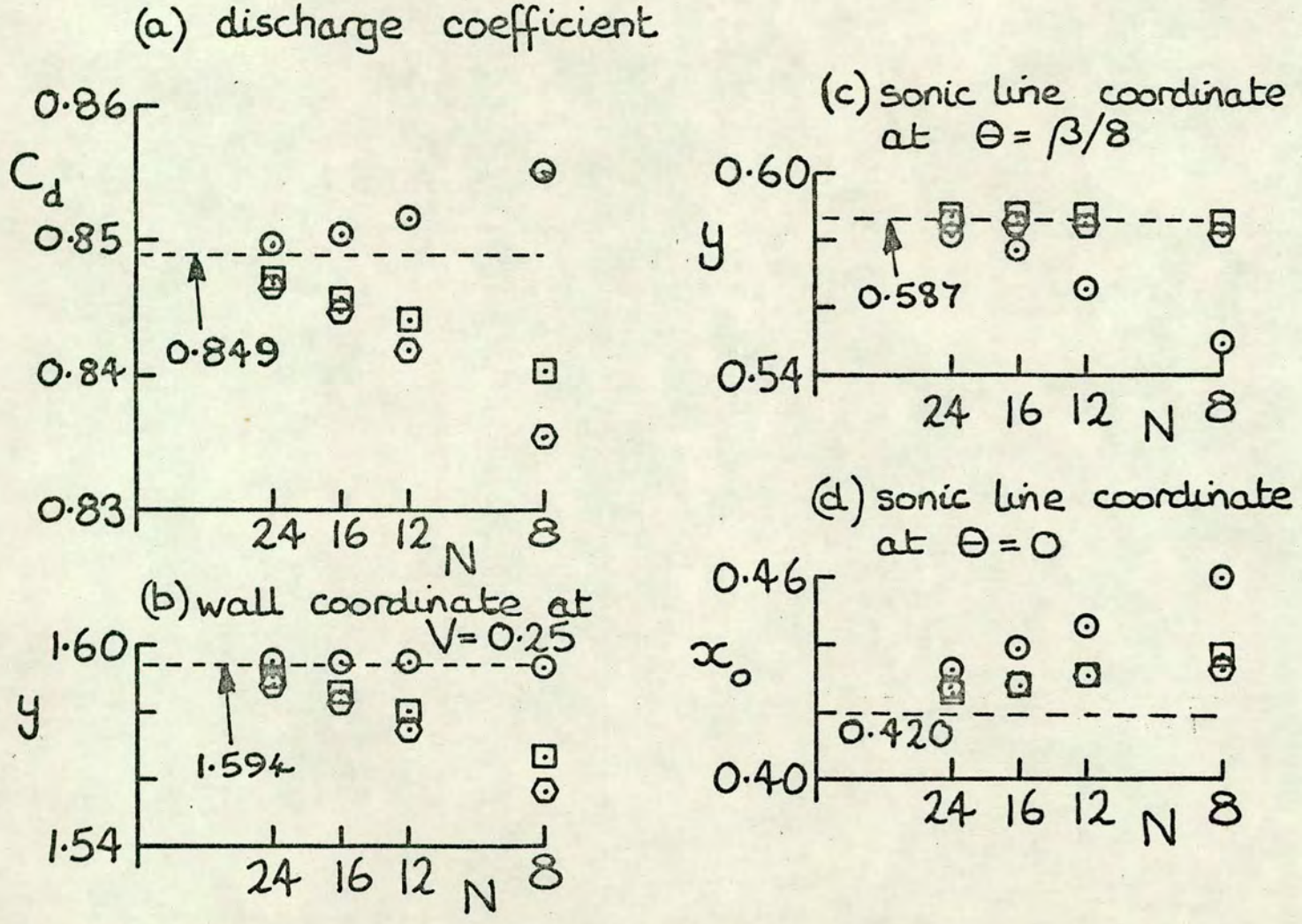

Fig. 3·6 Computed results : 2-D, choked flow.

($\beta = 90°$, $\gamma = 1.4$, $V_e = 0$) t = 1·0 -⊙ 1·5 -⊡ 2·0 -⊙

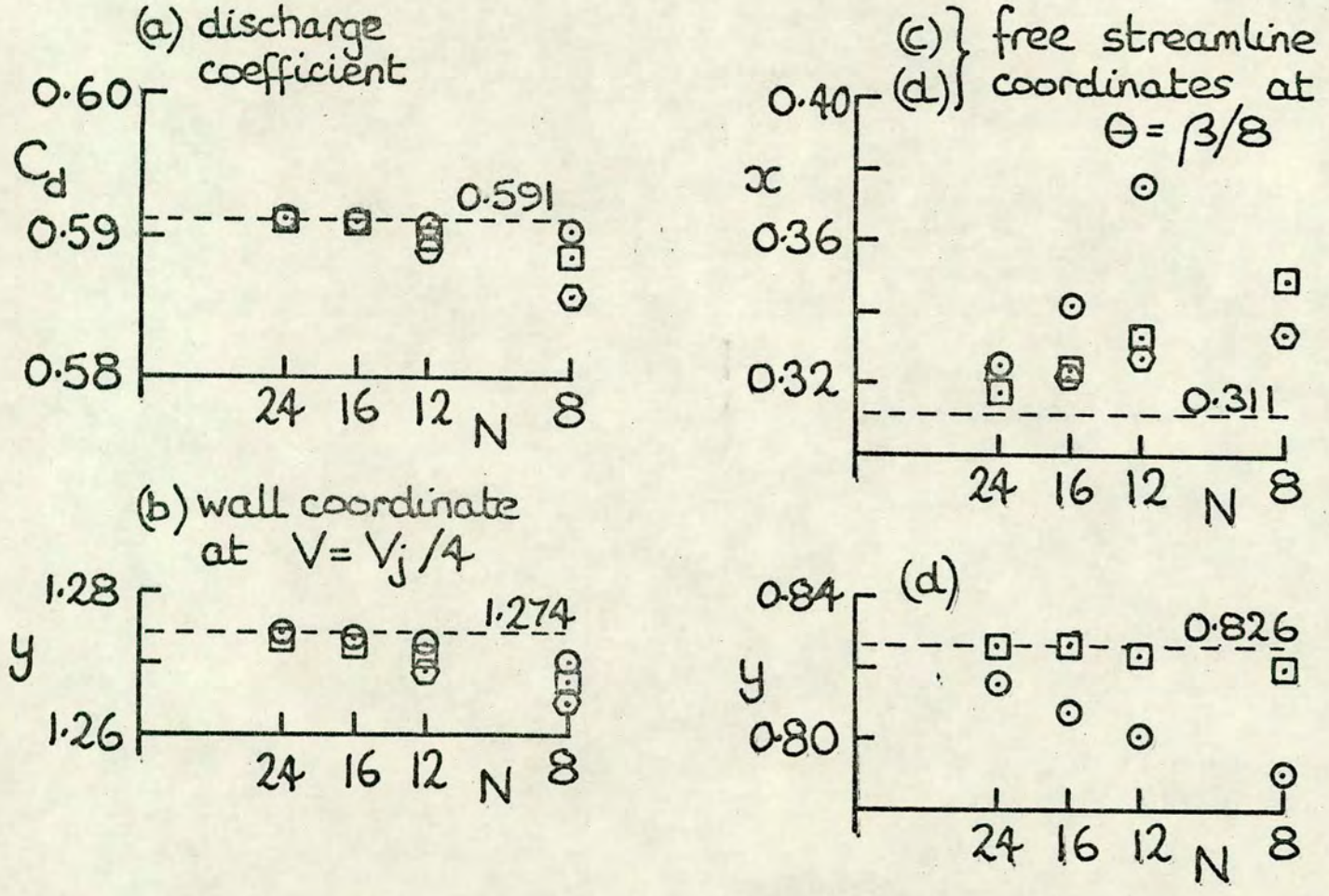

Fig. 3·7 Computed results : axially symmetric, incompressible.
($\beta = 90°$, $V_e = 0$) t = 1·0 -⊙ 1·5 -⊡ 2·0 -⊙

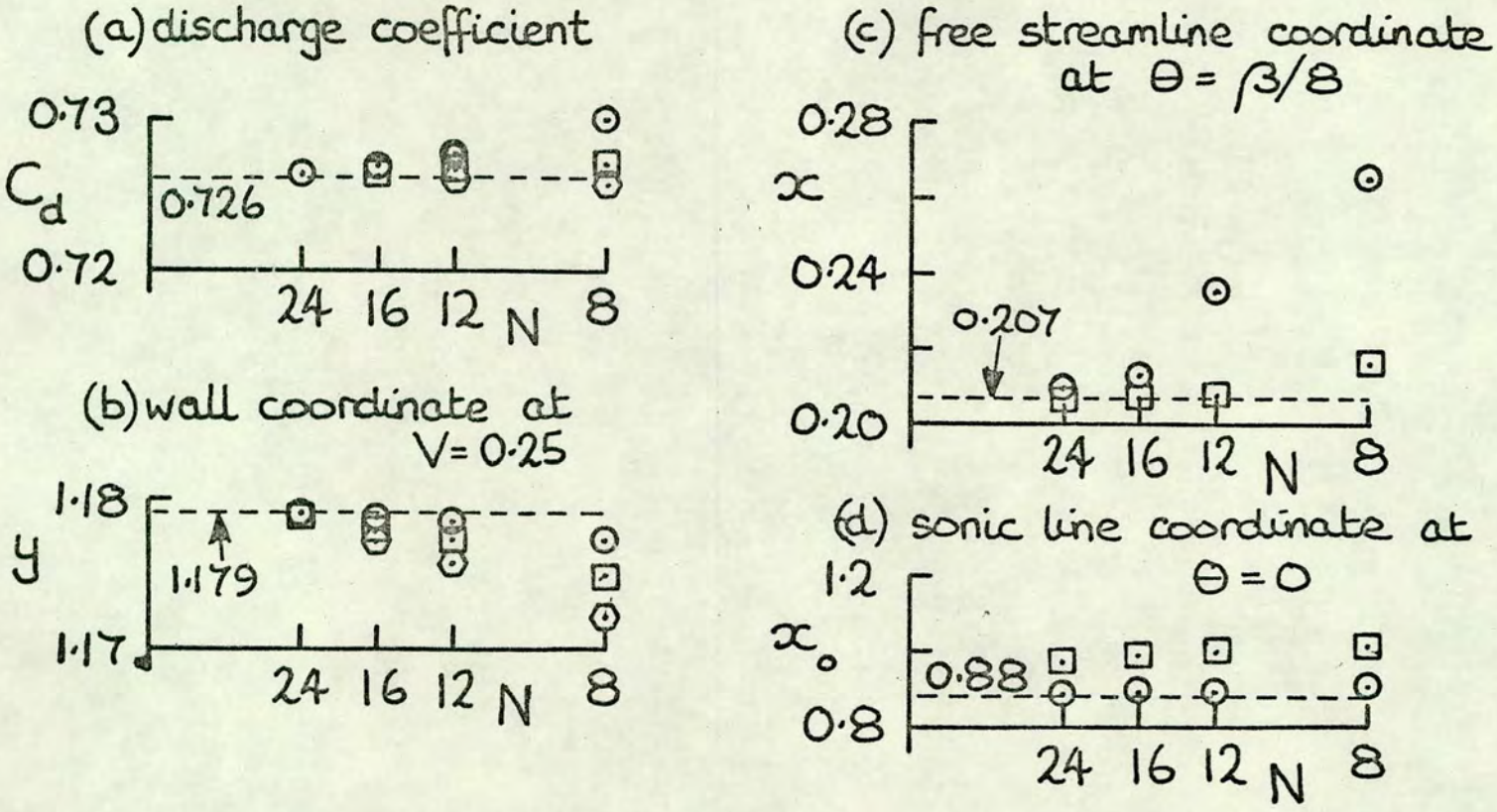

Fig. 3·8 Computed results : axially symmetric, critical flow.

($\beta = 90°$, $\gamma = 1.4$, $V_e = 0$) t = 1·0 – ⊙ 1·5 – ⊡ 2·0 – ⊙

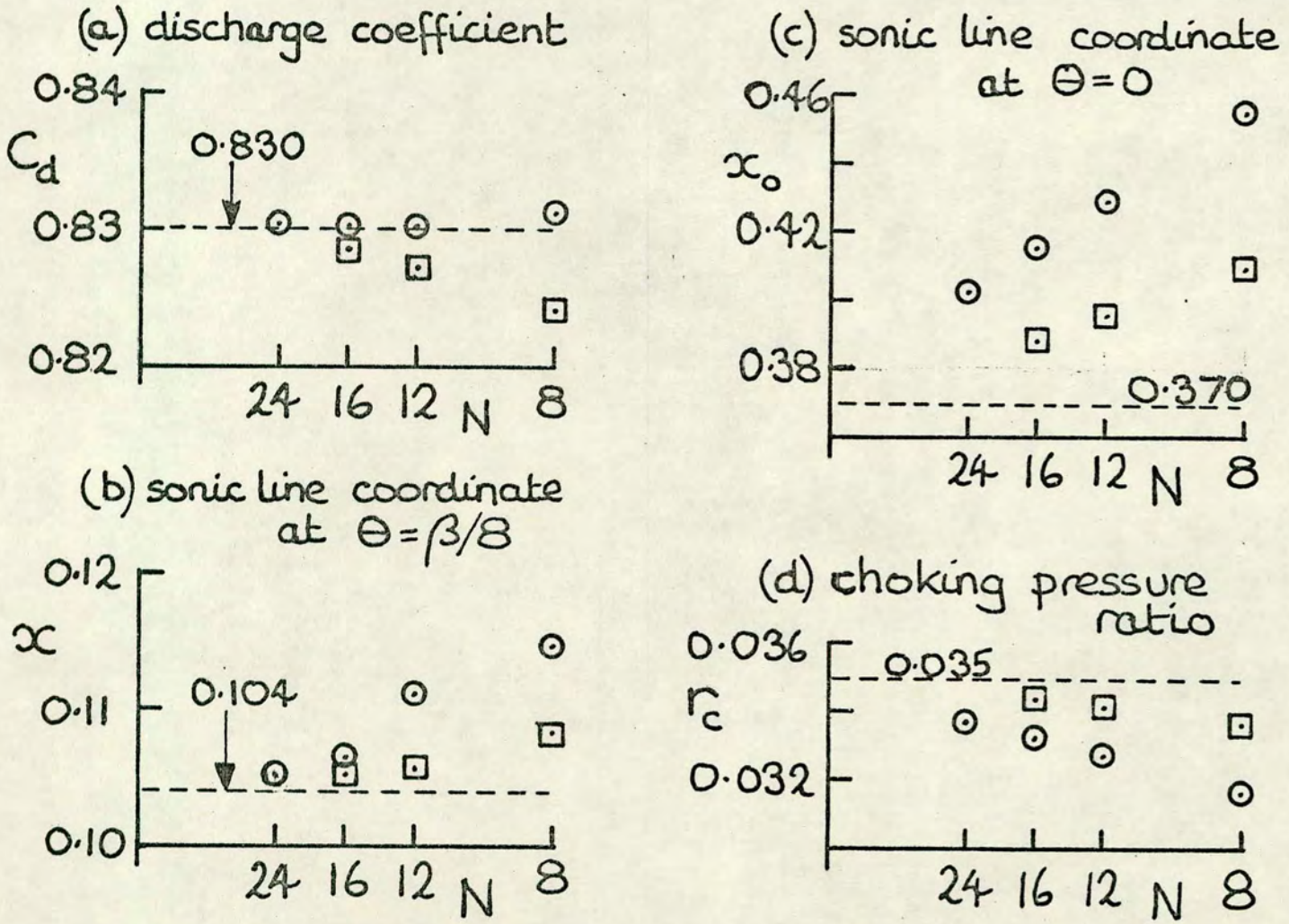

Fig. 3·9 Computed results: axially symmetric, choked flow.

($\beta = 90°$, $\gamma = 1.4$, $V_e = 0$) $t = 1.0$ – ⊙ 1.5 – ⊡

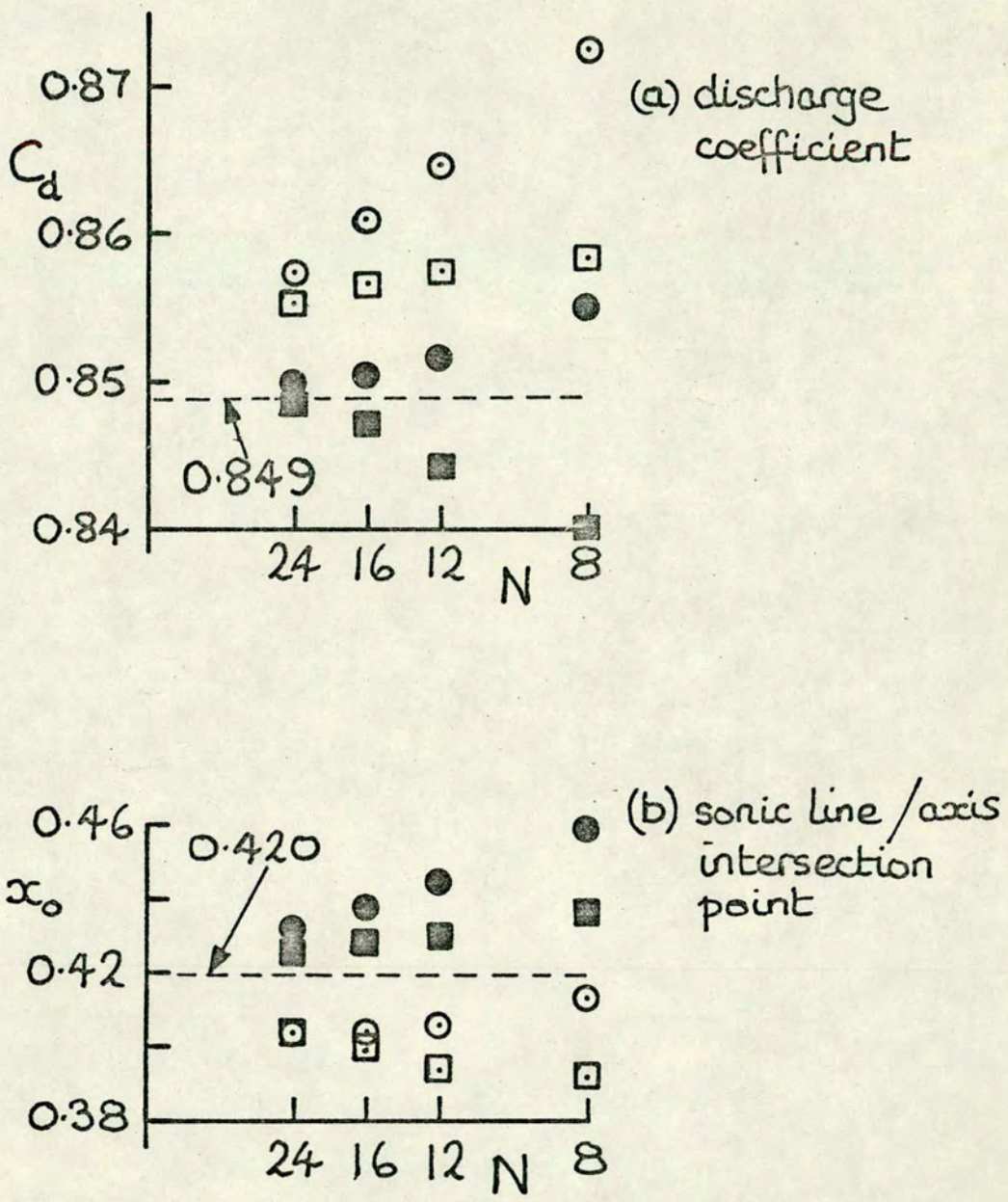

Fig. 3·10 Comparison of formulae used in characteristics calculations.

($\beta = 90°$, two-dimensional, choked)

t = 1·0 ⊙ } conventional formulae
1·5 ⊡ } (equations 3·23)

t = 1·0 ● } special formulae
1·5 ■ } (equations 3·25)

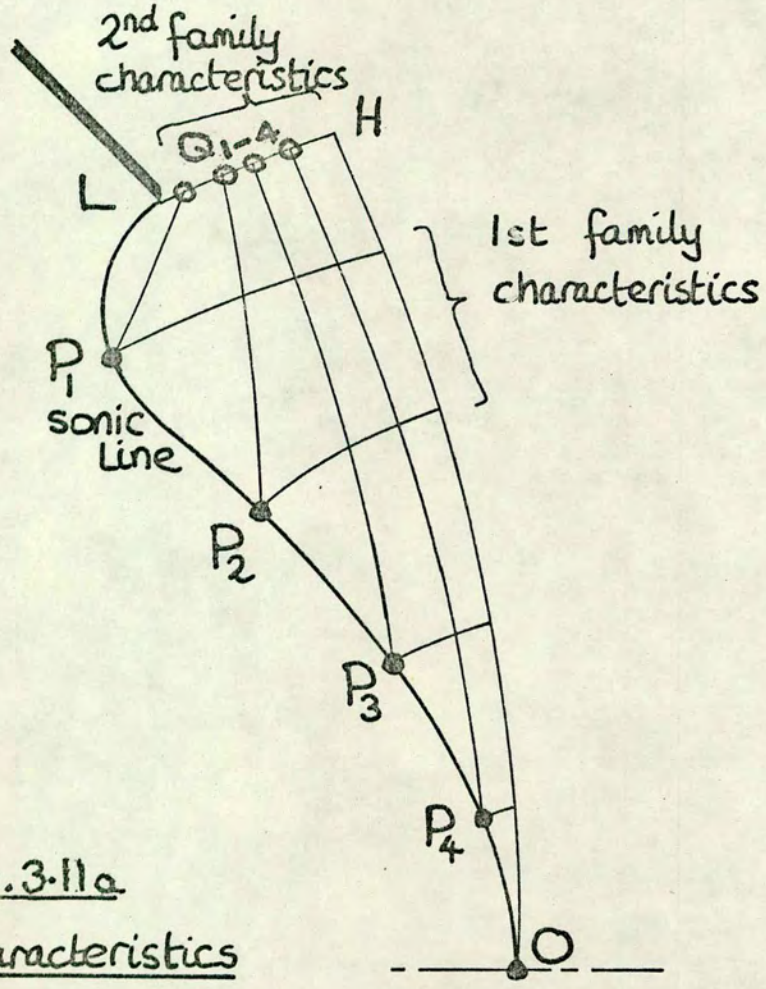

Fig. 3·11a

Characteristics network for arbitrary $\nu_s(\theta)$

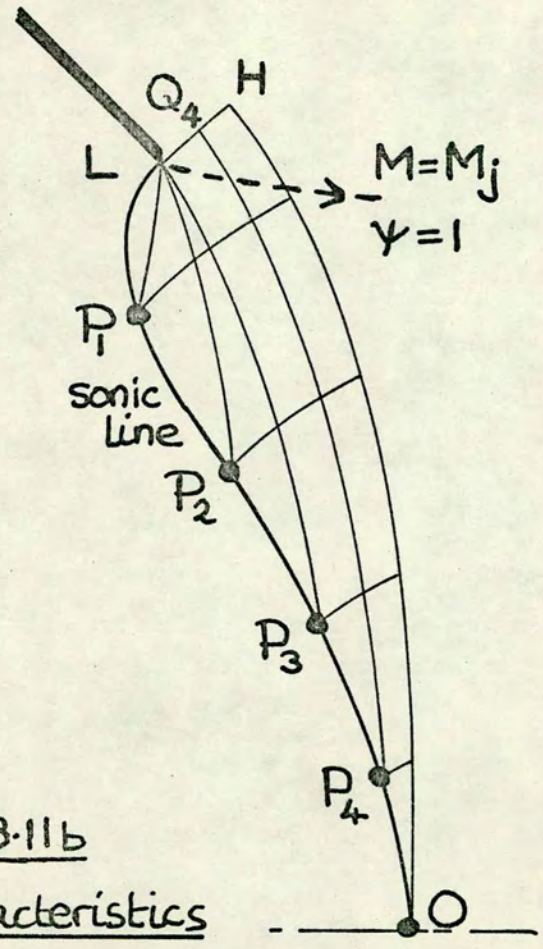

Fig. 3·11b

Characteristics network for correct $\nu_s(\theta)$

Fig. 4·1a Two-dimensional choked flowfield - $\beta = 90°$, $\gamma = 1.4$.
streamlines and lines of constant velocity.

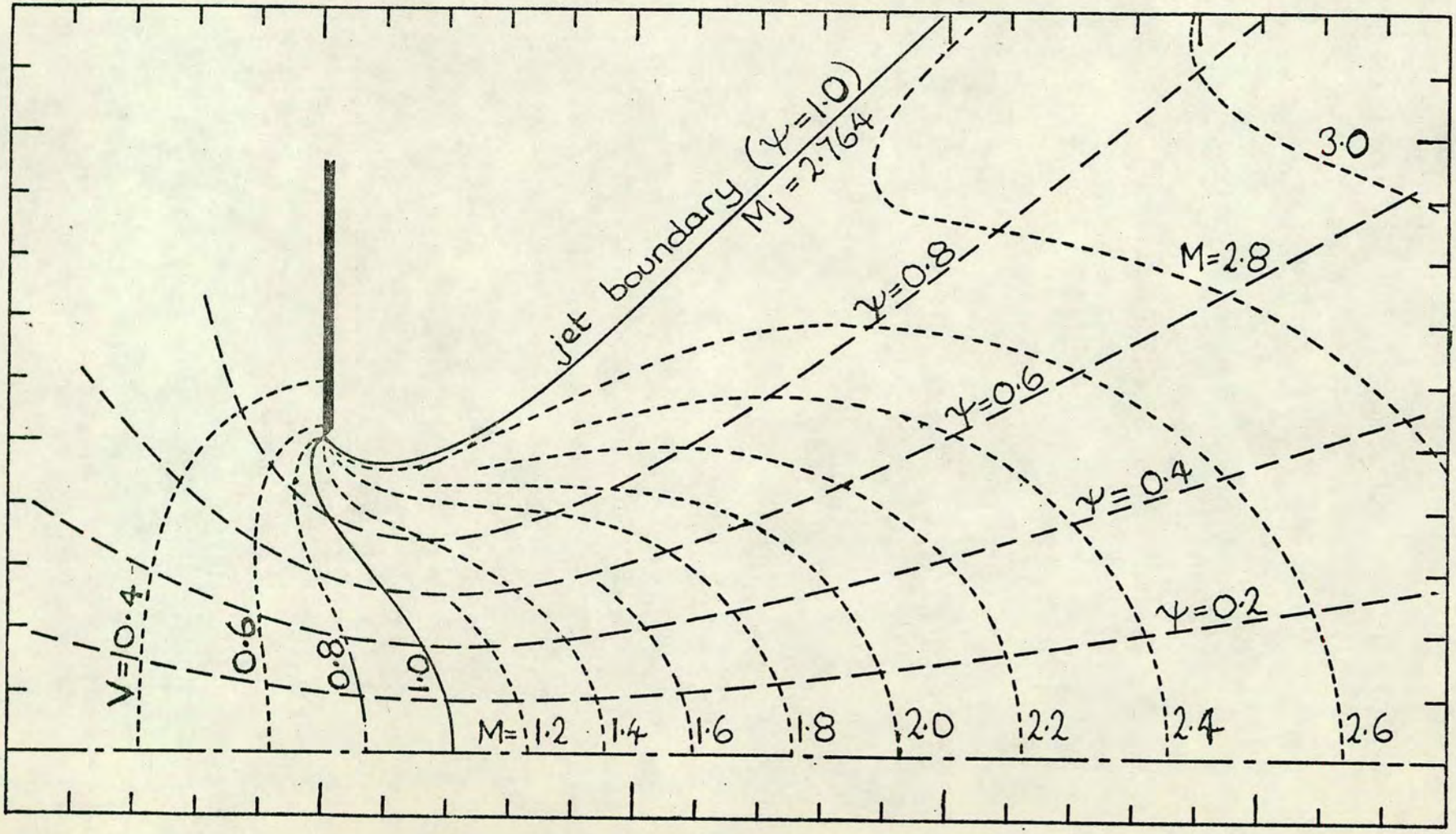

Fig. 4.16 Axially symmetric choked flowfield - $\beta = 90°$, $\gamma = 1.4$
streamlines and lines of constant velocity

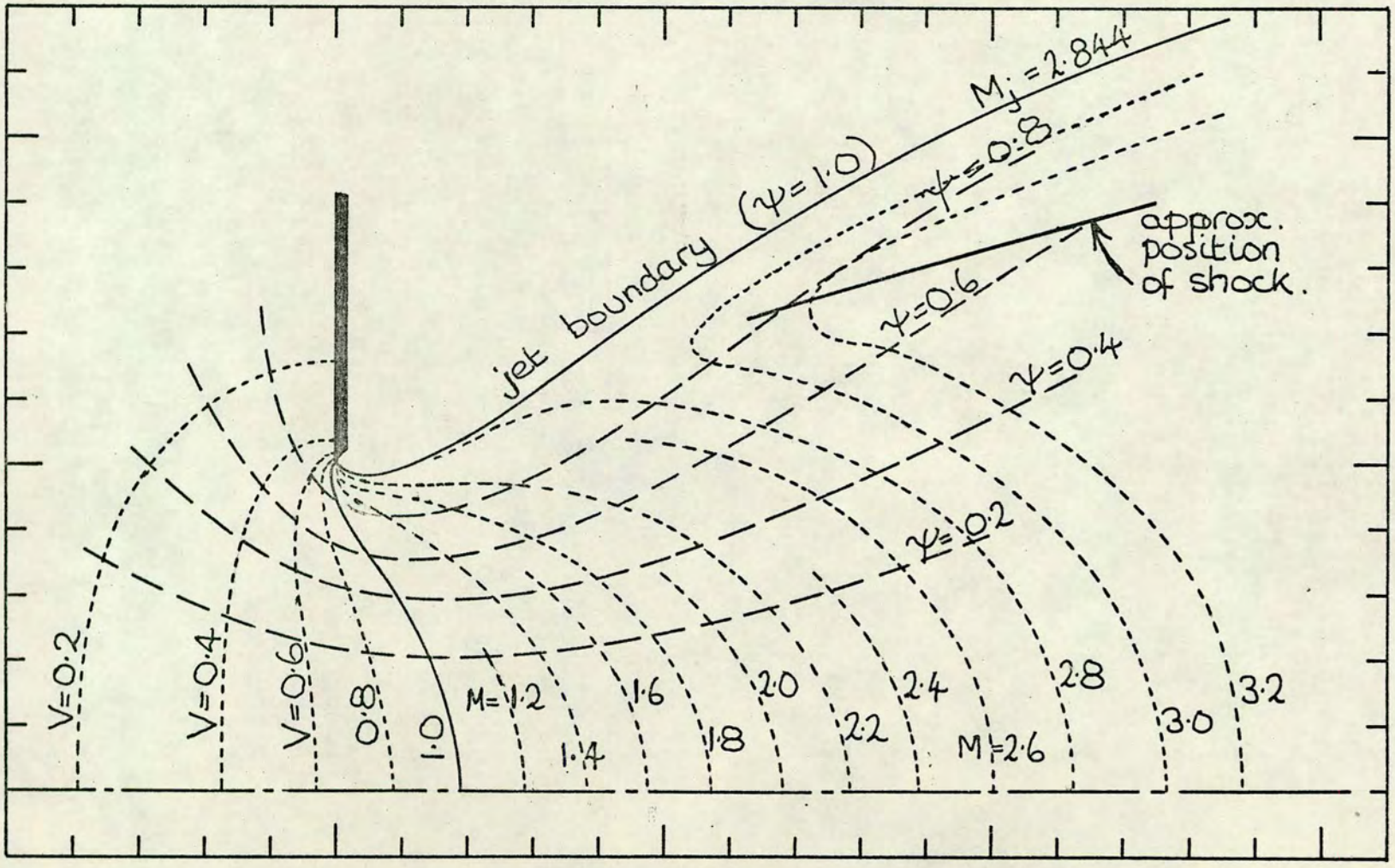

(a) two-dimensional

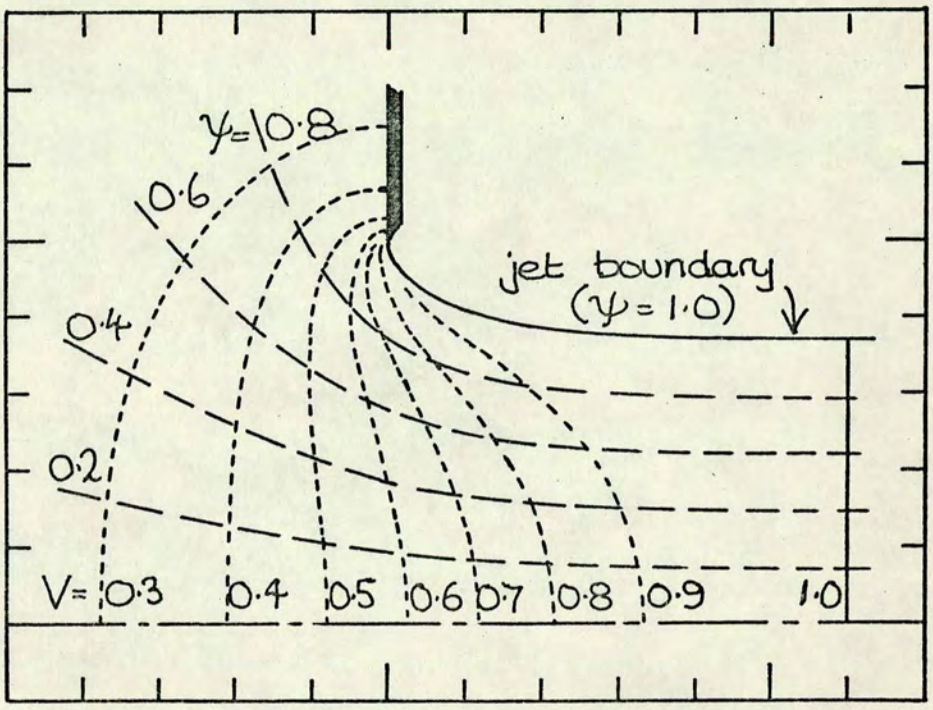

(b) axially symmetric

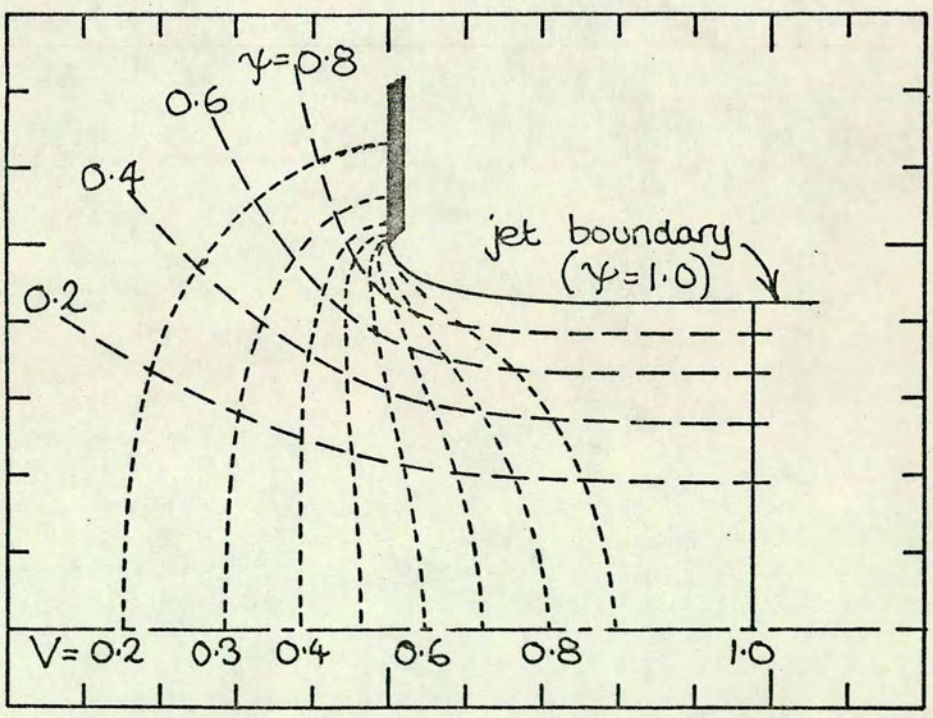

Fig. 4-2 Critical flowfields; $\beta = 90°$, $\gamma = 1.4$

(a) Two-dimensional

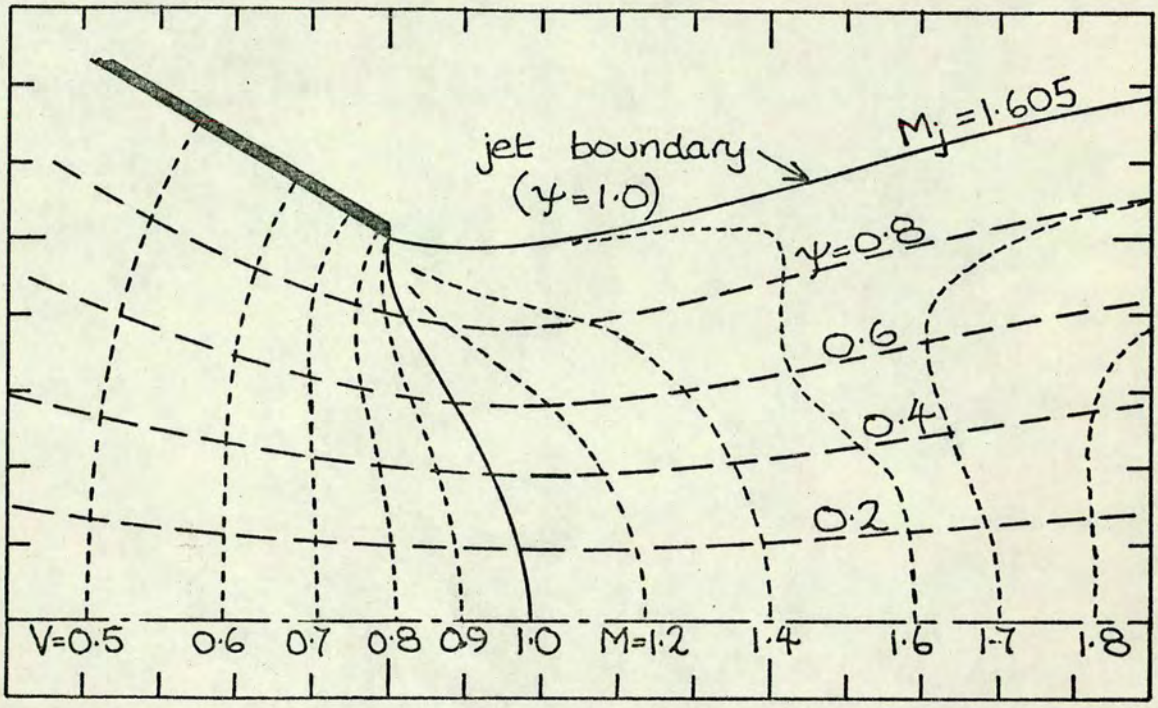

(b) axially symmetric

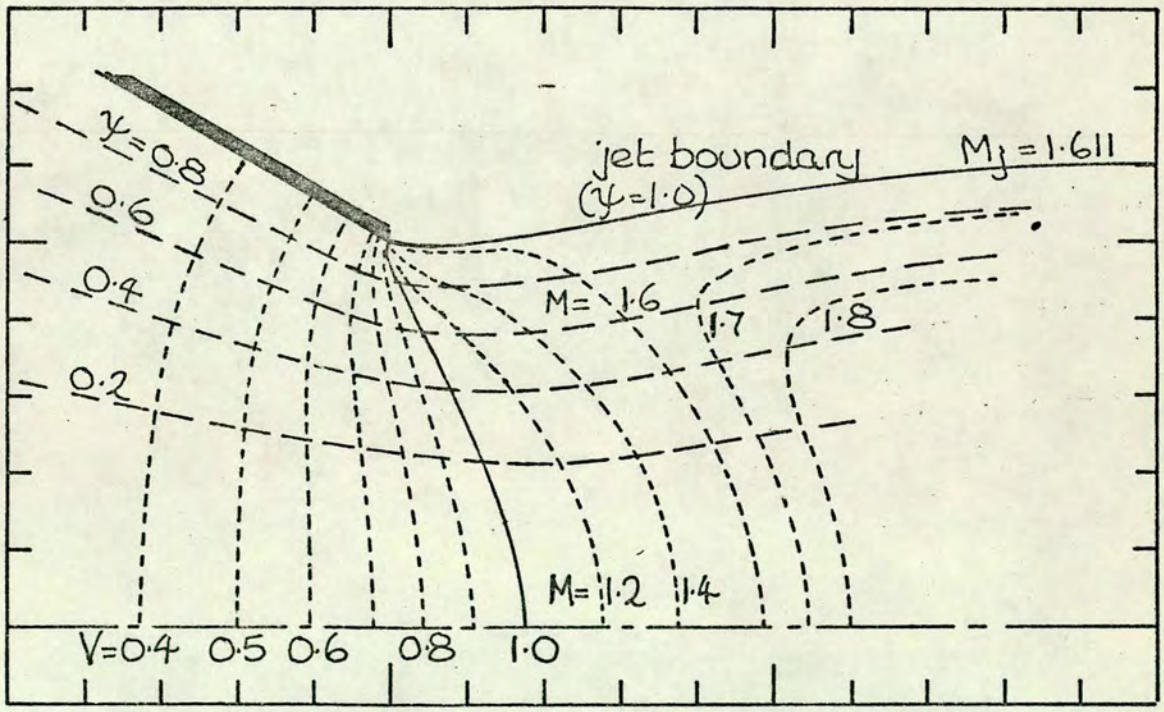

Fig. 4.3 Choked flowfields ; $\beta = 30°$, $\gamma = 1.4$.

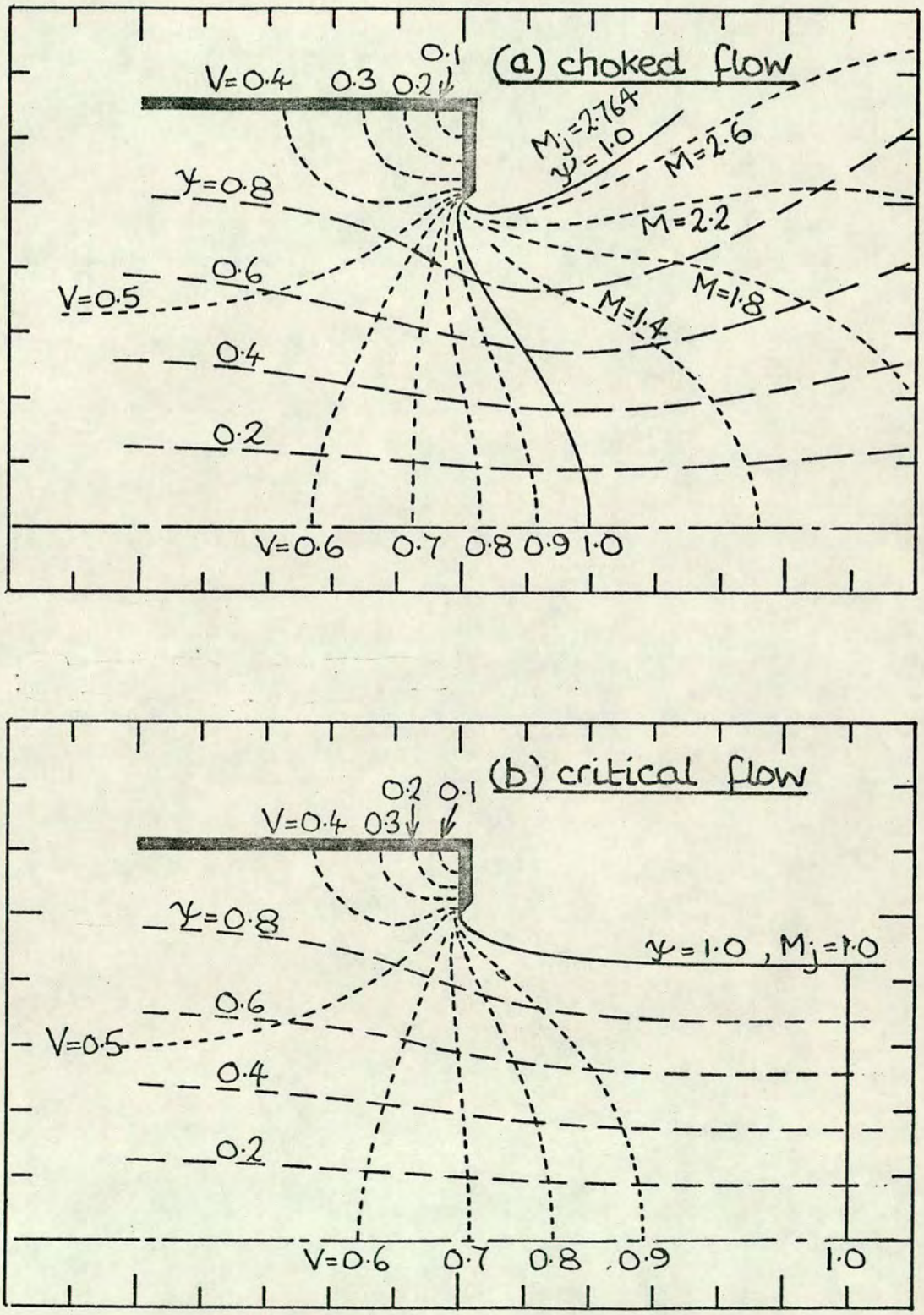

Fig. 4.4 Two-dimensional flowfields for V_e=0.5.

β=90°, γ=1.4

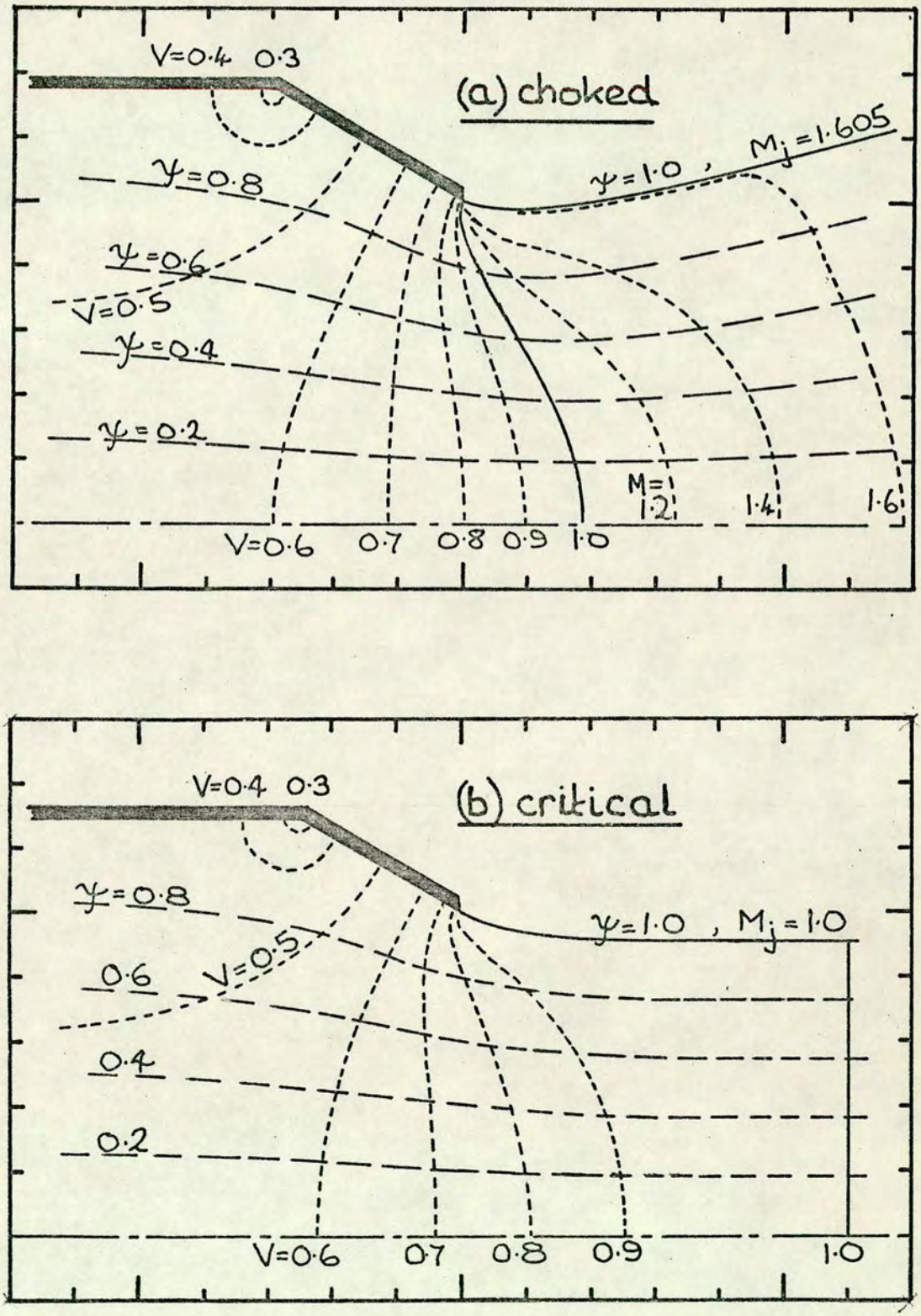

Fig. 4·5 Two-dimensional flowfields for V_e=0·5 β= 30°, γ= 1·4

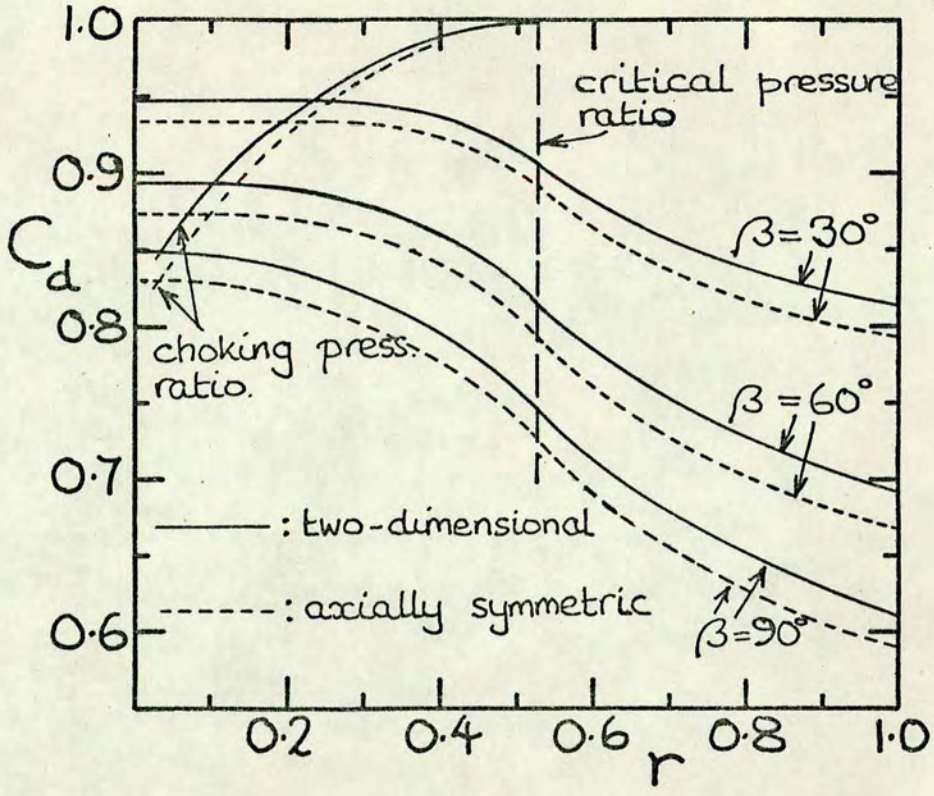

Fig. 4·6 Discharge coefficient as function of pressure ratio ($\gamma = 1.4$, $V_e = 0$)

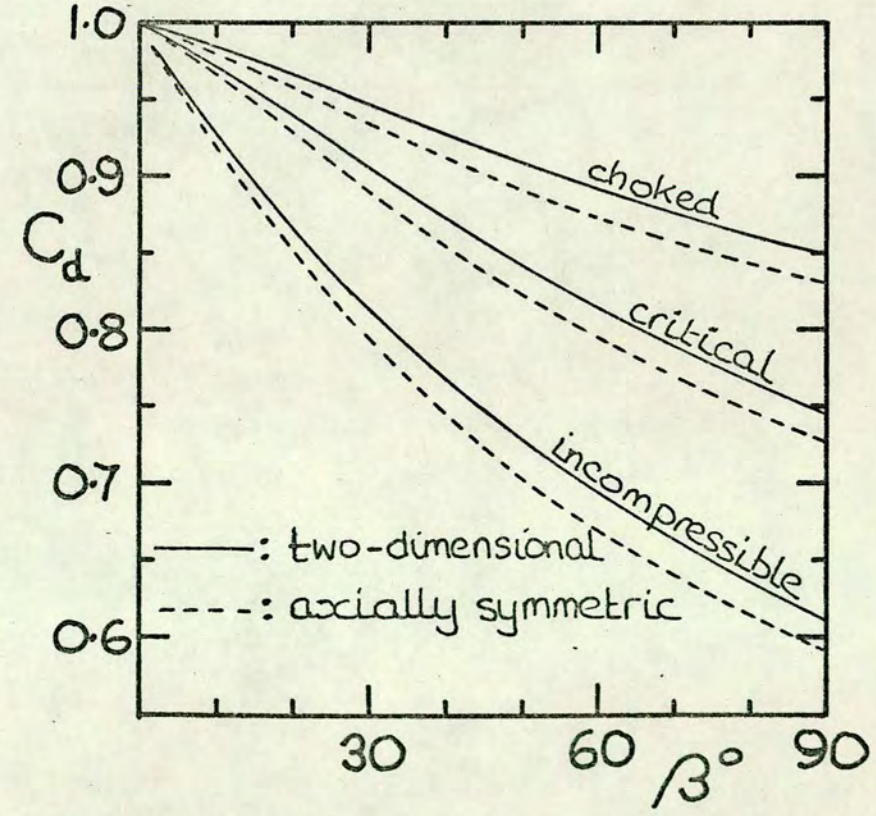

Fig. 4·7 Discharge coefficient as function of wall angle ($\gamma = 1.4$, $V_e = 0$)

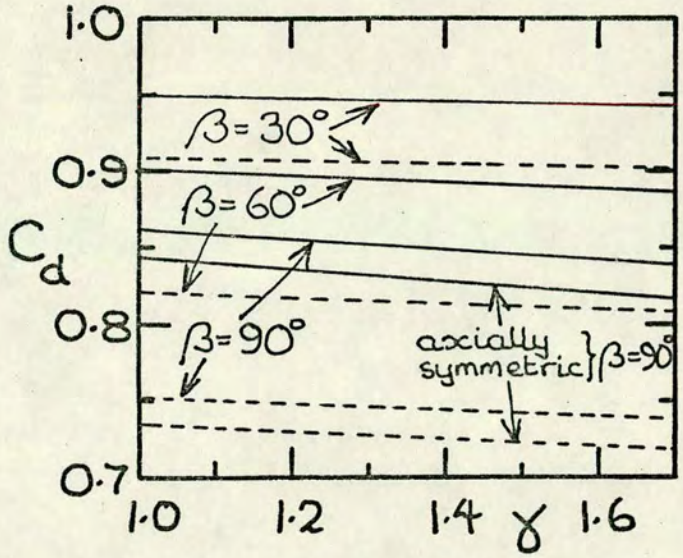

Fig. 4·8 Discharge coefficient as function of γ ($V_e = 0$)

[——: choked ------: critical]

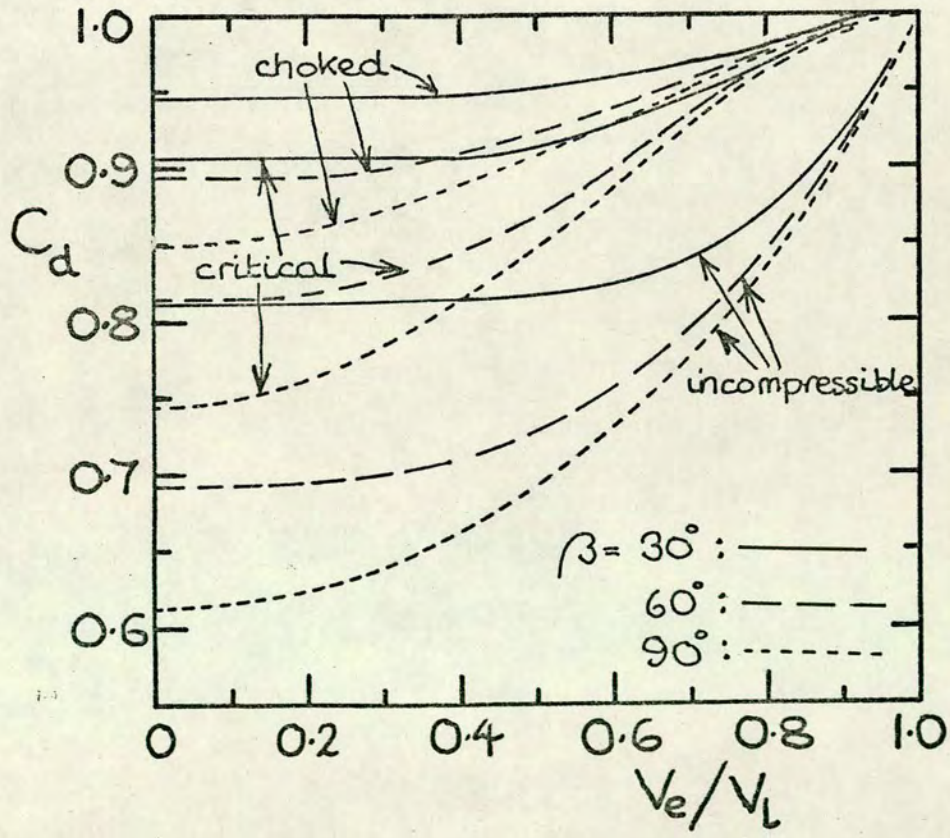

Fig. 4·9 Discharge coefficient as function of approach velocity (2-D, $\gamma = 1.4$)

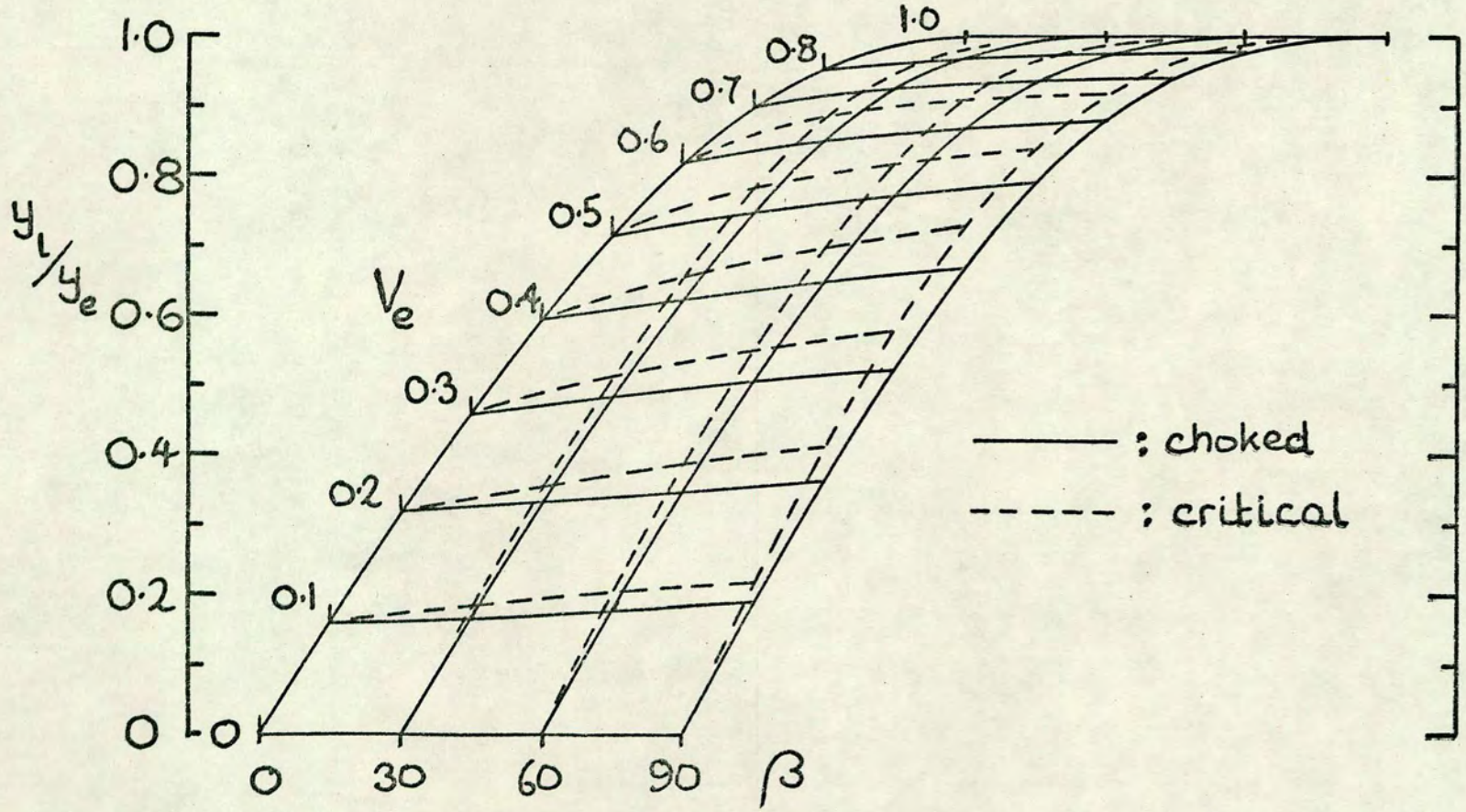

Fig. 4·10 Relationship between area contraction ratio and approach velocity (two-dimensional, $\gamma = 1.4$)

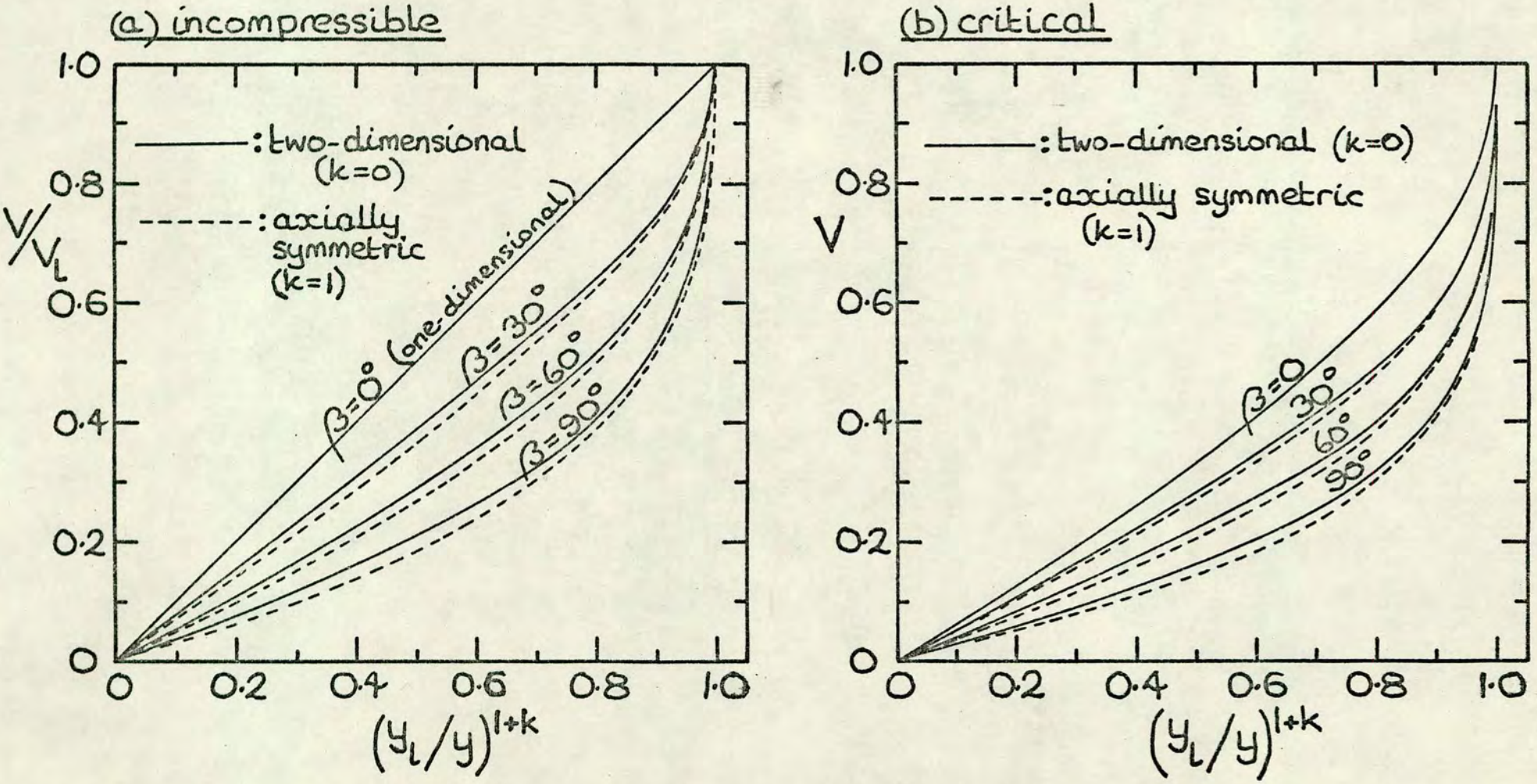

Fig. 4·11 Velocity distribution on nozzle wall ($\gamma = 1.4$, $V_e = 0$)

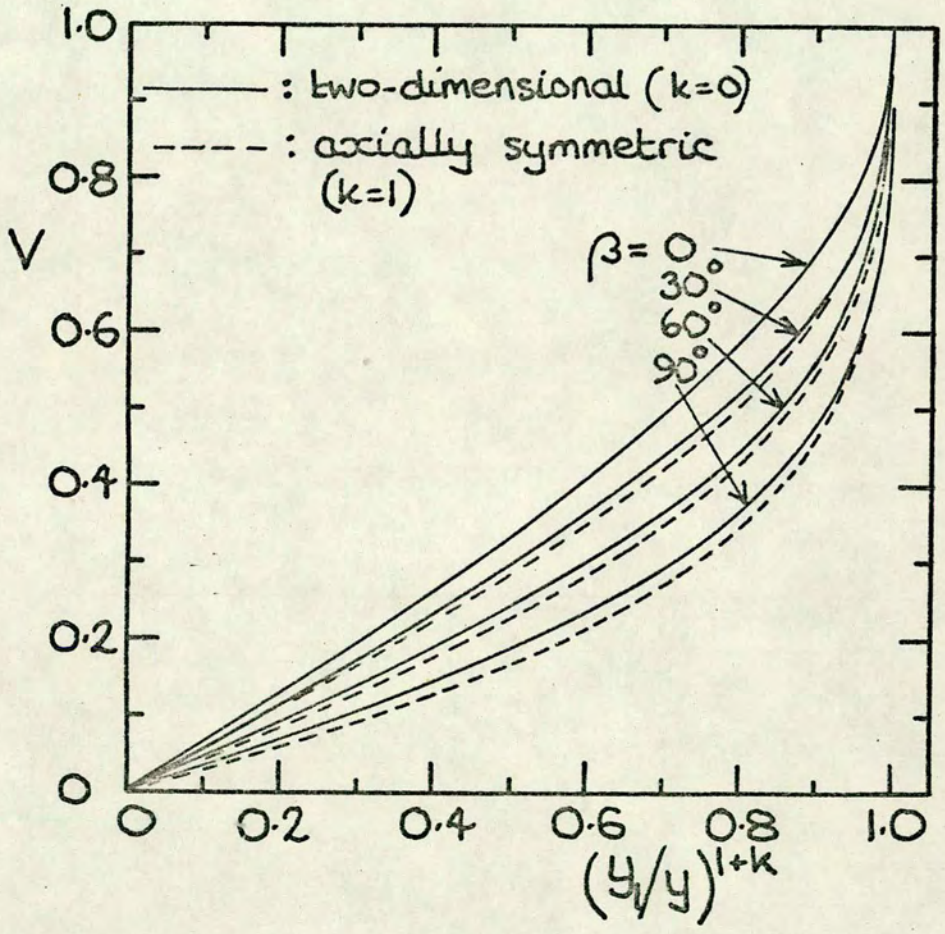

Fig. 4-11 (cont.) (c) choked

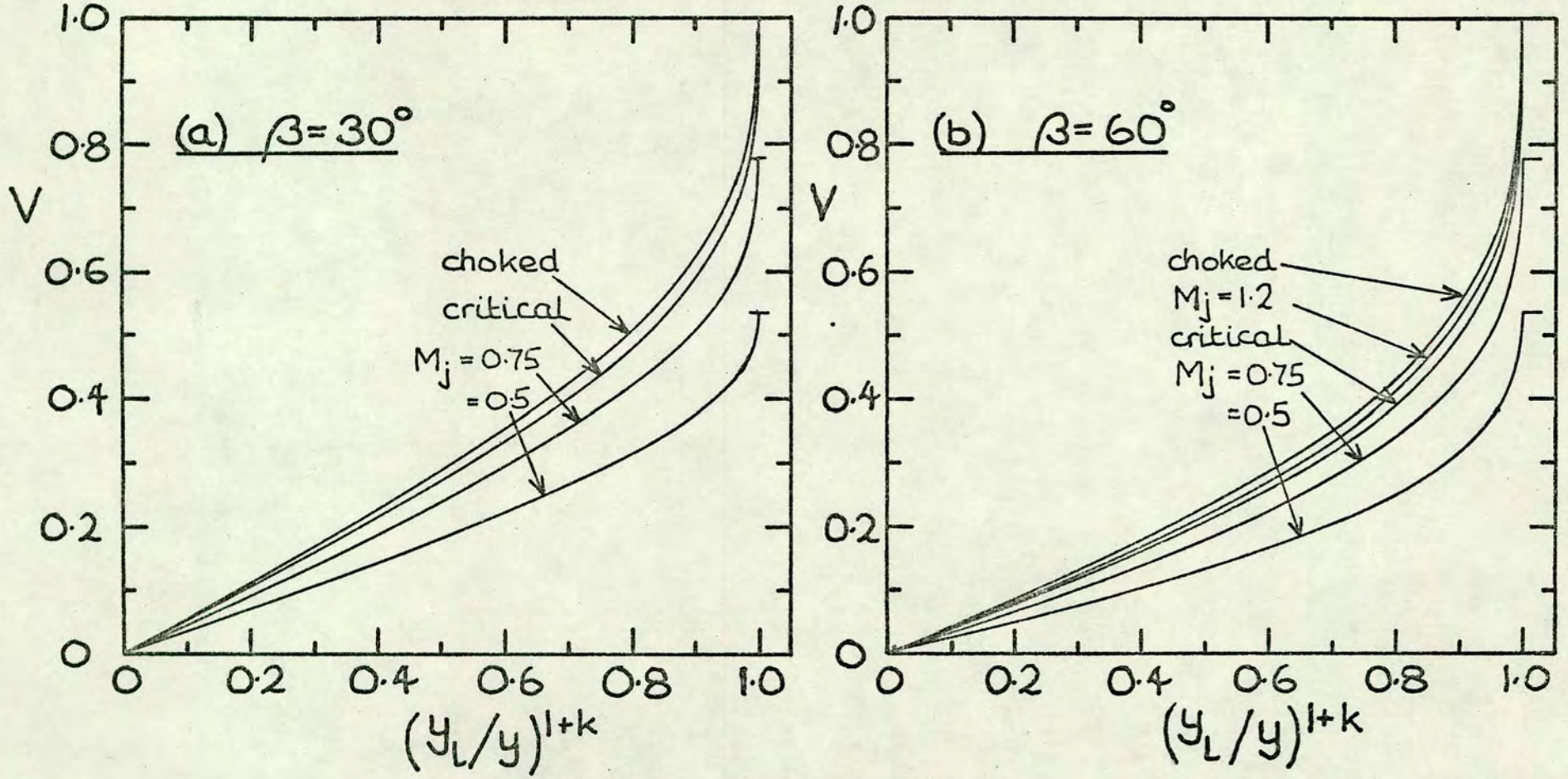

Fig. 4·12 Wall velocity distribution - effect of pressure ratio
(axially symmetric ; $V_e = 0$; $\gamma = 1.4$)

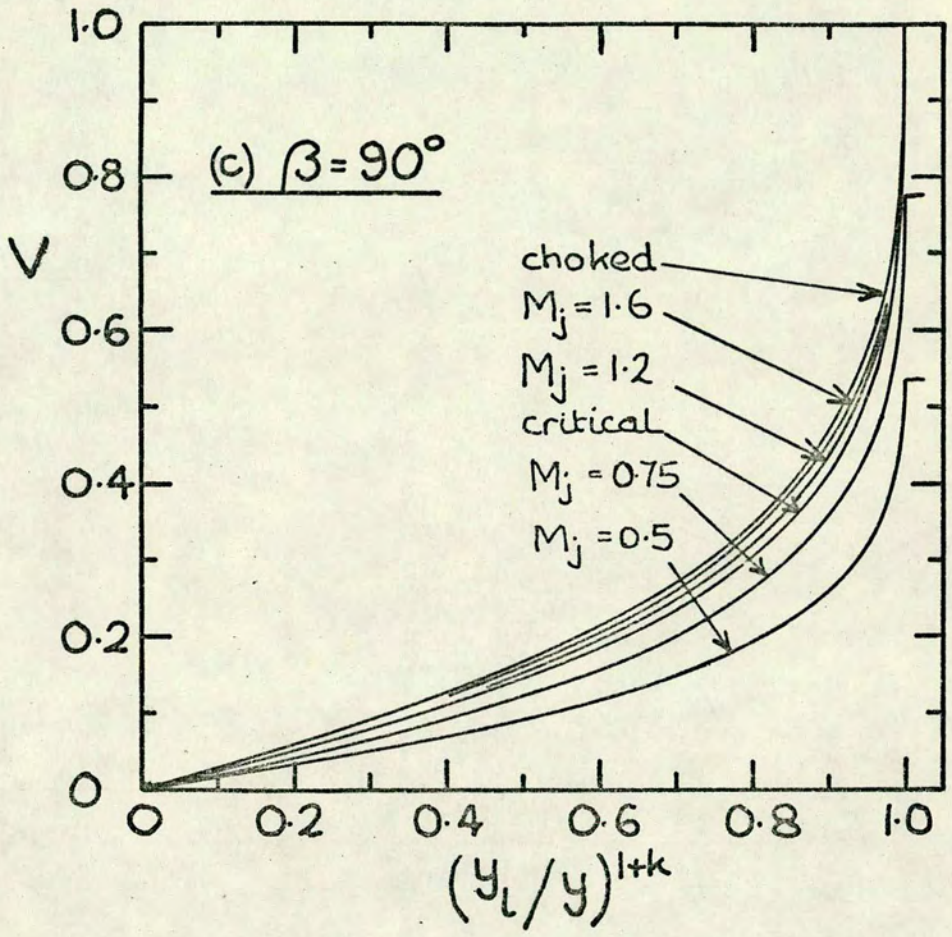
(c) β = 90°
V
choked
$M_j = 1.6$
$M_j = 1.2$
critical
$M_j = 0.75$
$M_j = 0.5$
1.0
0.8
0.6
0.4
0.2
0
0
0.2
0.4
0.6
0.8
1.0
$(y_l/y)^{1+k}$

Fig. 4·12 (cont.)

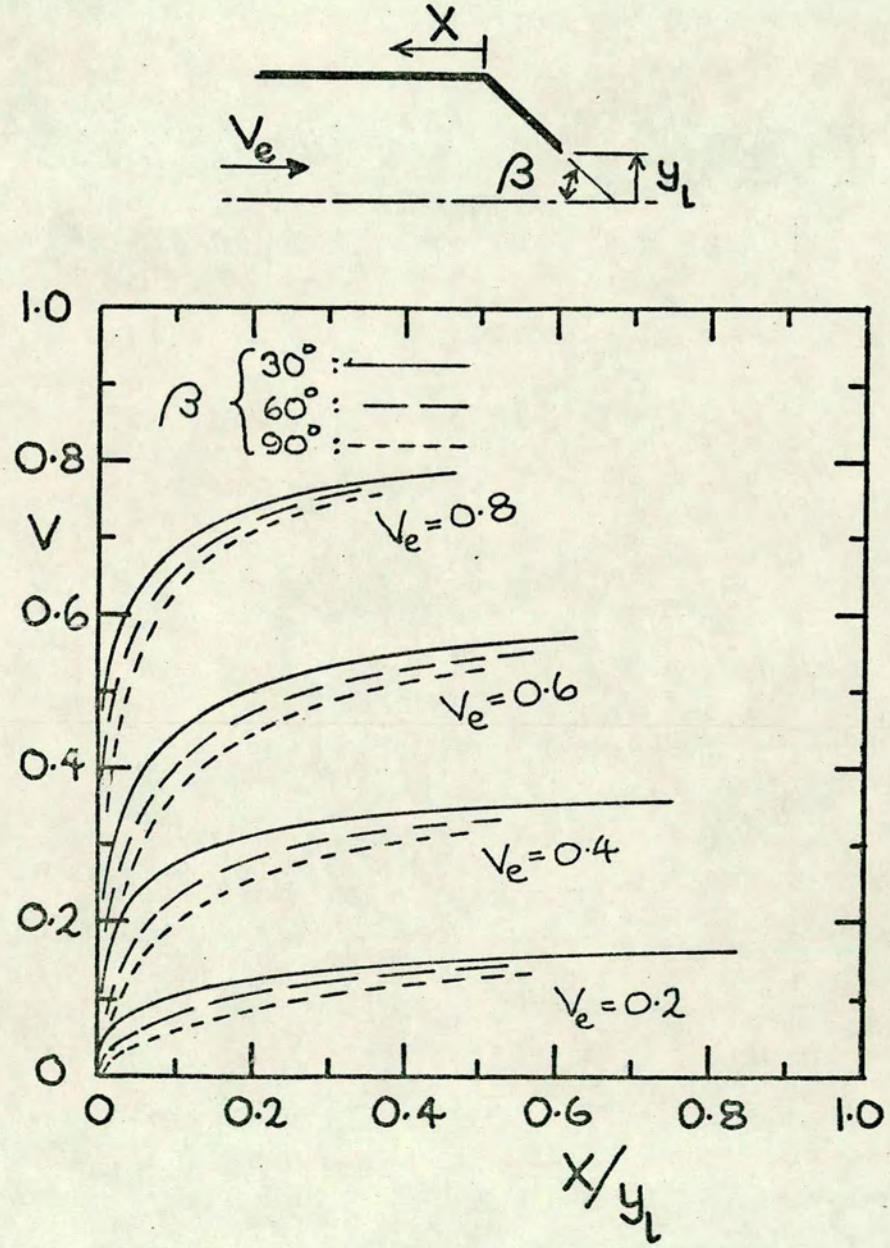

Fig. 4.13 Velocity along surface of approach duct – two-dimensional, choked, γ=1·4.

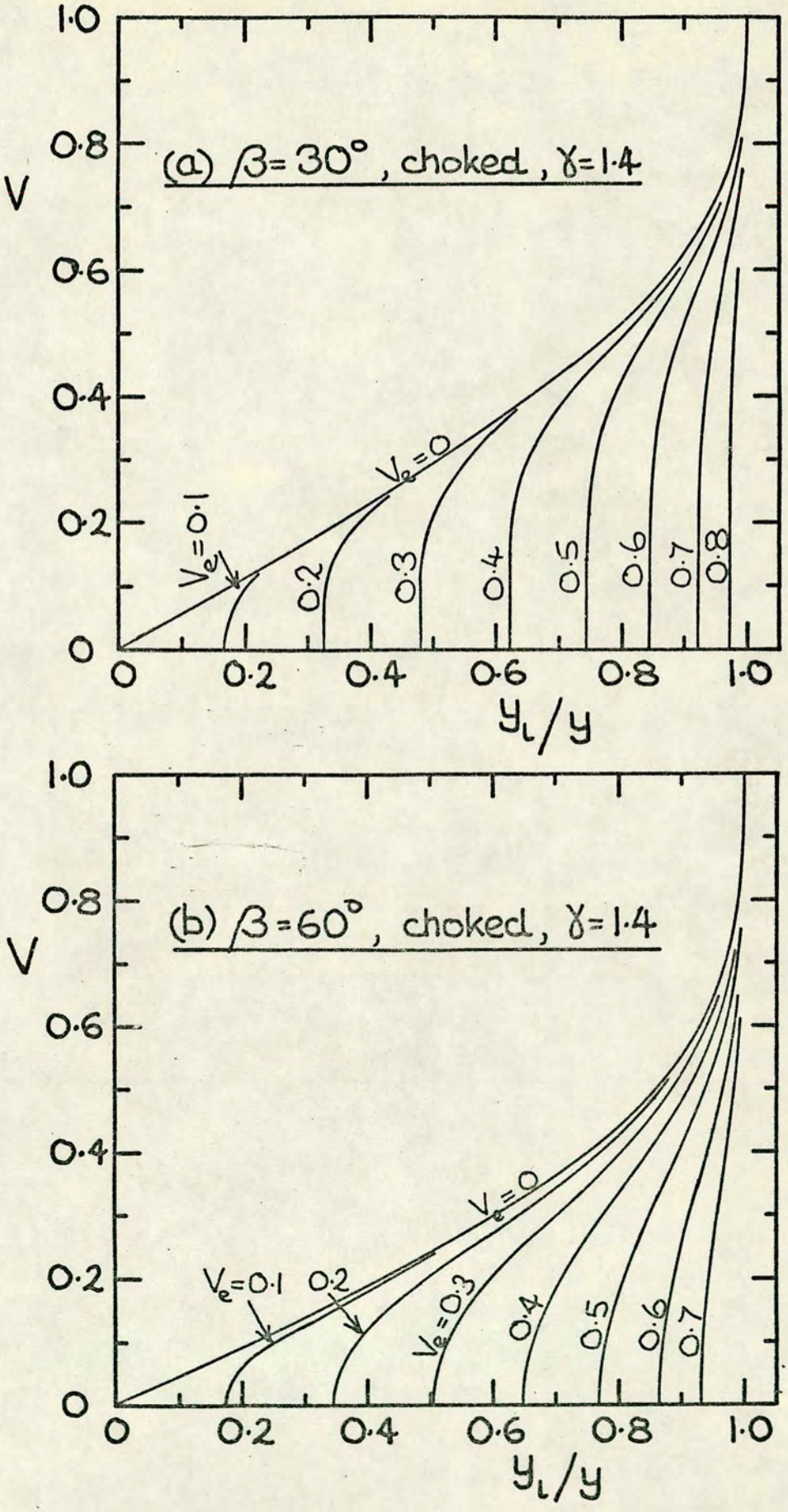

Fig. 4·14 Two-dimensional wall velocity as function of approach velocity

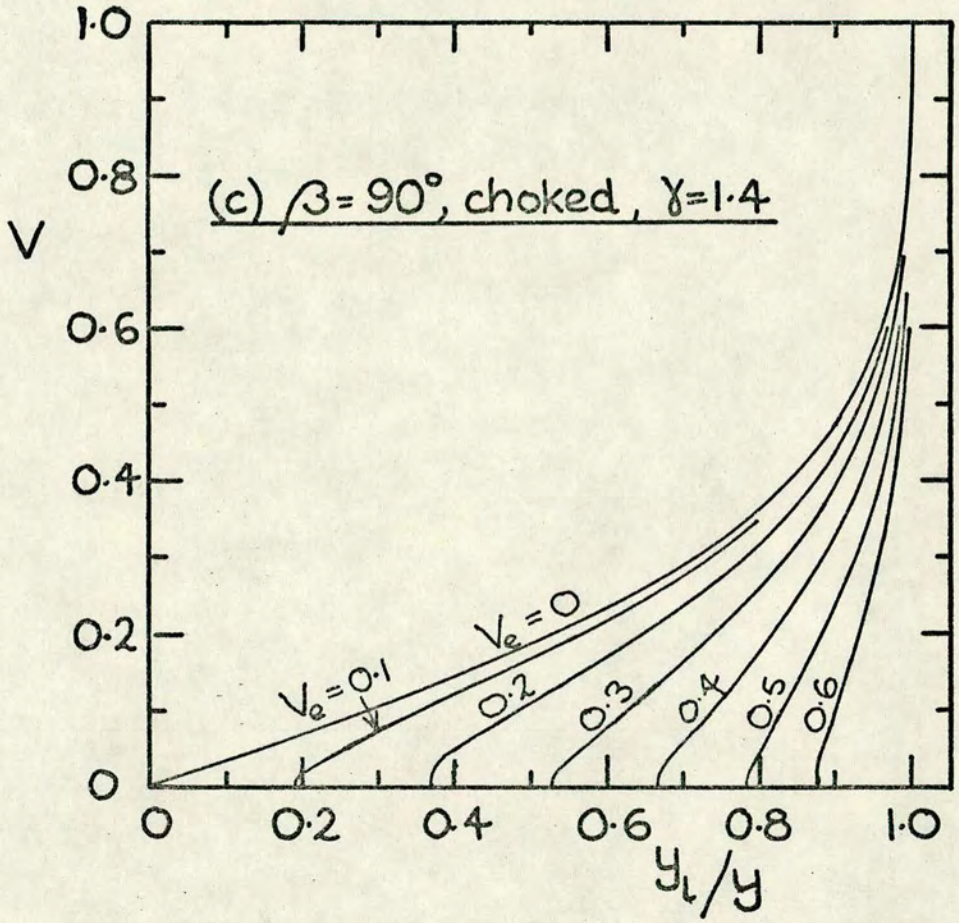
(c) β = 90°, choked, γ = 1·4
V
1·0
0·8
0·6
0·4
0·2
0
0
0·2
0·4
0·6
0·8
1·0
y_t/y
$V_e = 0$
$V_e = 0·1$
0·2
0·3
0·4
0·5
0·6

Fig. 4·14 (cont.)

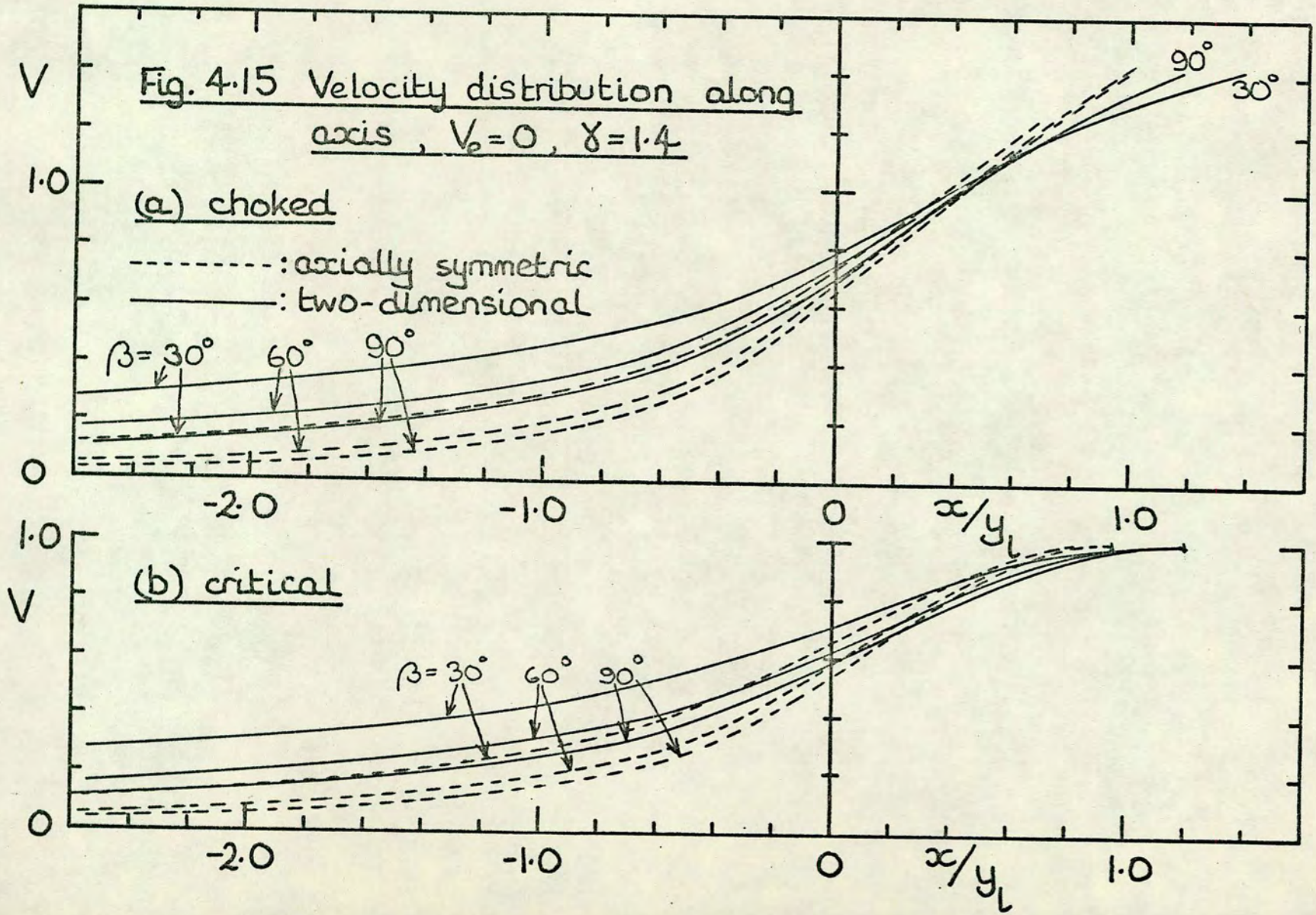
Fig. 4·15 Velocity distribution along axis, $V_e = 0$, $\gamma = 1.4$
(a) choked
--------: axially symmetric
————: two-dimensional
β = 30° 60° 90°
90°
30°
V
1·0
0
-2·0
-1·0
0
x/y_l
1·0
(b) critical
β = 30° 60° 90°
V
1·0
0
-2·0
-1·0
0
x/y_l
1·0

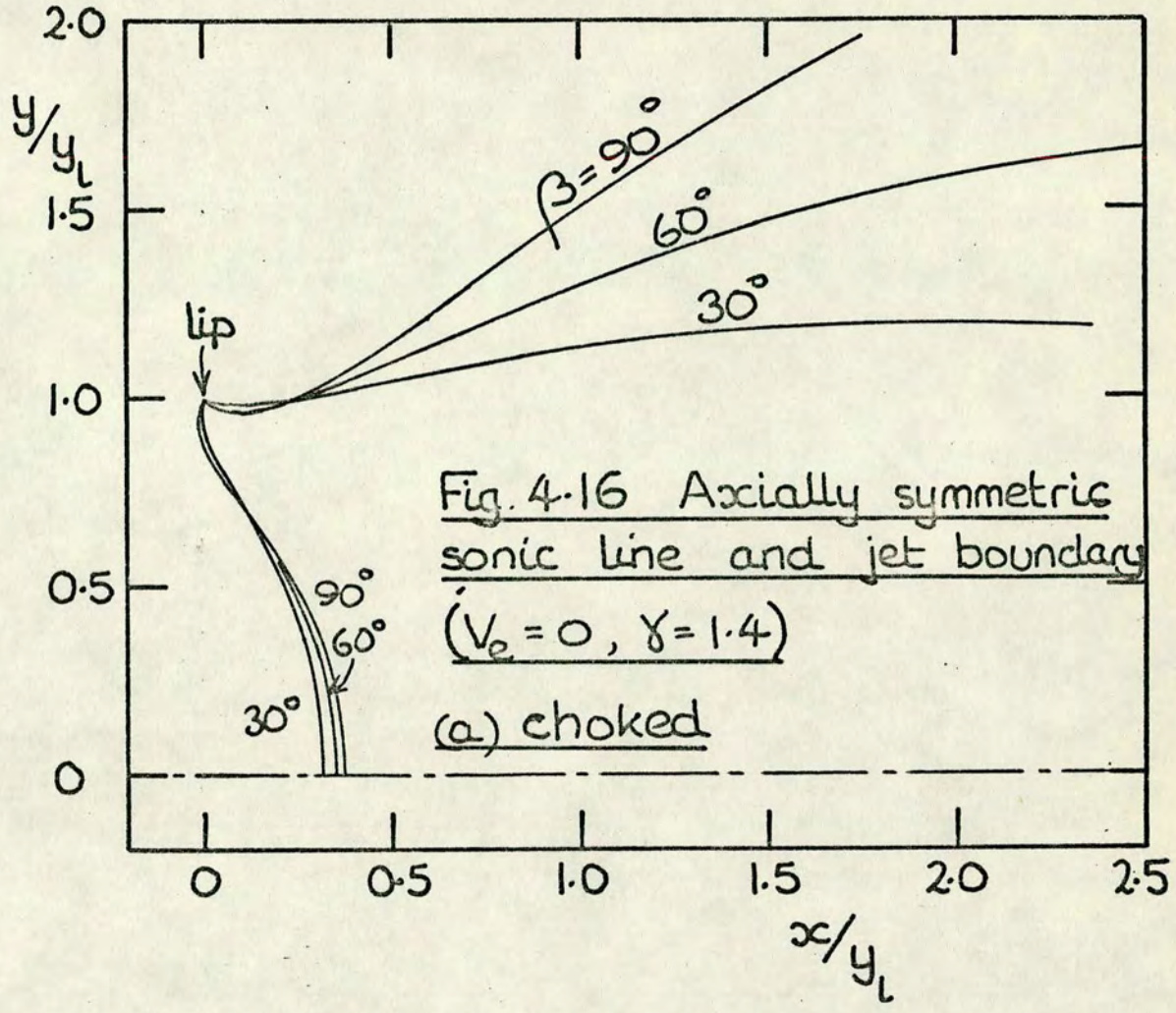

Fig. 4·16 Axially symmetric sonic line and jet boundary ($V_e = 0$, $\gamma = 1.4$)

(a) choked

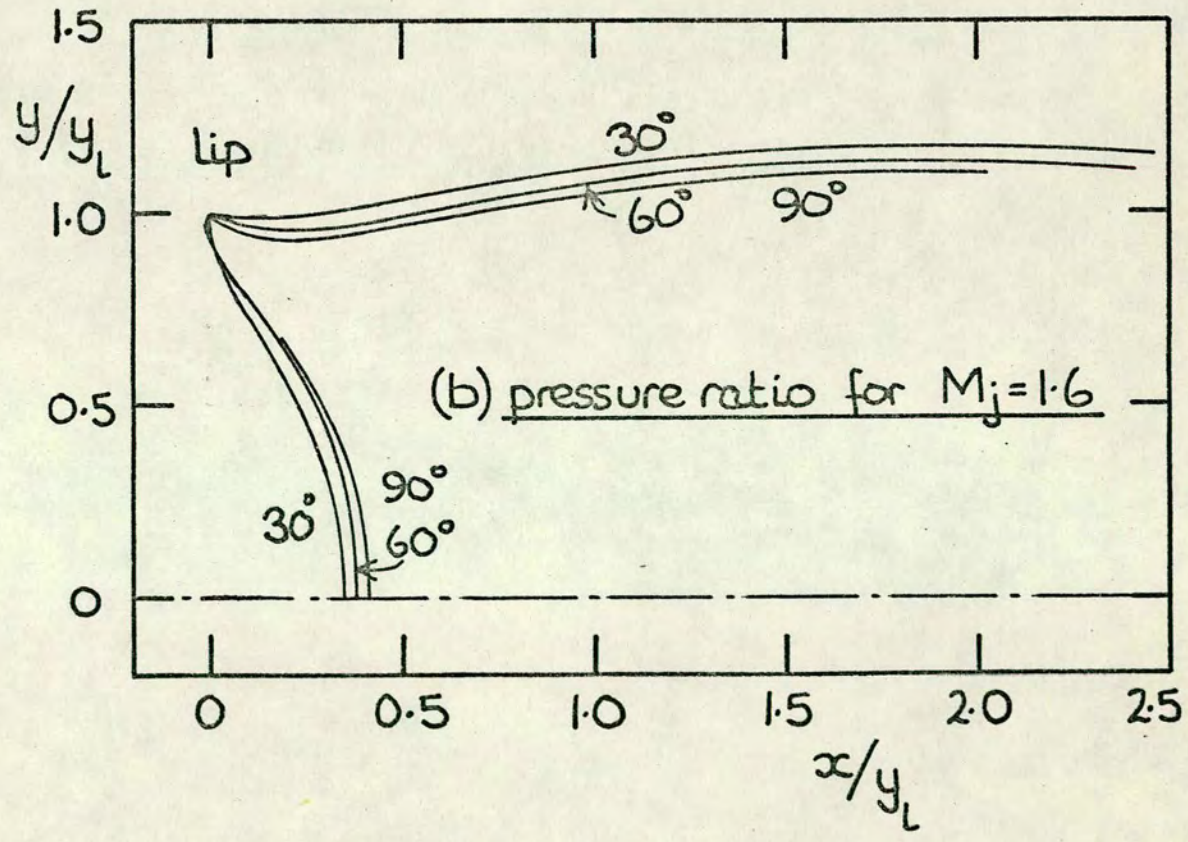

(b) pressure ratio for $M_j = 1.6$

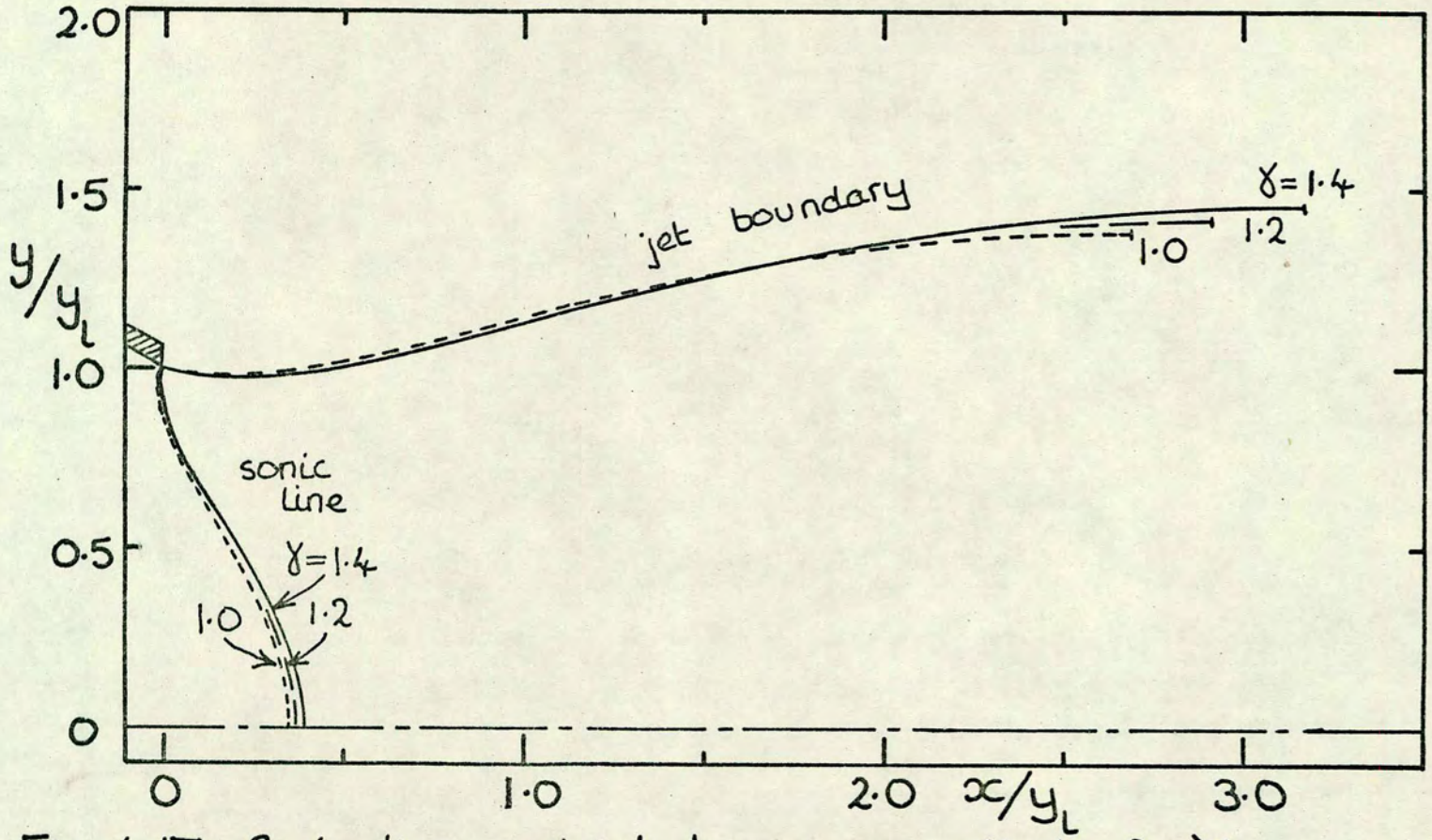

Fig. 4·17 Sonic line and jet boundary - effect of γ

(two-dimensional, choked, $\beta = 30°$, $V_e = 0$)

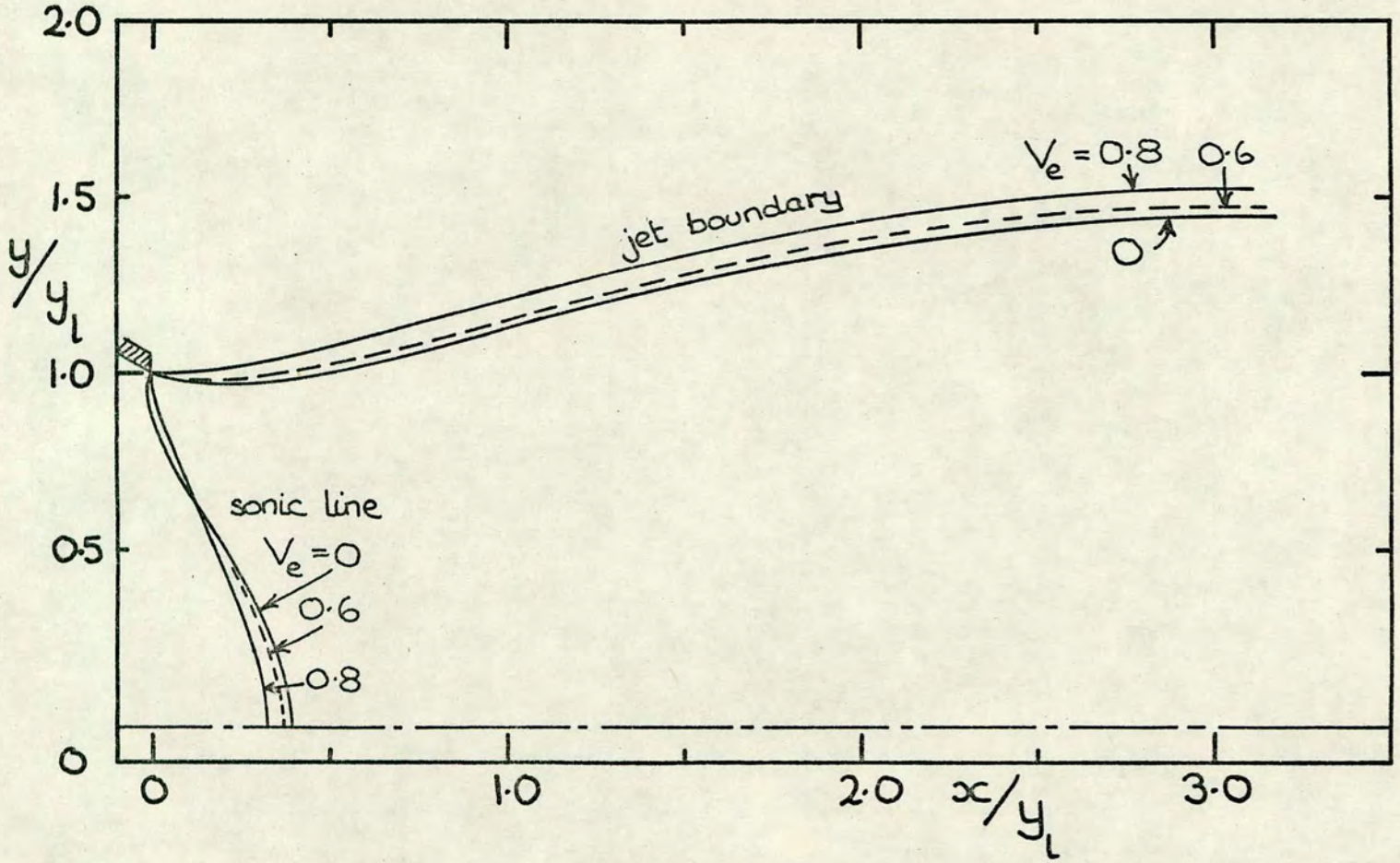

Fig. 4·18 Sonic line and jet boundary - effect of approach velocity.
(two-dimensional, choked, $\beta = 30°$, $\gamma = 1·4$)

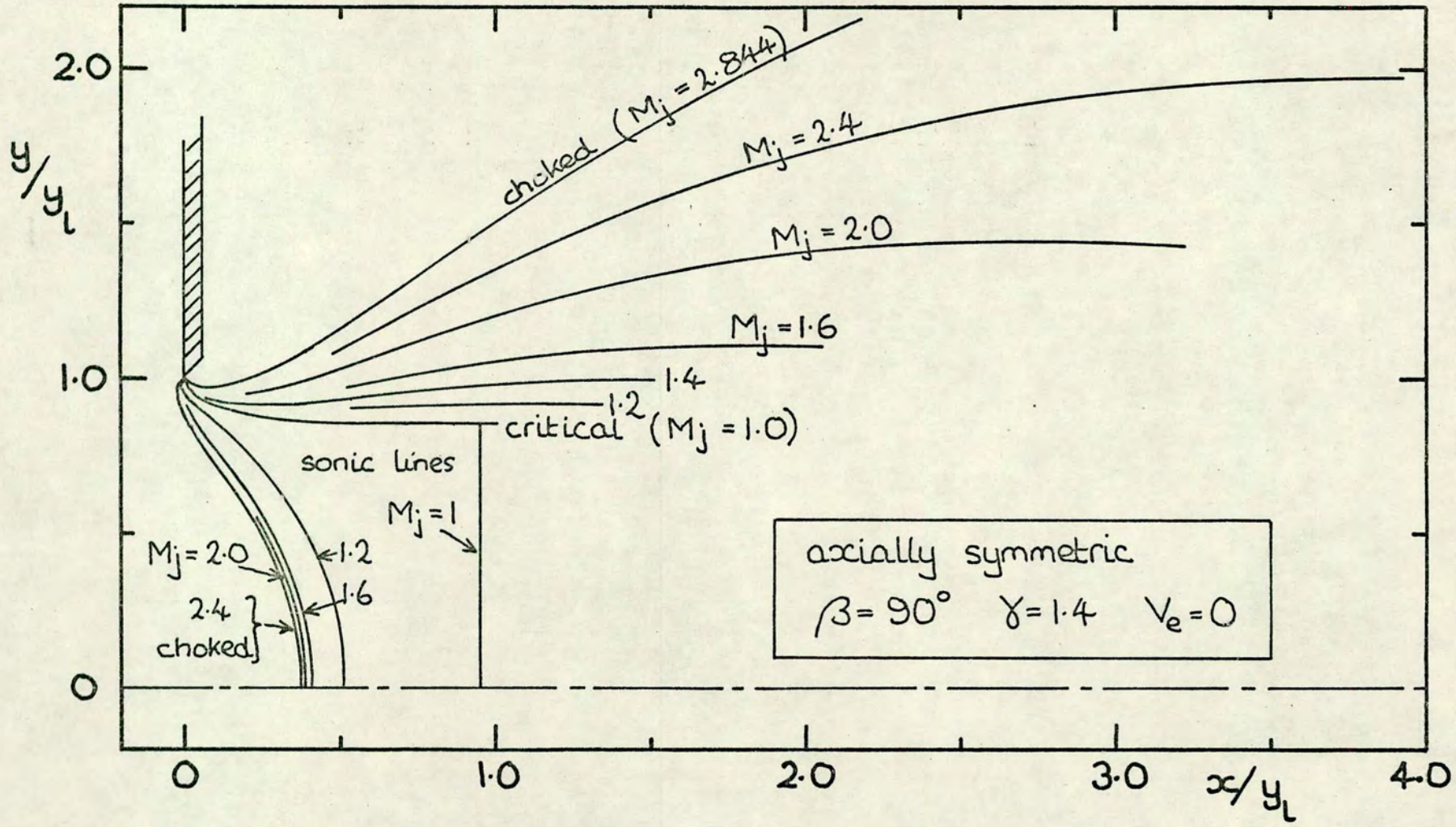

Fig. 4·19 Sonic line and jet boundary – effect of pressure ratio

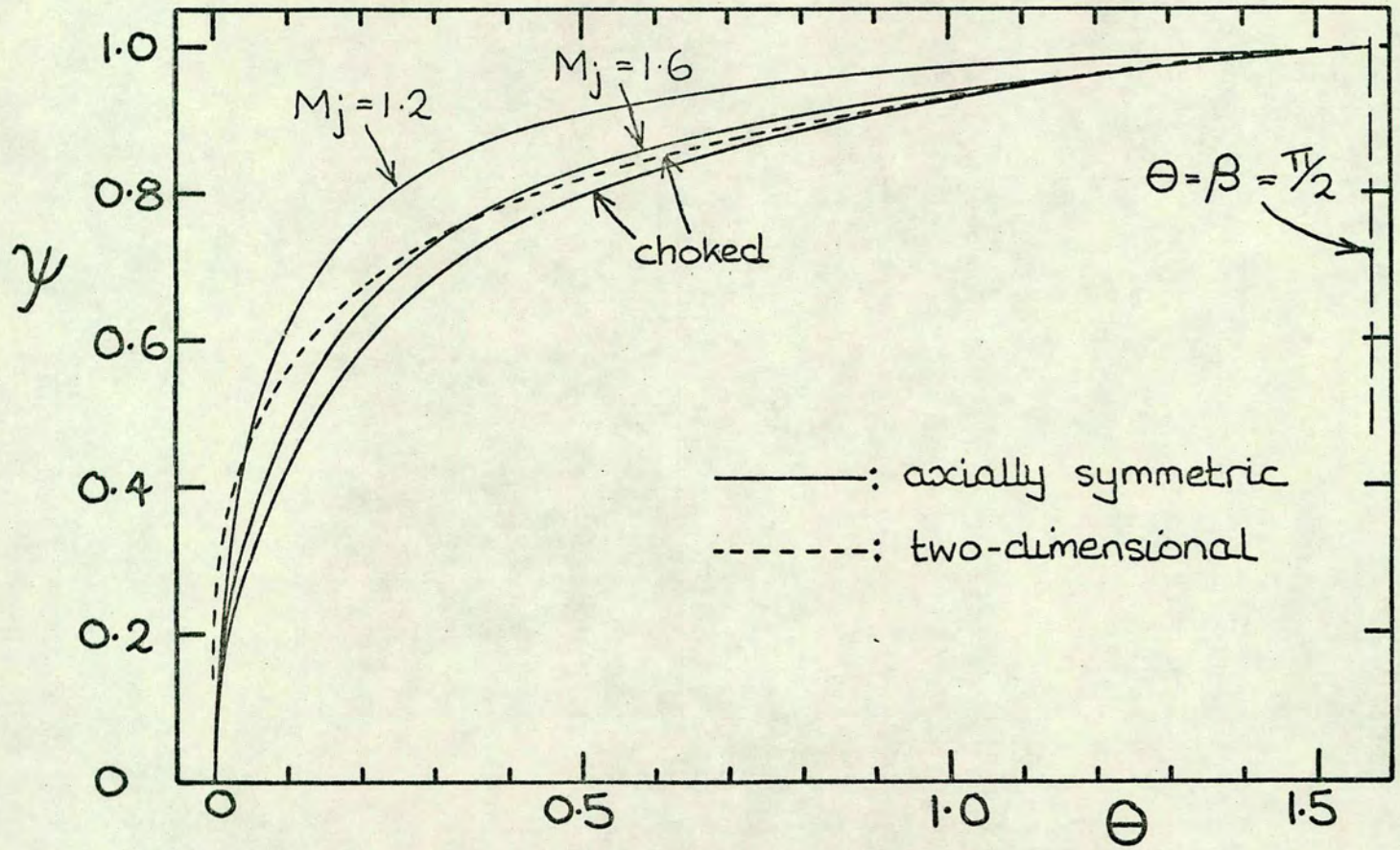

Fig. 4.20 Stream function distribution along sonic line : $\psi = \psi_s(\theta)$

$(\beta = 90^\circ \quad \gamma = 1.4 \quad V_e = 0)$

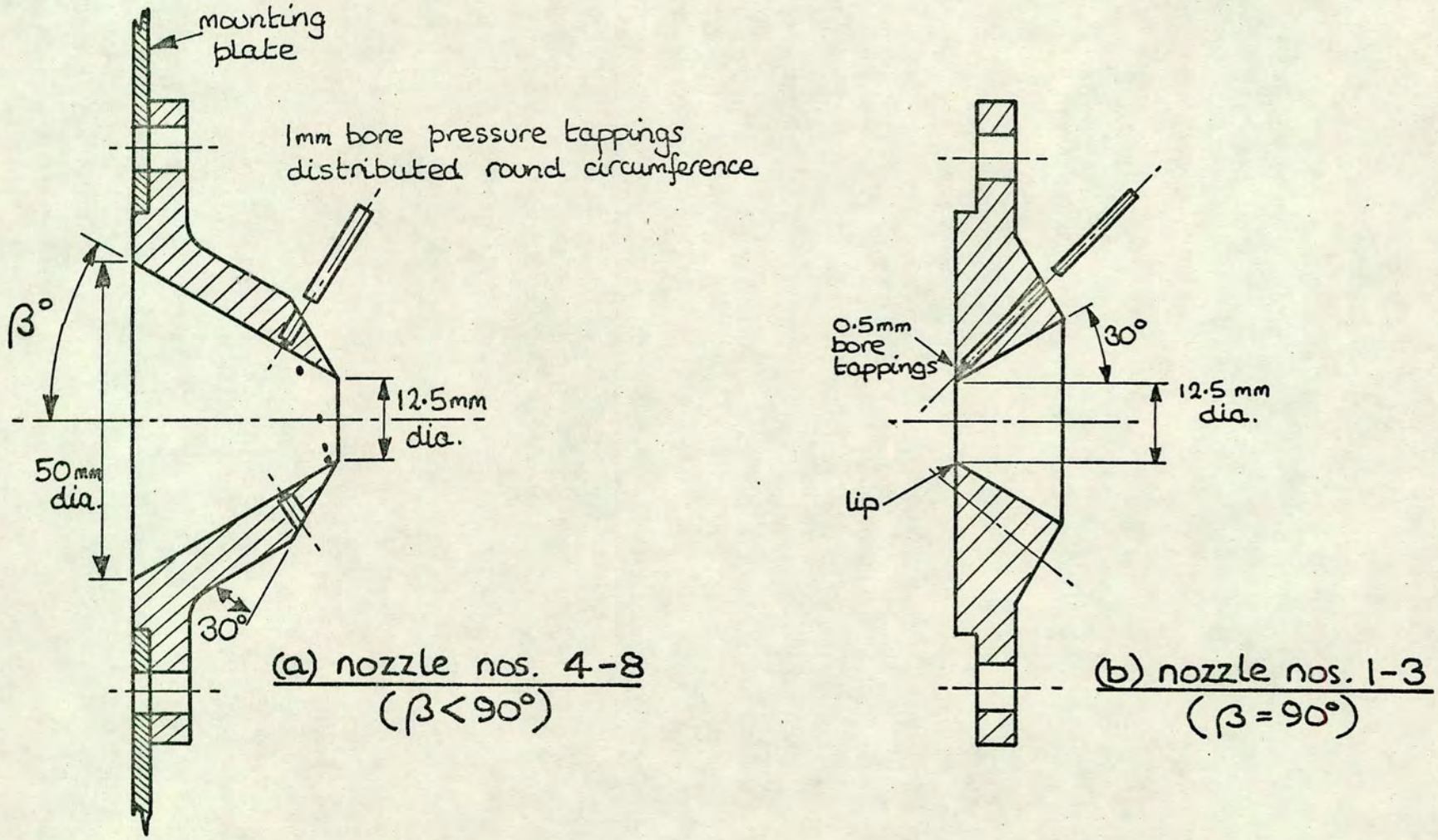

Fig. 5·1 Design of nozzles for axially symmetric experiments

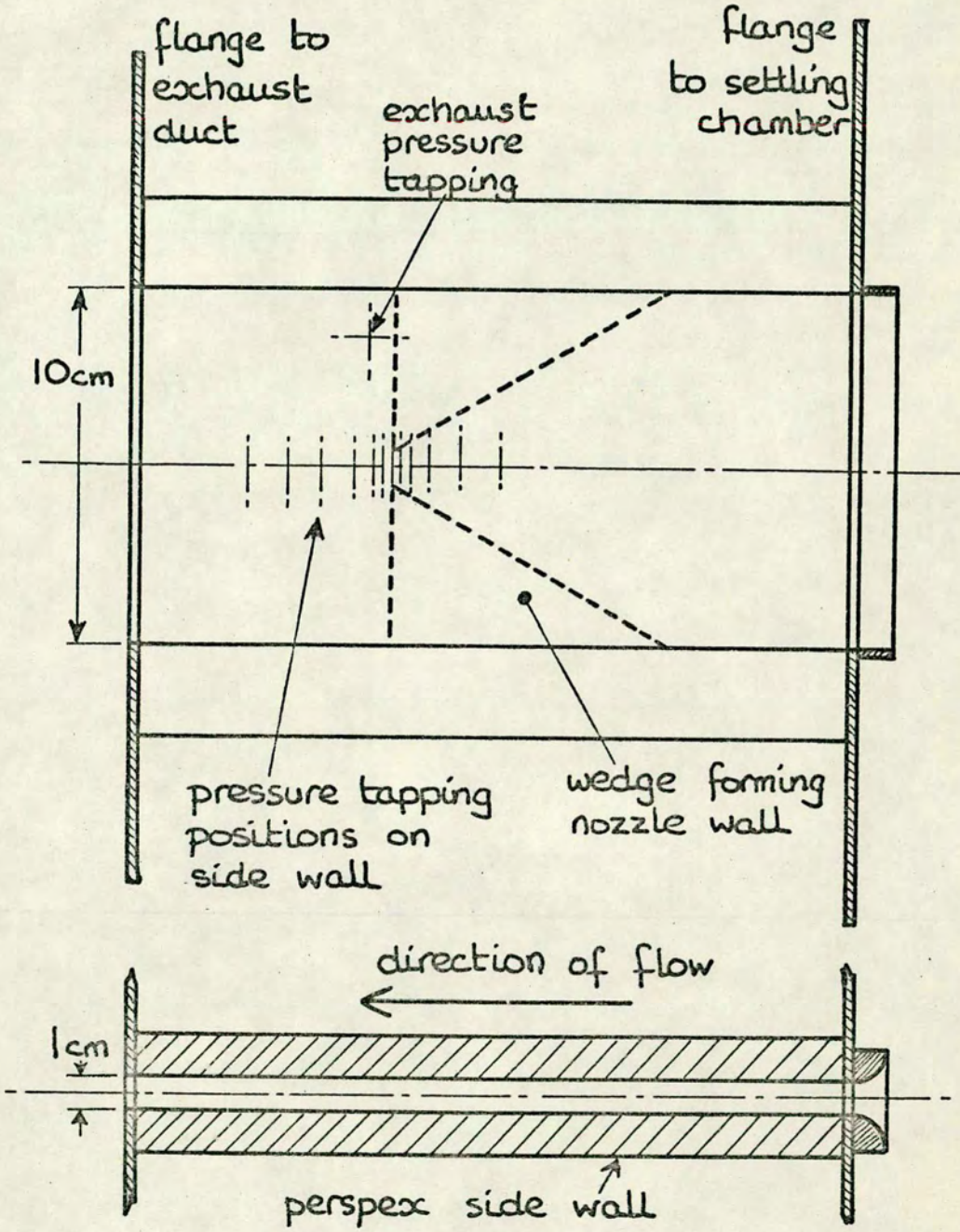

Fig. 5·2 Test section for two-dimensional experiments (showing case $\beta = 30°$)

scale : 1/2

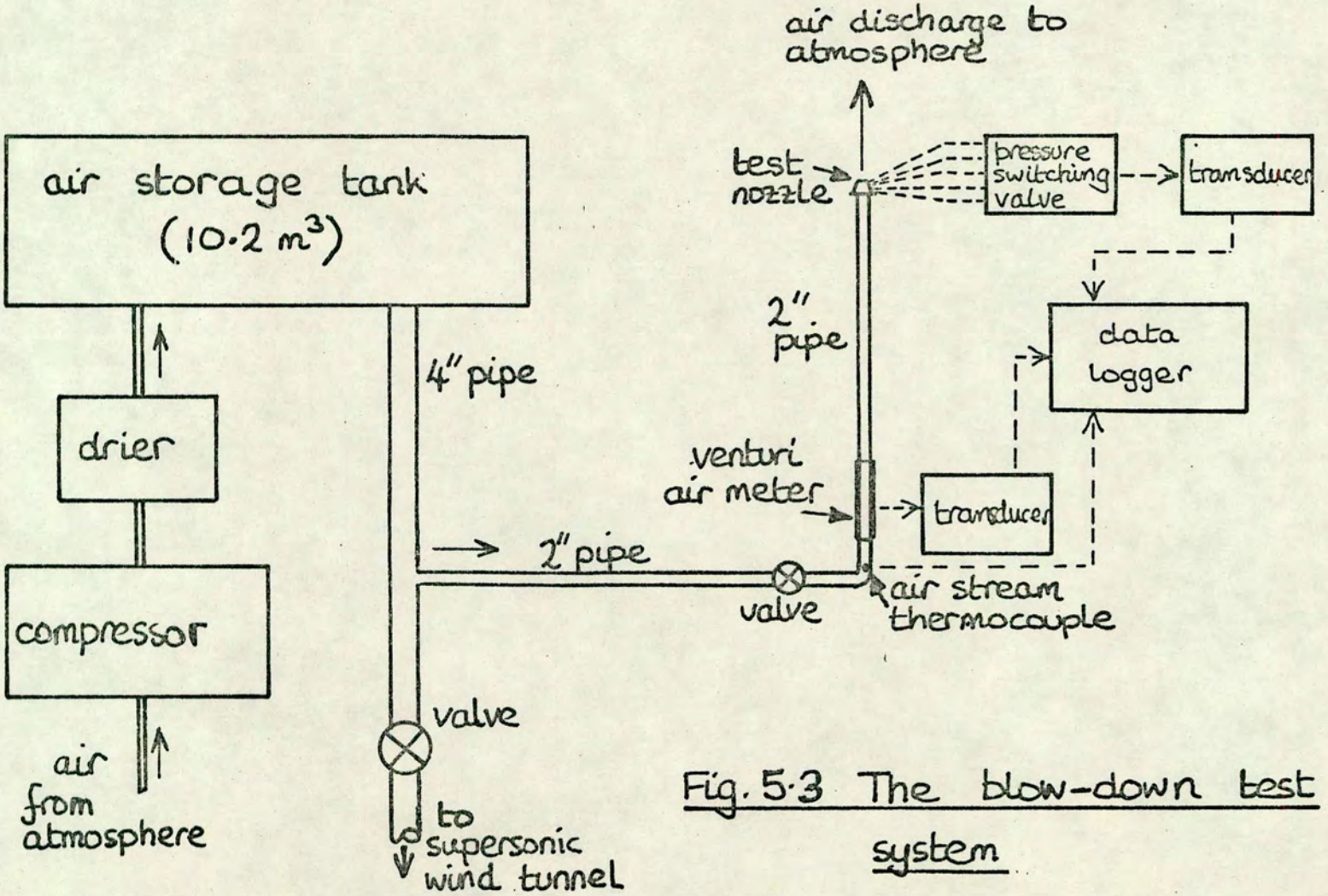

Fig. 5·3 The blow-down test system

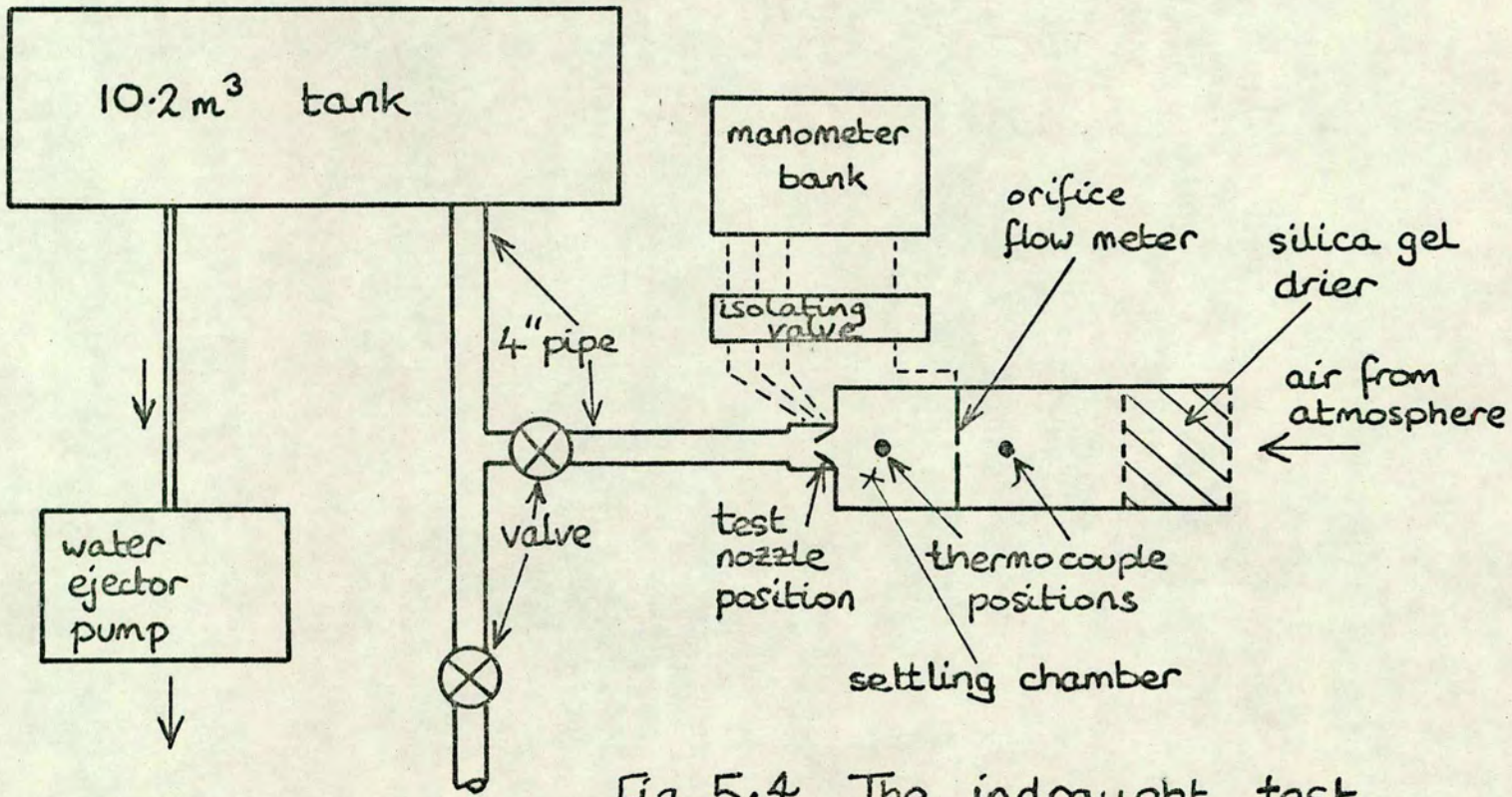

Fig. 5·4 The indraught test system

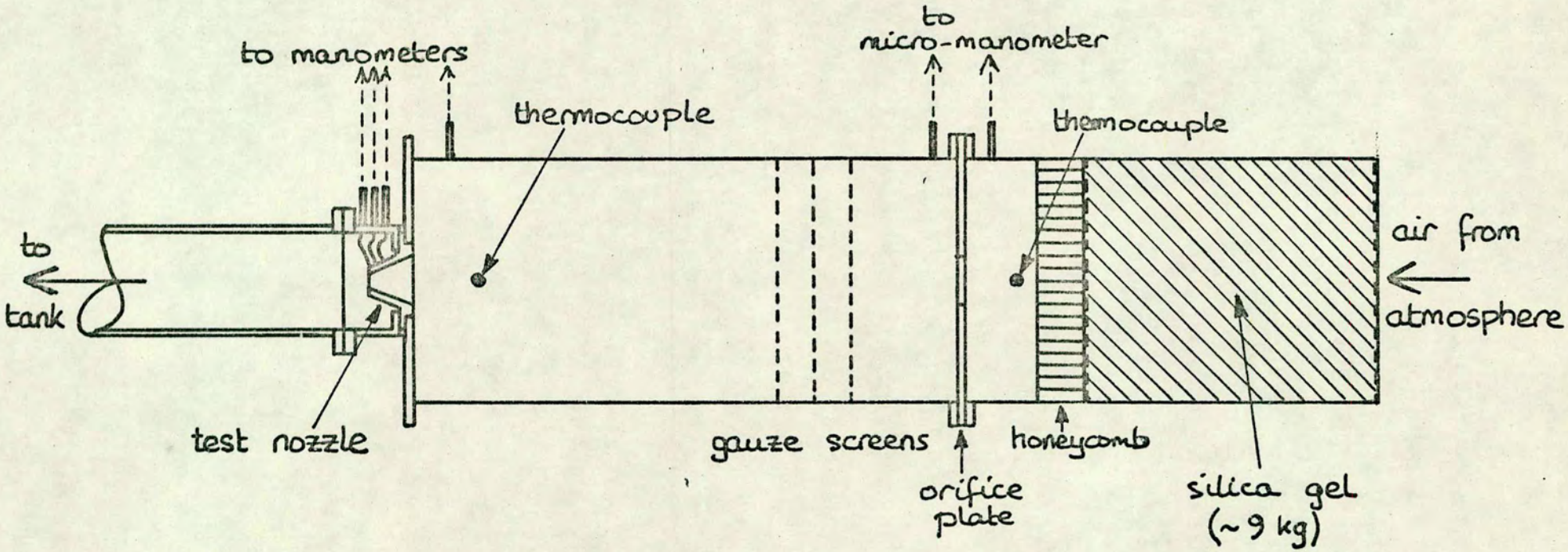

Fig 5.5 Indraught apparatus – test section

(scale : 1/6)

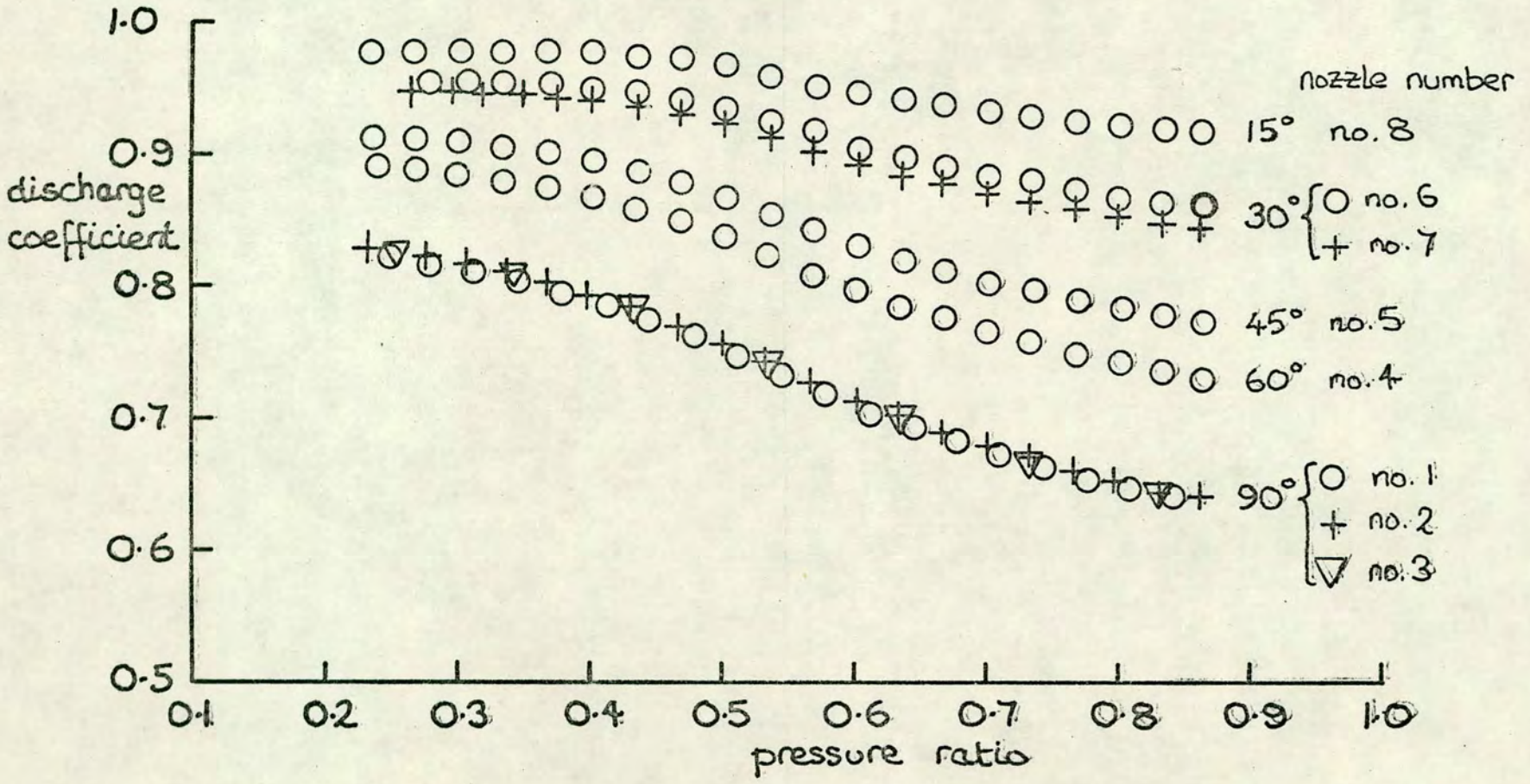

Fig. 5·6 Experimental results – discharge coefficients for axially symmetric nozzles.

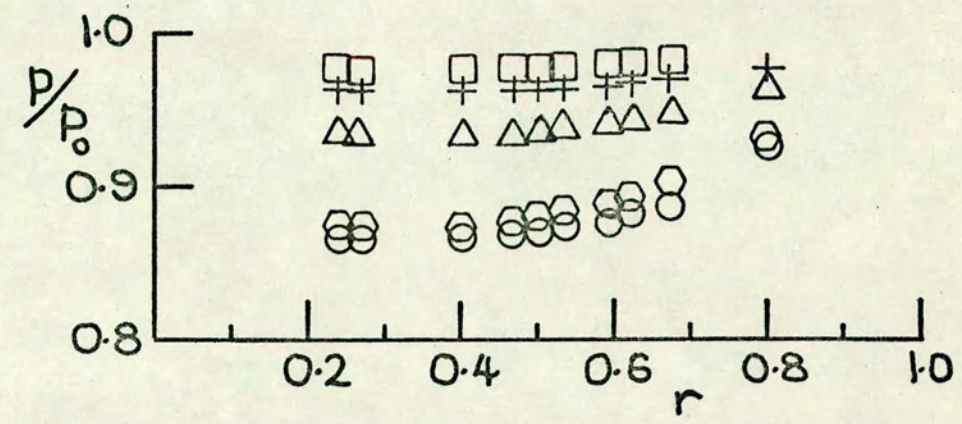

values of y_l/y } ○ : 0·894 △ : 0·773 □ : 0·598
○ : 0·885 + : 0·678

(a) nozzle no. 6 – $\beta = 30°$

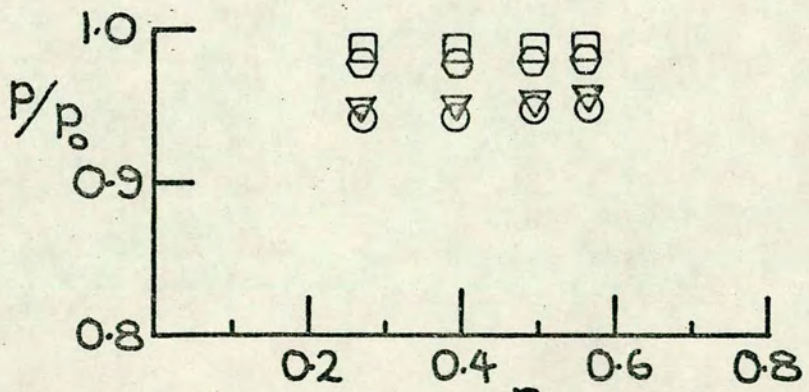

values of y_l/y } ○ : 0·825 ⬡ : 0·681
▽ : 0·814 □ : 0·596

(b) nozzle no 4 – $\beta = 60°$

Fig. 5·7 Experimental results – wall pressures on axially symmetric nozzles

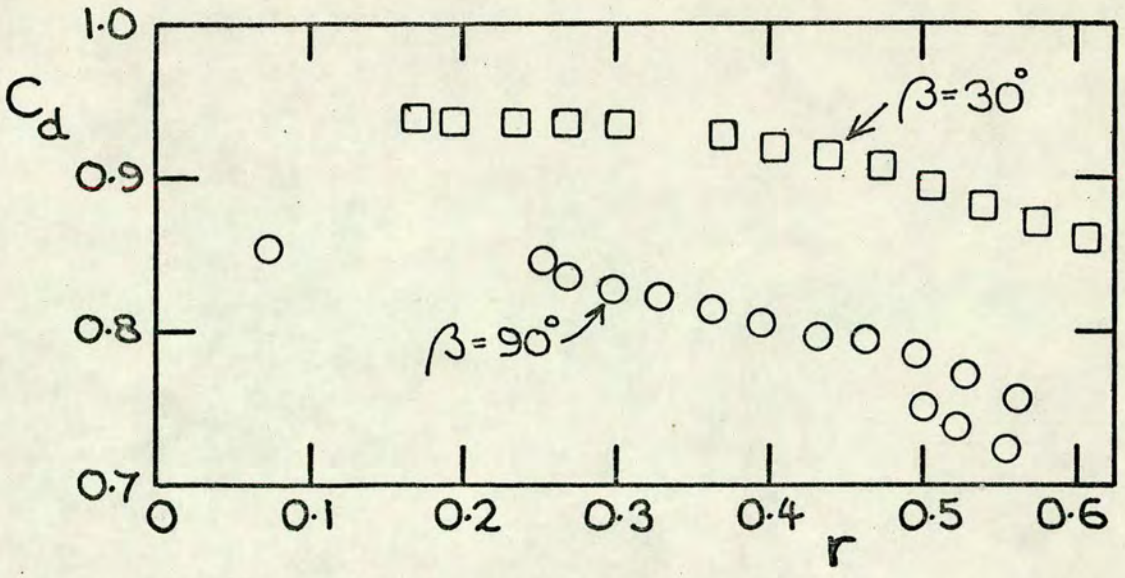

Fig. 5·8 Experimental results – discharge coefficients for two-dimensional nozzles

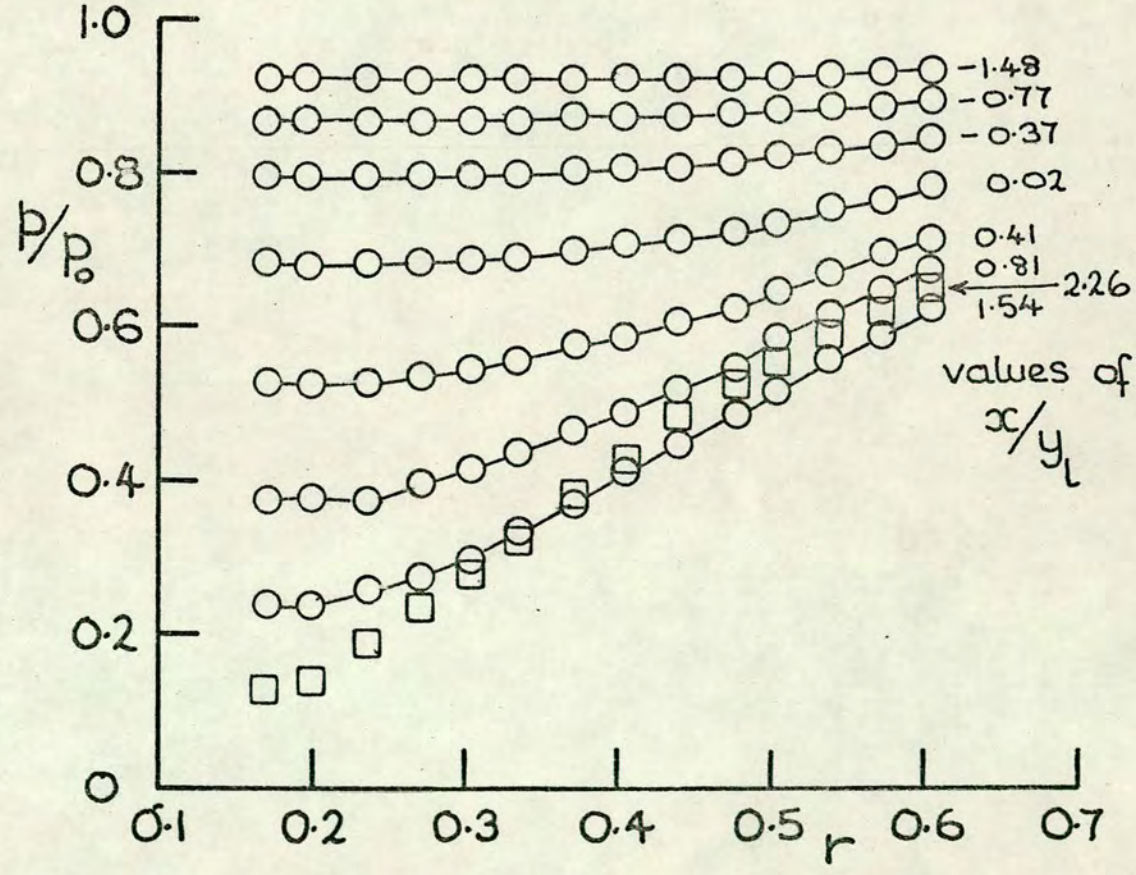

Fig. 5·9 Experimental results – pressures on axis for 30° two-dimensional nozzle

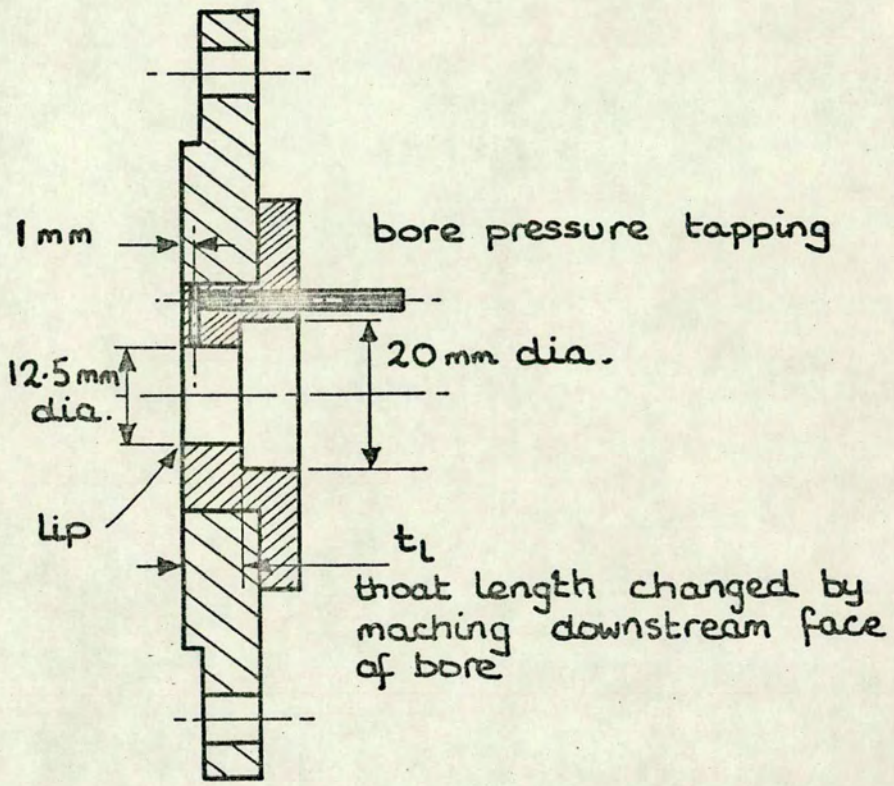

Fig. 5·10 Section through axially symmetric, parallel-throat nozzle

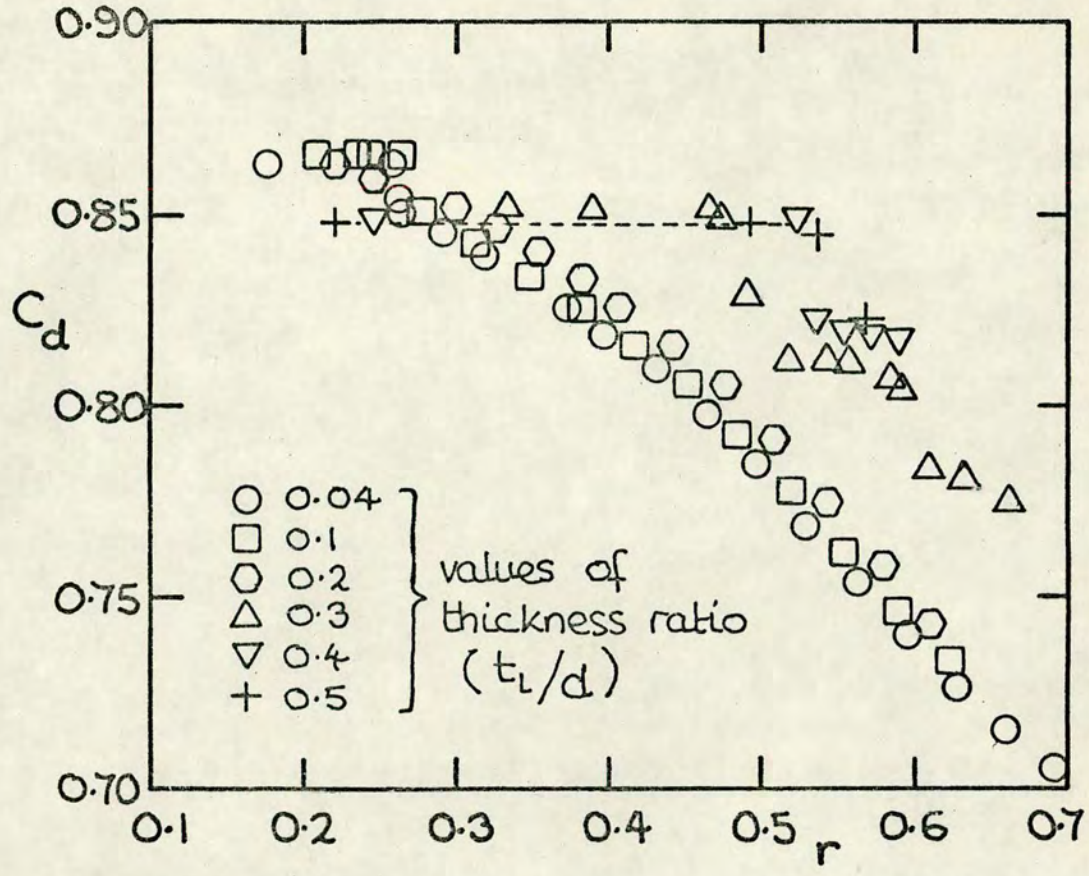

Fig. 5·11 Experimental values of discharge coefficient for parallel-throat nozzle

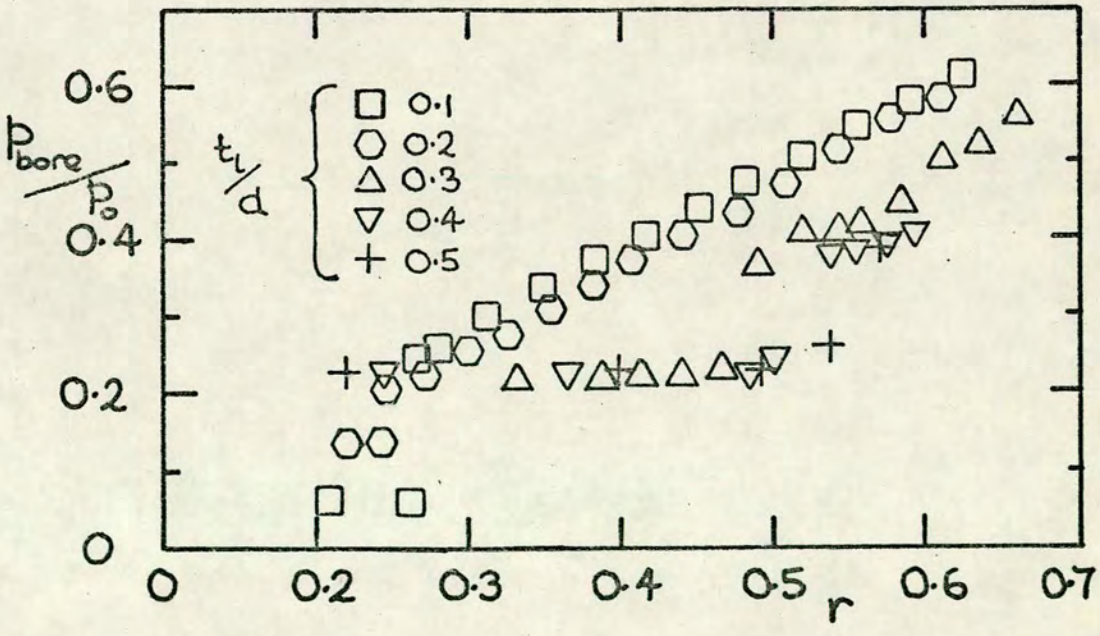

Fig. 5·12 Experimental values of bore pressure for parallel-throat nozzle

Fig. 6·1 Discharge coefficients, $\beta = 90°$, axially symmetric — theory and experiment.

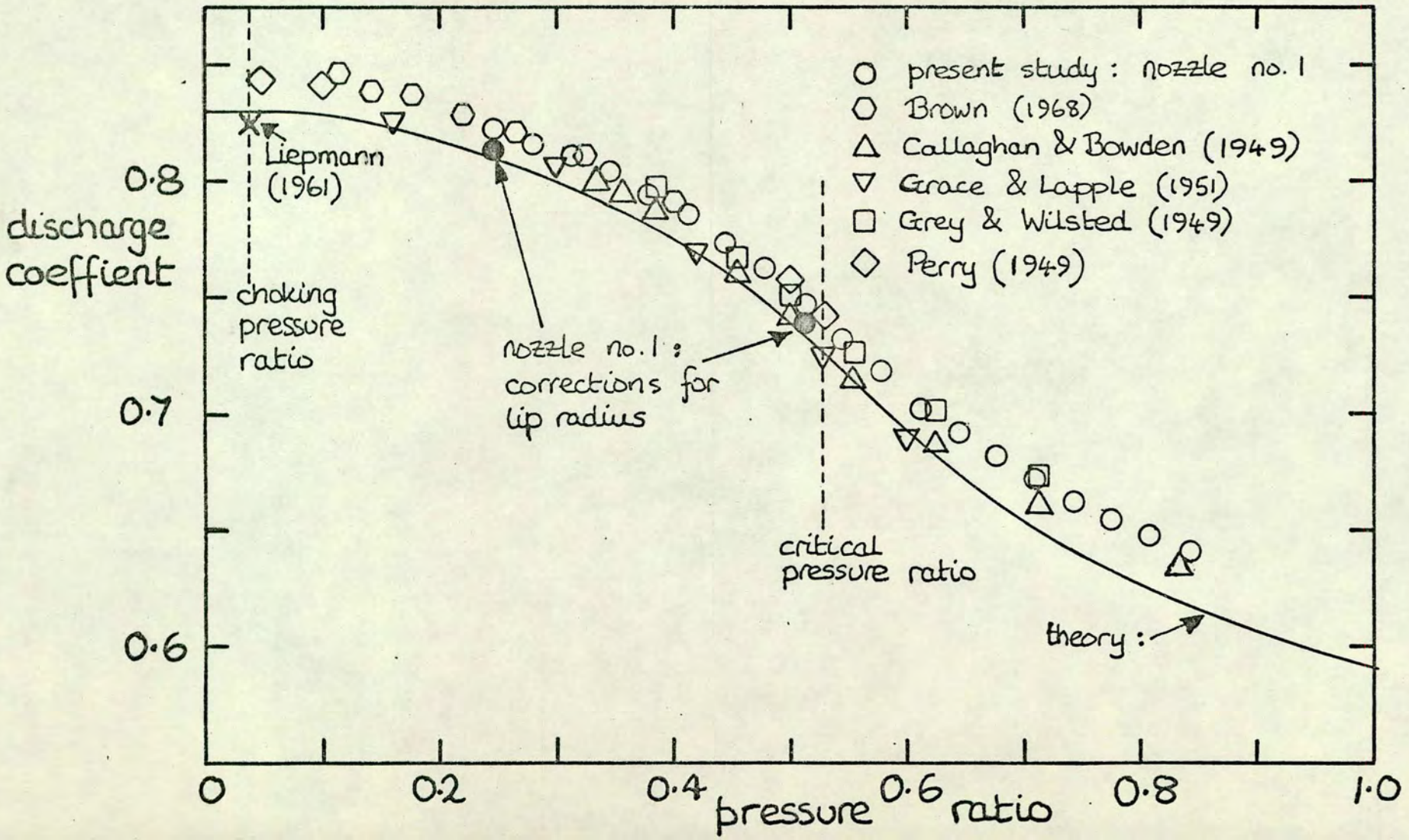

Fig. 6·2 Discharge coefficients, $\beta = 45°$ & $60°$, axially symmetric – theory and experiment

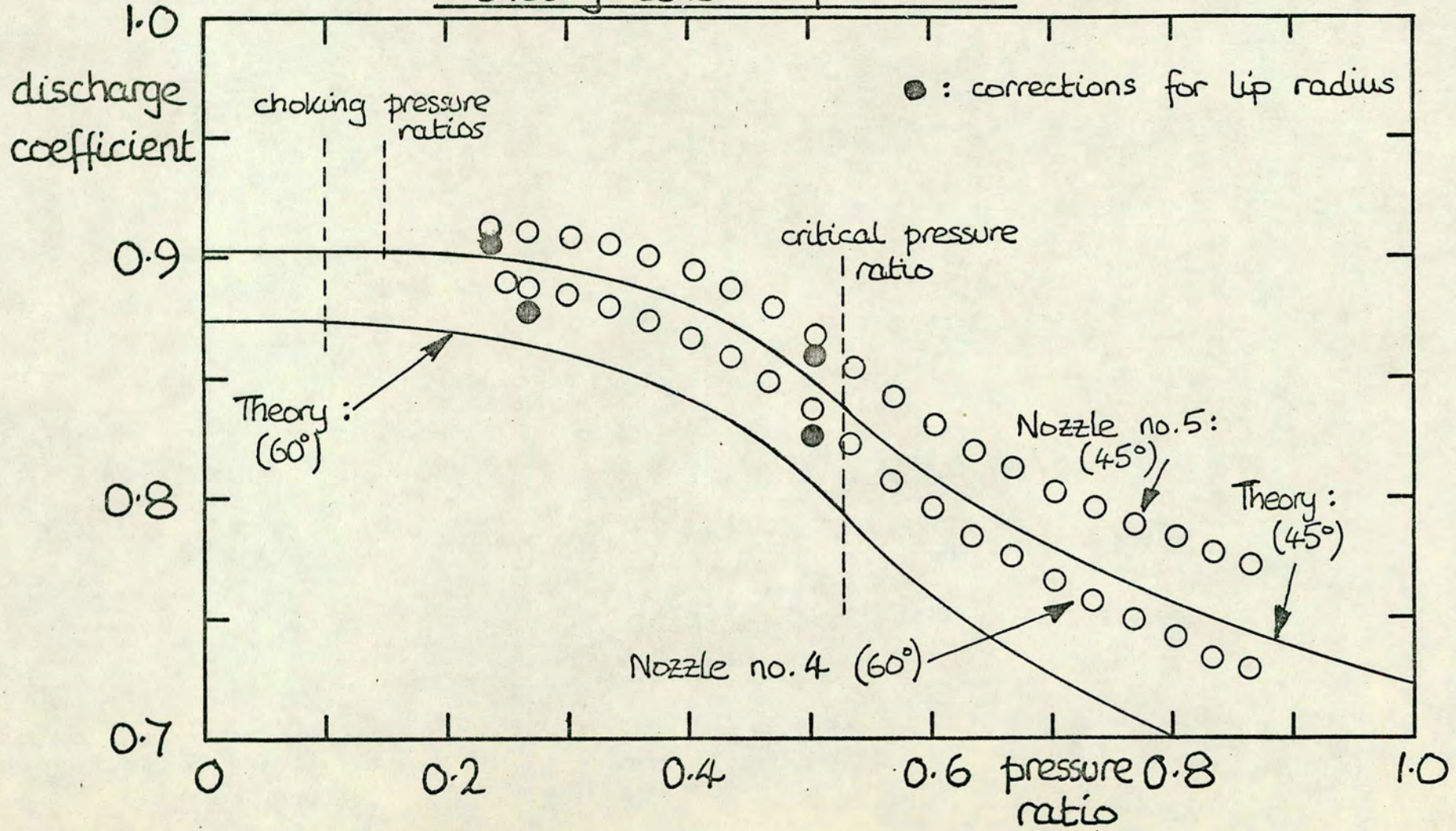

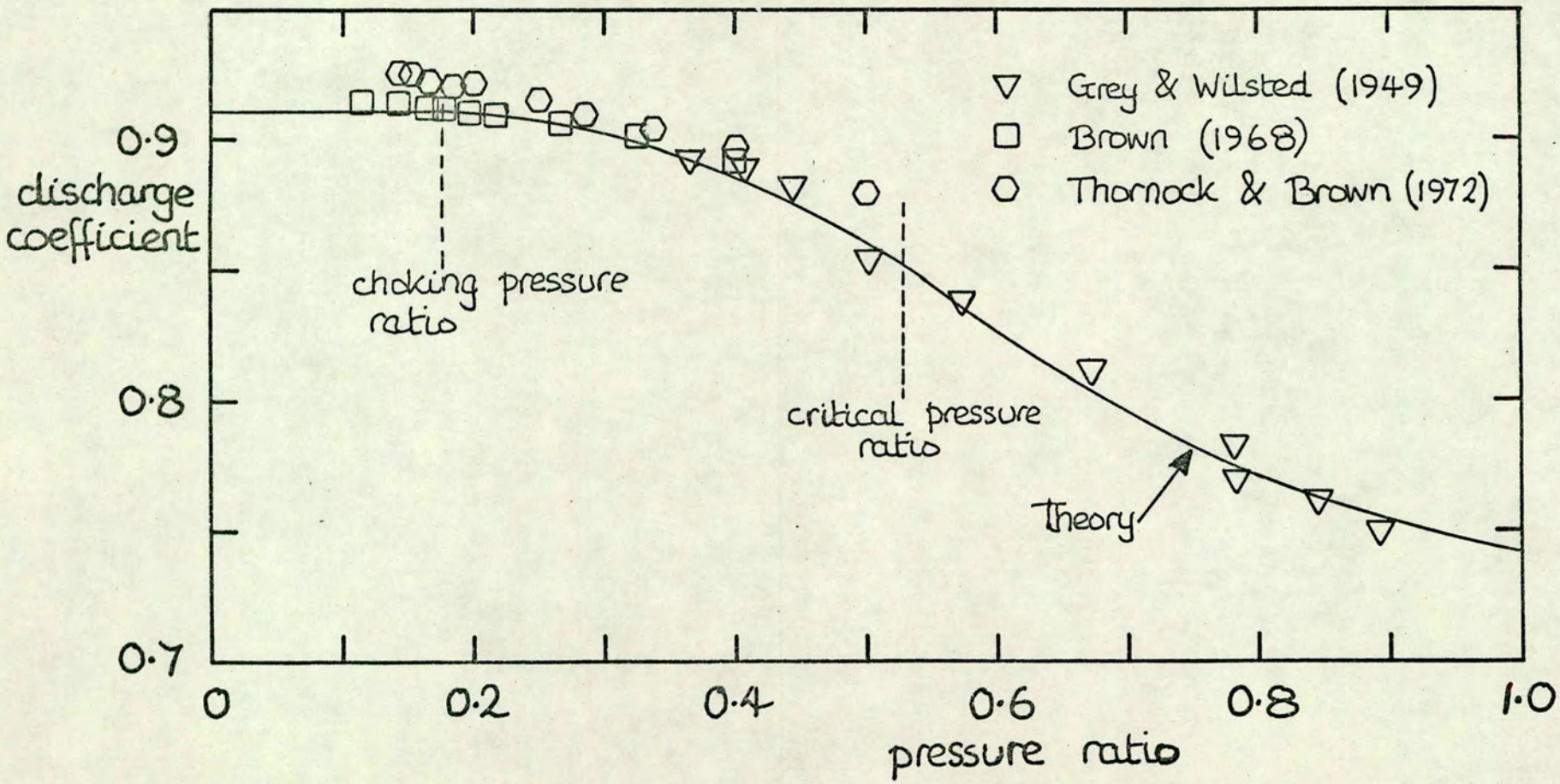

Fig. 6·3 Discharge coefficients, $\beta = 40°$, axially symmetric — theory and experiment

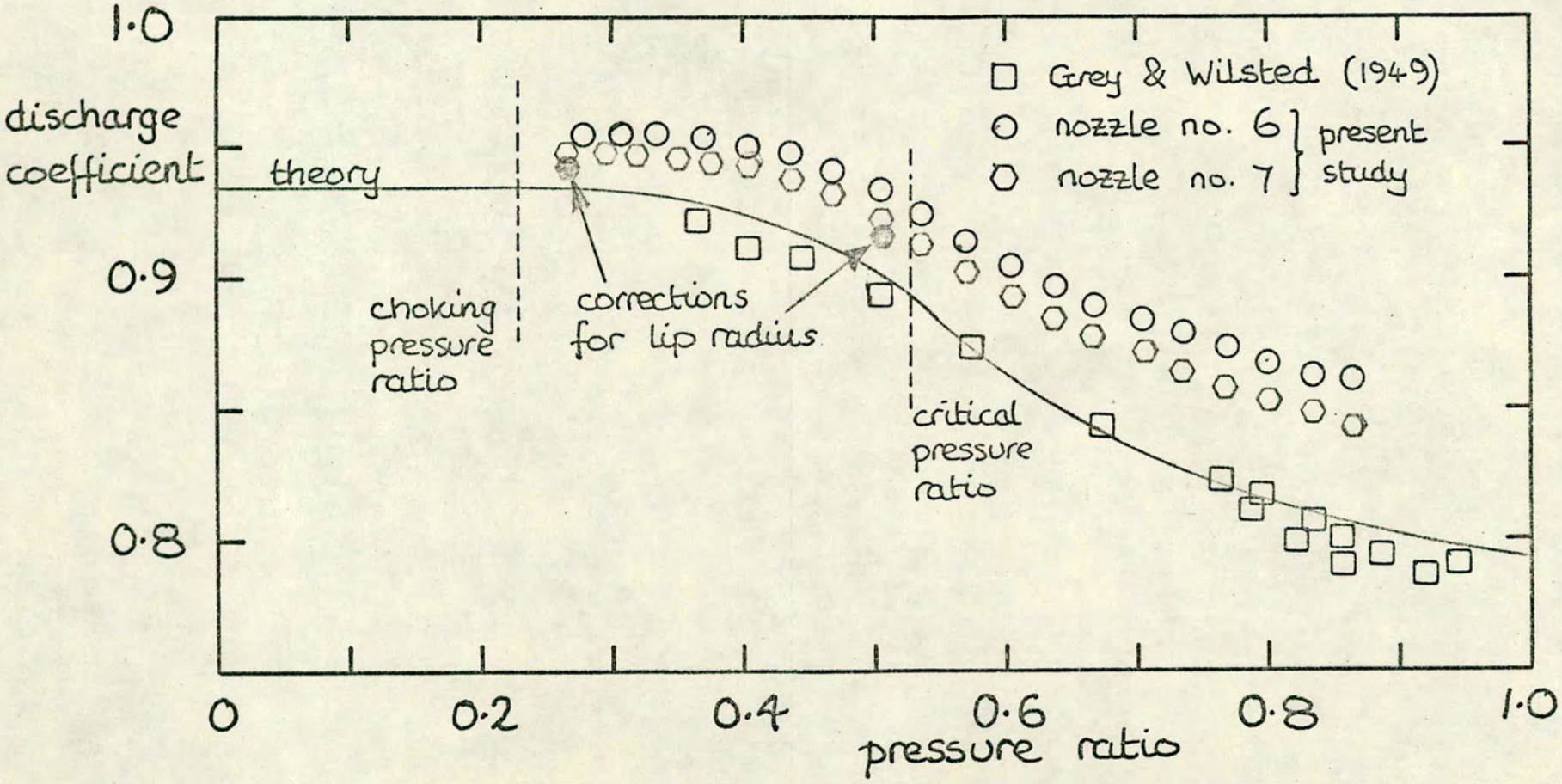

Fig. 6·4 Discharge coefficients, $\beta = 30°$ axially symmetric — theory and experiment.

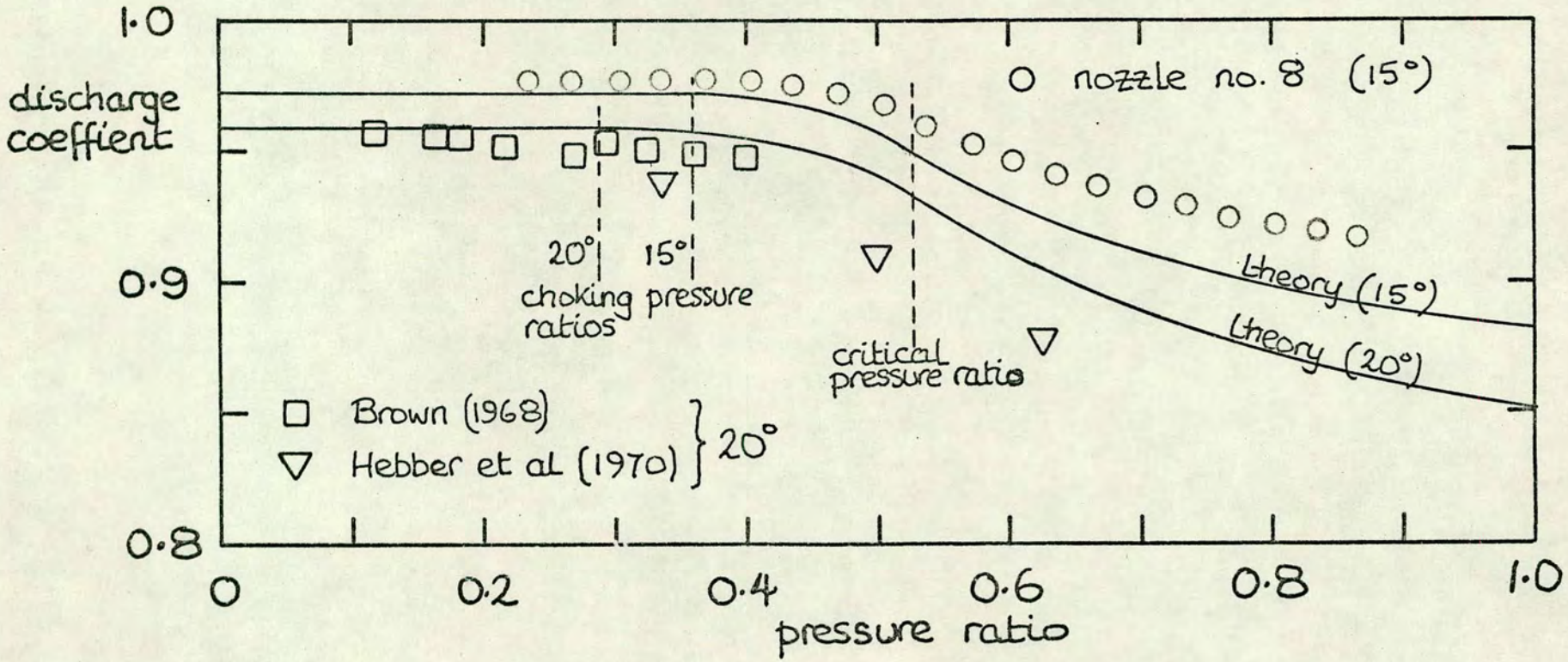

Fig. 6·5 Discharge coefficient, $\beta = 15°$ & $20°$, axially symmetric — theory and experiment.

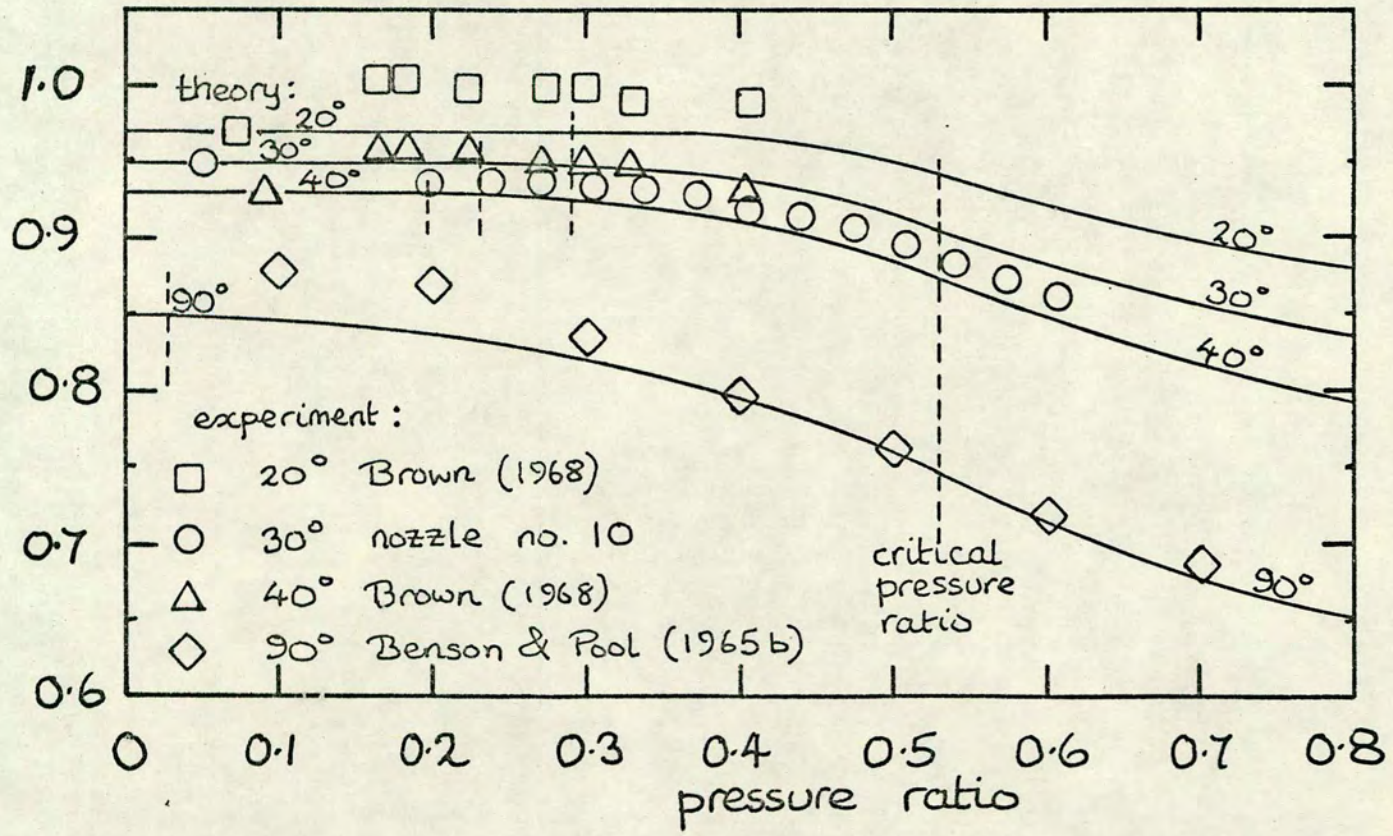

Fig. 6·6 Discharge coefficients – $\beta = 20°, 30°, 40°, \& 90°$ – two-dimensional, theory and experiment.

Fig 6·7 Axially symmetric wall velocities.

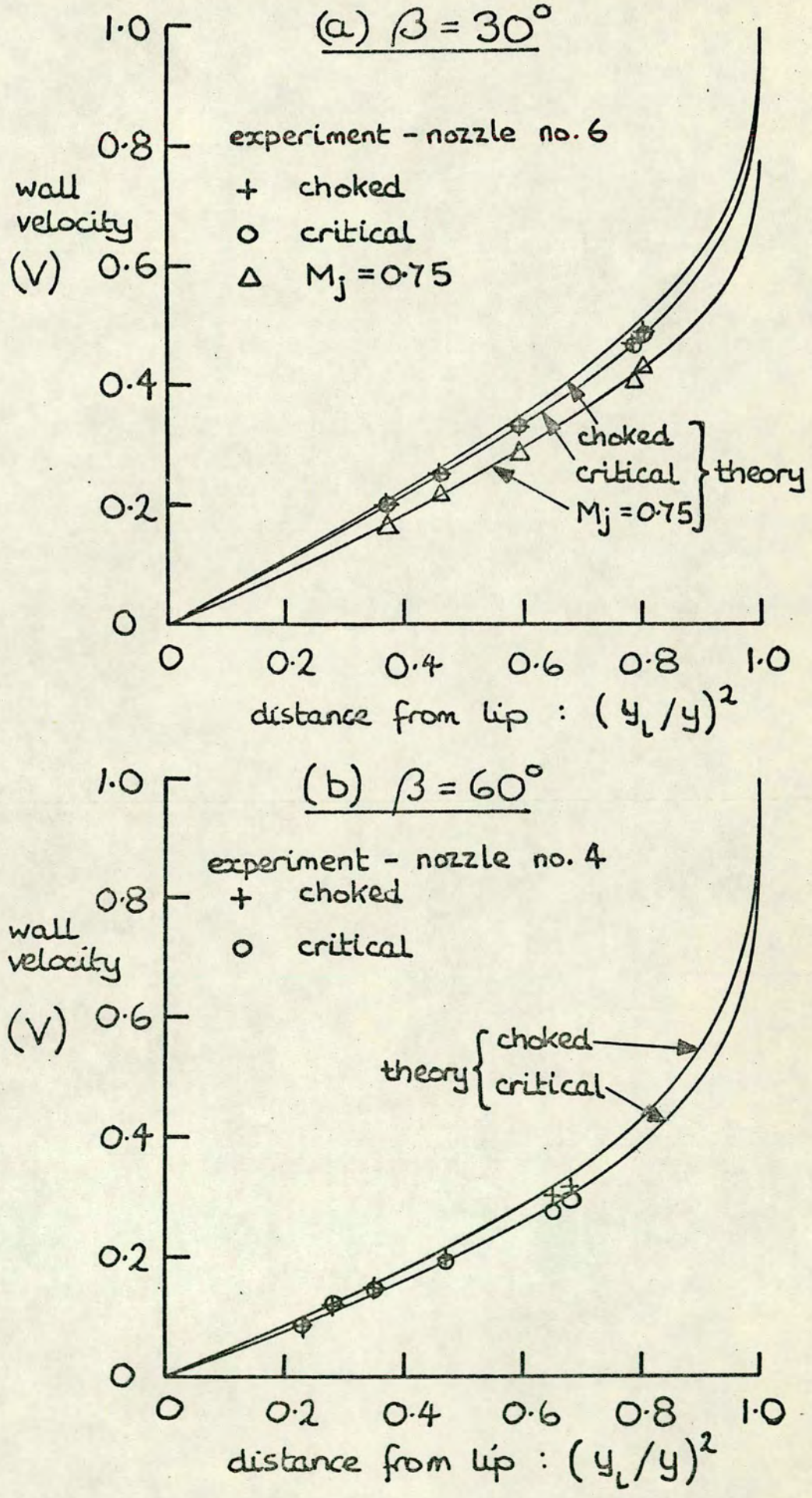

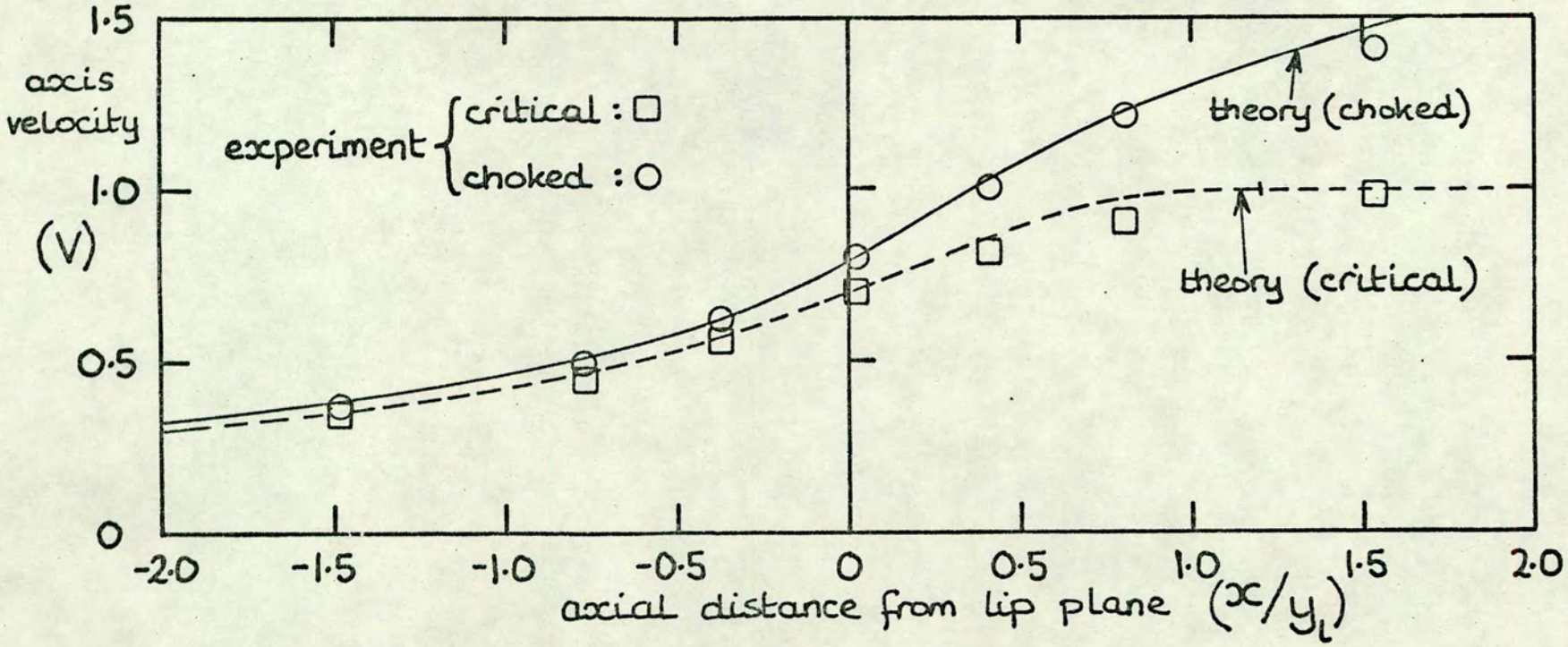

Fig. 6·8 Velocity on axis of two-dimensional nozzle ($\beta = 30°$) — theory and experiment.

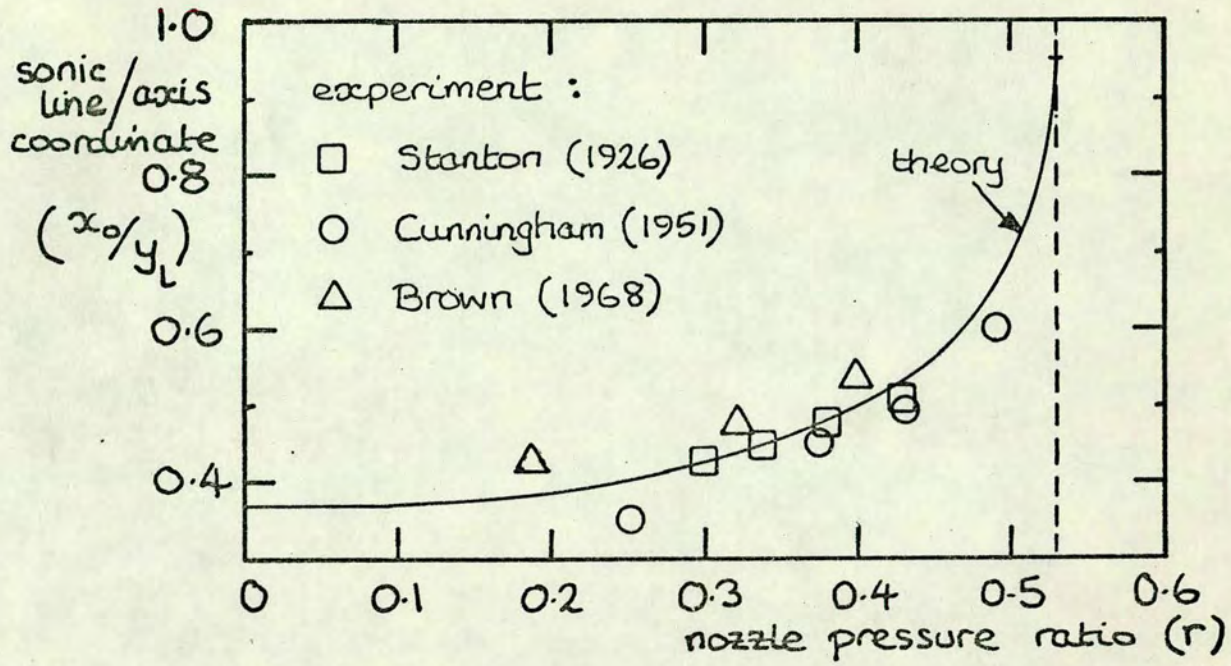

Fig. 6·9 Sonic-line/axis intersection point – effect of pressure ratio ($\beta = 90°$, $\gamma = 1.4$, axially symmetric)

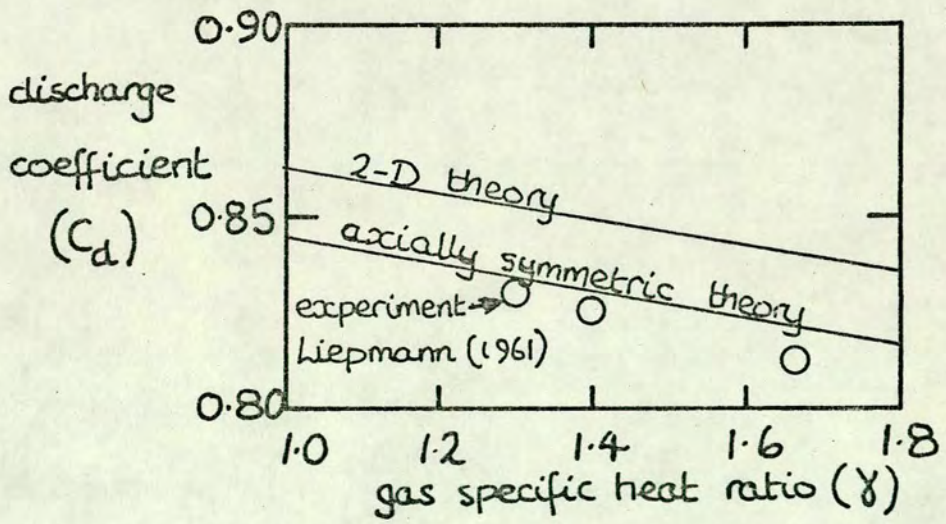

Fig. 6·10 Effect of γ on choked discharge coefficient. – $\beta = 90°$

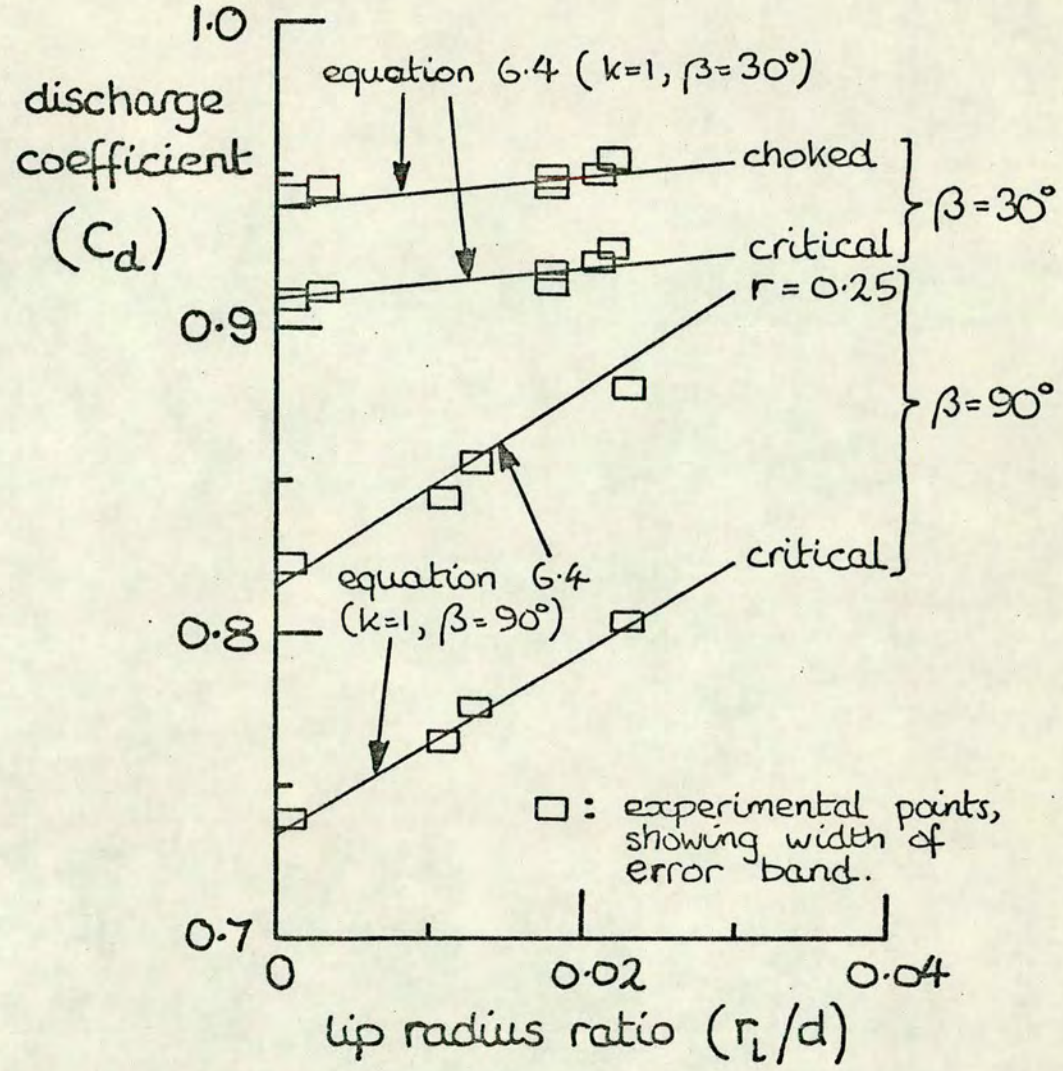

Fig. 6·11 Effects of lip radius (axially symmetric)

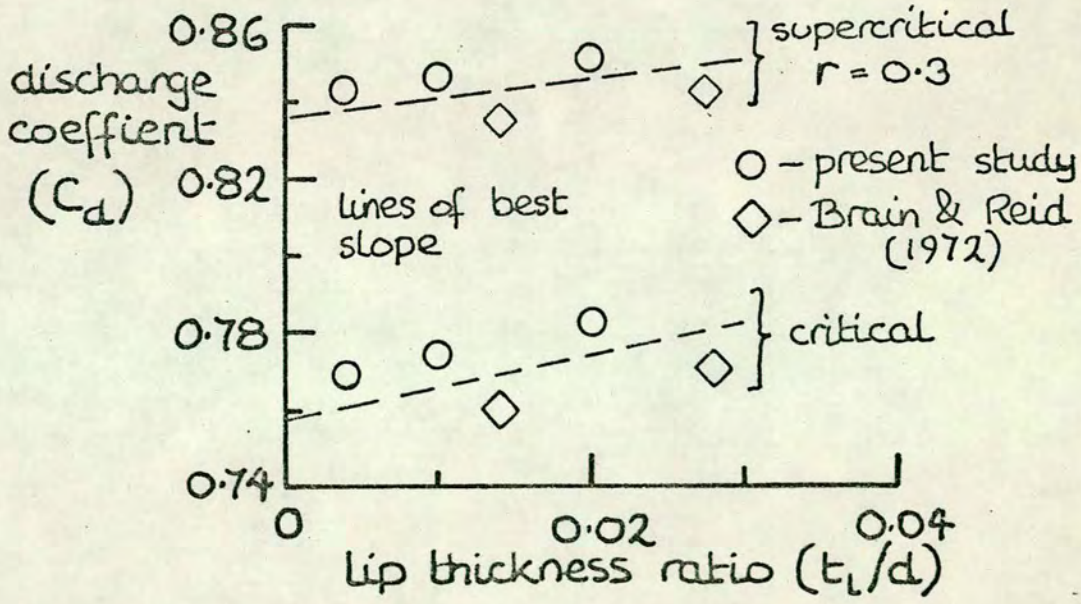

Fig. 6·12 Effect of parallel throat (β=90°)

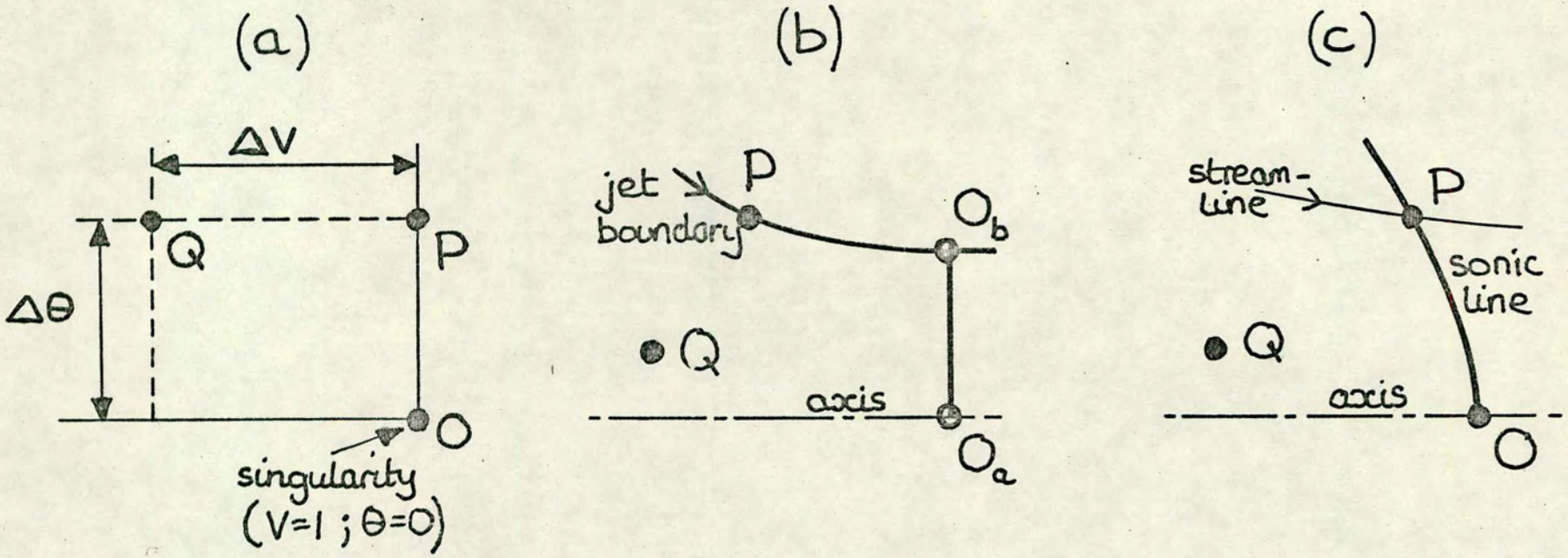

Fig. A1. (a) Corner of hodograph plane at (V=1 ; θ=0)
Corresponding region of physical plane for:
(b) critical flow
(c) supercritical flow.

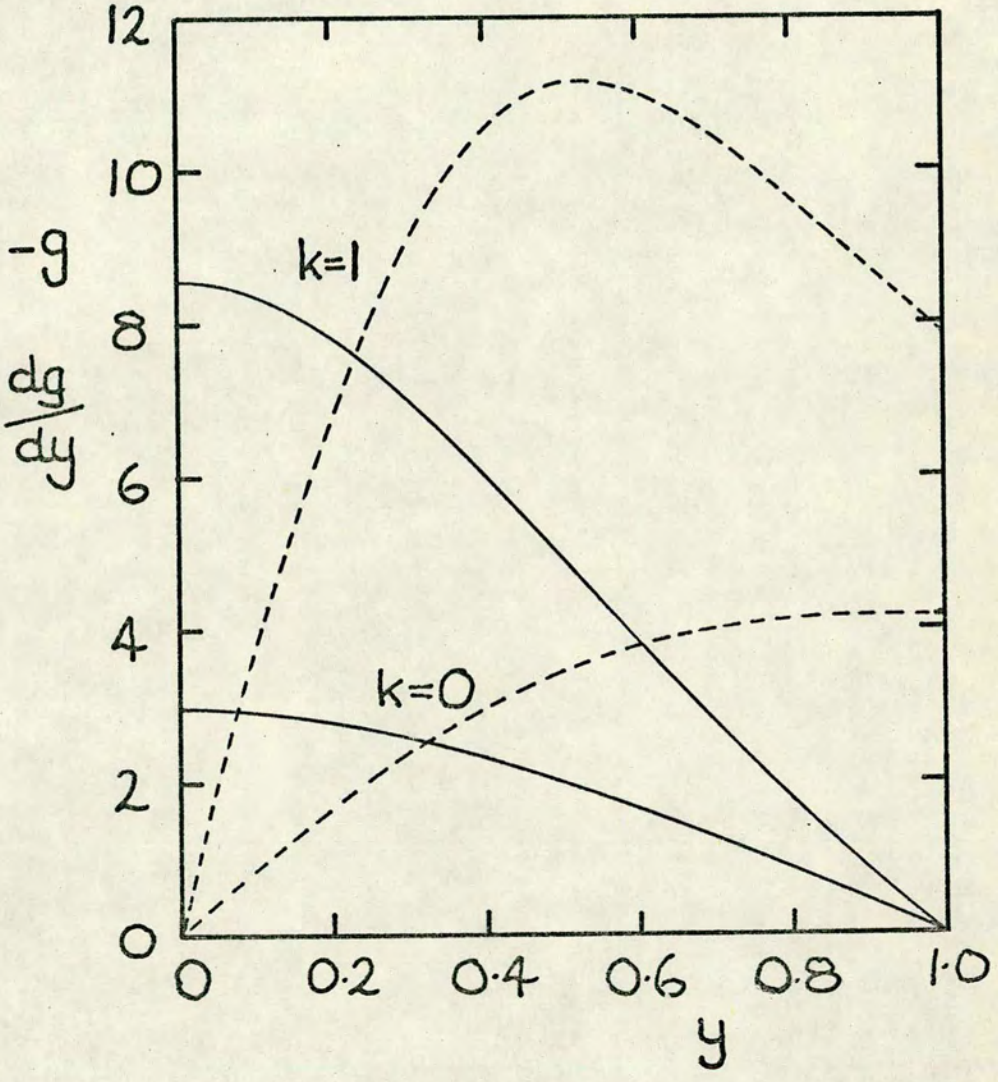

Fig. A2 Solutions to the equation:

$$g^2 - \frac{k}{y}\frac{dg}{dy} + \frac{d^2g}{dy^2} = 0$$

g : —— (n.b. -g plotted)

$\frac{dg}{dy}$: - - - -

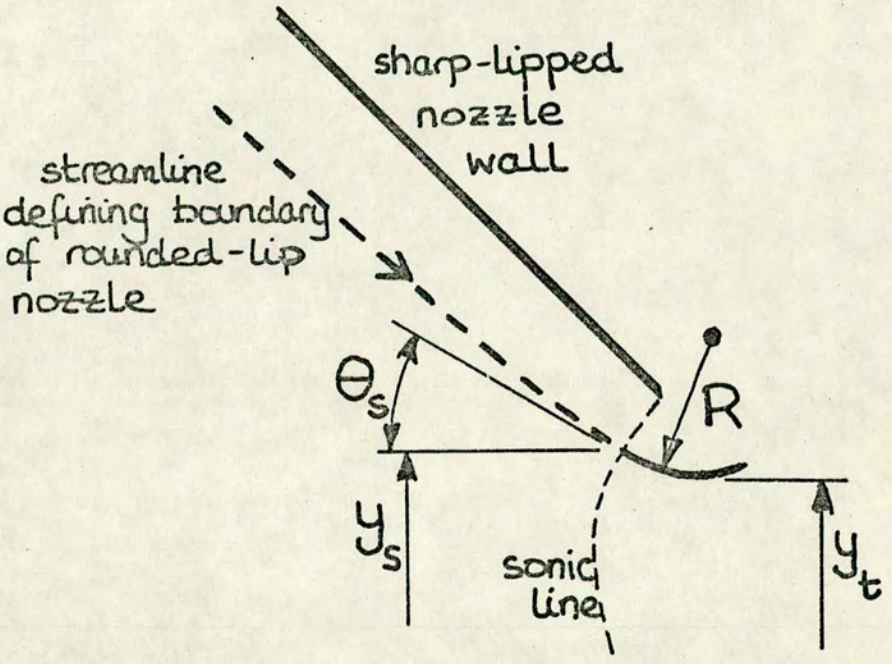

Fig. C1 Streamline defining nozzle with finite lip radius